DISS. ETH NO. 29785

EFFECTS OF CREEP ON THE INTERACTION BETWEEN TBM, LINING AND ROCK

A thesis submitted to attain the degree of

DOCTOR OF SCIENCES

(Dr. sc. ETH Zurich)

presented by

THOMAS LEONE

M.Sc. ETH Civil Eng., ETH Zurich

born on 04.12.1988

accepted on the recommendation of

Prof. Georgios Anagnostou

Dr. Alexandros N. Nordas

Prof. Daniele Peila

Prof. Frédéric Pellet

Dr. Marco Ramoni

2024

Acknowledgements

I would like to express my deepest gratitude to my supervisor Prof. Georgios Anagnostou (ETH Zurich) for supporting me and guiding me throughout all these years of my PhD studies in his institute. I am also deeply grateful to Dr. Alexandros N. Nordas who supported me in writing and structuring my work over the last years.

I extend my appreciation also to my second supervisor Dr. Marco Ramoni (Basler & Hofmann). Our valuable discussions and his corrections to the chapters of the dissertation helped me shape my work. Moreover, I am grateful to Prof. Daniele Peila (Politecnico di Torino) and Prof. Frédéric Pellet (INSA Lyon) for agreeing to serve as co-examiner and for their valuable feedback for the correction of my thesis.

I would also like to extend my gratitude to the Swiss National Science Foundation (SNF), which financed this dissertation within the framework of the SNF research project No. 200021_159982.

Thanks also goes to Dr. Erich Pimentel, who helped me improve my understanding on the physics of time dependency in creeping ground. Additionally, I would like to acknowledge my colleagues Thomas Pferdekämper and Antonia Nousiou for the valuable discussions and support of my work.

I am also deeply thankful to Locher Ingenieure AG, in particular to Marcel Rogenmoser (CEO) and Christoph Weiler (project manager) who gave me the opportunity to work in the company in parallel with finalising my dissertation.

Finally, I wish to thank my family, particularly my partner Isabella, for her continuous support and encouragement throughout the years of my PhD. I would like to dedicate this thesis in loving memory of my grandmother Rita (1929 - 2022) as well as my uncle Mario (1940 - 2023), who worked in underground construction for many years and gave me the inspiration to start my career in this field.

Thomas Leone

Zürich, January 2024

Summary

Mechanised tunnelling through squeezing ground is very demanding because the space available to accommodate ground deformations is limited. If the converging ground closes the shield gap in the machine area, a pressure starts to develop upon the shield and the tunnel boring machine (TBM) might get stuck. Behind the machine, if ground deformations are prevented by a stiff lining, a prohibitively high rock pressure develops, and the lining might get damaged. Shield jamming and lining damages are the main hazards while tunnelling in squeezing ground conditions, and may increase significantly construction cost.

Ground deformations are often assumed to occur instantaneously. This assumption might result in overestimating the rock pressure acting upon the shield during TBM advance and short standstills, as field records suggest that ground deformations develop over time. Time-dependency can be traced back to the rheological behaviour of the ground (creep) or to the dissipation of excess pore water pressure (consolidation).

This dissertation aims to help improve the design and construction of tunnels excavated with TBM in squeezing ground considering especially the effect of creep. More specifically, motivated by the simplified approach of typical TBM-ground interaction analyses, the present thesis: (i) analyses numerically the effect of creep on the evolution of rock pressure over time and proposes a novel method for simulating the TBM advance which improve the reliability of shield jamming and lining damage risk assessment in squeezing ground; (ii) develops an equation based on numerical results and pre-existing nomograms for estimating the required thrust force in order to prevent shield jamming under creeping squeezing ground conditions during ongoing TBM advance, as well as, during construction standstills; (iii) compares numerically the effect of creep and consolidation on shield tunnelling and discusses whether these could be distinguished in practical situations; (iv) investigates numerically whether the risk of shield jamming depends on the tunnel diameter and assess the effect of an adjacent tunnel on shield loading.

Zusammenfassung

Maschineller Vortrieb durch druckhafte Gebirge ist sehr anspruchsvoll, weil der verfügbare Platz um Baugrundverformungen zuzulassen sehr limitiert ist. Schliesst der Baugrund die Spaltbreite im Maschinenbereich, so entsteht ein Druck auf dem Schild und die Tunnelbohrmaschine (TBM) kann sich verklemmen. Dagegen wenn Verformungen hinter dem Schildbereich von einem starren Ausbau verhindert werden, kann sich ein sehr hoher Druck aufbauen und der Ausbau kann sich beschädigen. Verklemmen des Schildes und Beschädigung des Ausbaus sind die hauptsächlichen Gefährdungsbilder, welche im Tunnelbau im druckhaften Gebirge eintreten können und die Baukosten erheblich erhöhen können.

Verformungen vom Baugrund werden oft als zeitunabhängig angenommen. Diese Annahme kann zu einer Überschätzung der Schildbelastung während des Vortriebs und bei kurzen Stillständen führen. Feldmessungen zeigen jedoch, dass sich diese Verformungen langsam im Laufe der Zeit entwickeln. Zeitabhängigkeit kann aufgrund des rheologischen Verhaltens des Bodens (Kriechen) oder durch Dissipation von Porenwasserüberdruck (Konsolidation) herbeigeführt werden.

Diese Dissertation soll dazu beitragen, die Planung und den Bau von Tunneln, die im TBM Vortrieb im druckhaften Gebirge aufgefahren werden, zu verbessern, wobei insbesondere die Auswirkungen von Kriechen berücksichtigt werden. Motiviert durch den vereinfachten Ansatz einer typischen TBM-Baugrund Interaktionsanalyse untersucht die vorliegende Dissertation: (i) numerisch den Effekt von Kriechen auf den zeitabhängigen Gebirgsdruck und schlägt eine neue Methode zur Simulation des TBM-Vortriebs, welche die Zuverlässigkeit für die Bewertung des Risikos eines Schildverklemmens und einer Beschädigung des Ausbaus im druckhaften Gebirge verbessern; (ii) entwickelt eine Gleichung, welche auf numerischen Resultaten und vorhandene Nomogramme basiert, um die nötige Vorschubkraft zu ermitteln, um ein Verklemmen des Schildes zu verhindern. Dies in einen kriechenden druckhaften Baugrund während laufenden TBM-Vortrieb, und bei einem Vortriebsstopp; (iii) vergleicht numerisch den Effekt von Kriechen und Konsolidation auf TBM-Schildvortrieb, und erörtert, ob diese in praktischen Situationen unterschieden werden können; (iv) untersucht numerisch, ob das Risiko des Schildverklemmens vom Tunneldurchmesser abhängig ist und den Effekt eines nebenliegenden Tunnels auf die Schildbelastung.

Table of contents

1 Introduction

1.1 Motivation and problem statement

The excavation of long and deep tunnels relies largely on mechanised tunnelling because of the high TBM advance rate and construction efficiency, *e.g.* Brenner base tunnel (Lussu *et al*., 2019; Skuk and Wegscheider, 2015), Gotthard base tunnel (Ehrbar *et al*., 2016) and Mont Cenis base tunnel (Bufalini *et al*., 2017). Nevertheless, conventional tunnelling is still sometimes preferred in tunnel sections characterised by poor ground conditions because of the shield jamming hazard. In severe squeezing ground conditions high pressures may develop already upon the shield during tunnel excavation and impede the machine advance (Ramoni and Anagnostou, 2010a). This is due to the combination of the very limited space available in the machine area (*i.e.* overcut und shield conicity) and the high deformability and low strength of the surrounding ground. If the converging ground closes the shield annular gap, a pressure develops upon the shield which generates friction. If the installed thrust force is insufficient to overcome the shield-ground skin friction, the machine remains trapped, tunnel excavation is stopped, the machine has to be freed from the surrounding rock with dangerous and time-consuming auxiliary measures. On the other hand, behind the machine, if deformations are prevented from a stiff lining, high rock pressure develop which may lead to lining damage. Investigating the risk of hazard scenarios like shield jamming has been topic of the dissertation "On the feasibility of TBM drives in squeezing ground and the risk of shield jamming" held in the same institute of underground construction in the ETH Zurich (Ramoni, 2010). However, without taking into account the effect of time-dependency due to the rheological behaviour of the rock mass (creep). Thus, the present thesis analyses the effect of creep on the interaction between TBM, lining and rock in order to help improve the design and construction of tunnel excavated with TBM in squeezing ground.

1.2 Background and state of the art

Squeezing of the ground is generally time-dependent (Kovári and Staus, 1996). Its time-dependency may be traced back to creep and consolidation, but also chemical processes which are not topic of the present thesis. Creep is associated with the rheology of the ground and consolidation with the dissipation of excess pore pressure triggered by the tunnel excavation in water-bearing low-permeability grounds. Usually in tunnel design squeezing ground is considered being time-independent, thus deformations which take time to develop are assumed to occur

instantaneously and thus assuming that the machine is loaded immediately. However, if the rate of advance is sufficiently high, the convergence of the ground might not affect the machine area. Thus, it is important to investigate the time-dependent rock mass behaviour during tunnel excavation in detail, with particular focus to creep, in order to reduce the risk of shield jamming and improve construction efficiency.

General aspects related to the modelling of creep in tunnelling have been studied in numerous works, *e.g.* Corbetta (1990), Fritz (1981); Zienkiewicz *et al.* (1975) and Debernardi (2008). With a specific focus on shield tunnelling, several authors have investigated numerically the effect of creep on shield jamming during excavation (Swannell *et al.*, 2016; Barla, 2018; Barla *et al.*, 2014; Hasanpour *et al.*, 2015) and during TBM standstills (Mohammadzamani *et al.*, 2019; Zhang and Zhou, 2017). Other approaches are based on physical modelling (Arora *et al.*, 2021a, 2021b; Arora *et al.*, 2022) or artificial intelligence (Hou *et al.*, 2022). Lining overstressing due to creep during advance (Hasanpour *et al.*, 2015) and at steady state (De la Fuente *et al.*, 2020) has also been examined, considering additionally the effect of backfilling (Liu *et al.*, 2019), but it has attracted limited attention overall. In the above investigations there are two main limitations, as discussed hereafter.

Firstly, most existing investigations are limited to specific tunnelling projects, and hence the applicability of their conclusions is limited. A common conclusion is that creep is always favourable for the shield and lining loading during advance in comparison with time-independent models, and even more so for higher advance rates (Swannell *et al.*, 2016; Barla, 2018; Hasanpour *et al.*, 2015; Mohammadzamani *et al.*, 2019; Zhang and Zhou, 2017). This holds in most cases and is intuitively perceived as correct, since creep limits the extent of the squeezing deformations and pressures that develop during the short duration of excavation. Nonetheless, Ramoni and Anagnostou's (2011b) investigations into the consolidation effects in a similar context indicated that the thrust force may paradoxically increase with decreasing permeability (an equivalent effect to that of increasing viscosity) under certain conditions, which raises the question of whether the same counter-intuitive behaviour may also occur in the case of creep.

Secondly, all existing works on tunnelling in ground exhibiting a time-dependent behaviour simulate the TBM operation as a continuous process, without explicitly considering the regular standstills that always occur during a TBM drive (very short standstills for lining erection in between successive TBM strokes and shift- or day-long ordinary standstills for cutterhead inspections, disk replacements, TBM maintenance, face mappings, *etc.*), or the very long extraordinary standstills (due to construction site holiday shutdowns or accidental incidents, such as cave-ins). Regular standstills are incorporated into continuous simulations by considering a gross advance rate that is considerably lower than the actual net advance rate during TBM strokes (*e.g.,* Barla, 2018; Barla *et al.*, 2014; Hasanpour *et al.*, 2015; Swannell *et al.*, 2016); in some cases, this can be as low as 1 - 10 m/d (*e.g.*, Ramoni and Anagnostou, 2011b; Barla, 2018; Hasanpour *et al.*, 2015; Swannell *et al.*, 2016), which one can only assume is intended to cover longer extraordinary standstills. The effect of standstills has been examined in only a few works and this in a simplified manner, basically considering a gross advance rate (Mohammadzamani *et al.*, 2019; Zhang and Zhou, 2017). Only Ramoni and Anagnostou (2011b) explicitly simulated a

singular longer standstill upon completion of the excavation, but otherwise still incorporated the regular standstills during excavation via an average advance rate.

Furthermore, in literature many different constitutive models for simulating the effect of creep have been adopted. Most of them either have complex multiparametric formulations as the SHELVIP (Debernardi, 2008), 3SC (Sterpi and Gioda, 2009) and Lemaitre model (Boidy *et al.*, 2002); or they contradict field experience, as in the example of the CVISC model (Burgers, 1935; Itasca, 2019) which has shown to give a lining pressure equal to the *in-situ* stress at steady state conditions (De la Fuente *et al.* 2020); or simulate creep via only one additional parameter but consider time-dependency only in the elastic regime as the Ghaboussi model (Ghaboussi and Gioda, 1977), which is not suited for describing squeezing ground behaviour as deformations mainly occur in the plastic regime. More specifically in the research field of shield tunnelling through creeping ground the CVISC model has been mostly adopted (Swannell *et al.*, 2016; Hasanpour *et al.*, 2015; Mohammadzamani *et al.*, 2019; Zhang and Zhou, 2017) as it is the only model readily implemented in a commercial FE code (Itasca, 2019). Whereas others as Barla (2018) considered the SHELVIP model.

Although several existing works have separately examined the effects of creep (*inter alia* Sterpi and Gioda 2009; Hasanpour *et al.* 2015; Swannell *et al.* 2016; De la Fuente *et al.* 2020) or consolidation in tunnelling (*inter alia* Graziani and Ribacchi 2001; Anagnostou 2007; Vogelhuber 2007; Ramoni and Anagnostou 2011b) no one has compared and discussed the two time effects and their fundamental difference.

1.3   Research objectives and questions

The goal of the present thesis is to help improve the design and construction of tunnels excavated with TBM in squeezing ground. In this scope, the research objectives of the thesis are as follows:
- A simple constitutive model for squeezing ground with time dependent behaviour due to creep is formulated and implemented.
- A calibration method for determining the parameters of the aforementioned constitutive model is developed based on measurements of the time development of ground deformations.
- The effect of creep on the interaction between TBM, lining and rock under squeezing conditions is systematically investigated.
- Simple aids for a quick assessment of the shield jamming risk in creeping ground are developed.
- Consolidation and creep are compared.

Within the context of the objectives outlined above, the present thesis also focuses on the following questions, which have not been addressed in the literature thus far:
- Whether assuming a continuous simulation of the TBM advance may lead to an underestimation of the required thrust force to overcome shield-ground friction; this is important for assessing the risk of shield jamming.

- Which the fundamental differences in the phenomenological ground behaviour of a creeping and consolidating ground are,
- Whether it is possible to distinguish in practical situations creep from consolidation,
- What the influence of the tunnel size on the shield loading is,
- What the influence of an adjacent tunnel on the shield loading is.

1.4 Methodological approach

To fulfil the research objectives outlined in the previous section, the following: methodological approach is adopted.

Firstly, a simple constitutive model is formulated and implemented for creep. For this purpose, a linear elastic – viscous plastic constitutive model based upon Perzyna's (1966) overstress theory is considered. This model considers time-dependency only in the plastic regime with Mohr-Coulomb (MC) yield condition and thus, it is suitable for studying squeezing ground, where deformations mainly occur. Moreover, the model considers time-dependency only via one single viscosity parameter and therefore, enables better qualitative interpretation compared to more sophisticated models which describe the creep behaviour with more parameters, as *e.g.* 3SC (Sterpi and Gioda, 2009), CVISC (Burgers, 1935; Itasca, 2019), Lemaitre (Boidy *et al.*, 2002), SHELVIP (Debernardi, 2008). In addition, one advantage of this model is regarding its limit cases of very slow developing ground deformations and very fast developing ground deformations. In the former case the ground behaves as a linear elastic – perfectly plastic material obeying MC yield conditions, whereas in the latter case the ground behaves as a linear elastic material.

Secondly, the constitutive model parameters are calibrated. The constitutive model considered relies on a total of only 6 parameters: 2 elasticity constants (Young's modulus E, Poisson's ratio v), 3 plasticity constants (angle of internal friction ϕ, cohesion c, angle of dilation ψ), and the viscosity η that governs the viscoplastic behaviour. These parameters except the latter are well-known for squeezing ground material (*e.g.* Vrakas *et al.* 2018). On the other hand, the last parameter - the viscosity - is from engineering experience unknown. Thus, a simple tool is developed to estimate the viscosity for the case of an unsupported and rigidly supported tunnel, which if combined with field data gives the possibility to calibrate the viscosity parameter.

Thirdly, a systematic investigation into the effect of creep on shield and lining loading for a wide range of parameters relevant in tunnelling is performed. Investigations are performed considering an axisymmetric Finite Element (FE) model developed in Abaqus® (Dassault Systèmes, 2018) that simulates the mechanised excavation and lining installation sequence step-by-step (see, *e.g.*, Franzius and Potts, 2005). In order to assess the effect of creep, contours of plastic strains around the tunnel, convergences at the tunnel boundary, as well as, pressures over shield and lining are investigated, during TBM excavation but also during machine standstill. Moreover, as the pressures over the shield are known from the results of numerical computations, the required thrust force to overcome shield skin friction and thus to overcome a possible risk of shield jamming is calculated and specifically investigated for the effect of creep. In addition, as in literature simulations of the TBM advance are performed considering a continuous excavation of

the machine (*i.e.* no standstills for installation of the lining or maintenance are considered), discrete simulations are performed which take the actual TBM excavation into account (*i.e.* considering standstills for installation of the lining, for maintenance but also extraordinary). Finally, a semi-discrete approach is presented in which only the regular standstills are smeared but longer standstills are taken into account.

Fourthly, in order to allow a quick assessment of the risk of shield jamming an equation is developed which relies on: (i) existing nomograms that already assess the risk of shield jamming in a time-independent ground developed by Ramoni and Anagnostou (2010b), and (ii) transient numerical creep analyses. The proposed equation is based on a so-called "metamodel", that is a model with a unique formulation capable of reproducing the behaviour of multiple numerical models with distinct formulations.

Fifthly, a comparison between creep and consolidation is performed. This part is structured into two parts: in the first part the fundamental differences in the phenomenological ground behaviour are investigated, whereas the second part answers two practical question regarding the influence on the shield loading of (i) the tunnel size and (ii) an adjacent tunnel. Creep is considered as previously discussed via the own implemented and formulated simple constitutive model. On the other hand, consolidation is simulated assuming rock as a two-phase porous medium with unit Biot's coefficient, according to Terzaghi's principle of effective stresses. The rock is simulated obeying a linear elastic – perfectly plastic constitutive model with MC yield condition and a non-associated flow rule. For the seepage flow of the water Darcy's law is considered.

In the first part a simple plane-strain problem of a tunnel cross-section far behind the advancing face is examined first, with focus on the time-development of its radial displacement upon excavation in the absence of a tunnel support. This problem enables to demonstrate simple fundamental difference between the two mechanisms of time-dependency. Subsequently, the more complex and practically relevant problem of the interaction between ground, TBM and tunnel support in mechanised tunnelling is examined, with focus on the shield loading that develops during the advance of the TBM and during construction standstills, which is investigated considering the previously presented axisymmetric Finite Element (FE) model developed in Abaqus®.

The second part starts by investigating firstly the so called scale effect – influence of tunnel size – considering, as in the first part, a simple plane-strain problem of a tunnel cross-section far behind the advancing face, as it allows for a simpler qualitative interpretation of the fundamental considerations discussed. Subsequently, the more complex problem of ground, TBM and tunnel support interaction is examined, focusing on the differences in the required thrust force during TBM advance, as well as in the rate that this develops during a subsequent standstill, for tunnels of different size, and the risk of shield jamming in each case. In each of these problems, the influence of the tunnel size is assessed and compared between creeping and consolidating ground.

Afterwards the second part investigates the so called interaction problem – influence of an adjacent tunnel – however, instead of resorting to more complex, 3D, transient numerical simulations, the interaction problem is analysed in a simplified manner, using two 2D models

sequentially and adopting adequate and well-founded assumptions to facilitate the connection of their input and output parameters. The 2D models have been developed in Abaqus® (Dassault Systèmes, 2018) and comprise a plane strain model which considers the interaction between the two tunnels and an axisymmetric step-by-step model which considers the interaction of TBM-shield, lining and the surrounding ground. Herein, only the influence of the first already constructed tunnel on the shield loading of the second tunnel is investigated and not *vice versa*.

1.5   Organisation of the thesis

The present thesis is organised in the following way:

Chapter 2 investigates the effect of creep on the evolution of rock pressure over time, in order to improve the reliability of shield jamming and lining damage risk assessment in squeezing ground. The study is based on numerical simulations of typical mechanised tunnelling processes, generally consisting of shield advance phases alternating with shorter or longer standstills for lining installation, maintenance, *etc.* Creep is simulated (as throughout the thesis) as a linear elastic – viscous plastic constitutive model based upon Perzyna's (1966) overstress theory. The investigations in the present chapter demonstrate the following:

   (i)   Shield loading during advance increases with increasing viscosity under certain conditions, which contradicts the common perception in many existing works that creep is thoroughly favourable for shield jamming;

   (ii)   Creep is thoroughly unfavourable for shield loading during long standstills and long-term lining loading, due to the additional viscoplastic ground deformations manifested over time;

   (iii)   The commonly adopted simplifying assumption of continuous excavation with the gross advance rate is adequate only where standstills are very short (*e.g.* for lining erection during the stop-and-go shield tunnelling process), but otherwise underestimates the shield loading, even in cases of regular inspection and maintenance standstills lasting only a few hours.

   (iv)   Two application examples, the Fréjus safety gallery and the Gotthard Base tunnel, demonstrate the need to consider creep and the accuracy of modelling tunnel construction by a semi-discrete approach, where only the very short standstills for lining erection are considered via an average advance rate, but longer standstills are explicitly simulated.

Chapter 3 gives an equation for estimating the required thrust force in creeping rock under squeezing conditions during ongoing TBM advance, as well as during construction standstills. The method partially relies on existing design nomograms and is established via multiparametric nonlinear regression, considering the results of 12,300 transient numerical simulations that cover a wide range of *in-situ* stresses and ground, TBM, and creep parameters relevant in tunnelling practice. The proposed method approximates the numerical results with sufficient accuracy to provide a reliable basis for decision-making during design and a valuable tool for fast assessment

of the shield jamming risk. Its versatility and suitability in practical situations are demonstrated via two application examples from the Fréjus safety gallery and the Gotthard base tunnel.

Chapter 4 investigates numerically the basic time effects of creep and consolidation, placing focus on the time development of ground deformations and the complex interaction between ground, TBM and tunnel support during excavation and during construction standstills. The presented numerical simulations indicate several qualitative similarities between the two mechanisms of time-dependency, in respect of the time-development of ground deformations, the counter-intuitive behaviour of increasing shield loading with increasing rate of advance under certain conditions, as well as the thoroughly adverse effect of the additional time-dependent deformations taking place during construction standstills on the shield loading. However, they also underscore two prominent differences resulting from the fundamentally different nature of creep (a purely mechanical rheological process) and consolidation (a coupled hydromechanical process): First, the consistently more extensive plastic yielding in consolidating ground, which is partially associated with the seepage forces exerted by the pore water on the solid rock constituents. Second, the role of seepage forces as a potential destabilising agent particularly for the tunnel face, which does not happen in the case of creep and may be critical for shield and cutterhead jamming.

Chapter 5 compares creep and consolidation with respect to two practical questions. The first question is whether the risk of shield jamming depends on the tunnel diameter, *i.e.* how experiences obtained during the construction of a smaller-diameter tunnel (*e.g.* pilot tunnel) can be used to identify critical considerations or hazards during the construction of the larger-diameter main tunnel. The second question is the effect of an adjacent tunnel on shield loading; *i.e.* how the construction of a tunnel affects the subsequent construction of an adjacent, parallel tunnel. Both are investigated numerically. Investigations addressed to the first question demonstrate the following:

(i)   Time-development of the displacements in an unsupported opening are independent of the tunnel size in creeping ground, but proportional to the square of the tunnel radius in consolidating ground; in the latter case, however, the consolidation rate may also be much lower in cases where the geological setting poses limitations on the size of the seepage flow domain, as this may result in increased pore pressure gradients (seepage forces) that induce more extensive plastification;

(ii)   Focusing in the more complex problem of rock, TBM and tunnel support interaction: in the case of time-independent ground behaviour a larger radius is always more favourable in weak ground, while the opposite holds in better ground. In the case of time-dependent behaviour, a larger radius has been shown to be equally or more unfavourable in creeping and in consolidating ground, both during excavation and during a standstill, and this effect to be overall more pronounced in creeping ground, except for the case of small — and less practically relevant — construction standstills.

On the other hand, investigations addressed to the second question demonstrated:

(iii)   In creeping ground, the interaction is governed by the stress redistributions and plastification induced by the excavation of the first tunnel, which are limited within a narrow zone and generate overall more unfavourable conditions for the subsequently excavated second tunnel; however, this interaction has been shown to be generally minor in practically relevant cases where the second tunnel lies outside of the region of plastified ground.

(iv)   In consolidating ground, the excavation of the first tunnel relieves the pore pressures and increases the effective stresses and the shear strength in the surrounding ground, analogous to advance drainage which for mechanised tunnelling allows a remarkable reduction in the required thrust force of up to 85%.

2 Effects of creep on shield tunnelling through squeezing ground[1]

Abstract

The present chapter aims to improve the reliability of shield jamming and lining damage risk assessment in squeezing ground by analysing the effects of creep on the evolution of rock pressure over time. The study is based on numerical simulations of typical mechanised tunnelling processes, generally consisting of shield advance phases alternating with shorter or longer standstills for lining installation, maintenance, etc. A linear elastic—viscous plastic constitutive model based upon Perzyna's overstress theory is employed, which considers the time-dependency of plastic deformations via a single viscosity parameter. The investigations demonstrate the following: (i) shield loading during advance increases with increasing viscosity under certain conditions, which contradicts the common perception in many existing works that creep is thoroughly favourable for shield jamming; (ii) creep is thoroughly unfavourable for shield loading during long standstills and long-term lining loading, due to the additional viscoplastic ground deformations manifested over time; (iii) the commonly adopted simplifying assumption of continuous excavation with the gross advance rate is adequate only where standstills are very short (*e.g.*, for lining erection during the stop-and-go shield tunnelling process), but otherwise underestimates the shield loading, even in cases of regular inspection and maintenance standstills lasting only a few hours. Two application examples, the Fréjus safety gallery and the Gotthard Base tunnel, demonstrate the need to consider creep and the accuracy of modelling tunnel construction by a semi-discrete approach, where only the very short standstills for lining erection are considered via an average advance rate, but longer standstills are explicitly simulated.

---

[1] This chapter has been published with the following reference: Leone, T., Nordas, A.N. & Anagnostou, G. (2023). Effects of creep on shield tunnelling through squeezing ground. Rock Mechanics and Rock Engineering, doi: 10.1007/s00603-023-03505-x. The contributions of each author are given in Appendix F. The postprint version is considered for this chapter.

2.1   Introduction

In mechanised tunnelling through squeezing ground, jamming of the shield or damage to the lining may occur due to the development of substantial rock pressures on them (Ramoni and Anagnostou, 2010a). Squeezing is often time-dependent, due to consolidation or creep (Anagnostou, 2007). Time-dependency due to consolidation is relevant in medium- to low-permeability water-bearing ground, and is associated with the progressive dissipation of the excavation-induced excess pore pressures; its effects have been investigated *inter alia* by Graziani and Ribacchi (2001) and Ramoni and Anagnostou (2011b). The present chapter focuses on the creep-induced time-dependency of squeezing.

General aspects related to the modelling of creep in tunnelling have been studied in numerous works, *e.g.* Corbetta (1990), Fritz (1981); Zienkiewicz *et al.* (1975) and Debernardi (2008). With a specific focus on shield tunnelling, several authors have investigated numerically the effect of creep on shield jamming during excavation (Swannell *et al.*, 2016; Barla, 2018; Barla *et al.*, 2014; Hasanpour *et al.*, 2015) and during TBM standstills (Mohammadzamani *et al.*, 2019; Zhang and Zhou, 2017). Other approaches are based on physical modelling (Arora *et al.*, 2021a, 2021b; Arora *et al.*, 2022) or artificial intelligence (Hou *et al.*, 2022). Lining overstressing due to creep during advance (Hasanpour *et al.*, 2015) and at steady state (De la Fuente *et al.*, 2020) has also been examined, considering additionally the effect of backfilling (Liu *et al.*, 2019), but it has attracted limited attention overall. In the above investigations there are two main limitations, as discussed hereafter.

First, most existing investigations are limited to specific tunnelling projects, and hence the applicability of their conclusions is limited. A common conclusion is that creep is always favourable for the shield and lining loading during advance in comparison with time-independent models, and even more so for higher advance rates (Swannell *et al.*, 2016; Barla, 2018; Hasanpour *et al.*, 2015; Mohammadzamani *et al.*, 2019; Zhang and Zhou, 2017). This holds in most cases and is intuitively perceived as correct, since creep limits the extent of the squeezing deformations and pressures that develop during the short duration of excavation. Nonetheless, Ramoni and Anagnostou's (2011b) investigations into the consolidation effects in a similar context indicated that the thrust force may paradoxically increase with decreasing permeability (an equivalent effect to that of increasing viscosity) under certain conditions, which raises the question of whether the same counter-intuitive behaviour may also occur in the case of creep. Considering the above, and the limited attention given to the aspect of long-term lining loading, there is scope for a more systematic investigation on the effects of creep which considers a wide range of practically relevant parameters.

Secondly, all existing works on tunnelling in ground exhibiting a time-dependent behaviour simulate the TBM operation as a continuous process, without explicitly considering the regular standstills that always occur during a TBM drive (very short standstills for lining erection in between successive TBM strokes and shift- or day-long ordinary standstills for cutterhead inspections, disk replacements, TBM maintenance, face mappings, *etc.*), or the very long extraordinary standstills (due to construction site holiday shutdowns or accidental incidents, such

as cave-ins). Regular standstills are incorporated into continuous simulations by considering a gross advance rate that is considerably lower than the actual net advance rate during TBM strokes (*e.g.,* Barla, 2018; Barla *et al.*, 2014; Hasanpour *et al.*, 2015; Swannell *et al.*, 2016); in some cases, this can be as low as 1 - 10 m/d (*e.g.*, Ramoni and Anagnostou, 2011b; Barla, 2018; Hasanpour *et al.*, 2015; Swannell *et al.*, 2016), which one can only assume is intended to cover longer extraordinary standstills. The effect of standstills has been examined in only a few works and this in a simplified manner, basically considering a gross advance rate (Mohammadzamani *et al.*, 2019; Zhang and Zhou, 2017). Only Ramoni and Anagnostou (2011b) explicitly simulated a singular longer standstill upon completion of the excavation, but otherwise still incorporated the regular standstills during excavation via an average advance rate. As is seen later in this chapter, the continuous simulation of the TBM advance may lead to a severe underestimation of the required thrust force, thus misleading the feasibility assessment of a TBM drive and the decision-making during design.

This chapter aims to bridge the aforementioned knowledge gaps via a comprehensive and systematic numerical investigation into the following aspects: the effect of creep on the thrust force during advance or standstills and on the lining loads far behind the face under steady state conditions (*i.e.* after practically all time-dependent deformations have been completed), considering the range of viscosities relevant in tunnel engineering practice; the conditions under which the counter-intuitive behaviour (paradox) of higher thrust force during advance compared to that of time-independent problems is manifested (analogously to Ramoni and Anagnostou, 2011b for consolidation); and the adequacy of considering the standstills by means of an equivalent average advance rate (hereafter referred to as "smearing" of standstills).

This chapter proceeds in Section 2.2 with basic considerations on the constitutive modelling of creep in rock and the selection of an adequate model for the present investigations. Additionally, it explains the model behaviour and proposes a simple way of estimating viscosity in tunnelling boundary value problems. Subsequently, Section 2.3 introduces the computational model adopted in the numerical simulations of the construction process.

Section 2.4 presents a systematic investigation into the effect of creep on shield and lining loading for a wide range of parameters relevant in tunnelling. Additionally, it demonstrates that disregarding creep, and thus assuming for simplicity that squeezing occurs instantaneously upon excavation, is not necessarily a conservative simplification, but may instead result in an underestimation of the pressure developing upon the shield, and thus of the necessary thrust force during TBM advance. This apparent paradox is explained as the result of two competing effects of the slower deformation development: the ground on the one hand establishes contact with the shield later, which is favourable, but on the other hand experiences less stress relief ahead of the face, which is unfavourable. The latter is also the reason that the long-term lining loading is always higher in the presence of creep.

Section 2.5 addresses the question of excavation standstill modelling, by comparing the adequacy of various approaches. It shows that considering an average advance rate is adequate only for the stop-and-go process of shield tunnelling, where the very short standstills required for lining

erection frequently and regularly alternate with the short net advance phases during TBM strokes; conversely, shift- or day-long standstills, such as those regularly required for inspections and maintenance works, and longer extraordinary standstills must be considered explicitly. It also introduces a "semi-discrete" approach, where only the standstills during the stop-and-go process are smeared, but the longer standstills are simulated explicitly.
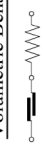
Finally, Section 2.6 demonstrates the effects of creep, as well as the importance of an adequate modelling of standstills and the accuracy of the proposed semi-discrete simulation method, via two application examples concerning the Fréjus safety gallery and the Gotthard base tunnel.

2.2   Constitutive modelling

A broad range of constitutive models has been adopted in existing works, encompassing different combinations of mechanical (time-independent) and rheological (time-dependent) counterparts. Table 2.1 provides an overview of some of the most widely employed models in the literature.

In the present chapter, which analyses creep effects based on numerical parametric investigations, the main criteria for model selection are its formulation simplicity, since models with fewer parameters enable a better qualitative interpretation of the results, and the consideration of time-dependency in the plastic regime, where squeezing deformations mainly occur. The only model readily implemented in a commercial FE code is CVISC (Burgers, 1935; Itasca, 2019); however, it fulfils neither of the above criteria and has also been shown to predict a lining pressure equal to the *in-situ* stress at steady state conditions (De la Fuente *et al.* 2020), which contradicts field experience. Although this is not important for modelling the processes in the vicinity of the advancing tunnel face, it is important for the investigation of lining overstressing at steady state conditions considered in the present chapter. From the remaining models, SHELVIP, 3SC and Lemaitre have more complex multiparametric formulations, while the Ghaboussi model, although simpler, only considers viscoelasticity (*cf.* Table 2.1).

Table 2.1. Overview of constitutive models with rheological behaviour

Constitutive model	SHELVIP[a]	3SC[b]	CVISC[c]	Lemaitre[d]	MC-Perzyna[e]	Ghaboussi model[f]
Mechanical analogy	Hooke, St.Venant, Generalised Bingham	Volumetric Behaviour: St.Venant Hooke; Deviatoric Behaviour: Hooke Kelvin Bingham	Volumetric Behaviour: St.Venant Hooke; Deviatoric Behaviour: St.Venant Burger	Hooke, Generalised Bingham	Hooke Bingham	Volumetric Behaviour: Hooke; Deviatoric Behaviour: Hooke Kelvin
Nr. of parameters	11	9	9	8	6	5
Yield condition	Drucker Prager	Mohr Coulomb	Mohr Coulomb	Von Mises, Drucker Prager[g]	Mohr Coulomb	-
Elastic time dependency	no	yes	yes	no	no	yes
Plastic time dependency	yes	yes	no	yes	yes	no
Time-dependency theory	overstress theory[h]	Newton's viscosity law and overstress theory[h]	Newton's viscosity law	overstress theory[h]	overstress theory[h]	Newton's viscosity law
Deviatoric/volumetric time-dependency	deviatoric	deviatoric	Deviatoric	deviatoric	deviatoric	deviatoric
Tunnel projects	Lyon Turin[i] Kishanganga[j]	Lyon Turin[k]	Xiangjiaba[l], Lyon Turin[m], Raticosa[n], Fréjus[o]	Raticosa[n]	-	-
Commercial FE software	-	-	FLAC 2D|3D[p]	-	-	-
Predicted creep test stages	primary and secondary	primary and secondary	primary and secondary	primary and secondary	secondary	primary

(a) Debernardi (2008)
(b) Sterpi and Gioda (2009)
(c) Burgers (1935) ; Itasca (2019)
(d) Boidy et al. (2002)
(e) Zienkiewicz and Cormeau (1974); Corbetta (1990); Bernaud (1991)
(f) Ghaboussi and Gioda (1977)
(g) Pellet (2004)
(h) Perzyna (1966)

(i) Debernardi (2008); Barla et al. (2012)
(j) Barla et al. (2014)
(k) Barla et al. (2012)
(l) Y. Zhang et al. (2015)
(m) Barla et al. (2008); Pellet (2009)
(n) Bonini et al. (2007)
(o) De la Fuente et al. (2020)
(p) Itasca (2019)

Considering the above and the objective of this chapter, which is to improve the fundamental understanding of time-dependent effects on shield jamming and lining overstressing, it is sufficient to consider the simplest possible constitutive model. An isotropic, linear elastic and viscous perfectly plastic model is adopted based on Hooke's law and Bingham's rheological model (Table 2.1), with a Mohr-Coulomb (MC) yield condition and a non-associated viscoplastic flow rule after Perzyna's (1966) overstress theory. The model, hereafter referred to as "MC-Perzyna", considers solely plastic time-dependency, and hence strain rate can be resolved into an elastic part and an inelastic part that incorporates the combined viscous and plastic effects:

$$\dot{\boldsymbol{\varepsilon}} = \dot{\boldsymbol{\varepsilon}}^{el} + \dot{\boldsymbol{\varepsilon}}^{vp} \tag{2.1}$$

The elastic part $\dot{\boldsymbol{\varepsilon}}^{el}$ depends linearly on the stress rate, according to Hooke's law, while the inelastic part is given by the following expression:

$$\dot{\boldsymbol{\varepsilon}}^{vp} = \frac{f}{\eta}\frac{\partial g}{\partial \boldsymbol{\sigma}}, \tag{2.2}$$

where f is the MC yield function, g the plastic potential function and η the viscosity. Eq. 2.2 involves the assumption that the inelastic strain rate depends on the excess stresses lying above the yield surface.

The model formulation encompasses in total only 6 parameters: 2 elasticity constants (Young's modulus E, Poisson's ratio v), 3 plasticity constants (angle of internal friction ϕ, cohesion c, angle of dilation ψ), and the viscosity η that governs the viscoplastic behaviour. Its simplicity enables an easier qualitative interpretation of the computational results. Although an isotropic model cannot capture the non-uniformity of rock deformations and pressure over the tunnel circumference, it can still be used to obtain reasonable estimates for anisotropic rocks if necessary, considering an appropriate set of equivalent parameters (Mezger, 2019). Systematically incorporating anisotropic effects in the context of the presented parametric studies would anyway increase their already substantial size and the complexity of the computational model, as it would require 3D computations that consider different combinations of anisotropy plane orientations and stiffness, strength and viscosity anisotropies.

The MC-Perzyna model has been implemented in Abaqus® (Dassault Systèmes, 2018) as a user-defined material (UMAT) subroutine. The key aspects of its formulation and numerical implementation are outlined in the Appendix A, the subroutine is given in Appendix B and its validation in Appendix C.

While engineers have some experience in estimating common material parameters, such as the modulus of elasticity, compressive strength, or friction angle, this is less true for the parameters that determine the rate of creep, *i.e.* the viscosity η for the constitutive model adopted here. If experiences of the temporal development of squeezing or results of field measurements from adjacent underground openings are available, these could be used to back-calculate the viscosity. As an aid for a simplified back-analysis, consideration is given in the sequel to the plane-strain, rotationally symmetric problem of a deep, cylindrical, and uniformly supported tunnel of radius R, crossing homogeneous rock subjected to a uniform and hydrostatic *in-situ* stress field. The

tunnel boundary is instantaneously unloaded from the *in-situ* stress (σ_0) to zero support pressure ($\sigma_R = 0$) and the radial displacement (u) development over time is monitored.

The MC-Perzyna model predicts a purely elastic instantaneous displacement that agrees with the well-known analytical solution of Kirsch (1898). If yielding occurs in the ground around the tunnel, viscoplastic displacements start taking place at a rate governed by the viscosity η. For the borderline case $\eta = 0$ (time-independent model) all plastic displacements occur instantaneously, and the response is described by the well-known elastoplastic solution (see, *e.g.*, Anagnostou and Kovári 1993). For the other borderline case $\eta \rightarrow \infty$ (infinitely viscous model) no viscoplastic displacements occur within all practically relevant time periods. In intermediate cases $0 < \eta < \infty$ the displacement increases at a decreasing rate, and at steady state (*i.e.,* after the viscoplastic deformations have been practically completed) tends asymptotically to the elastoplastic solution.

The displacement of the considered unsupported tunnel depends in general on all independent problem parameters, specifically the initial stress σ_0, the tunnel radius R, the time t, the viscosity η and the other five material constants:

$$u = f\left(\sigma_0, \ R, \ t, \ \eta, \ E, \ v, \ f_c, \ \phi, \ \psi\right). \tag{2.3}$$

Based upon dimensional analysis, and considering that the elastoplastic deformations are inversely proportional to the Young's modulus (Anagnostou and Kovári 1993), Eq. 2.3 can be written in the following nondimensional form (see, *e.g.*, Ramoni and Anagnostou, 2010b), which expresses the normalised displacement (left hand side term) as a function of the normalised time (first right hand side term):

$$\frac{uE}{R\sigma_0} = f\left(\frac{tE}{\eta}, \ \frac{f_c}{\sigma_0}, \ \phi, \ \psi, \ v\right). \tag{2.4}$$

One can readily verify that the time required to achieve a given percentage, *e.g.,* 95%, of the time-dependent displacement increment is solely a function of the material constants:

$$\frac{t_{95}E}{\eta} = f\left(\frac{f_c}{\sigma_0}, \ \phi, \ \psi, \ v\right). \tag{2.5}$$

This relationship was quantified numerically by means of rotationally symmetric plane strain computations and is presented graphically in Figure 2.1a. A similar relationship is obtained in the case where a rigid support is instantaneously applied over the tunnel boundary upon unloading, as shown in Figure 2.1b, where t_{95} denotes the time required for 95% of the final pressure to develop on the lining.

For the case of an unsupported tunnel, t_{95} decreases with increasing ϕ and f_c/σ_0 (Fig. 2.1a), since higher strength parameters result in smaller total viscoplastic deformations, and thus a shorter time for attaining 95% of their final value. A similar trend is observed in the case of a rigid support, but t_{95} is practically constant. Interestingly, t_{95} is smaller by at least one order of magnitude than the case of an unsupported tunnel, which indicates that providing support to the ground, and thus fully constraining the viscoplastic deformations, accelerates the stress relief that

would otherwise occur through said deformations. Practically relevant cases, *i.e.,* a lining of finite stiffness providing a finite support pressure after a certain ground pre-deformation, may lie between the curves of the two cases in Figure 2.1.

The diagrams in Figure 2.1 allow the viscosity η to be determined in a simple manner, based upon the observed time-development of deformations (which provides an indication as to t_{95}) and the estimated values of the strength parameters (f_c, ϕ), Young's modulus E, and initial stress σ_0.
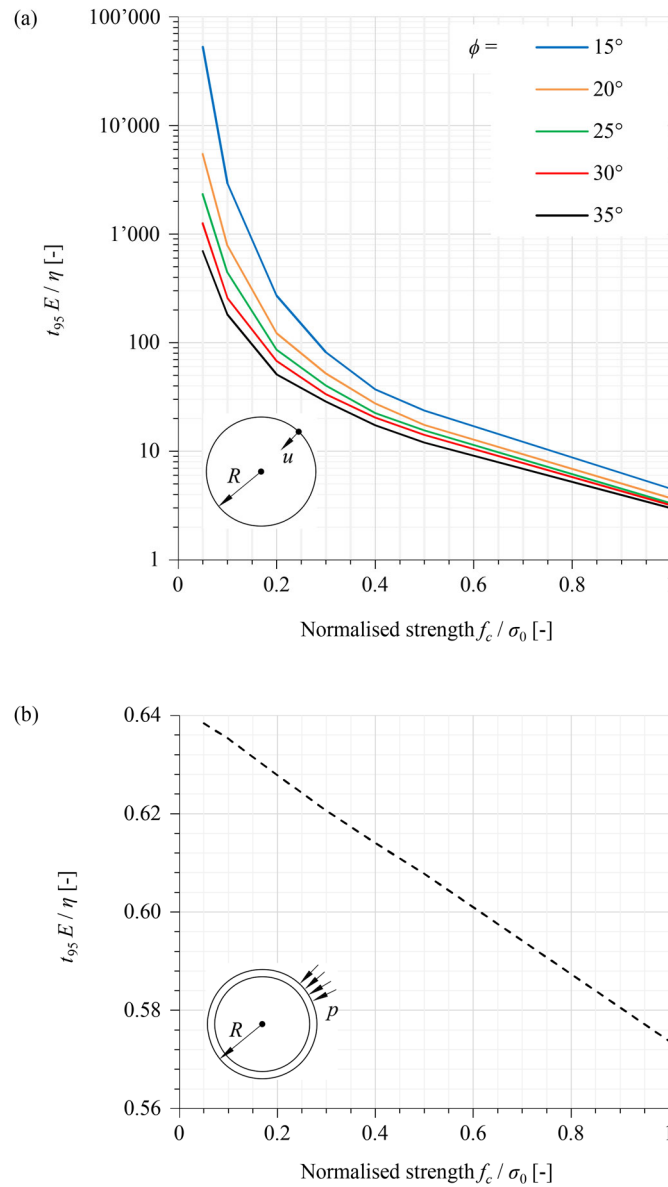
Figure 2.1.   Normalised time t_{95} as function of the strength parameters: (a) unsupported tunnel; (b) tunnel with rigid support ($v = 0.25$, $\psi = \phi$ - 20°)

2.3   Computational model of TBM advance

For the numerical investigations presented in the next sections, an axisymmetric Finite Element (FE) model has been developed in Abaqus$^®$ (Dassault Systèmes, 2018) that simulates the mechanised excavation and lining installation sequence step-by-step (see, *e.g.*, Franzius and Potts, 2005), as well as the subsequent transient processes during a standstill of arbitrary duration (Fig. 2.2). In addition to the trivial assumptions underlying rotationally symmetric tunnel analyses (*e.g.,* a uniform and hydrostatic *in-situ* stress field, homogeneous and isotropic rock, *etc.*; *cf.* Section 2.2), the model assumes negligible TBM weight, and thus uniform tunnel support and overcut around the shield, as well as uniform backfilling around the segmental lining.

At each numerical excavation step, part of the ground is removed ahead of the advancing tunnel face (round length *s*) and an equal part of lining is installed immediately behind the shield tail. The model considers the actual times required for excavating the ground with the TBM cutterhead and for installing one ring of the segmental lining and allows each excavation step to be simulated either discretely (short phases of continuous advance alternating with short standstills; the so-called "stop-and-go") or continuously (continuous advance at a smeared rate and no standstill).

The tunnel face is considered unsupported. The shield is modelled with non-linear radial springs, which consider no loading (zero stiffness) for rock convergences smaller than the overcut ΔR, and a linear elastic stiffness K_s for the portion of convergences that exceeds ΔR. The lining is modelled with elastic radial springs of stiffness K_l, assuming that it is in direct contact with the ground immediately upon installation due to backfilling. The consideration of distinct shield and lining installation points enables capturing the ground unloading immediately behind the shield tail and its reloading over the lining (Fig. 2.2). For more details the reader is referred to Ramoni and Anagnostou (2010b). The MC-Perzyna model (Section 2.2) is adopted for the ground.
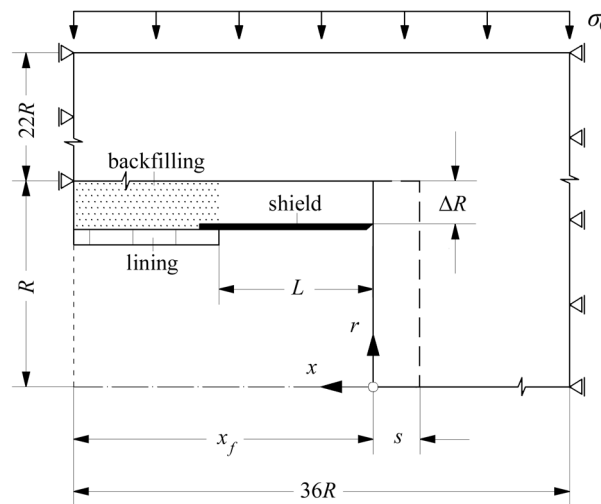
Figure 2.2.   Computational domain (not to scale)

For the spatial discretisation of the computational domain, a structured mesh encompassing 36822 4-noded, linear, quadrilateral, axisymmetric finite elements (FEs) have been employed, as shown in Figure 2.3. In the radial direction (r), the element size varies with an exponential bias between $0.02R$ at the tunnel boundary and $2.5R$ at the upper far field boundary. Along the longitudinal x-axis of the tunnel, the element size is constant and equal to the round length s (Figs. 2.2, 2.3). Introducing a single FE within each round length enables eliminating the saw-shaped fluctuations in the distribution of the radial rock pressure that are typically observed in step-by-step simulations (Cantieni and Anagnostou, 2009). The round length s is taken as 0.25, except for cases where a specific length of the segmental lining rings is considered; in such cases, s is taken equal to the ring length. The various round lengths considered in different simulations are always sufficiently small to ensure enhanced prediction accuracy (Franzius and Potts, 2005).

The developed computational model provides *inter alia* the longitudinal profile of the ground pressure $\sigma_R(x)$ acting upon the shield and the lining. The thrust force required for overcoming shield skin friction can then be evaluated from the following expression:

$$F_r = \mu\, 2\pi R \int_0^L \sigma_R(x)\, dx = \mu\, 2\pi R L\, \overline{\sigma}_R\ ,\qquad (2.6)$$

where μ is the shield skin friction coefficient, L the shield length, and $\overline{\sigma}_R$ the mean pressure over the shield. In each numerical simulation, the excavated tunnel stretch is considered sufficiently long for the thrust force to become constant and the standstill stage is initiated thereafter.

The validation of the step-by-step computation is performed for the case of zero viscosity in Appendix C.3.
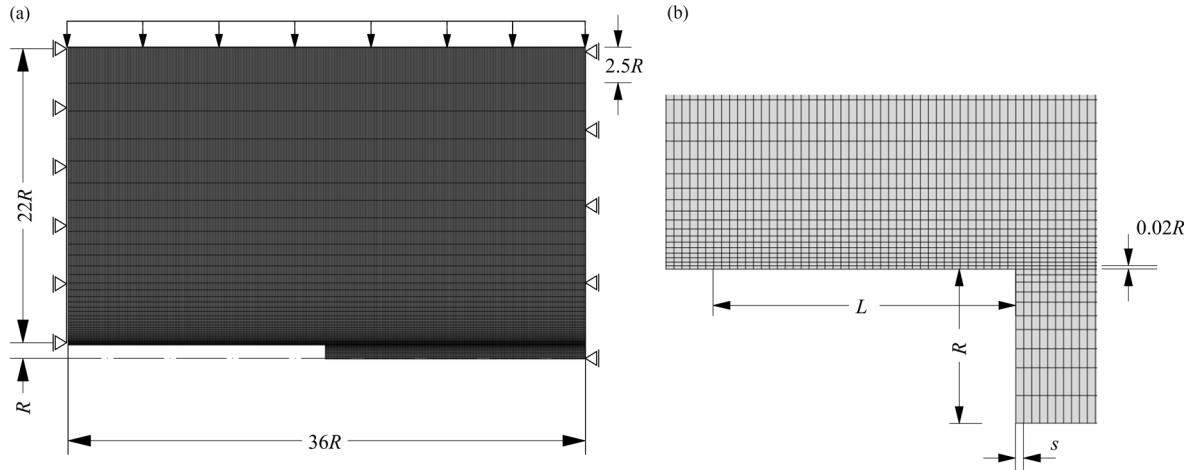
Figure 2.3.   Finite element mesh configuration (a) and detail in the vicinity of the tunnel face (b)

2.4   Effects of creep on rock pressure

The effects of creep on the shield and lining loading are numerically investigated in this section using the computational model presented in Section 2.3, considering a continuous excavation at an average advance rate of 20 m/d followed by a standstill and the parameters given in Table 2.2.

Table 2.2.   Parameters considered in numerical computations of Sections 2.3 - 2.5

Ground			
Young's Modulus	E	[MPa]	1000
Poisson's ratio	v	[-]	0.25
Angle of internal friction	ϕ	[°]	25
Dilatancy angle	ψ	[°]	5
Uniaxial compressive strength	f_c	[MPa]	1.25
Viscosity	η	[MPa·d]	variable
In-situ stress	σ_0	[MPa]	25
TBM			
Boring radius	R	[m]	5
Shield length	L	[m]	10
Annular gap (overcut)	ΔR	[cm]	12.5
Shield radial stiffness	K_s	[MPa/m]	2000[a]
Shield skin friction coefficient	μ	[-]	0.1, 0.15[b]
Boring force	F_b	[MN]	17
Lining			
Radial stiffness	K_l	[MPa/m]	100[a]
Computational model			
Round length	s	[m]	0.25
Model size in radial direction	R_m	[m]	110
Model size in longitudinal direction	L_m	[m]	180

[a] Conservative assumption after Ramoni and Anagnostou (2010b)

[b] Sliding and static friction coefficients with lubricated shield extrados after Ramoni and Anagnostou (2011a)

2.4.1   Basic behaviour

First, the basic behaviour of the system is examined, with the focus on the rock-shield-lining interaction. Three cases of viscosity are considered: a very low viscosity, characterising practically time-independent behaviour (η = 0.5 MPa·d, t_{95} = *ca.* 30 sec – 1 d in the boundary value problems of Figs. 2.1b and 2.1a, respectively); an intermediate viscosity, at which steady state is reached within hours or months (η = 200 MPa·d, t_{95} = *ca.* 3 hours – 14.5 months after Figs. 2.1b and 2.1a, respectively); and a high viscosity, which would result in time-dependent deformations for several months or years (η = 300,000 MPa·d, t_{95} = *ca.* 6.5 months – 1830 years after Figs. 2.1b and 2.1a, respectively).

Figures 2.4a – 2.4c show the equivalent plastic strain ε^p (magnitude of plastic strain vector) around the tunnel heading during advance (black lines), after a 6-month standstill (red lines), and at steady state (green lines) for the three viscosity cases. In the low-viscosity case (Fig. 2.4a) time-dependency is negligible; all plastic deformations occur practically simultaneously with excavation and remain practically constant over time (green and red lines coincide). Conversely, in the high-viscosity case (Fig. 2.4c), where time-dependency is very pronounced, plastic deformations in the immediate vicinity of the tunnel are negligible during excavation and within the 6 months of the standstill, and only occur later. In the intermediate case (Fig. 2.4b), plastic deformations occur partially during excavation and partially within the 6-month standstill, mainly in the ground ahead of the face, and remain constant thereafter (green and red lines coincide).

The occurrence of plastic deformations, or the lack thereof, is reflected in the longitudinal rock pressure and convergence profiles (Figs. 2.4d – 2.4f and 2.4g – 2.4i, respectively). In the low-viscosity case, the ground deformations during excavation, and thus the contact area with the shield (Fig. 2.4g) and the exerted pressure (Fig. 2.4d), are the greatest amongst the three cases, and increase only slightly during the standstill. Conversely, in the high-viscosity case there is no contact between ground and shield during excavation, as elastic convergences do not exceed the overcut ΔR (Fig. 2.4i), while during the standstill viscoplastic deformations develop extremely slowly and exert a small pressure on the shield (Fig. 2.4f). For the intermediate viscosity, contact between shield and ground already occurs during excavation (Fig. 2.4h) over a smaller area compared to the low-viscosity case; however, the prevention of additional viscoplastic deformations during the 6-month standstill by the static shield results in the most unfavourable shield loading among the three cases (Fig. 2.4e). The local pressure peak close to the unsupported face, which has also been observed in the investigations of Ramoni and Anagnostou (2011b) into the effects of consolidation on shield jamming, is associated with plastic yielding of the core ahead of the face, and has been shown to vanish in the presence of a sufficient face support.

These results clearly indicate that the interplay between standstill duration and viscosity is the most critical aspect. These effects are investigated in the sequel in more detail.
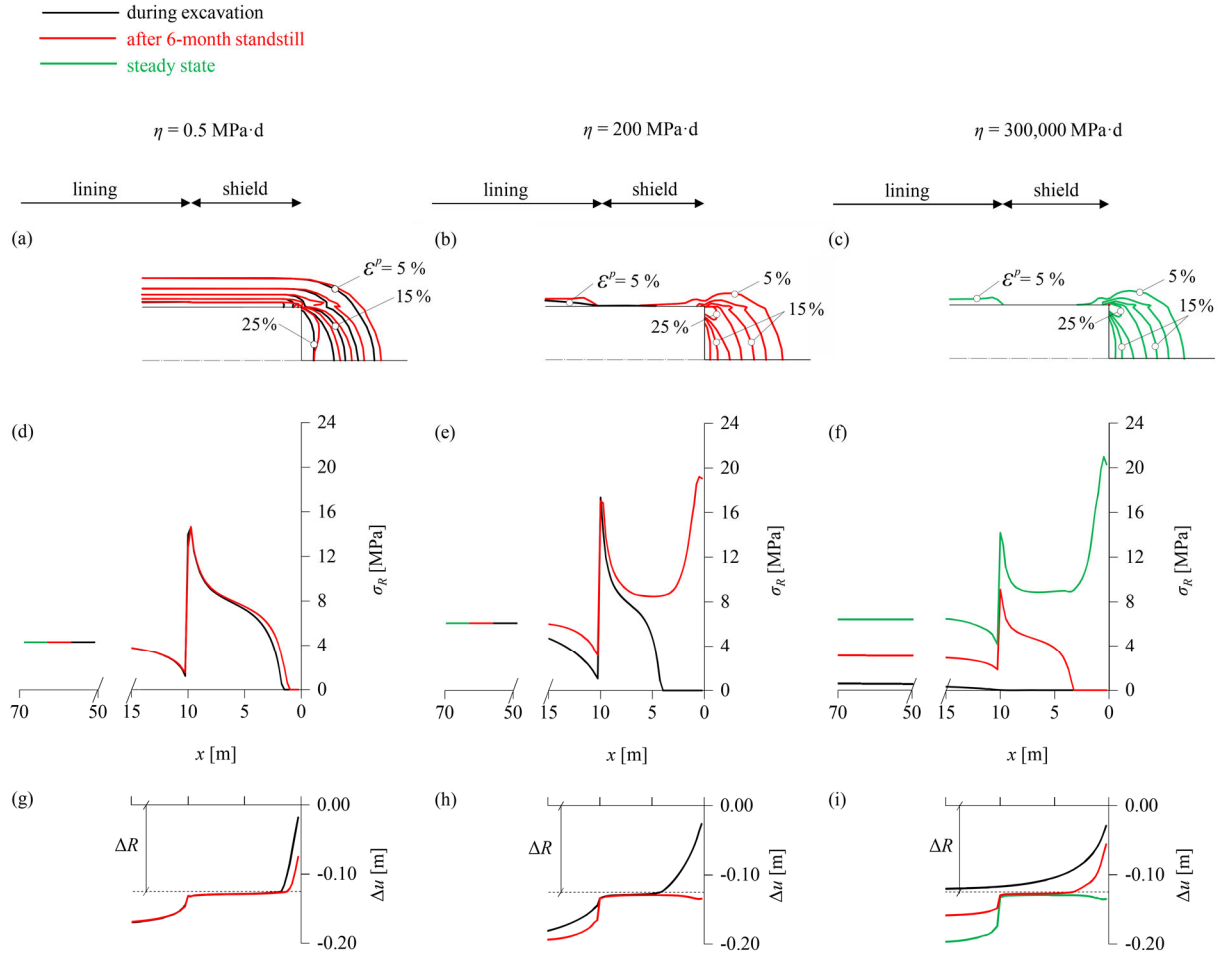
Figure 2.4.   Contour-lines of plastic strain for $\eta = 0.5$ MPa·d (a), $\eta = 200$ MPa·d (b) and $\eta = 300,000$ MPa·d (c); longitudinal rock pressure distribution for $\eta = 0.5$ MPa·d (d), $\eta = 200$ MPa·d (e) and $\eta = 300,000$ MPa·d (f); and longitudinal convergence profile for $\eta = 0.5$ MPa.d (g), $\eta = 200$ MPa·d (h) and $\eta = 300,000$ MPa·d (i) during advance (black), after a 6-month standstill (red) and at steady state (green) (advance rate 20 m/d; other parameters: Table 2.2)

2.4.2   Time-development of shield loading during standstills

Figure 2.5 shows the increase in the average rock pressure developing upon the shield ($\overline{\sigma}_R$) during the standstill and, on the second vertical axis, the corresponding thrust force required to overcome shield skin friction (F_r; Eq. 2.6). For the low viscosity (solid line), the behaviour is almost time-independent and steady state is reached practically already during excavation; the thrust force increases only slightly and only for a few hours, remaining practically constant thereafter. This is also reflected in the rock pressures and convergences in Figs. 2.4d and 2.4g, where the red lines which hold after a 6-month standstill are very close to the black lines which hold for the conditions during excavation. For the high viscosity (dotted line), the annular gap remains open during excavation (see black line in Fig. 2.4i); the ground establishes contact with the shield during a standstill, after about 40 days (point P_3), and subsequently exerts an increasing pressure which, after about 500 days, exceeds the pressure that would develop in the case of practically time-independent behaviour (point P_4); however, this case is irrelevant from the practical engineering

viewpoint since standstill durations are typically much shorter. Nevertheless, a similar behaviour can be observed for the moderate viscosity too (dashed line). In this case, the instantaneous thrust force is smaller than with the time-independent model ($\eta = 0.5$ MPa·d) but reaches the same value very rapidly during a standstill (within less than 1 day; point P_1) and a value about 50% higher after almost 10 days (point P_2). This case is therefore the most critical from a practical engineering viewpoint.

In conclusion, assuming that the plastic deformations develop instantaneously is in no way a conservative assumption: Models that disregard creep may overestimate the shield loading during excavation but considerably underestimate the rock pressure developing during (even short) standstills.
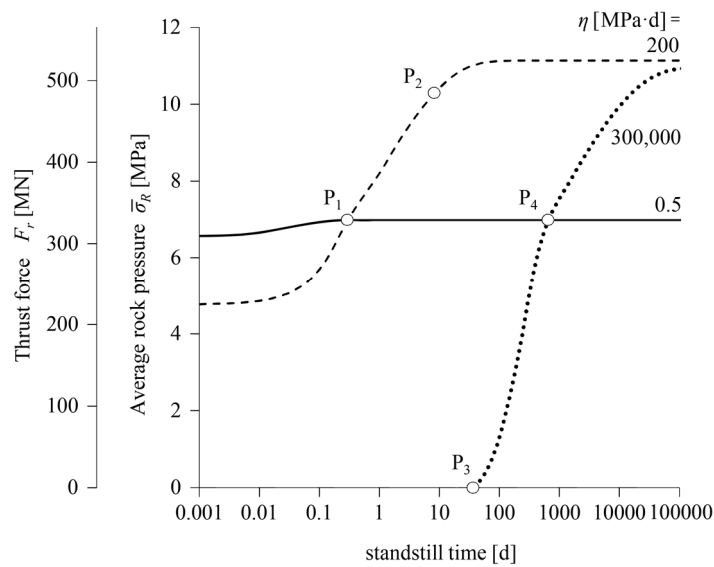
It

Figure 2.5.   Increase in the thrust force and in the average rock pressure developing on the shield during a standstill (advance rate 20 m/d; other parameters: Table 2.2)

2.4.3 Effect of viscosity on shield loading

Figure 2.6 shows the effect of viscosity on the average rock pressure developing upon the shield and on the thrust force during advance, after a 6-month standstill and at steady state. The second abscissa axis shows the time required to reach practically steady state conditions in the plane strain problem of a rigidly supported tunnel of Fig. 2.1b, thus providing a sense of the creep intensity for any given η-value. The rock pressure is identical in all three time-instances for very small viscosities, where the behaviour is practically time-independent. The curves separate thereafter, since additional viscoplastic deformations that occur over time increase the pressure on the shield; this effect is more pronounced in the case of intermediate and high viscosities, for which the conditions during advance are far away from the ones at steady state. With increasing viscosity, the rock pressure increases to a maximum value and thereafter decreases, becoming zero (no contact between ground and shield) for sufficiently large values, both during excavation and after a standstill. Conversely, the steady-state curve remains constant after a point, since contact will eventually occur after a sufficiently long time, even for extremely high viscosity values. The 6-month and the steady-state curves coincide for viscosities up to about 1000 MPa·d, as in this range steady state is reached in less than 6 months.
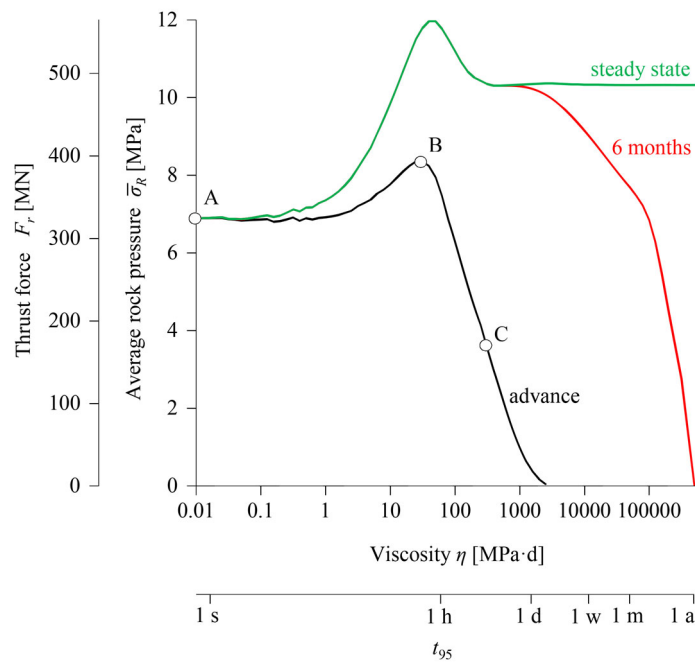
Figure 2.6.   Thrust force and average rock pressure developing on the shield as a function of the viscosity η (advance rate 20 m/d; other parameters: Table 2.2)

2.4.4   Analysis of the counter-intuitive behaviour

The peak in the relationship between rock pressure and viscosity is counter-intuitive at first glance. One would expect the pressure to monotonically decrease with increasing viscosity, due to delayed occurrence of viscoplastic deformations. This seemingly paradoxical behaviour is explained with reference to Figure 2.7, which shows the equivalent plastic strains (Fig. 2.7a) and the longitudinal rock pressure and convergence profiles (Figs. 2.7b, 2.7c, respectively) during advance for cases A, B and C annotated on Figure 2.6.

Figure 2.7 demonstrates two counteracting effects of increasing viscosity: (i), the annular gap closes later, and hence the contact area between ground and shield decreases (Fig. 2.7c), whereas, (ii), stress relief in the ground ahead of the face is less pronounced (Fig. 2.7b) due to the smaller plastic deformations (Fig. 2.7a), and hence the pressure transferred to the shield when excavating the ground is higher. In case A, where the behaviour is practically time-independent, contact occurs closer to the face than in cases B and C (Fig. 2.7c), but the relaxation of the ground ahead of the face is much greater, as the plastic zone is much more extended (Fig. 2.7a) and the radial stresses are much lower (Fig. 2.7b). In case B, the contact point moves further behind the tunnel face than in case A (Fig. 2.7c); however, the stresses exerted on the shield are higher because the pre-excavation stresses are higher (Fig. 2.7b), and the contact occurs close enough to the face for this influence to be relevant. In case C with the highest viscosity, the pre-excavation stresses ahead of the face are even higher than in case B (Fig. 2.7b) but contact is established too far behind the face (Fig. 2.7c) for the average shield loading to be influenced, and the latter is thus lower than in case B.

In conclusion, it can be said that for the range of lower viscosities (between points A and B), the effect of the pronounced stress relief (ii) dominates over that of the contact area (i), whereas the opposite holds in the range of higher viscosities (between points B and C). This interplay produces the counter-intuitive behaviour, which has not been reported in the literature thus far, but is unfavourable for shield jamming during advance and also later on (Fig. 2.6).
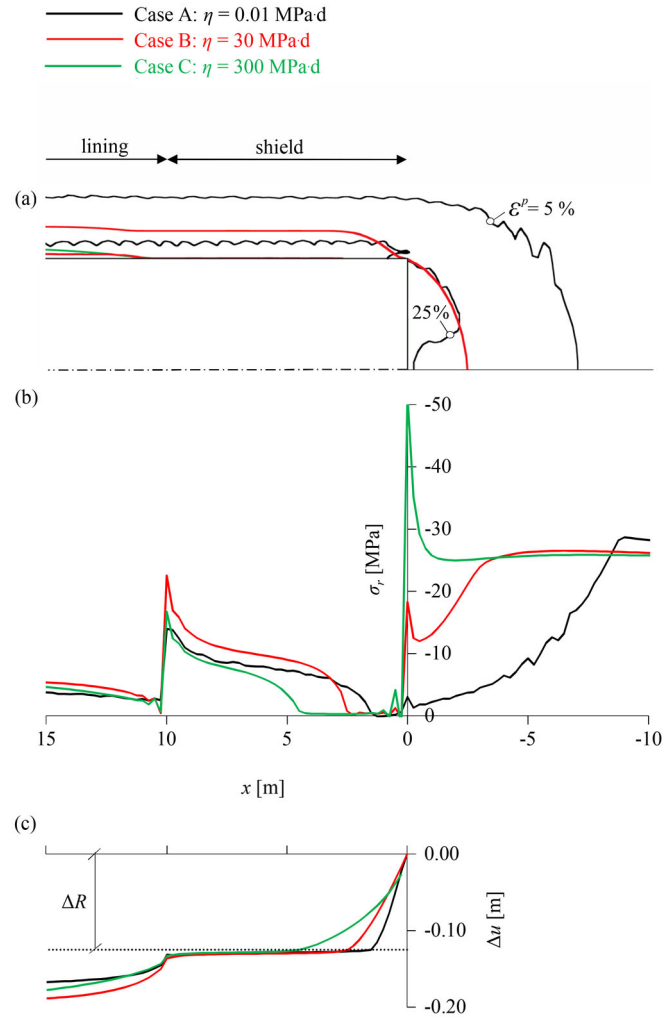
Figure 2.7.   Contour-lines of plastic strain (a), longitudinal rock pressure and radial stress distribution (b), and longitudinal convergence profile (c) during advance for η = 0.01 MPa·d (black), η = 30 MPa·d (red) and η = 300 MPa·d (green) (advance rate 20 m/d; other parameters: Table 2.2)

2.4.5   Effect of viscosity on lining loading

Figure 2.8 shows the effect of viscosity on the pressure that develops on the lining at a cross-section far behind the face (distance $10R$) at steady-state conditions. With increasing viscosity, the lining pressure increases practically monotonically and reaches a maximum value at very high viscosities, for which the ground response to tunnelling is practically elastic in the vicinity of the advancing heading. The higher the viscosity, the lower will be the short-term lining load, the lesser will be the stress relief that the ground experiences before lining installation, and the greater will be the stress relief of the ground over time that will be accommodated by the lining (see green lines of steady-state lining pressure in Figs. 2.4d – 2.4f). This effect is qualitatively similar in the case of consolidation: a low permeability (equivalent to high viscosity) is more unfavourable for the final lining loading since the excess pore pressure dissipation and the resulting ground relaxation due to consolidation happen long after the excavation (Ramoni and Anagnostou, 2011b).
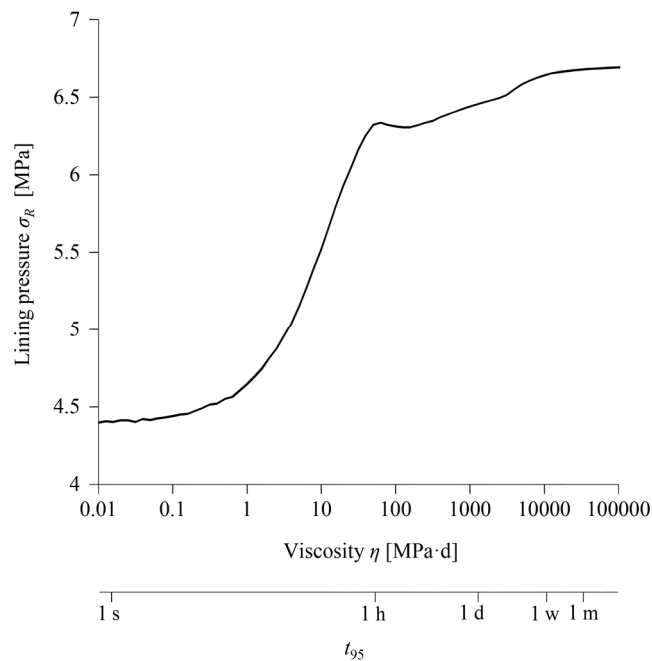
Figure 2.8.   Steady-state lining pressure at a distance of 5 diameters behind the tunnel face as a function of the viscosity η (advance rate 20 m/d; other parameters: Table 2.2)

2.5 Modelling of standstills

Regular TBM operation can be idealised as a discrete process of periodically repeated excavation cycles of duration ΔT, as shown in Figure 2.9. Each cycle starts with a stop-and-go phase, where continuous boring takes place over a period $\Delta T_1 = L_T / v_N$, L_T being the length of one lining ring and v_N the net advance rate, followed by a short standstill for the erection of the lining ring over a period ΔT_2. The installation of N lining rings is followed by an ordinary standstill for cutterhead inspections, disk replacements, maintenance, face mappings, *etc*. over a period ΔT_3, which typically ranges between a few hours and $1 - 2$ days. The total duration of one excavation cycle can thus be expressed as $\Delta T = N (\Delta T_1 + \Delta T_2) + \Delta T_3$. Exceptional incidents, *e.g.* cave-ins, may also occur at any point during the advance ("extraordinary standstills"), forcing the TBM to remain at standstill for much longer periods.
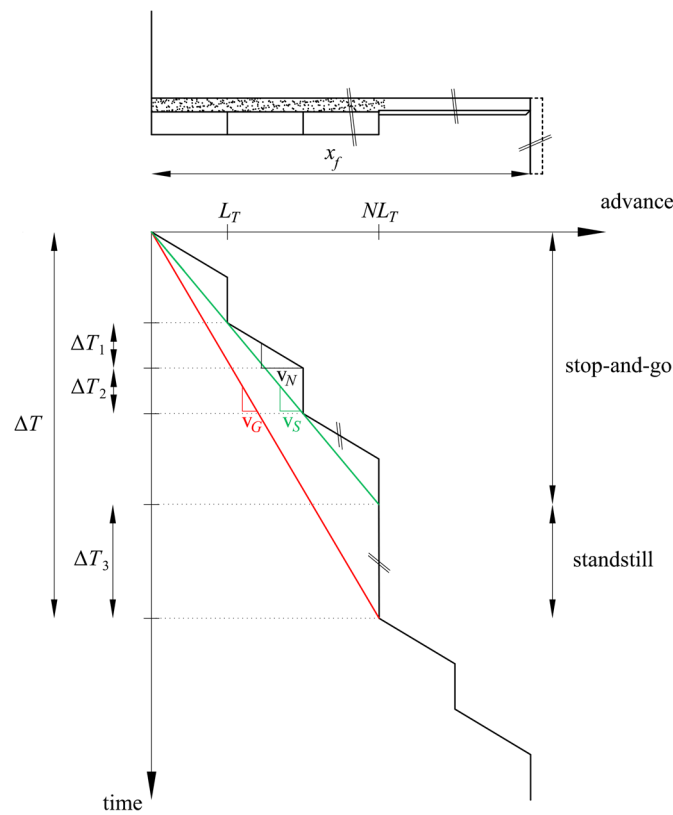
Figure 2.9.   Parameters for discrete, semi-discrete and continuous simulations of a full TBM operation cycle consisting of several stop-and-go cycles followed by one standstill.

As mentioned in the Introduction, all existing works on ground exhibiting time-dependent response to tunnelling simulate the TBM advance as continuous (*e.g.,* Ramoni and Anagnostou, 2011b; Barla *et al.*, 2014; Barla, 2018; Hasanpour *et al.*, 2015; Mohammadzamani *et al.*, 2019; Zhang and Zhou, 2017, *etc.*), which is equivalent to a smearing of the full excavation cycle considering a gross advance rate v_G (red line in Fig. 2.9). The latter is considerably lower than the net advance rate v_N, according to the following expression:

$$v_G = v_N \left(1 + \frac{\Delta T_2}{\Delta T_1}\right)^{-1} \left(1 - \frac{\Delta T_3}{\Delta T}\right). \tag{2.7}$$

An intermediate approach to considering the gross advance rate is to smear only the very short standstills for lining erection during the stop-and-go phase (ΔT_2), considering an equivalent advance rate v_S (green line in Fig. 2.9), with

$$v_S = v_N \left(1 + \frac{\Delta T_2}{\Delta T_1}\right)^{-1}, \tag{2.8}$$

but otherwise explicitly simulate the longer ordinary standstills (ΔT_3). This so-called "semi-discrete" approach was also adopted in the computations in Section 2.4.

In the following, the accuracy of the simplified method that considers continuous excavation with the gross advance rate and of the proposed semi-discrete simulation will be assessed in relation to a formally correct discrete simulation, based on the predicted required thrust force. The total required thrust force during TBM advance consists in general of a boring force and a friction force (Eq. 2.6), which is evaluated considering the sliding shield skin friction coefficient. For the TBM restart after a standstill only the friction force needs to be considered, which, however, must be evaluated for the higher static shield skin friction coefficient. This distinction is only possible in discrete simulations; in semi-discrete and continuous simulations, the thrust force is assumed equal to the maximum between its values during advance and during TBM restart after a standstill. For the results discussed hereafter, a typical value of 17 MN is assumed for the boring force.

As the boring force is constant, the total required thrust force depends only on the friction force or, equivalently, the average shield pressure $\overline{\sigma}_R$ (Eq. 2.6). In a discrete simulation, $\overline{\sigma}_R$ depends in general on the *in-situ* stress σ_0, on the material constants of the ground (E, v, f_c, ϕ, ψ, η), on the shield and lining stiffnesses (K_s, K_l), on the geometric parameters (R, L, ΔR, L_T) and on the process parameters (v_N, N, ΔT_1, ΔT_2, ΔT_3, ΔT). Considering the parameter dimensions, the inverse proportionality between the Young's modulus E and the displacements in elastoplastic media (Anagnostou and Kovári, 1993; Ramoni and Anagnostou, 2010b) and the interdependencies of some parameters (*e.g.*, $\Delta T_1 = L_T / v_N$), $\overline{\sigma}_R$ can be expressed in the following non-dimensional form:

$$\frac{\overline{\sigma}_R}{\sigma_0} = f\left(\frac{E \Delta R}{\sigma_0 R}, v, \frac{f_c}{\sigma_0}, \phi, \psi, \frac{L}{R}, \frac{K_s R}{E}, \frac{K_l R}{E}, \frac{\eta v_N}{E R}, \frac{L_T}{R}, \frac{\Delta T_2}{\Delta T_1}, \frac{\Delta T_3}{\Delta T}, \frac{v_N \Delta T}{R}\right). \tag{2.9}$$

In the proposed semi-discrete simulation, the list of parameters reduces as follows:

$$\frac{\overline{\sigma}_R}{\sigma_0} = f\left(\frac{E\Delta R}{\sigma_0 R}, \nu, \frac{f_c}{\sigma_0}, \phi, \psi, \frac{L}{R}, \frac{K_s R}{E}, \frac{K_l R}{E}, \frac{\eta v_S}{ER}, \frac{\Delta T_3}{\Delta T}, \frac{v_S \Delta T}{R}\right), \qquad (2.10)$$

and in the fully continuous simulation as follows:

$$\frac{\overline{\sigma}_R}{\sigma_0} = f\left(\frac{E\Delta R}{\sigma_0 R}, \nu, \frac{f_c}{\sigma_0}, \phi, \psi, \frac{L}{R}, \frac{K_s R}{E}, \frac{K_l R}{E}, \frac{\eta v_G}{ER}\right). \qquad (2.11)$$

Using Eqs. 2.7 and 2.8, the dimensionless arguments of Eqs. 2.10 and 2.11 related to time-dependency can be expressed as functions of the independent dimensionless parameters of Eq. 2.9.

Section 2.5.1 evaluates the accuracy of the semi-discrete simulation of the stop-and-go phase, while Section 2.5.2 considers a full operation cycle, investigating the adequacy of the continuous and semi-discrete simulations. In both sections the basic behaviour is analysed first, followed by a parametric study that considers a common range of normalised net advance rates $\eta v_N/E/R = 10^{-5} - 10^4$ and a constant normalised segment length $L_T/R = 0.2$.

2.5.1 Stop-and-go phase

The effect of the proposed smearing of a stop-and-go advance (Eq. 2.8) is examined in Figure 2.10, which shows the typical development of the thrust force along the tunnel according to the results of a discrete simulation (TBM strokes with continuous advance for ΔT_1 with v_N, alternating with standstills for ΔT_2) and a semi-discrete simulation (continuous advance with v_S and no standstill). The discrete simulation predicts a saw-shaped curve where the upper-values correspond to the TBM restart phases and the low-values correspond to the continuous advance phases. The smeared simulation, by contrast, predicts a smooth curve, which captures reasonably well the upper values of the discrete simulation.

Figure 2.11 shows the error of semi-discrete simulations (with respect to fully discrete simulations) as a function of the ratio $\Delta T_2/\Delta T_1$. As expected, the error is smallest for very small $\Delta T_2/\Delta T_1$, where the advance becomes practically continuous. In all other cases, except for 5 outliers, the overall error falls below 10%, indicating that the accuracy of a semi-discrete approach over the stop-and-go phase is adequate in engineering terms.
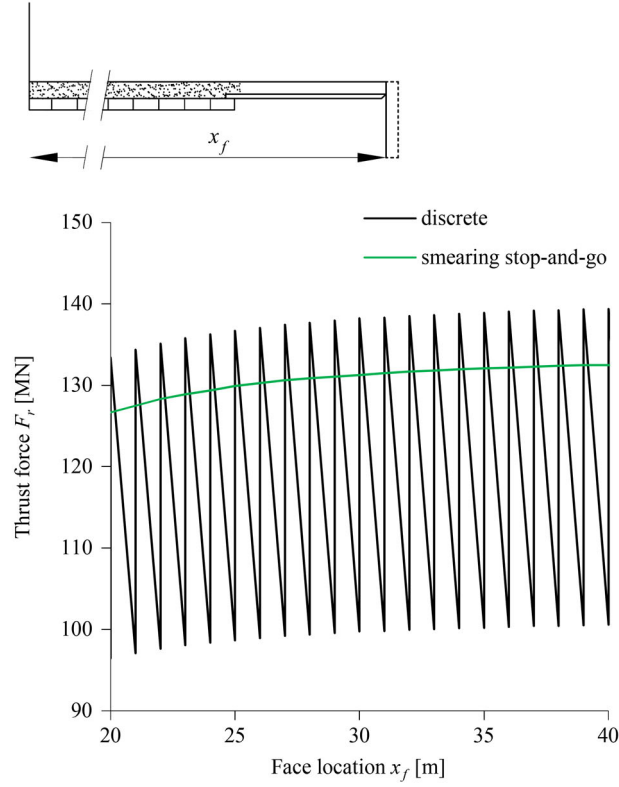
Figure 2.10.   Thrust force evolution during the stop-and-go TBM operation based on discrete and semi-discrete simulations ($\Delta R = 0.25$ m, $L_T = 1$ m, $v_N = 50$ m/d, $v_S = 25$ m/d, $\eta = 60$ MPa·d, $\Delta T_2 = \Delta T_1$; other parameters: Table 2.2)
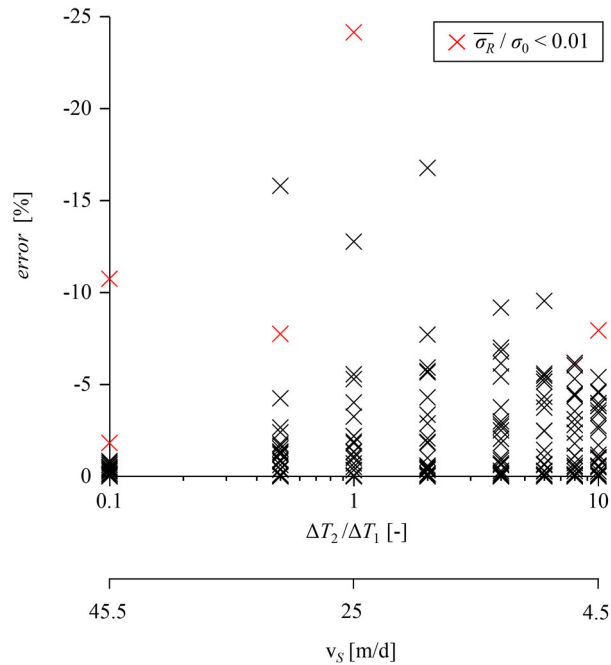
Figure 2.11.   Error of semi-discrete simulations of the stop-and-go phase with respect to discrete simulations versus normalised lining erection duration ($E\Delta R/\sigma_0/R = 1, 2$; $f_c/\sigma_0 = 0.05, 0.2$; $\phi = 25°$; $L/R = 2$; $K_s R/E = 10$; $K_l R/E = 0.5$; $\eta v_N/E/R = 10^{-5}, 10^{-4}, ... , 10^4$; $L_T/R = 0.2$; $\Delta T_3/\Delta T = 0$, other parameters: Table 2.2; 640 computations in total)

2.5.2 Full excavation cycle

Full excavation cycles consisting of 16 hours long stop-and-go TBM operations alternating with 8 hours long maintenance standstills (2+1 shifts) are considered. Figure 2.12 shows the time-face location diagram (bottom) and the required thrust force along the tunnel (top), as determined from the three simulations, that is from the discrete simulation (black lines; $v_N = 50$ m/d), the semi-discrete simulation (green lines; $v_S = 25$ m/d) and the continuous simulation (red lines; $v_G = 17$ m/d).

During the 8 hour maintenance standstill at xf = 16.5 m (point A) the necessary thrust force increases by a factor of 4 (from 56 MN to 224 MN) because the shield partially prevents the development of the time-dependent deformations. Upon restart of the TBM (point A), the thrust force remains high during the advance through the plastified ground ahead of the tunnel face, starts decreasing as the TBM approaches the plastic zone boundary, and rapidly drops (complete unloading) when the shield exits the plastic zone and enters the adjacent, still elastic, rock. Subsequently, it starts increasing again due to ground plastification ahead of the face, reaching lower values in comparison to point A (ca. 56 MN, similar to the stop-and-go phase preceding point A). After the stop-and-go period (point B), the thrust force increases again substantially during the maintenance standstill (ca. 240 MN; point C), and the whole excavation cycle is repeated thereafter. The continuous simulation (red line) underestimates the maximum thrust force by more than 40% (point D: 140 vs. 240 MN), while the semi-discrete simulation (green line) approximates it to within 15% (point E: 205 vs. 240 MN).
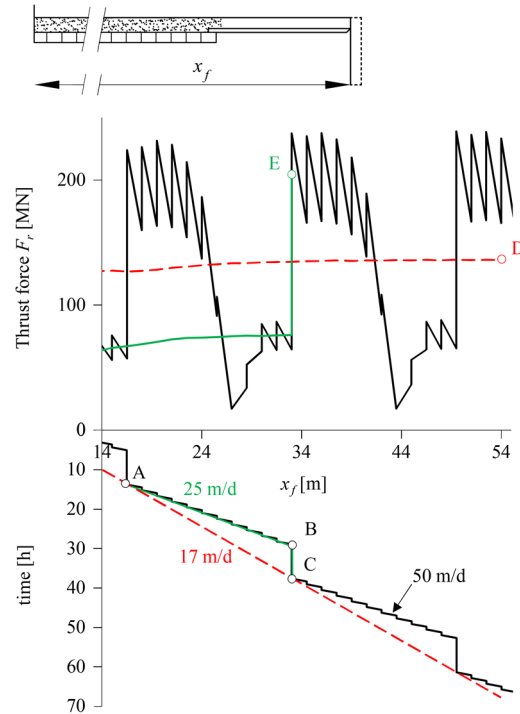
Figure 2.12. Thrust force evolution during two full excavation cycles based on discrete, semi-discrete and continuous simulations ($\Delta R = 0.25$ m, L = 10.5 m, $L_T = 1.5$ m, $\eta = 100$ MPa·d, $\Delta T_2 = \Delta T_1 = 0.72$ h, $\Delta T_3 = 8$ h, $\Delta T = 24$ h, $v_N = 50$ m/d, $v_S = 25$ m/d, $v_G = 17$ m/d; other parameters: Table 2.2)
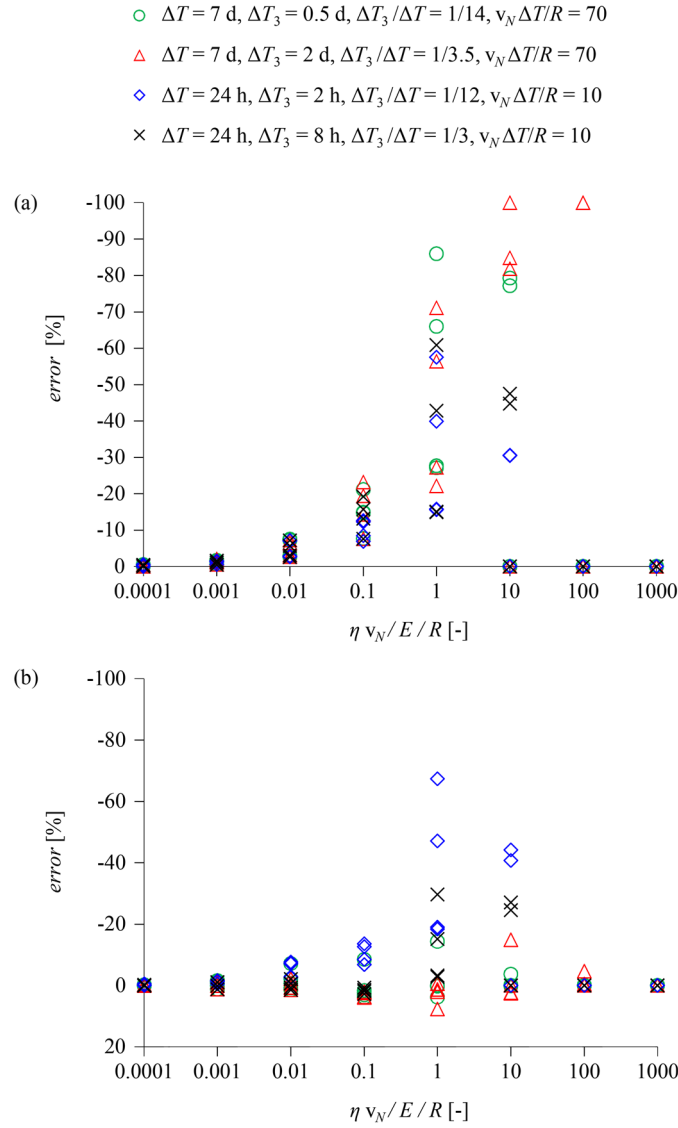
Figure 2.13. Error of continuous (a) and of semi-discrete simulations (b) of a full excavation cycle with respect to discrete simulations versus normalised net advance rate $\eta\,v_N\,/E/R$ in four stop-and-go and standstill scenarios ($E\Delta R/\sigma_0/R = 1$, 2; $f_c/\sigma_0 = 0.05$, 0.2; $\phi = 25°$; $L/R = 2$; $K_sR/E = 10$, $K_lR/E = 0.5$; $L_T/R = 0.2$; $\Delta T_2/\Delta T_1 = 1$, other parameters: Table 2.2; 320 computations in total for each diagram)

Figures 2.13a and 2.13b show the error of continuous and semi-discrete simulations, respectively, with respect to fully discrete simulations, as a function of the normalised net advance rate $\eta\,v_N\,/E/R$. The parametric study assumes $\Delta T_2\,/\Delta T_1 = 1$ (*i.e.*, the time for one lining ring erection equals to the duration of one TBM stroke), $\Delta T_3\,/\Delta T = 1/14$, 1/12, 1/3.5, 1/3, and $v_N\Delta T/R = 10$, 70, which for a 10 m diameter tunnel and a net advance rate of 50 m/d covers the following realistic scenarios:

- 6.5 d stop-and-go followed by a 0.5 d standstill ($\Delta T_3 = 0.5$ d, $\Delta T = 7$ d);
- 5 d stop-and-go followed by a 2 d standstill ($\Delta T_3 = 2$ d, $\Delta T = 7$ d);
- 22 h stop-and-go followed by a 2 h standstill ($\Delta T_3 = 0.083$ d, $\Delta T = 1$ d);
- 16 h stop-and-go followed by an 8 h standstill ($\Delta T_3 = 0.33$ d, $\Delta T = 1$ d).

For very small viscosities or advance rates, the error is zero, as expected, since there is no time-dependency. The error increases with increasing viscosity in both cases, exceeding 30% in continuous simulations for values $\eta \, v_N /E/R$ greater than 1. (The 100% errors for very high $\eta \, v_N /E/R$ correspond to cases where the continuous simulation predicts zero shield pressure.) The error of the semi-discrete simulation is considerably smaller and does not exceed 20% for $\eta \, v_N /E/R$ below $0.1 - 1$ or beyond 10. In the range $1 - 10$ the error is considerable, indicating that the proposed approach is inapplicable and that TBM simulations must consider even the short standstills of the stop-and-go process explicitly.

2.6   Application examples

The importance of considering the effects of creep (Section 2.4) and adequately modelling the excavation standstills during the construction process (Section 2.5) is demonstrated in this section via two application examples. The first example analyses the TBM drive during construction of the Fréjus safety gallery, whereas the second presents a feasibility assessment of a TBM drive through the conventionally excavated Sedrun North critical zone of the Gotthard base tunnel.

2.6.1   Fréjus safety gallery

The 13 km long Fréjus highway tunnel connecting Modane (France) to Bardonecchia (Italy) is located on the French-Italian border in the Western Alps. Construction started in 1974 by conventional tunnelling (full-section drill and blast with 4.5 m advance steps) and the tunnel opened to road traffic in 1980. The single main tube of the tunnel has an approximately NS orientation and crosses three alpine lithotypes at a maximum depth of 1800 m, the principal being the Piemontaise zone that consists of calc-schist with phyllitic and carbonate facies. In 2009 works started on a parallel safety gallery located 50 m from the highway tunnel. The 6.5 km long stretch of the gallery in France was excavated between 2011 and 2013, with drill and blast over the first 650 m and with a single shield TBM over its remaining part. The latter crosses black and green schist between chainages $650 - 1500$ m, anhydrite between chainages $1500 - 1750$ m, and calc-shist between chainages $1750 - 6500$ m (Schivre *et al.*, 2014; De la Fuente *et al.*, 2020).

To ensure that the TBM was able to adjust to various adverse scenarios previously encountered during the highway tunnel construction in the 70s, the following specifications were used (Schivre *et al.*, 2014): shield length of 11.2 m; nominal shield diameter of 9.37 m with conicity of 60 mm on the diameter; nominal boring diameter of 9.46 m (90 mm overcut on the diameter at the tunnel crown in the shield front), adjustable to 9.56 m or 9.66 m (to accommodate an increase of the overcut by 100 and 200 mm on the diameter, respectively); and installed thrust force of 106 MN.

Monitoring data were collected during the TBM drive from 10 hydraulic jacks installed over the upper shield extrados. The data indicated maximum average convergences of up to 300 mm in two zones in calc-schist, between chainages $1750 - 3000$ m and $4300 - 6500$ m (*cf.* Fig. 8 in Vinnac *et al.*, 2014). The higher convergences in these zones are partially attributed to buckling of rock layers along the schistosity planes oriented parallel to the tunnel axis, which resulted in the detachment of rock blocks and their collapse on the shield and lining. Despite these effects, the TBM specifications, the use of the intermediate overcut in parts and the continuous adjustment

of the TBM operation based on real-time monitoring data, enabled an uneventful drive with a moderate thrust force up to 30 MN in the calc-shist zone. The maximum thrust force of 52 MN was recorded in the anhydrite zone (*ca.* chainage 1550 m), where the recorded convergences were, however, much lower (*cf.* Fig. 8 in Vinnac *et al.*, 2014).

The present application example analyses the TBM drive through the calc-schist zone, based upon fully discrete transient numerical simulations that consider the effects of creep (Section 2.3). Comparative computations are also conducted to assess the accuracy of the time-independent ($\eta = 0$) and time-dependent ($\eta > 0$) continuous models usually employed, and of the semi-discrete model proposed in Section 2.5. The simulations do not consider the anhydrite zone, where the maximum thrust force was recorded, since the adopted computational model is not suitable for capturing the additional time-dependency related to chemical processes in anhydrite ("swelling").

2.6.1.1   Adopted parameters

The parameters adopted in the simulations are given in Table 2.3. A $t_{95} = 60 - 120$ days, indicating moderate creep intensity, is estimated from monitoring data for the convergence evolution over time at chainage 5080 m of the highway tunnel. The data concerns the most unfavourable direction over the horseshoe-shaped profile, normal to the schistosity planes (*cf.* Fig. 4b in De la Fuente *et al.*, 2020), and was recorded prior to the installation of the final lining. The estimated t_{95} is used to determine the expected range of viscosity η after Figure 2.1a (open tunnel profile with low support resistance), considering additionally two parameter sets for calc-schist: (i) the set reported by Vinnac *et al.* (2014), and, (ii), a set calibrated based on the monitoring data. For simplicity, set (ii) is chosen to be identical to (i), except for the Young's modulus E; the latter is adjusted such that the maximum radial displacement predicted by a ground response curve (GRC; Anagnostou and Kovári, 1993) for an unsupported opening matches the one of the monitoring data. The GRC for set (i) gives a maximum displacement of *ca.* 600 mm on the diameter, which includes the ground pre-deformation ahead of the tunnel face. On the other hand, the monitoring data indicates maximum long-term convergence (*i.e.,* displacement relative to the tunnel face) of *ca.* 480 mm on the diameter, in the most unfavourable cross-sectional orientation. Assuming that the pre-deformation is 50% of the total displacement far behind the face (typically 30-70%), the latter is *ca.* 2*480 = 960 mm. A Young's modulus of 7500*600/960 = *ca.* 4700 MPa is thus adopted in set (ii), 1.6 times lower compared to set (i). Since f_c and ϕ are identical in the two sets, η is estimated at the same point of Figure 2.1a using only different E values; the η-ranges of the two sets are thus linearly dependent by a factor of 1.6.

2.6.1.2   Analysis of TBM drive

The fully discrete model predicts contact between shield and ground only when considering the nominal overcut of 60 mm and the lowest viscosity value of 1700 MPa·d for set (ii). Figure 2.14 shows with black lines the time-face location diagram (bottom) and the required thrust force along the tunnel (top) for this case. Analogously to Section 2.5 two full excavation cycles are considered, each consisting of 16-hour long stop-and-go TBM operations (2 shifts; part between

points A, B) alternating with 8-hour long maintenance phases (1 shift; part between points B, C), with realistic typical durations for the various operations (Table 2.3). The maximum predicted thrust force is 41 MN, very close to the maximum value of 30 MN recorded in the critical zones (Fig. 8 in Vinnac *et al.*, 2014). Differences may be partially attributed to the asymmetric loading of the shield resulting from the detachment of blocks following buckling, which cannot be captured by the adopted rotationally symmetric computational model (Section 2.3). When considering the nominal overcut with higher viscosity values for any of the two parameter sets, or the intermediate overcut of 110 mm with any of the viscosity values and parameter sets, the model predicts no contact between shield and ground, and hence the thrust force is constant and equal to the boring force (these cases are not shown in Fig. 2.14).
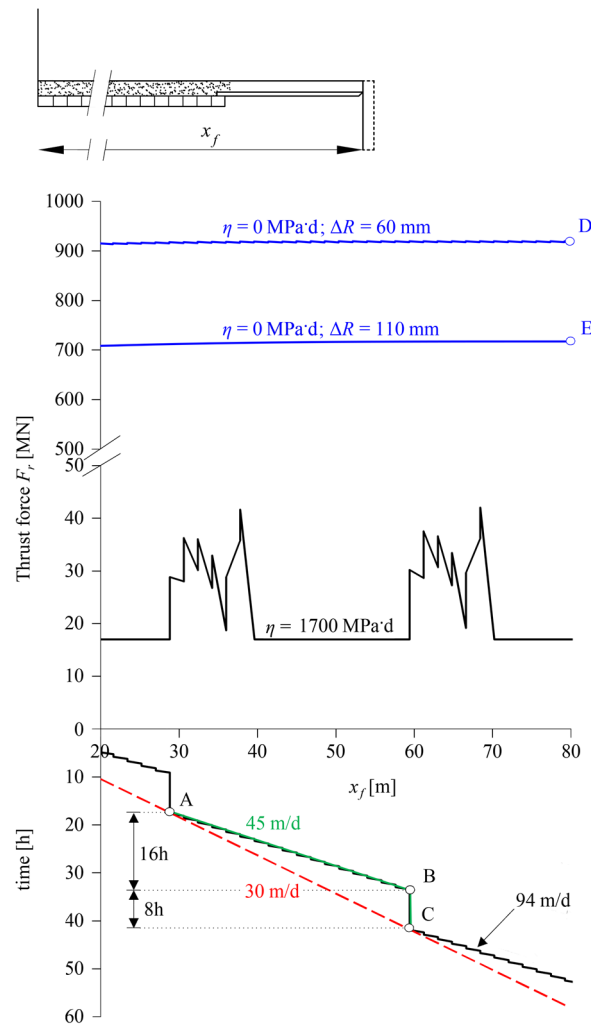

Figure 2.14. Fréjus safety gallery: Thrust force evolution predicted by discrete and time-independent continuous simulations of two full excavation cycles (parameters: Table 2.3)

Table 2.3.   Parameters considered in application examples

Ground			Fréjus safety gallery	Gotthard Base tunnel
Young's modulus	E	[MPa]	7500[a], 4700[b]	$1000 \pm 15\%$[r]
Poisson's ratio	v	[-]	0.2[a]	0.25
Angle of internal friction	ϕ	[°]	35[a]	27 ± 3[s]
Dilatancy angle	ψ	[°]	15[c]	5 ± 2[s]
Uniaxial compressive strength	f_c	[MPa]	3.8[a]	1.3 ± 0.3[s]
Time to reach 95% of displacement	t_{95}	[d]	60 – 120[d]	
Viscosity	η	[MPa·d]	2700 – 5400[e] 1700 – 3400[f]	10 - 100[t]
Overburden	H	[m]	1200 – 1400[g]	800
In-situ stress	σ_0	[MPa]	40[h]	20
TBM				
Nominal boring radius	R	[m]	4.73[i]	5
Shield Length	L	[m]	11.2[i]	10
Overcut	ΔR	[mm]	60, 110[j]	200
Shield thickness	d_s	[mm]	75	75
Young modulus of the shield (steel)	E_s	[GPa]	210	210
Shield stiffness[k]	K_s	[MPa/m]	704	630
Coefficient of shield skin friction	μ	[-]	0.3, 0.4[l]	0.1, 0.15[u]
Maximal cutter force[m]	F_c	[kN]	267	267
Number of cutters	n	[-]	63[i]	63[v]
Thrust force (boring process)[n]	F_b	[MN]	17	17
Lining				
Lining thickness	d_l	[mm]	400[i]	500
Young's modulus of the lining (concrete)	E_c	[GPa]	35	35
Lining stiffness[k]	K_l	[MPa/m]	626	700
Segmental ring width	L_T	[m]	1.8[i]	1.5
Construction process				
Time for one ring advance[o]	ΔT_1	[min]	28	36
Time for one ring build	ΔT_2	[min]	30	30
Duration of the longer standstill	ΔT_3	[h]	8	8
Time for one cycle	ΔT	[h]	24	24
Net advance rate	v_N	[m/d]	94[p]	60
Smeared stop-and-go advance rate [q]	v_S	[m/d]	45	33

[a]   Residual values after Table 1 in Vinnac *et al.* (2014)
[b]   Calibrated based on monitoring data at Chainage 5080 of the Fréjus road tunnel (De la Fuente *et al.*, 2020); see Section 2.6.1
[c] $\psi = \phi$-20º
[d]   Estimated from monitoring data of convergence development over time at Chainage 5080 (Fig. 4b in De la Fuente *et al.*, 2020)
[e]   Estimated after Fig. 2.1a for $f_c/\sigma_0 = 0.1$, $\phi = 35°$, $t_{95} E / \eta = 167$, $t_{95} = 60$ - 120 d, $E = 7500$ MPa
[f]   Estimated after Fig. 2.1a for $f_c/\sigma_0 = 0.1$, $\phi = 35°$, $t_{95} E / \eta = 167$, $t_{95} = 60$ - 120 d, $E = 4687.5$ MPa
[g]   After Fig. 8 in Vinnac *et al.* (2014) for the critical squeezing zone between chainages 4500 and 5300 m
[h]   Rounded value of higher horizontal *in-situ* stress (lateral earth pressure coefficient of 1.2-1.4), considering overburdens of 1200-1400 m and unit weight of 27 kN/m³ (Vinnac *et al.*, 2014)
[i]   Schivre *et al.* (2014)
[j]   Equivalent uniform overcuts for rotationally symmetric analyses; taken equal to the value in the middle of the shield length, considering nominal and intermediate overcuts of 90 and 190 mm on the diameter in the shield front, and conicity of 60 mm on the diameter after Schivre *et al.* (2014): (90+60/2)/2 = 60 mm, (190+60/2)/2 = 110 mm on the radius.
[k] $K_l = E_l d_l / R^2$; $K_s = E_s d_s / R^2$
[l]   Sliding and static friction coefficient without shield extrados lubrication; after Table 2.3 in Ramoni and Anagnostou (2011a)
[m]   After Sänger (2006)
[n] $F_b = n F_c$
[o] $\Delta T_1 = L_T / v_N$
[p]   Average of 50 - 80 mm/min after Fig. 8 in Vinnac *et al.* (2014)
[q]   Eq. 2.6
[r]   After Fig. 5 in Vrakas *et al.* (2018), E_{50}-value for 20 MPa *in-situ* stress
[s]   After Table 1 in Vrakas *et al.* (2018)
[t]   After Section 5.5.1 in Cantieni *et al.* (2011)
[u]   Sliding and static friction coefficient with shield extrados lubrication after Table 2.3 in Ramoni & Anagnostou (2011a)
[v]   Assumed value; taken equal to that of the Fréjus application example

2.6.1.3 Accuracy evaluation of semi-discrete and continuous simulations

Both the semi-discrete and the continuous time-dependent models fail to capture the shield ground contact that actually occurred, for both overcuts and viscosity ranges. The prediction error is moderate and justifiable in this specific case, due to the relatively high viscosity values and the very conservative TBM specifications. The accuracy of these models can thus not be assessed in this example. Either way, the applicability of the semi-discrete model would be questionable in this case, since the normalised net advance rate $\eta\,v_N/E/R$ ranges between 7 and 14, which overlaps with the region of highest errors in Figure 2.13b.

Most interesting are the results of the time-independent continuous models. These overestimate the required thrust force excessively, predicting values between 720 MN for a 110 mm overcut (point E in Fig. 2.14) and 920 MN for a 60 mm overcut (Point D in Fig. 2.14), *ca.* 24-30 times higher compared to those observed in reality. Such values lie far beyond technical limits for TBMs and would be thoroughly misleading for a feasibility assessment of the TBM drive. This result clearly demonstrates that relying on continuous time-independent models in cases of moderately to pronouncedly creeping ground may prove excessively conservative, erroneous and misleading.

2.6.2 Gotthard Base tunnel

The 57 km long Gotthard Base railway tunnel in Switzerland was constructed between 1999 and 2011 and opened to traffic in 2016. Its two main tubes cross four geological zones from north to south: the Aar Massif (AM), the Intermediate Tavetsch Massif (TM), the Gotthard Massif (GM) and the penninic gneiss (PM) (Mezger *et al.*, 2013, Vogelhuber *et al.*, 2023). Over the major part of the tunnel crossing the AM, GM and PM zones, which consist of competent gneisses and granites with very few local geologically disturbed regions, the conditions for tunnelling were favourable overall and hard rock TBMs were used. Conversely, over the 1100 m long stretch crossing the southern part of the AM zone (Clavaniev zone) and the northern part of the TM zone at 800 m depth, heavily and pronouncedly variable squeezing conditions were both anticipated and encountered during construction. This critical zone consists of alternating layers of kakiritic gneisses, slates and phyllites, and is commonly referred to as "Sedrun North". The observed variability of squeezing is attributed to differences in the degree of kakiritization, the schistosity orientation and the competent-weak rock layer alternations (Mezger *et al.*, 2013).

The unfavourable conditions for mechanised tunnelling in Sedrun North necessitated resorting to conventional, full-face excavation of the 10 m diameter circular tunnel cross-section, with over-excavation of up to 0.8 m, systematic anchoring of the cross-section and various auxiliary measures, including systematic bolting of the tunnel face (Vogelhuber *et al.*, 2023). In the first stage, a yielding support was installed, consisting of two overlain sliding steel rings connected by friction loops, to accommodate convergences in a controlled manner and allow for stress relief of the ground. In the second stage, after the rate of convergences slowed down, a $0.3 - 0.6$ m thick shotcrete ring was initially applied, followed later by an *in situ*-cast final lining with maximum thickness of 1.2 m. The maximum average radial convergence was *ca.* 40 cm, with peak values as high as 70 cm measured at specific points over the tunnel boundary (Kovári *et al.*, 2008).

The main aim of the present example is to reassess the feasibility of the TBM drive through Sedrun North, considering our knowledge today about the mechanical behaviour of the kakirites, the latest thrust prediction methods and the current state of TBM technology. Concerning the latter, Ramond and Schivre (2019; pp. 32) provide an overview of the installed nominal thrust in single-shield TBMs used in some of the most important tunnelling projects between 2000 and 2019. One can readily identify values as high as, *e.g.*, 140 MN in the Pajares tunnel in Spain, or 155 MN in the Brenner Base tunnel crossing Austria and Italy. Installing additional thrust is possible with an appropriate modification of the TBM, *e.g.,* by installing removable auxiliary hydraulic jacks. This approach was used during the construction of Section 4 of the 10 m diameter Pajares tunnel between 2007 and 2009, where the nominal thrust of 140 MN was initially increased to 193 MN and subsequently to 225 MN, following jamming of the TBM due to the pronounced squeezing conditions (Ramoni and Anagnostou, 2010b). Considering that an installed thrust of 225 MN was materialised 15 years ago, moderately higher values appear thoroughly feasible with incremental developments of current technology.

The feasibility of mechanised tunnelling is assessed with the aid of fully discrete, transient numerical simulations which consider the effects of creep and a reliable set of parameters collected from various rigorous investigations on the Gotthard Base tunnel. Additionally, comparative computations are performed to assess the adequacy for decision-making during design of the proposed semi-discrete model (Section 2.5), the time-independent ($\eta = 0$) and time-dependent ($\eta > 0$) continuous models (which currently constitute the standard in both engineering practice and research), and the design nomograms of Ramoni and Anagnostou (2010b).

2.6.2.1 *Adopted parameters*

The parameters adopted in the computations are given in Table 2.3 and discussed hereafter.

The elasticity and plasticity parameter ranges are taken after Vrakas *et al.* (2018), which consider the results of 90 consolidated drained triaxial compression tests on kakiritic samples from Sedrun North. During the project planning phase between 1998 and 2000, 55 of these tests were conducted (Vogelhuber, 2007), and a further 35 during the construction phase between 2004 and 2007 (Anagnostou *et al.*, 2008), as part of a large experimental programme undertaken by the ETH Rock Mechanics laboratory.

The range of viscosity $\eta = 10 - 100$ MPa·d corresponds to the one estimated by Cantieni *et al.* (2011), based on *in-situ* monitoring data for the tunnel face extrusion during a construction standstill at chainage 2090 m. The data was recorded using reverse-head-extensometers installed along the tunnel axis and showed that the extrusion stopped after 30 days and that 95% of its final value was achieved within about 20 days, thereby indicating a rather low viscosity. The estimation of viscosity by Cantieni *et al.* (2011) is performed analogously to Section 2.2, assuming that the time-development of extrusion is similar to that of the radial displacement in a cross-section far behind the face. Formally speaking, unlike the radial displacement, the extrusion is also influenced by the stress redistributions taking place ahead of the face in the longitudinal direction, and considering this effect may lead to a different viscosity range. However, the differences are

not expected to be significant, considering that the rheological properties of the material are unique, hence the order of magnitude of the viscosity is expected to be the same. Viscosities within the same order of magnitude will lead, as seen in Figure 2.6, to similar thrust forces and thus the conclusions remain valid.

A single shield TBM with shield length equal to the 10 m tunnel diameter is considered. Very low sliding and static shield skin friction coefficients are adopted (μ = 0.1 and 0.15, respectively), which can be achieved via lubrication of the shield extrados (*cf.* Table 2.3 in Ramoni and Anagnostou, 2011a), and a large overcut is assumed (ΔR = 200 mm), which can be materialised with existing overboring systems (*cf.* Table 2.2 in Ramoni and Anagnostou, 2011a). These specifications are deliberately selected to be as favourable as possible, while typical specifications for the shield and lining are otherwise considered. Analogously to Section 2.5, two full excavation cycles are assumed, consisting of 16-hour stop-and-go TBM operations (2 shifts) alternating with 8-hour maintenance phases (1 shift) with typical, realistic durations.

2.6.2.2   Feasibility assessment

Figure 2.15 shows the predicted range of the required thrust force, considering the inherent uncertainties associated with the stiffness, strength, and viscosity of the ground (*cf.* Table 2.3), as well as different simulation methods. The feasibility assessment is discussed with reference to the four black bars, which correspond to fully discrete simulations. From top to bottom, these show the predicted range considering: (i) the expected range of viscosity η = 10 – 100 MPa·d in combination with the mean strength and stiffness parameters; (ii) the minimum expected viscosity η = 10 MPa·d in combination with the expected range of the strength and stiffness parameters; (iii) the maximum expected viscosity η = 100 MPa·d in combination with the expected range of the strength and stiffness parameters; and, (iv), the expected ranges of the viscosity, strength and stiffness parameters.
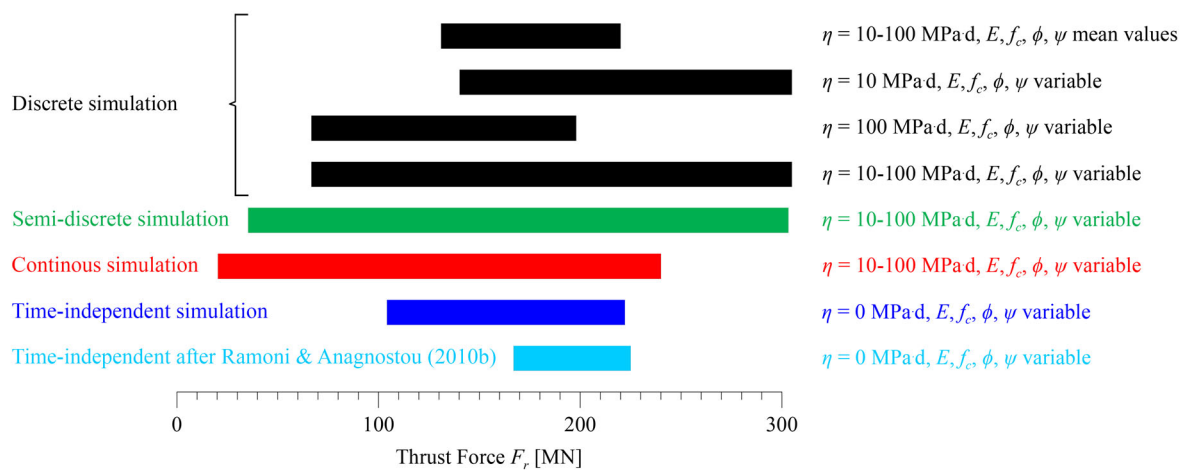
Figure 2.15. Gotthard base tunnel: Predicted thrust force range from discrete, semi-discrete and continuous time-dependent and time-independent simulations of two full excavation

A comparison of the 1st bar with the 2nd and 3rd bars shows that the uncertainty associated with the strength and stiffness parameters of the ground is far more critical than that associated with the viscosity and leads to a much broader range. The 4th bar, which embeds all uncertainties, indicates a maximum thrust force of 300 MN, which corresponds to the combination of the minimum viscosity $\eta = 10$ MPa·d with the minimum strength and stiffness (upper end of bar 2).

It must be considered that the determined value of 300 MN corresponds to the worst possible combination of all material parameters, which is also assumed to prevail along the entire length and over the entire cross-section of the tunnel (due to the assumptions of homogeneous ground and rotational symmetry, respectively; *cf.* Section 2.3). In reality, such a combination is very unlikely and could only occur over narrow weak zones interspersed between zones of more or less competent rock with superior stiffness and strength properties. The presence of competent zones is a well-established characteristic of the geological formations in Sedrun North (*cf.* Mezger *et al.*, 2013), and has a favourable influence with respect to shield jamming: it reduces ground deformations in the weaker zones due to the shear stresses mobilised at their interfaces and the resulting longitudinal arching effect of the ground (so-called "wall-effect"). The value of 300 MN is thus a clearly pessimistic estimate, and lower values would be more realistic.

However, based upon the preceding discussion regarding feasible thrust force values in single shield TBMs, even an installed thrust of 300 MN appears to be a viable prospect with current technological developments. An increase of 75 MN with respect to the 225 MN that was materialised 15 years ago is not extreme and can probably be accommodated with a suitable TBM design. In conclusion, from today's perspective, a TBM drive prospect appears feasible overall.

2.6.2.3 *Accuracy evaluation of semi-discrete and continuous simulations and design nomograms*

In the following, the adequacy of the proposed semi-discrete, continuous time-dependent and time-independent models, and of the design nomograms of Ramoni and Anagnostou (2010b) is assessed with reference to the results of the fully discrete model. The comparison is based on the respective predicted ranges of thrust force shown in Figure 2.15, considering the mechanical parameters and viscosity of the ground as variable within their expected ranges.

The semi-discrete model (green bar) captures very accurately the range of the fully discrete one (4th black bar), predicting an almost identical maximum value and a slightly lower minimum value (which is anyway irrelevant from a feasibility assessment viewpoint). Therefore, it allows for the same conclusions to be drawn in practical engineering terms also within the context of the feasibility assessment discussed previously.

Conversely, the continuous time-dependent model (red bar) systematically underestimates the predictions of the fully discrete one (4th black bar). While the underestimation of the low-end of the range is subcritical, the underestimation of the high-end is misleading for feasibility assessment and decision-making. Specifically, the 240 MN maximum value is sufficiently high

to raise an alert, but otherwise points towards a thoroughly feasible TBM drive, especially when the favourable influence of the wall-effect is considered.

The same applies to the continuous time-independent model (blue bar), which predicts an even lower required thrust force of 220 MN that is thoroughly feasible even without considering the wall-effect influence. The fact that the time-independent model prediction is lower than that of time-dependent simulations is attributed to the paradox discussed in Section 2.4 and shown in Figure 2.6, which manifests itself within the expected range of viscosity $\eta = 10 - 100$ MPa·d.

The design nomograms (light blue bars) of Ramoni and Anagnostou (2010b), which were established on the basis of the time-independent continuous simulations, predict the same maximum value, as expected. The only difference is that the nomograms embed the conservative assumptions of very high and very low stiffnesses for the shield and lining, respectively, and hence they systematically overestimate the low end of the range predicted by continuous time-independent simulations that consider the actual stiffnesses.

2.7 Conclusions

This chapter presented an investigation into the effect of the time-dependency of squeezing on shield jamming and lining overstressing, along with a comparative evaluation of different approaches for simulating TBM advance and considering excavation standstills in transient numerical computations. The simplest possible MC-Perzyna constitutive model was adopted, which considers time-dependency solely in the plastic regime via a single viscosity parameter η, and allows the magnitude of the viscosity in tunnelling boundary value problems to be directly quantified and the results to be qualitatively interpreted in a simple manner (Section 2.2). The key contributions of the present chapter are summarised hereafter.

First, the common notion that creep is thoroughly favourable for shield jamming during advance has been disputed. Within a certain viscosity range, a counter-intuitive behaviour occurs, where the thrust force increases with increasing viscosity, due to the interplay of two counter-acting effects (Section 2.4): (i) viscosity delays the closure of the annular gap, thus reducing the contact area between shield and ground, while, (ii), it also limits plastic deformations, thus limiting stress relief in the ground ahead of the tunnel face and increasing the pressure transferred to the shield after every excavation increment. Beyond this range, the thrust force starts decreasing with increasing viscosity, since contact between shield and ground happens sufficiently far from the tunnel face for the effect of face stiffening to have an influence. The aforementioned paradox also appears in standstills and at steady-state conditions, where the thrust force required also increases due to the manifestation of additional viscoplastic deformations over time. This increase makes creep thoroughly unfavourable during standstills, even in the range of viscosities where its influence may be favourable during advance.

Second, creep has been shown to be thoroughly unfavourable for the steady-state lining loads far behind the face (Section 2.4). Viscosity reduces the plastic deformations in the vicinity of the face, and hence greater plastic deformations develop over time, which are constrained by the lining, thus increasing the pressure acting upon it.

Third, a semi-discrete approach has been proposed to simulate the TBM advance, which can be idealised as stop-and-go phases alternating with regular standstills for maintenance works (Section 2.5). This smears only the short standstills during the stop-and-go phase, but otherwise explicitly simulates the regular ordinary standstills. The proposed approach approximates the required thrust force to within 10% if a maintenance standstill is not considered (or is very small in proportion to the stop-and-go phase) and within 20% otherwise, provided that the values of the normalised net advance rate $\eta v_N /E/R$ lie outside the range $1 - 10$. Therefore, it provides the same basis for decision-making as the "exact" discrete model in practical tunnel engineering situations, and outperforms the fully continuous simulations usually considered in the literature (Section 2.6).

3 An estimation equation for the TBM thrust force in creeping rock[2]

Abstract

Shield jamming due to insufficient thrust force poses a critical hazard in mechanized tunnelling through squeezing ground. The time-dependency of squeezing due to creep can substantially alter the thrust force requirements, and the use of existing design tools that neglect it might therefore be misleading for the feasibility assessment of mechanized tunnelling or the design of the TBM. This chapter develops an equation for estimating the required thrust force in creeping rock under squeezing conditions during ongoing TBM advance, as well as during construction standstills. The method uses and extends the applicability of existing design nomograms through design equations established via multiparametric nonlinear regression, considering the results of 12,300 transient numerical simulations that cover a wide range of *in-situ* stresses and ground, TBM, and creep parameters relevant in tunnelling practice. The proposed method approximates the numerical results with sufficient accuracy to provide a reliable basis for decision-making during design and a valuable tool for fast assessments of the shield jamming risk. Its versatility and suitability in practical situations are demonstrated via two application examples from the Fréjus safety gallery and the Gotthard base tunnel.

---

[2] This chapter has been published with the following reference: Leone, T., Nordas, A.N. & Anagnostou, G. (2023). An estimation equation for the TBM thrust force in creeping rock. Computers and Geotechnics, 165, 105802, doi: 10.1016/j.compgeo.2023.105802. The contributions of each author are given in Appendix F. The postprint version is considered for the present chapter.

3.1   Introduction

Shield jamming occurs when the installed thrust force of the TBM is insufficient to overcome the shield skin friction generated by the rock pressure, which develops over time due to TBM advance (Ramoni & Anagnostou, 2010a), creep (Debernardi, 2008, Corbetta, 1990, Fritz, 1981, Zienkiewicz *et al.*, 1975) or excess pore pressure dissipation and consolidation in the case of saturated ground (*e.g.* Graziani and Ribacchi, 2001; Ramoni and Anagnostou, 2011b). The effects of creep on shield loading, the subject of this and the previous chapter, have been increasingly studied in the last 15 years. A recent review can be found in Section 2.2 of the previous chapter.

An estimation of the required thrust force and a quick assessment of the risk of shield jamming can be performed using existing design aids, such as the nomograms developed by Ramoni and Anagnostou (2010b), which cover a very wide range of *in-situ* stresses, ground and TBM parameters relevant in tunnelling practice. Since these nomograms were developed for the case of time-independent rock behaviour, their applicability is uncertain in the case of creep: Figure 3.1 compares the predictions of the design nomograms (ordinate axis) with those of transient numerical simulations considering creep (*abscissa* axis), for 12,300 computational cases covering the entire viscosity range relevant in tunnelling practice and the range of ground and TBM parameters considered in the design nomograms, as given in Table 3.1 (the computational model and relevant assumptions are discussed in Section 3.2). It is apparent that disregarding creep may substantially overestimate the rock pressure that develops upon the shield, and thus also the required thrust force, in the vast majority of cases (points above 1:1 line), being adequate only in cases where the effect of creep is negligible (points close to the 1:1 line), while in a few cases disregarding creep can even lead to an underestimation of the rock pressure (points below 1:1 line). The latter, although seemingly paradoxical, is attributed to the interplay of two counteracting effects of creep, which have been examined in detail in Section 2.4.4 in the previous chapter: on the one hand creep limits the ground convergences around the shield, which reduces the rock pressure acting upon it, but on the other hand it leads to less stress relief of the ground ahead of the tunnel face, which results in increased load transferring to the shield.

Table 3.1.   Parameter range considered for metamodel development

Ground			
Poisson's ratio	v	[-]	0.25
Angle of internal friction	ϕ	[°]	15, 20, 25, 30, 35
Dilatancy angle	ψ	[°]	$\max(\phi\text{-}20°,1°)$
Normalised overcut	$E\Delta R/R/\sigma_0$	[-]	1, 2, 3, 4, 5
Normalised strength	f_c/σ_0	[-]	0.05, 0.1, 0.2, 0.3, 0.4, 0.5
TBM & lining			
Normalised advance rate	$v_S\eta/E/R$	[-]	$10^{-5} : 10^{3}$ [a]
Normalised standstill time	tE/η	[-]	$0 - \infty$ [b]
Normalised shield stiffness	$K_s R/E$	[-]	10
Normalised shield length	L/R	[-]	2
Normalised lining stiffness	$K_l R/E$	[-]	0.5

[a]   82 equally-spaced values with increment 0.1 in logarithmic scale
[b]   9 equally-spaced values in logarithmic scale between advance and steady-state
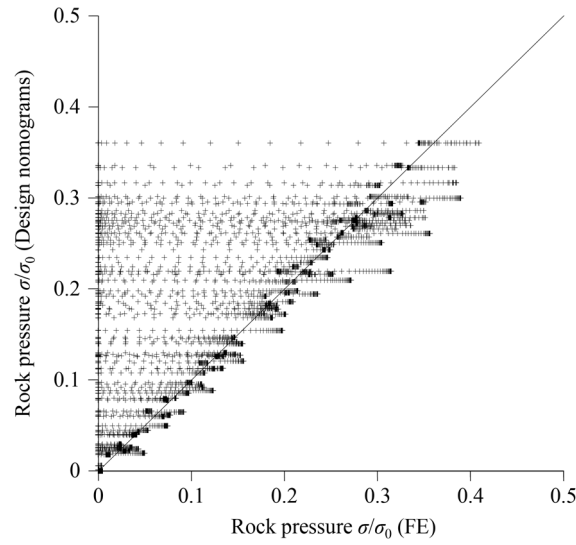
Figure 3.1.   Normalised rock pressure average over the shield: predictions without considering creep (after Ramoni and Anagnostou, 2010b) vs. results of TBM advance numerical simulations considering creep (12,300 data points)

Considering the above and building upon the previous works (Ramoni and Anagnostou 2010b, Chapter 2), a design equation for the average rock pressure σ developing upon the shield during advance and standstills in the presence of creep (hereafter referred to as "rock pressure" or simply "pressure") is presented in this chapter. The equation uses the design nomograms of Ramoni and Anagnostou (2010b) and is formulated considering the typical time development of the rock pressure shown with solid lines in Figure 3.2. (The dashed lines show the approximation based on the proposed design equation and will be discussed later.) A distinction is made as to whether shield – ground contact already occurs during advance (case I) or only during a standstill, after a certain time t_c (case II). In both cases, the rock pressure

$$\sigma = \sigma_{t=0} + \Delta\sigma(t) \ , \tag{3.1}$$

where $\sigma_{t=0}$ denotes its value during advance, while $\Delta\sigma$ denotes its increase during a standstill and can be expressed as follows:

$$\Delta\sigma(t) = \begin{cases} 0, & \text{if } t \le t_c, \\ g(t)\,\Delta\sigma_{t=\infty}, & \text{if } t > t_c, \end{cases} \tag{3.2}$$

where $\Delta\sigma_{t=\infty}$ is the maximum possible increase, holding in cases where steady-state conditions are reached during the standstill, and the function g describes the time evolution of rock pressure. Eqs. 3.1 and 3.2 consider cases I and II of Figure 3.2 via $t_c = 0$ and $\sigma_{t=0} = 0$, respectively.
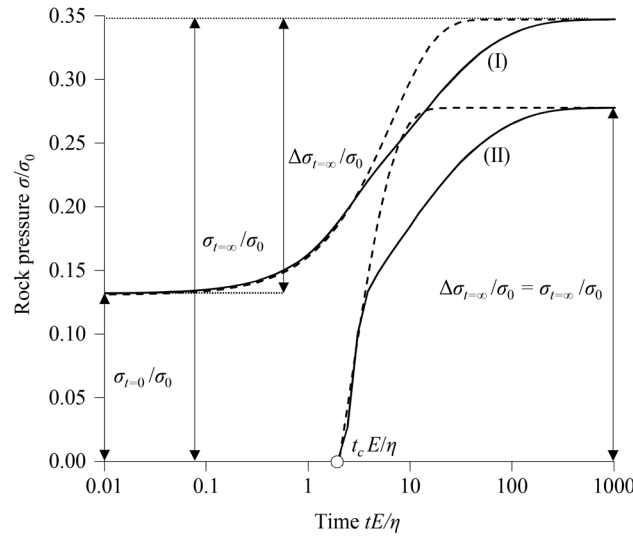
Figure 3.2.   Typical rock pressure development during a standstill according to transient numerical simulations (solid lines) and metamodel approximations (dashed lines): shield-ground contact during advance (I), later contact (II) ($E\Delta R/R/\sigma_0 = 2$, $f_c/\sigma_0 = 0.05$, $\phi = 25°$, $\eta\, v_S/E/R = 0.251$ (I), $\eta\, v_S/E/R = 1000$ (II); other parameters: Table 3.1)

The components on the r.h.s. of Eqs. 3.1 and 3.2 are expressed as functions of the significant problem parameters and time via multiparametric nonlinear regression, based on the results of the 12,300 transient numerical simulations that cover the practically relevant parameter range (Table 3.1), considering 9 time-instances between advance and steady state for each simulation (110,700 data points in total). The proposed method constitutes a so-called "metamodel", that is a model with a unique formulation capable of reproducing the behaviour of multiple numerical models with distinct formulations. The metamodel approximates the thrust force during advance, during a standstill of arbitrary duration, and at steady-state conditions, with sufficient accuracy to assist decision-making in practical tunnel design. For shield jamming assessments in creeping rock, it therefore constitutes a valuable tool which is considerably faster than, and eliminates the need for, sophisticated transient numerical simulations.

This chapter starts with an outline of the computational assumptions adopted in the parametric investigations in Section 3.2. Subsequently, Sections 3.3, 3.4 and 3.5 respectively present the metamodel formulation for approximating the rock pressure during advance ($\sigma_{t=0}$), its maximum increment at steady-state conditions ($\Delta\sigma_{t=\infty}$), and the contact time t_c and time function g required for the estimation of $\Delta\sigma(t)$ at any arbitrary time. Section 3.6 discusses the metamodel limitations and presents a quantitative assessment of its accuracy. Finally, Section 3.7 explains the metamodel use step-by-step and assesses its performance via two application examples, the Fréjus safety gallery and the Gotthard base tunnel.

3.2 Computational assumptions and significant parameters

3.2.1 Computational model

An axisymmetric Finite Element (FE) model has been developed in Abaqus® (Dassault Systèmes, 2018), which simulates the mechanised excavation and lining installation sequence step-by-step, as well as the transient processes during a subsequent standstill (Fig. 3.3). For a detailed description of all computational assumptions, the reader is referred to Section 2.3 in the previous chapter. The semi-discrete simulation approach discussed in Section 3.1 is adopted, where the sequence of stop-and-go cycles during TBM advance is simulated continuously considering a smeared advance rate v_S, whereas the subsequent standstill is simulated explicitly by a transient analysis in which the TBM is static (Section 2.5 of the previous chapter).

The numerical model takes into account the different installation points of the shield and the lining (immediately behind the face and at the end of the shield, respectively) as well as their different contact conditions (annular gap around the shield; see Ramoni and Anagnostou 2010b). The shield and lining are taken as linearly elastic, while the soil is assumed to obey a linearly elastic and viscoplastic constitutive model with a Mohr-Coulomb yield condition and a non-associated viscoplastic flow rule. The constitutive model considers deviatoric rheological behaviour based upon Perzyna's (1966) theory and is defined via six parameters: the five common elasticity and plasticity parameters (Young's modulus E, Poisson's ratio v, cohesion c, angle of internal friction ϕ and angle of dilation ψ), and the viscosity η that controls the time-dependency of plastic deformations due to creep (Section 2.2 of the previous chapter). The validation of the step-by-step computation is performed for the case of zero viscosity in Appendix C.3.
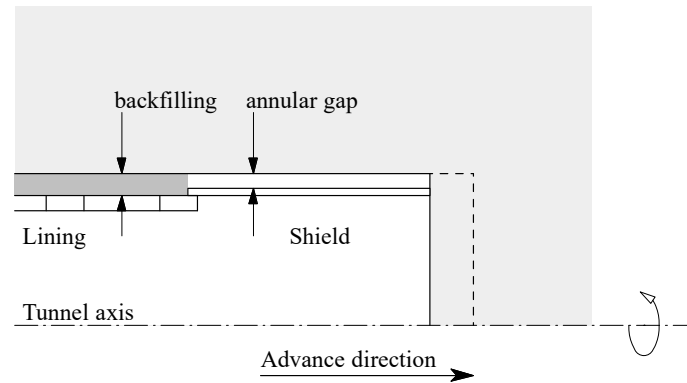
Figure 3.3.   Schematic representation of the problem and of the axisymmetric computational model

Any numerical analysis of the parametric study starts with a simulation of the TBM advance for a certain tunnel stretch, the length of which is defined such that the rock pressure attains a constant value, and continues with the standstill stage until reaching steady state. The analysis provides the longitudinal distribution of the rock pressure during advance and at any time instance during the standstill, which subsequently enables its average value over the shield (σ) to be determined via integration, and the required thrust force F_r to be calculated as follows:

$$F_r = \mu\, 2\pi R L \sigma + F_b \;\; \text{(during boring)}, \tag{3.3}$$

$$F_r = \mu_{st}\, 2\pi R L \sigma \;\; \text{(restart after a standstill)}, \tag{3.4}$$

where μ and μ_{st} respectively denote the sliding and the static shield skin friction coefficients, F_b denotes the thrust force required for boring, and R and L denote the tunnel radius and shield length, respectively.

3.2.2   Model limitations

Due to the practical imponderables associated with identifying the most appropriate constitutive model and determining the rock mass parameters, the simplest and most widely used elastoplastic model in tunnelling (isotropic, linear-elastic, perfectly plastic material with Mohr-Coulomb yield criterion) was chosen in combination with the simplest possible formulation of viscoplasticity (the one-parameter Perzyna model). The appropriateness of this model must, of course, be assessed on a case-by-case basis.

The calculation model assumes that the rock can be considered homogeneous and isotropic at the scale of the tunnel cross-section, but in reality squeezing rock formations can consist of alternating weaker and harder layers.

If the layers are thin in relation to the tunnel diameter, a homogeneous model can still be considered, but in combination with transverse isotropy. The layer-related anisotropy would generally lead to an uneven distribution of rock deformations over the tunnel circumference, which cannot be captured by an isotropic model. The latter can nevertheless be used in certain cases to obtain reasonable estimates, provided that it is appropriately calibrated and considers equivalent isotropic parameters (Mezger and Anagnostou, 2019).

In the case of large-scale heterogeneity of the geological formation, the homogenisation described above is not possible. Considering a homogeneous material with the parameters of the weaker component of the actual formation would generally overestimate convergences and rock pressures, as the adjacent competent layers have a stabilising effect (Mezger *et al.* 2013, Mezger and Anagnostou 2019). The degree of conservatism of the homogeneous model can be assessed using Nordas *et al.* (2023a).

In this chapter, time-dependence is considered due to creep (related to the rheological-mechanical behaviour of the soil), but not due to consolidation (related to hydromechanical coupling). The

model is not applicable to low-permeability water bearing rocks where the time-dependence of the response to tunnelling is due to excess pore pressure dissipation and consolidation. In cases where consolidation plays a role, the shield-ground interaction should be investigated based on coupled hydromechanical simulations (see, *e.g.*, Ramoni and Anagnostou 2011b).

3.2.3 Significant parameters

The rock pressure normalised with respect to the *in-situ* stress σ_0 depends in general on the following dimensionless parameters (Chapter 2):

$$\sigma^* = \frac{\sigma}{\sigma_0} = f\left(\frac{E\Delta R}{\sigma_0 R}, \nu, \frac{f_c}{\sigma_0}, \phi, \psi, \frac{L}{R}, \frac{K_s R}{E}, \frac{K_l R}{E}, \frac{v_S \eta}{ER}, \frac{tE}{\eta}\right). \tag{3.5}$$

where ΔR is the annular gap (overcut) around the shield, f_c is the uniaxial compressive strength of the ground, K_s and K_l are the radial shield and lining stiffnesses, respectively, and t is the standstill duration. The parametric investigations consider only the case of a single-shield TBM with $L/R = 2$, which is common for typical cross-sections of traffic tunnels, and embed the assumptions adopted in the design nomograms of Ramoni and Anagnostou (2010b), specifically: $K_s R/E = 10$ and $K_l R/E = 0.5$, which lead overall to conservative predictions, $\nu = 0.25$, and $\psi = \max\{\phi - 20°; 1\}$. Considering the above, Eq. 3.5 simplifies as follows:

$$\sigma^* = f\left(\frac{E\Delta R}{\sigma_0 R}, \frac{f_c}{\sigma_0}, \phi, \frac{v_S \eta}{ER}, \frac{tE}{\eta}\right). \tag{3.6}$$

For brevity, the following notation is henceforth adopted for the dimensionless parameters: $\Delta R^* = E\,\Delta R / (\sigma_0\,R), f_c^* = f_c / \sigma_0, v_S^* = v_S\,\eta / (ER), t^* = t\,E / \eta$. The parameter values considered are given in Table 3.1, where the dimensionless ground and TBM parameters $(\Delta R^*, f_c^*, \phi)$ are selected analogously to the design nomograms, while the dimensionless advance rate (v_S^*) covers the practically relevant range for tunnelling boundary value problems established in Chapter 2. The combination of the parameter values in Table 3.1 results in a total of 12,300 computational cases, with 9 time-instances considered in each case for the thrust force evaluation during standstills (110,700 data points in total).

3.3   Rock pressure during advance $\sigma_{t=0}$

The rock pressure developing during advance ($\sigma_{t=0}$) depends solely on ΔR^*, f_c^*, ϕ and v_S^* (*cf.* Eq. 3.6 for $t = 0$). The solid line in Figure 3.4 shows the typical variation of $\sigma^*_{t=0}$ ($= \sigma_{t=0}/\sigma_0$) with the advance rate v_S^* for a given ΔR^*, f_c^* and ϕ, as determined by transient numerical simulations.

For a very slow advance or in the absence of creep ($v_S^* \rightarrow 0$), the entire plastic deformations occur practically simultaneously with the advance of the tunnel heading and the normalised rock pressure σ/σ_0 corresponds to the value determined from the design nomograms. (Note that σ/σ_0 is identical with the normalised required thrust force given in the ordinates of the design nomograms.) With increasing v_S or η, a smaller portion of plastic deformations occurs during advance and a larger portion develops progressively over time (viscoplastic deformations), and hence the rock pressure during advance tends to decrease. However, within a specific range of v_S^* - values, the rock pressure increases locally, in some cases exceeding the value for $\eta \rightarrow 0$, due to the paradox discussed in Section 3.1. Beyond this local peak, the rock pressure decreases monotonically, dropping to zero in the case of a very fast advance or a high viscosity (high v_S^* - values), where ground convergences do not exceed the overcut ΔR and no shield – ground contact occurs.

The numerically determined distribution (solid line in Fig. 3.4) can be approximated using the following exponential function that neglects the small peak in the range of the paradox (dashed line in Fig. 3.4):

$$\sigma^*_{t=0} = \sigma^*_{t=0,\eta=0} \; e^{-Bv_s^*}, \tag{3.7}$$

where $\sigma^*_{t=0,\;\eta=0}$ denotes the value determined from the design nomograms of Ramoni and Anagnostou (2010b) that do not consider creep ($\eta = 0$), while the coefficient B depends solely on ΔR^*, ϕ and f_c^*. Multiparametric regression of the 12,300 data points obtained from the numerical simulations during advance (*cf.* Table 3.1) and minor manipulations lead to the following functional form for B:

$$B = \frac{1}{2}\frac{\Delta R^{*\,2}}{1 - f_c^*}. \tag{3.8}$$

Figure 3.5 compares the rock pressure predictions of transient numerical simulations with those of the metamodel (Eqs. 3.7, 3.8). The metamodel achieves a coefficient of determination $R^2 = 0.97$.

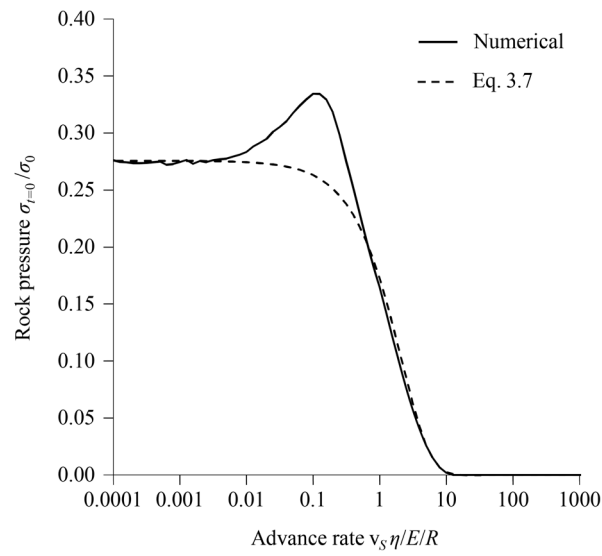Figure 3.4.   Typical relationship between the advance rate and the rock pressure during advance: transient numerical simulations (solid line), metamodel approximations (dashed line) ($E\Delta R/R/\sigma_0 = 1$, $f_c/\sigma_0 = 0.05$, $\phi = 25°$; other parameters: Table 3.1)

Figure 3.5.   Rock pressure during advance: metamodel vs. numerical predictions (12,300 simulations; parameters: Table 3.1)

3.4   Increase in rock pressure during standstills that reach steady state

One can readily verify that the maximum possible increase in the rock pressure during a standstill (*i.e.* the increase $\Delta\sigma_{t=\infty}$ up to steady state; $\Delta\sigma_{t=\infty} = \sigma_{t=\infty} - \sigma_{t=0}$) depends only on $\Delta R^*, f_c^*, \phi, v_S^*$ (*cf.* Eq. 3.6 for $t = 0$ and $t \to \infty$, respectively). The solid line in Figure 3.6 shows the typical variation of the normalised increase $\Delta\sigma^*_{t=\infty}$ ($= \Delta\sigma_{t=\infty}/\sigma_0$) with v_S^* for given $\Delta R^*, f_c^*$ and ϕ, as determined by transient numerical simulations.

The observed behaviour can be explained analogously to Section 3.3. For very slow advance or in the absence of creep ($v_S^* \to 0$) $\Delta\sigma_{t=\infty} = 0$, since the entire plastic deformations occur almost simultaneously with the advance and rock pressure remains constant and equal to $\sigma_{t=0}$ over time. With increasing v_S or η, a larger portion of viscoplastic deformations takes place over time and hence $\Delta\sigma_{t=\infty}$ increases. The observed local peak in the pressure over advance rate line is associated with the paradox (Section 3.1). For very fast advance or high viscosity (high values of v_S^*), where the response is purely elastic during advance and all plastic deformations occur over time, the distribution tends asymptotically to a limit value, which will be denoted as $\Delta\sigma_{t=\infty, v_S=\infty}$ hereafter.

The numerically determined distribution (solid line in Fig. 3.6) can be approximated as follows (dashed line in Fig. 3.6):

$$\Delta\sigma^*_{t=\infty} = \max\left\{ \frac{\Delta\sigma^*_{t=\infty, v_s=\infty}}{1 + C_1 \, v_s^{*-C_2}} ; 0 \right\}, \tag{3.9}$$

where $\Delta\sigma^*_{t=\infty, vs=\infty} = \Delta\sigma_{t=\infty, vs=\infty}/\sigma_0$, C_1 and C_2 depend only on ΔR^*, ϕ and f_c^*. Multiparametric regression of the 12,300 data points obtained from the numerical simulations at steady-state conditions (*cf.* Table 3.1), and minor manipulations, yield the following functional forms:

$$\Delta\sigma^*_{t=\infty, v_s=\infty} = \max\left\{1 - 0.02\phi - f_c^* - 0.005\,\Delta R^* + 0.03\,\phi\,f_c^* - 0.002\,\phi\,\Delta R^* - 0.5\,f_c^*\Delta R^* + 0.005\,\phi\,\Delta R^* f_c^* ; 0\right\}$$
, $$\tag{3.10}$$

$$C_1 = e^{-C_2\left(3 - 0.07\,\phi - 9\,f_c^* - 0.1\,\phi\,f_c^* - \Delta R^* + 0.06\,\phi\,\Delta R^* + 1.5\,f_c^*\,\Delta R^* + 0.3\,\phi\,f_c^*\Delta R^*\right)}, \tag{3.11}$$

$$C_2 = 0.8 - 0.005\,\phi - 0.2\,\Delta R^* + 0.01\,\phi\,\Delta R^* + 2\,f_c^*\Delta R^* - 0.04\,\phi\,f_c^*\,\Delta R^*. \tag{3.12}$$

Due to the approximate nature of Eq. 3.10, it is possible that negative values are obtained for $\Delta\sigma_{t=\infty}$ in Eq. 3.9 in borderline cases of very small $\Delta\sigma^*_{t=\infty,vs=\infty}$ (*i.e.* practically purely elastic ground behaviour between advance and steady state). Eq. 3.9 is expressed in a conditional form to circumvent such instances.

Figure 3.7 compares the $\Delta\sigma_{t=\infty}$ predictions of the transient numerical simulations and of the metamodel (Eqs. 3.9 – 3.12). The metamodel achieves an $R^2 = 0.95$.
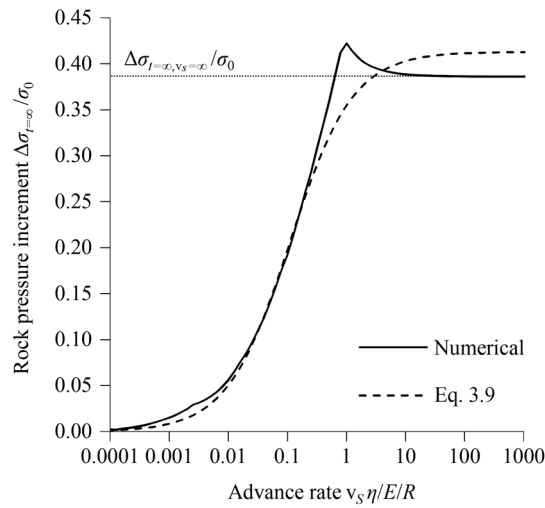
Figure 3.6. Typical relationship between the advance rate and the increase in rock pressure during a standstill that reaches steady state: transient numerical simulations (solid line), metamodel approximations (dashed line) ($E\Delta R/R/\sigma_0 = 2$, $f_c/\sigma_0 = 0.05$, $\phi = 20°$; other parameters: Table 3.1)
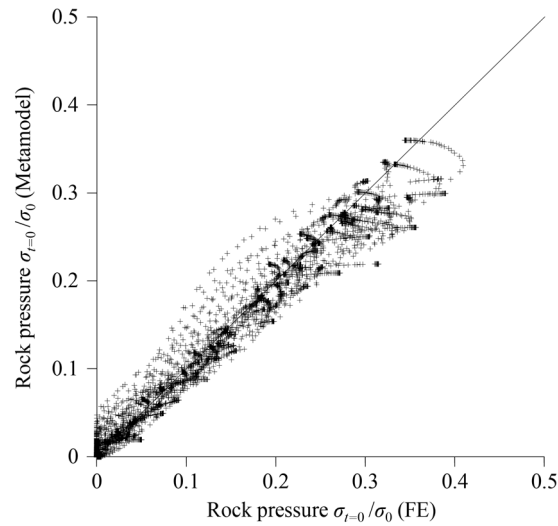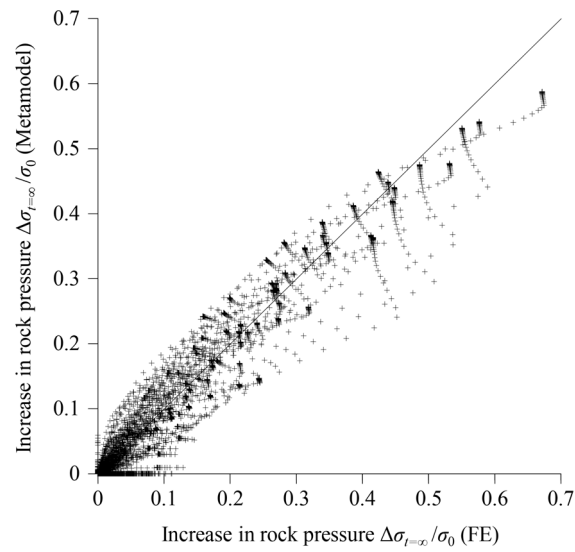

Figure 3.7. Increase in rock pressure during a standstill that reaches steady state: metamodel vs. numerical predictions (12,300 simulations; parameters: Table 3.1)

3.5   Increase in rock pressure during standstills of given duration $\Delta\sigma(t)$

The increase $\Delta\sigma(t)$ in pressure over time is determined by the time function g (*cf.* Eq. 3.2, Fig. 3.2), which can be approximately taken as follows (dashed lines in Fig. 3.2):

$$g(t) = \max\left\{1 - e^{-A\left(t^* - t_c^*\right)}; 0\right\},$$

(3.13)

where the normalised contact time t_c^* and the coefficient A depend on ΔR^*, f_c^*, ϕ and v_s^*. The following expressions for A and t_c^* are obtained from multiparametric regression of the 110,700 data points resulting from the 12,300 numerical simulations, where 9 time-instances are considered in each (*cf.* Table 3.1):

$$A = \max\left\{1.5\left(D_1\left(1 - e^{-D_2 v_s^*}\right) + D_3\right); 0\right\},$$

(3.14)

$$t_c^* = \max\left\{1.5\left(\Delta R^* - 1\right)\left(1 - e^{-D_4\left(v_s^* - 1\right)}\right); 0\right\},$$

(3.15)

where

$$D_1 = e^{-0.02\,\phi\,\Delta R^* - 0.3\Delta R^*},$$

(3.16)

$$D_2 = e^{0.7\Delta R^* f_c^* \phi - 5\Delta R^* f_c^*} - 1,$$

(3.17)

$$D_3 = 0.0015\,\phi - 0.0175$$

(3.18)

and

$$D_4 = \max\left\{e^{0.3\Delta R^*} - 1.2; 0\right\}.$$

(3.19)

Analogously to Section 3.4, the conditional forms in Eqs. 3.14, 3.15 and 3.19 are introduced to eliminate cases of negative values resulting from the approximate nature of the mathematical expressions, so as to ensure consistency with the physical problem.

3.6   Quantitative assessment of metamodel accuracy

Based upon the results presented in Section 3.3 to 3.5, the rock pressure at any time instance t can be determined after Eqs. 3.1 and 3.2, by evaluating $\sigma_{t=0}$ using Eqs. 3.7 and 3.8 in Section 3.3, $\Delta\sigma_{t=\infty}$ using Eqs. 3.9-3.12 in Section 3.4, and g using Eqs. 3.13-3.19 in Section 3.5.

Figure 3.8 compares the rock pressure predictions of the transient numerical simulations (*abscissa* axis) with those of the full metamodel for all 110,700 data points (9 time-instances, including advance and steady-state, for each of the 12,300 computational cases; *cf.* Table 3.1). The metamodel attains an $R^2 = 0.96$. Evidently there is some scatter of the data points around the 1:1 line, which means that any given metamodel prediction corresponds to a range of numerical predictions. Notwithstanding this, the high coefficient of determination achieved indicates that the vast majority of data points fall very close to the 1:1 line and the instances of scattered data points are substantially fewer in comparison and far less probable. It must be noted, however, that the accuracy of the metamodel is noticeably inferior in the range of very low normalised rock pressures between 0 – 0.1, and hence its applicability is limited, or even uncertain, in such cases.

Besides the inherently approximate nature of the metamodel formulation, its prediction accuracy in a specific case may be influenced by the underlying assumptions, comprising mainly: (i) the assumed fixed ratio of the shield length to the tunnel radius $L/R = 2$ (*cf.* Section 3.2); (ii) the conservative assumptions for the normalised radial stiffnesses of the shield and lining adopted also in the design nomograms ($K_sR/E = 10$, $K_lR/E = 0.5$;), which overestimate the rock pressure; and (iii) the adopted semi-discrete simulation approach, which underestimates the rock pressure of discrete simulations by less than 10% during this phase and 20% during a full excavation cycle, however in the latter case it produces a much larger error for values of $\eta\,v_N/E/R$ between 1 and 10, where v_N is the net advance rate during TBM strokes (*cf.* Section 2.5 of the previous chapter).

Notwithstanding the above, the purpose of the proposed metamodel is not to evaluate the thrust force with the maximum possible accuracy (this would necessitate detailed case-by-case analyses), but rather to rapidly provide a first reliable basis for decision-making in design and construction. The application examples presented in the next section have been selected to showcase the aforementioned limitations, but also the metamodel's value and usefulness for fast and reliable assessments of shield jamming in creeping rock, as an alternative to performing costly and time-consuming transient numerical simulations.
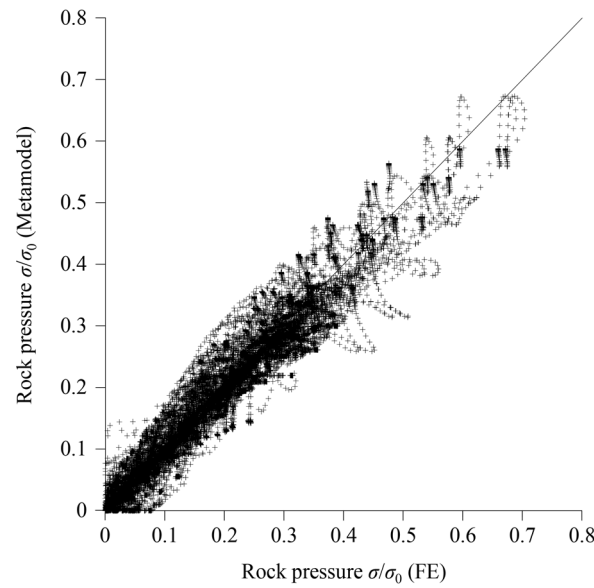
Figure 3.8.   Rock pressure during standstills: metamodel vs. numerical predictions (110,700 data points
= 9 time-instances x 12,300 simulations; parameters: Table 3.1)

3.7   Application examples

In the previous chapter, the effect of the creep-induced time-dependency of squeezing on shield
loading and the required thrust force was demonstrated via two application examples: the analysis
of the TBM drive through the Fréjus safety gallery, and the feasibility assessment of a TBM drive
through the conventionally excavated Sedrun North critical zone of the Gotthard base tunnel. In
both examples, fully discrete transient numerical simulations were conducted to determine the
thrust force evolution along the tunnel during two full days of TBM operation, which were
assumed to consist of 16-hour long stop-and-go phases and an 8-hour long maintenance standstill.

In this section, the results of these application examples will be used as benchmarks to assess the
performance of the metamodel presented in Sections 3.3-3.5 and its suitability for systematic
employment as a design aid in practical situations. For a detailed description of the projects and
a discussion on the adopted assumptions and parameters, the reader is referred to Sections 2.6.1
and 2.6.2 of the previous chapter. The parameters relevant in the present context are given in
Table 2.3 of the previous chapter, while the use of the metamodel is explained step-by-step in
Table 3.2, which provides an exemplary computation for selected parameter sets of both
examples.

Table 3.2.   Exemplary metamodel computations for the application examples

Input parameters			Fréjus safety gallery		Gotthard Base tunnel	
In-situ stress	σ_0	[MPa]	40		20	
Young's modulus	E	[MPa]	4700		1000	
Angle of internal friction	ϕ	[°]	35		27	
Dilatancy angle	ψ	[°]	15		5	
Uniaxial compressive strength	f_c	[MPa]	3.8		1.3	
Viscosity	η	[MPa·d]	1700	3400	10	100
Nominal boring radius	R	[m]	4.73		5	
Shield length	L	[m]	11.2		10	
Overcut	ΔR	[mm]	60		200	
Coefficient of sliding friction	μ	[-]	0.3		0.1	
Coefficient of static friction	μ_{st}	[-]	0.4		0.15	
Thrust force for boring	F_b	[MN]	17		17	
Smeared advance rate	v_S	[m/d]	45		33	
Standstill duration	t	[h]	8		8	
Dimensionless parameters						
Normalised overcut	ΔR^*	[-]	1.490		2.0	
Normalised uniaxial strength	f_c^*	[-]	0.095		0.065	
Normalised advance rate	v_S^*	[-]	3.441	6.882	0.066	0.660
Normalised standstill time	t^*	[-]	0.922	0.461	33.333	3.333
Computation for TBM advance						
Normalised pressure for $\eta=0$	$\sigma^*_{t=0,\,\eta=0}$	[-]	0.245 [a]		0.203 [b]	
Coefficient (Eq. 3.8)	B	[-]	1.227		2.139	
Normalised pressure (Eq. 3.7)	$\sigma^*_{t=0}$	[-]	0.004	0	0.176	0.049
Thrust force (max. of Eqs. 3.3 and 3.4)	F_r	[MN]	33	17	166	48
Possible metamodel error						
Normalised pressure range[c]		[-]	0-0.015	0-0.015	0.12-0.21	0-0.075
Thrust force range (max. of Eqs. 3.3 and 3.4)		[MN]	17-80	17-80	113-198	17-71
Absolute difference		[MN]	-16 / +63	-0 / +63	-53 / +32	-31 / +23

Table 3.2. (Continued)

Computation for standstill

Norm. pres. inc. for $t = \infty$, $v_s = \infty$ (Eq. 3.10)	$\Delta\sigma^*_{t=\infty,vs=\infty}$	[-]	0.087		0.233	
Coefficient (Eq. 3.11)	C_1	[-]	0.081		0.072	
Coefficient (Eq. 3.12)	C_2	[-]	0.933		0.925	
Norm. pressure inc. for $t = \infty$ (Eq. 3.9)	$\Delta\sigma^*_{t=\infty}$	[-]	0.085	0.086	0.123	0.211
Coefficient (Eq. 3.16)	D_1	[-]	0.225		0.186	
Coefficient (Eq. 3.17)	D_2	[-]	14.803		5.092	
Coefficient (Eq. 3.18)	D_3	[-]	0.035		0.023	
Coefficient (Eq. 3.19)	D_4	[-]	0.364		0.622	
Coefficient (Eq. 3.14)	A	[-]	0.390	0.390	0.114	0.304
Normalised time to contact (Eq. 3.15)	t^*_c	[-]	0.433	0.649	0	0
Time function (Eq. 3.13)	g	[-]	0.174	-	0.978	0.637
Normalised pressure increment (Eq. 3.2)	$\Delta\sigma^*$	[-]	0.015	0	0.120	0.134
Normalised pressure (Eq. 3.1)	σ^*	[-]	0.019	0	0.296	0.183
Thrust force (max. of Eqs 3.3 and 3.4)	F_r	[MN]	101	17	279	172
Possible metamodel error						
Normalised pressure range[d]		[-]	0-0.1	0-0.081	0.18-0.38	0.12-0.23
Thrust force range (max. of Eqs 3.3 and 3.4)		[MN]	17-533	17-431	170-358	113-217
Absolute difference		[MN]	-84/+432	-0 / +414	-109 / +79	-59 / +45

[a]   After Ramoni and Anagnostou (2010b), Fig. 9, nomogram for $\phi = 35°$; interpolation for $f_c/\sigma_0 = 0.095$ and $(\Delta R/R)(E/\sigma_0) = 1.49$ between the curves for $f_c/\sigma_0 = 0.05$ and 0.1

[b]   After Ramoni and Anagnostou (2010b), Fig. 9, interpolation for $\phi = 27°$ between the diagrams for $\phi = 25°$ and $30°$; interpolation for $f_c/\sigma_0 = 0.065$ and $(\Delta R/R)(E/\sigma_0) = 2.0$ between the curves for $f_c/\sigma_0 = 0.05$ and 0.1

[c]   Numerically determined $\sigma^*_{t=0}$ - range (*abscissae* of Fig. 3.5) corresponding to the $\sigma^*_{t=0}$ - value after metamodel Eq. 3.7

[d]   Numerically determined σ^* - range (*abscissae* of Fig. 3.8) corresponding to the σ^* - value after metamodel Eq. 3.1

3.7.1 Fréjus safety gallery

Figure 3.9 shows the time-face location diagram (bottom) considering stop-and-go TBM operation (*e.g.* AB) and standstills (*e.g.* BC), as well as the required thrust force along the tunnel (top) determined by discrete simulations that consider the actual problem parameters in Table 2.3 of the previous chapter (black line) and the metamodel (red lines). The results correspond to the parameter set with the lowest Young's modulus of 4,700 MPa and the lowest viscosity of 1,700 MPa·d, in combination with the smallest overcut of 60 mm (see Table 2.3 of the previous chapter); for all other combinations of either Young's modulus with the corresponding extreme viscosity values and any of the overcuts, both the discrete simulations and the metamodel predict no contact between shield and ground, and thus a constant thrust force equal to the boring force (17 MN). The predictions of the design nomograms for the two overcuts are also given in the same figure for comparison.

Fully discrete numerical creep simulations predict a maximum thrust force of 41 MN, which is fairly close to the maximum value of 30 MN recorded in reality. On the other hand, disregarding creep predicts excessively high values of 760 and 1300 MN for overcuts of 110 and 60 mm,

respectively. This results from neglecting the effect of creep which is considerable here. Notwithstanding the general value of the design nomograms, which constitute the only reasonable method in most cases due to the absence of data regarding the actual time-dependent behaviour of the ground, in this specific case their application would be highly misleading in terms of thrust requirements.

The metamodel, Ih considers creep in a simplified way, also overestimates the thrust force in this specific case. The metamodel predicts a thrust force of 101 MN (solid red line), which is higher by factor of about 3 than the force predicted by discrete numerical simulations and the actual thrust force, with a very wide range of possible values between $17 - 533$ MN (dashed red lines; *cf.* Table 3.2). The reasons for the poor quality of the metamodel predictions are explained below.

First and foremost, the metamodel accuracy is inferior in the range of very low normalised rock pressures $0 - 0.1$ (Section 3.6) and exhibits a considerable scatter around the value 0.019 predicted in this case (Table 3.2). The broad range of absolute thrust force values of $17 - 533$ MN results from this scatter, as well as from their high sensitivity to small variations in the normalised rock pressure for the specific problem parameters; indicatively, an increase of the normalised pressure in the third decimal point from 0.019 to 0.02 results in an absolute thrust force increase by 5 MN, which amounts to 12.5% of the value predicted by discrete simulations.

Secondly, the metamodel has been developed using the semi-discrete simulation approach. This underestimates the discrete simulation predictions by more than 20% when considering a full excavation cycle (ABC in Fig. 3.9) if the values of the normalised net advance rate $\eta \, v_N / E \, R$ fall within the range $1 - 10$, as for the case under consideration where $\eta \, v_N / E \, R = 7.2$ (*cf.* Table 2.3 of the previous chapter). For the assumed specifications of the excavation cycle (Table 2.3 of the previous chapter) the error amounts to *ca.* 30%, as estimated from Figure 2.13b, considering that the ground parameters adopted here are within the range of parameter values considered there.

Finally, the dimensionless values of the shield and lining stiffness corresponding to the actual problem parameters are $K_s \, R/E = 0.71$ and $K_l \, R/E = 0.63$ (Table 2.3 of the previous chapter), whereas the metamodel assumes a very stiff shield with $K_s \, R/E = 10$ and a soft lining with $K_l \, R/E = 0.5$ (Table 3.1). While the actual lining stiffness is close to the assumed one, the actual shield stiffness is 14 times lower, and hence the metamodel may substantially overestimate the thrust force predicted by discrete simulations (*cf.* Section 3.6 and Fig. 5 in Ramoni and Anagnostou, 2010b). It is mentioned here indicatively, that for the parameters in Table 2.3 of the previous chapter with a 60 mm overcut, this overestimation amounts to 40% in the absence of creep (1300 MN determined from design nomograms that assume $K_s \, R/E = 10$ and $K_l \, R/E = 0.5$ vs. 920 MN determined from time-independent computations that consider the actual $K_s \, R/E = 0.71$ and $K_l \, R/E = 0.63$; see blue lines in Fig. 2.14 of the previous chapter).

Considering that both the design nomograms and the metamodel are inapplicable in this case, a closer examination of the problem based upon transient numerical simulations is the only viable option, as presented in Section 2.6.1 of the previous chapter.
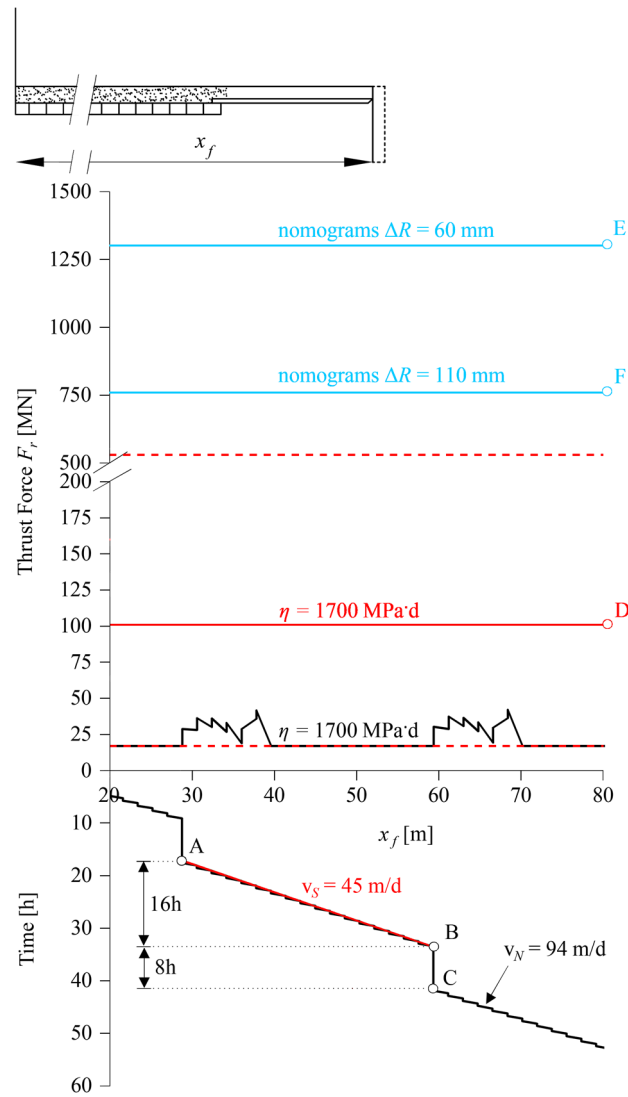
Figure 3.9.   Fréjus safety gallery: Thrust force evolution predicted by discrete simulations of two full excavation cycles (black line), metamodel (red solid line) and time-independent design nomograms (blue lines) after Ramoni and Anagnostou (2010b) (parameters: Table 2.3 of the previous chapter)

3.7.2   Gotthard Base tunnel

Section 2.6.2 of the previous chapter demonstrated that the prospect of a TBM drive through the Sedrun North critical section of the Gotthard Base tunnel appears feasible overall with the current state of TBM technology and current knowledge of the ground conditions. The feasibility assessment was based on the expected range of thrust force values, which was determined from fully discrete transient numerical simulations that considered the uncertainties associated both with the mechanical parameters and the viscosity of the ground (Table 2.3 of the previous chapter). Using the results of the discrete simulations as a benchmark, Section 2.6.2 of the previous chapter additionally demonstrated that semi-discrete simulations accurately approximate the expected thrust force range, thus providing a reliable basis for decision-making and feasibility assessments.

Based upon these results, the present application example assesses the adequacy and accuracy of the proposed metamodel via a comparison of its predicted thrust force range with that of fully discrete and semi-discrete simulations. Unlike the case of the Fréjus safety gallery examined in the previous example, the metamodel is applicable in the present case, since: (i) its normalised rock pressure predictions for the problem parameters (Table 2.3 of the previous chapter) are far away from the critical range of small values $0 - 0.1$ where the accuracy of the metamodel deteriorates; (ii) the normalised net advance rate $v_N{}^*$ lies outside the range $1 - 10$ for all parameter combinations (Table 2.3 of the previous chapter), and hence the error of the semi-discrete simulations over a full excavation cycle is less than 20%; and (iii) the assumed shield and lining stiffnesses will still lead to an overestimation of the thrust force, but this effect is counteracted by the underestimation resulting from the semi-discrete simulation approach.

Figure 3.10 shows the ranges determined from the discrete (black bar) and semi-discrete (green bar) simulations, the metamodel (red bar), and the design nomograms (blue bar) for comparison. It is apparent that the metamodel approximates the discrete simulation range very accurately, providing predictions that are only slightly on the safe side (maximum thrust force 320 MN vs. 300 MN). The overestimation is attributed to the aspects discussed above and can be seen in both the high and low ends of the discrete range, as opposed to the semi-discrete simulations which predict a broader range of values overall. When disregarding time-dependency, a much narrower range is predicted, which underestimates the maximum value considerably but still provides a reasonable indication of the anticipated thrust force magnitude for feasibility assessments. Because of the less pronounced creep in this case, the predictions of the design nomograms are much more accurate than in the case of the Fréjus safety gallery discussed previously.

Conclusively, the metamodel provides the same basis for decision-making as the fully discrete simulations and is adequately accurate for the assessment of shield jamming and the feasibility of mechanised tunnelling, which highlights its value as a design aid that can eliminate the need for transient numerical simulations.
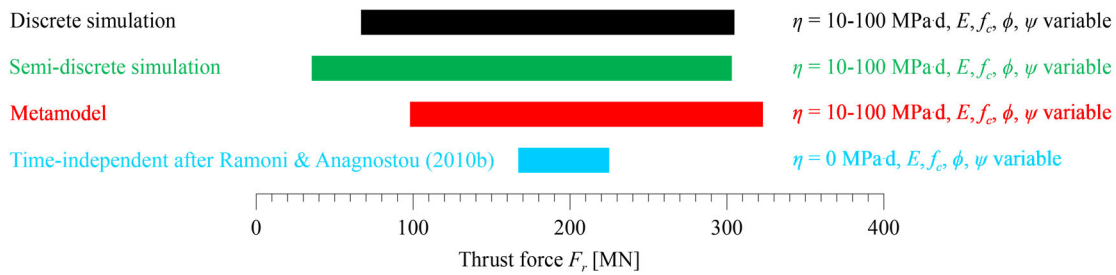
Figure 3.10.   Gotthard base tunnel: Predicted thrust force ranges (parameters: Table 2.3 of the previous chapter)

3.8   Conclusions

The present chapter proposed an equation (metamodel) for estimating the thrust force required to overcome shield skin friction when a ground exhibits creep. The equation uses and extends the applicability of the design nomograms of Ramoni and Anagnostou (2010b). It was developed via multiparametric regression, using the results of 12,300 simulations of TBM advance and the transient processes during subsequent standstills (total of 110,700 data points, corresponding to 9 time-instances per simulation), which cover a wide range of *in-situ* stresses and the ground, TBM, and creep parameters relevant in tunnel engineering practice (*cf.* Sections 3.2 – 3.5).

Besides its inherently approximate nature, the proposed metamodel embeds a number of limitations (Section 3.2.2 and 3.6), and it may be inapplicable in cases of very low normalised rock pressure values (Section 3.6). The example of the Fréjus safety gallery illustrated the limitations of the metamodel, while its application on the Gotthard Base tunnel showed that it can provide an equivalent basis for decision-making to fully discrete, transient numerical simulations (Section 3.7).

Provided that data regarding the time-dependent ground behaviour are available, the metamodel constitutes a valuable design aid for a fast assessment of shield jamming and the feasibility of mechanised tunnelling with reasonable accuracy in engineering terms, thus eliminating the need for transient numerical simulations, whilst offering greater accuracy than the design nomograms of Ramoni and Anagnostou (2010b). In the absence of such data, the design nomograms, which do not consider creep, remain the only reasonable and practicable approach for assessing the required thrust force.

4 Creep versus consolidation in tunnelling through squeezing ground – Part A: Basic time-effects[3]

Abstract

Although squeezing ground may undergo rapid convergences following tunnel excavation, its behaviour is often markedly time-dependent due to creep or consolidation. The effects of creep and consolidation on shield tunnelling are comparatively evaluated in the present and next chapter, with the aim of demonstrating their qualitative similarities and distinctive features. The present chapter investigates the basic time effects, placing focus on the time development of ground deformations and the complex interaction between ground, tunnel boring machine (TBM) and tunnel support during excavation and during construction standstills. The presented numerical simulations indicate several qualitative similarities between the two mechanisms of time dependency, in respect of the time-development of ground deformations, the counter-intuitive behaviour of increasing shield loading with increasing rate of advance under certain conditions, as well as the thoroughly adverse effect of the additional time-dependent deformations taking place during construction standstills on the shield loading. However, they also underscore two prominent differences resulting from the fundamentally different nature of creep (a purely mechanical rheological process) and consolidation (a coupled hydromechanical process): First, the consistently more extensive plastic yielding in consolidating ground, which is partially associated with the seepage forces exerted by the pore water on the solid rock constituents. Second, the role of seepage forces as a potential destabilising agent particularly for the tunnel face, which does not happen in the case of creep and may be critical for shield and cutterhead jamming. Building upon these investigations, the next chapter compares creep and consolidation with respect to the transferability of experiences about the required thrust force to tunnels of different diameter or to adjacent tunnels.

---

[3] This chapter has been published with the following reference: Leone, T., Nordas, A.N. & Anagnostou, G. (2024). Creep versus consolidation in tunnelling through squeezing ground—Part A: Basic Time Effects. Rock Mechanics and Rock Engineering. doi: 10.1007/s00603-023-03720-6. The contributions of each author are given in Appendix F. The postprint version is considered for the present chapter.

4.1 Introduction

Squeezing, the phenomenon of relevant rock deformations or pressures in tunnelling, may occur rapidly or develop slowly, over a period of days, weeks, or even months depending on the nature of the ground (Kovári and Staus 1996; Barla 2001; Anagnostou and Kovári 2005). The time-dependency of squeezing can be caused by the rheological properties of the ground (creep), by stress redistributions associated with transient seepage flow in the case of low-permeability, saturated ground (consolidation), or both. Physicochemical processes (such as disintegration of serpentine rock, rock dissolution in karstic formations, crystal-growth in anhydritic rocks) may, too, result in time-dependent deformations, but affect tunnel construction – the subject of this chapter – rather rarely (Anagnostou and Kovári 2005, Anagnostou 2007).

Creep is associated with rheological processes, which are of a purely mechanical nature and thus in general independent of the presence of pore water. Creep has been shown to be more pronounced when the ground is overstressed, particularly when approaching failure state, hence it is especially evident under squeezing conditions (Fritz 1981, Anagnostou and Kovári 2005; Anagnostou 2007).

Consolidation is relevant in water-bearing ground of low permeability and is associated with the transient seepage flow triggered by the tunnel excavation. Seepage flow enables the progressive dissipation of the excavation-induced excess pore pressures in the vicinity of the tunnel, thus inducing variations in the effective stresses and ground deformations. These processes occur more or less rapidly depending on the ground permeability and continue until a steady state is reached. Pore pressure has been known to intensify squeezing phenomena (Kovári and Staus 1996; Steiner 1996) and its effect may be decisive in deep tunnels, *e.g.* the Gotthard Base railway tunnel in Switzerland (Vogelhuber 2007), and subaqueous tunnels, *e.g.* the Lake Mead Intake No. 3 Tunnel in the USA (Anagnostou *et al.* 2010, 2018, Anagnostou and Zingg 2013) or the planned Gibraltar Strait Tunnel connecting Spain and Morocco (Pliego 2005; Lombardi *et al.* 2009; Anagnostou 2014).

In tunnelling practice, it is not always directly distinguishable whether the source of time-dependency of the ground behaviour is creep, consolidation, or the superposition of both. This is partially due to the different perception concerning the presence and influence of the pore water depending on the nature of the rock: in zones of fractured rock with increased permeability, the pore water presence can be identified directly, whereas in zones of low-permeability rock the pore water may be "invisible", as the water ingress is very limited, often in spite of the high prevailing pore pressure gradients (Anagnostou 2016).

An early identification of the actual source of time-dependency is valuable for the tunnel design, due to the fundamentally different nature of rheological processes (purely mechanical) and consolidation processes (coupled hydromechanical): It is particularly important in the context of laboratory testing during the project planning phase, in respect of selecting suitable processes and equipment for extracting, preserving, and testing the rock samples. In addition, it may be crucial for the choice of mitigation measures and the assessment of their effectiveness. For example,

advance drainage is irrelevant in the case of creep, but has proven to be particularly effective in numerous tunnelling projects where consolidation processes posed a concern, *e.g.* the Lake Mead Intake No. 3 Tunnel in the USA (Anagnostou and Zingg, 2013) and the Vereina railway tunnel in Switzerland (Steiner, 1996). Advance drainage relieves the pore pressures and allows the ground to consolidate, thereby increasing its undrained shear strength and leading to reduced short-term convergences in the vicinity of the tunnel heading (Anagnostou, 2009a), while it also eliminates the high pore pressure gradients during the early stages of consolidation, in turn additionally limiting convergences in the long term (Anagnostou, 2009b); furthermore, it is beneficial for the stability of both the tunnel face and also grouting cylinders in fault zones (Anagnostou and Zingg 2013).

Taking the above into consideration, the question arises of what the fundamental differences in the phenomenological ground behaviour are, and whether these could help distinguish creep from consolidation in practical situations. Although several existing works have separately examined the effects of creep (*inter alia* Sterpi and Gioda 2009; Hasanpour *et al.* 2015; Swannell *et al.* 2016; De la Fuente *et al.* 2020; Chapter 2) or consolidation in tunnelling (*inter alia* Graziani and Ribacchi 2001; Anagnostou 2007; Vogelhuber 2007; Ramoni and Anagnostou 2011b), this question has not been addressed in the literature thus far. With the aim of bridging this knowledge gap, this chapter evaluates comparatively some fundamental aspects of creep and consolidation in tunnelling, based upon transient numerical simulations. Emphasis is placed on the time development of ground deformations and the problems of shield or cutterhead jamming in mechanised tunnelling. To enable an easier qualitative interpretation of the fundamental aspects discussed, consideration is given to the simplified rotationally symmetric boundary value problem of a deep, cylindrical, and uniformly supported tunnel of radius R_0, crossing homogeneous and isotropic rock; the rock is subjected to a uniform and isotropic *in-situ* stress field (σ_0) and, in the case of consolidation, to a uniform and isotropic *in-situ* pore pressure field (p_0) as well, with values equal to the ones prevailing at the elevation of the tunnel axis.

This chapter starts by presenting the computational assumptions adopted in the numerical simulations (Section 4.2). Subsequently, to gain an insight into creep and consolidation, the simple plane-strain problem of a tunnel cross-section far behind the advancing face is examined first, with focus on the time-development of its radial displacement (u) upon excavation in the absence of a tunnel support (Section 4.3). This problem enables a simple demonstration of a fundamental difference between the two mechanisms of time-dependency, that is the consistently greater extent of ground plastification in the case of consolidation, which is partially associated with the effect of seepage forces.

Subsequently, the more complex and practically relevant problem of ground, TBM and tunnel support interaction in mechanised tunnelling is examined, with focus on the shield loading that develops during the advance of the TBM and during construction standstills (Section 4.4). It is shown that, despite the fundamentally different nature of the two mechanisms, the shield loading is ultimately governed by the same counter-acting effects of the delayed deformation development compared to the case of rapid squeezing: the ground behind the face deforms less, which is

favourable for shield loading, but the ground ahead of the face it experiences less plastic yielding and stress relief, which is unfavourable for shield loading; this interaction is also shown to produce a similar counter-intuitive effect of the advance rate on shield loading in both mechanisms under certain conditions. Furthermore, Section 4.4 discusses the similar adverse influence that continuing ground deformations during standstills, highlighting the uncertainties of time-independent models for jamming assessment.

Finally, Section 4.5 takes a closer look into the effect of the seepage forces, one important distinguishing feature between creep and consolidation, and investigates their role as a destabilising agent under certain conditions, which may cause excessive radial convergences of the cross-section or excessive extrusion and failure of the face.

Apart from the fundamental similarities and differences examined in the present chapter, the next chapter investigates potential differences between creep and consolidation with respect to the practical tunnel engineering question of experience transfereability: Can experience from tunnelling on the required thrust be used to assess the required thrust force in a tunnel with a different diameter or in an adjacent tunnel with the same diameter? How does the tunnel diameter affect the risk of shield jamming? Does the construction of a tunnel have an impact on the shield loading in a neighbouring tunnel built later?

4.2   Computational assumptions

Numerical models have been formulated in Abaqus® (Dassault Systèmes, 2018) for a 12 m diameter cylindrical tunnel ($R_0 = 6$ m) to simulate the problems of a tunnel cross-section under plane strain conditions and an advancing tunnel heading (Fig. 4.1). The model specifications are discussed hereafter and summarised in Table 4.1, along with the material parameters adopted in the numerical simulations.

4.2.1   Assumptions common to creep and consolidation analyses

In the transient mechanical analyses considering creep, a traction equal to the *in-situ* stress σ_0 prevailing at the depth of the tunnel is prescribed at the far-field boundary of the computational domain, 400 m (*ca.* $67R_0$) away from the tunnel axis. A linear elastic-viscous perfectly plastic constitutive model is adopted for the rock, with a Mohr-Coulomb yield condition and a non-associated viscoplastic flow rule according to Perzyna's theory (Perzyna, 1966). This is suitable for modelling rheological processes in squeezing ground, where the dominant portion of time-dependent deformations is plastic. The model formulation encompasses 5 mechanical parameters, namely Young's Modulus E, Poisson's ratio v, uniaxial compressive strength f_c, angle of internal friction φ, and angle of dilation ψ, as well as a single rheological parameter, the viscosity η, which determines the rate of viscoplastic deformation development due to creep. The model has been implemented in Abaqus® (Dassault Systèmes, 2018) as a user-defined material (UMAT) subroutine; details on its formulation and numerical implementation can be found in Appendix A, whereas the subroutine is given in Appenix B.

In the coupled hydromechanical consolidation analyses, the uniform traction σ_0 is also prescribed at the far-field boundary, while a uniform pore pressure, equal to the *in-situ* pore pressure p_0 prevailing at the depth of the tunnel, is prescribed at a distance from the tunnel axis equal to the water table level; this has been shown to be an adequate simplification for rotationally symmetric analyses (Ramoni and Anagnostou, 2011b). On account of the potential development of negative pore pressures upon unloading under undrained conditions (see, *e.g.*, Vogelhuber, 2007, Graziani & Ribacchi 2001), a mixed hydraulic boundary condition is prescribed at the tunnel boundary, which alternates between: an atmospheric pressure (Dirichlet) condition $p = 0$ when seepage flow takes place from the ground to the tunnel, *i.e.* $dq/dr > 0$; and a no-flow (Neuman) condition ($q = 0$) when seepage flow tends to take place from the tunnel to the ground in the presence of negative pore pressures, *i.e.* $dq/dr < 0$ (*cf.* Ramoni & Anagnostou 2011b). This ensures seepage flow only from the ground towards the opening and not *vice versa*.

The rock is modelled as a two-phase porous medium with unit Biot's coefficient, according to Terzaghi's principle of effective stresses. Seepage flow is modelled based on Darcy's law, considering a constant permeability k. An isotropic, linear elastic-perfectly plastic constitutive model with a MC yield criterion and a non-associated flow rule is adopted, with five mechanical parameters (E, v, f_c, φ, ψ). The solid grains and pore water are assumed incompressible in relation to the rock, which is reasonable for weak deformable ground; under this assumption, the condition of constant water content becomes equivalent to that of constant volume during the instantaneous undrained ground response to tunnelling.

4.2.2   Model of tunnel cross-section far behind the advancing face

For a tunnel cross-section far behind the face, plane strain conditions can be assumed. The plane strain model (Fig. 4.1a) simulates the ground response to excavation via an instantaneous unloading of the tunnel boundary from the *in-situ* stress σ_0 to zero support pressure ($\sigma_R = 0$). The tunnel boundary subsequently remains unsupported throughout the transient analysis and the evolution of its radial displacement over time is monitored.

Due to rotational symmetry, the problem can be analysed as 1D, considering a single strip in the $r – x$ plane of the computational domain with fixed and impermeable edges (flux $q = 0$). The strip is discretised with a structured finite element (FE) mesh of 4-noded, linear, quadrilateral, axisymmetric elements, encompassing 240 elements along the radial direction r, with exponentially variable size between $0.02R_0$ at the tunnel boundary and $3.7R_0$ at the upper far field boundary, and 1 element along the out-of-plane *x*-axis.

4.2.3   Model of advancing tunnel heading

The model of the advancing tunnel heading simulates the transient processes during ongoing mechanised excavation and lining installation, as well as during a subsequent TBM standstill of arbitrary duration. Besides the trivial assumptions underlying rotational symmetry, the latter presupposes also a negligible TBM weight, and thus uniform tunnel support and overcut around the shield, as well as uniform backfilling around the segmental lining. The excavation process, which in reality consists of intervals of continuous TBM propulsion alternating with standstills for lining erection, is simulated as continuous with an average advance rate v. The consideration of an average rate for the stop-and-go advance has been shown to be a sufficiently accurate simplification in most cases (Chapter 2). The step-by-step method is adopted (see, *e.g.*, Franzius and Potts, 2005), where at each numerical excavation step part of the ground is removed ahead of the face (round length $s = 1$ m; Fig. 4.1b) and an equal part of lining is installed immediately behind the shield.

The tunnel face is considered unsupported, which is reasonable considering that open shield TBMs are employed in most practical cases of mechanised tunnelling through squeezing rocks. The shield of length L is modelled with non-linear radial springs, which consider no loading (zero stiffness) for convergences below the radial overcut ΔR, and a linear elastic stiffness K_s for the portion of convergences that exceeds ΔR. The lining is modelled with elastic radial springs of stiffness K_l, assuming it is in direct contact with the ground immediately upon installation due to backfilling. The ground unloading behind the shield tail and its reloading over the lining are considered via the specification of distinct installation points for the shield and the lining; details can be found in Ramoni and Anagnostou (2010b) and Chapter 2. The left and bottom model boundaries are considered impermeable ($q = 0$), while the *in-situ* pore pressure p_0 is prescribed at the right model boundary, over a distance equal to the far-field radius of the seepage flow domain R_p (equal to the water table level; *cf.* Section 4.2.1)

The computational domain is discretised with a structured mesh of 11532 four-noded, linear, quadrilateral, axisymmetric finite elements (FEs). The element size in the radial direction varies exponentially from $0.02R_0$ at the tunnel boundary to $3.7R_0$ and $0.18R_0$ at the upper and lower model boundaries, respectively. The element size along the tunnel axis is constant and equal to the round length $s = 1$ m. Introducing a single FE within each round length eliminates the typical saw-shaped distribution of the radial rock pressure over the shield and lining observed in step-by-step simulations (Cantieni and Anagnostou, 2009). The selected round length is sufficiently small to ensure enhanced prediction accuracy (Franzius and Potts, 2005). An excavation length of $10R_0$ (60 excavation steps) is simulated.

The model enables determining the longitudinal profile of the rock pressure $\sigma_R(x)$ acting upon the shield at any time instance and, subsequently, its average value $\overline{\sigma}_R$ via integration over the shield length L. The simulated excavation length of $10R_0$ is sufficiently long for $\overline{\sigma}_R$ to become constant, and the standstill is initiated thereafter.
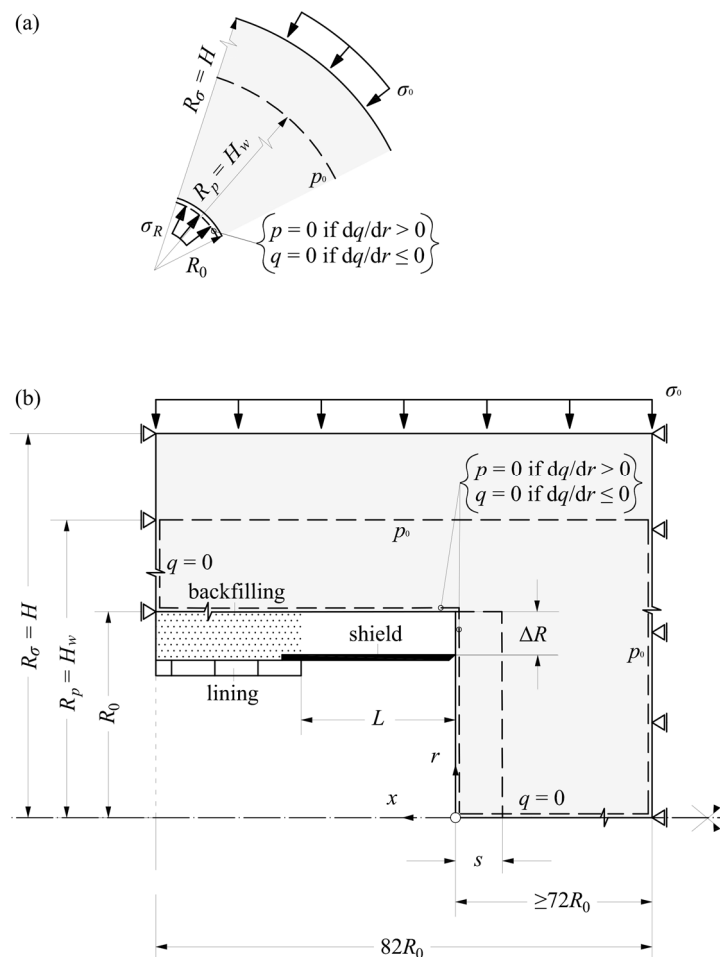
Figure 4.1. Computational models for the plane strain problem (a) and for the axisymmetric problem (b)

Table 4.1.   Parameters adopted in the numerical simulations

Ground

Young's Modulus, E	[GPa]	1
Poisson's ratio, v	[-]	0.25
Uniaxial compressive strength, f_c	[MPa]	2 [a], 0.3 [b], 0.5 [b]
Angle of internal friction, ϕ	[°]	25
Dilatancy angle, ψ	[°]	5
Depth of cover, H	[m]	400
In-situ stress at tunnel axis, σ_0	[MPa]	10
Water table level above tunnel axis, H_w	[m]	100, 400
In-situ pore pressure at tunnel axis, p_0	[MPa]	1, 4
Viscosity η	[MPa·d]	$[10^{-5} - 10^6]$ [a]
Permeability k	[m/s]	$[10^{-2} - 10^{-16}]$ [a], 10^{-9} [b]

TBM

Boring radius, R_0	[m]	6
Radial overcut, ΔR	[m]	0.05
Longitudinal gap due to cutterhead retraction, Δx	[m]	0.2 [b]
Shield length, L	[m]	12
Young's modulus of steel E_s	[GPa]	210
Shield thickness d_s	[cm]	15
Radial shield stiffness, K_s	[MPa/m]	875
Static cutterhead skin friction coefficient, μ_{st}	[-]	0.15 [b]
Static cutterhead friction coefficient, $\mu_{st,c}$	[-]	0.15, 0.45 [b]
Advance rate, v	[m/d]	30

Lining

Young's modulus of concrete E_c	[GPa]	30
Lining thickness d_l	[m]	0.75
Radial lining stiffness K_l	[MPa/m]	625

Model

Round length, s	[m]	1
Far-field radius of the computational domain, R_σ	[m]	400
Far-field radius of seepage flow domain, R_p	[m]	100, 400

[a] Considered only in Sections 4.3 and 4.4

[b] Considered only in Section 4.5

4.3   Time-dependent contraction of a tunnel cross-section far behind the face

The radial displacement of the unsupported tunnel boundary u depends in general on all independent problem parameters, *i.e. in-situ* stress σ_0, tunnel radius R_0, material constants, time t and, in the case of creep, additionally on the viscosity η:

$$u = f\left(\sigma_0, R_0, E, \nu, f_c, \phi, \ \psi, t, \eta\right). \tag{4.1}$$

In the case of consolidation, the permeability k, the *in-situ* pore pressure p_0, the unit weight of the pore water γ_w and the size (far-field radius) of the seepage flow domain R_p considered in the numerical model (Table 4.1) appear additionally in the parameter list:

$$u = f\left(\sigma_0, R_0, E, \nu, f_c, \phi, \psi, t, \ k, \ p_0, \gamma_w, R_p\right). \tag{4.2}$$

Following dimensional analysis, Eqs. 4.1 and 4.2 can be respectively written as

$$\frac{u}{R_0} = f\left(\frac{E}{\sigma_0}, \nu, \frac{f_c}{\sigma_0}, \ \phi, \ \psi, \ \frac{tE}{\eta}\right) \tag{4.3}$$

and

$$\frac{u}{R_0} = f\left(\frac{E}{\sigma_0}, \nu \frac{f_c}{\sigma_0}, \phi, \psi, \frac{tkE}{\gamma_w R_0^2}, \frac{p_0}{\sigma_0}, \frac{R_p}{R_0}\right). \tag{4.4}$$

Figure 4.2 shows the normalised radial displacement u/R_0 as a function of the normalised time t^*, which is defined as tE/η in the case of creep (black line) and $tkE/(\gamma_w R_0^2)$ in the case of consolidation (dashed and solid red lines for two values of the *in-situ* pore pressure $p_0 = 1$ and 4 MPa, respectively). Very low values of t^* correspond to the conditions during rapid excavation, where the instantaneous ground response can be considered; the latter is purely elastic in the case of creep and undrained in the case of consolidation. Very high values of t^* correspond to steady-state conditions, where all viscoplastic deformations have developed in the case of creep and all excavation-induced excess pore pressures have dissipated in the case of consolidation (drained conditions).
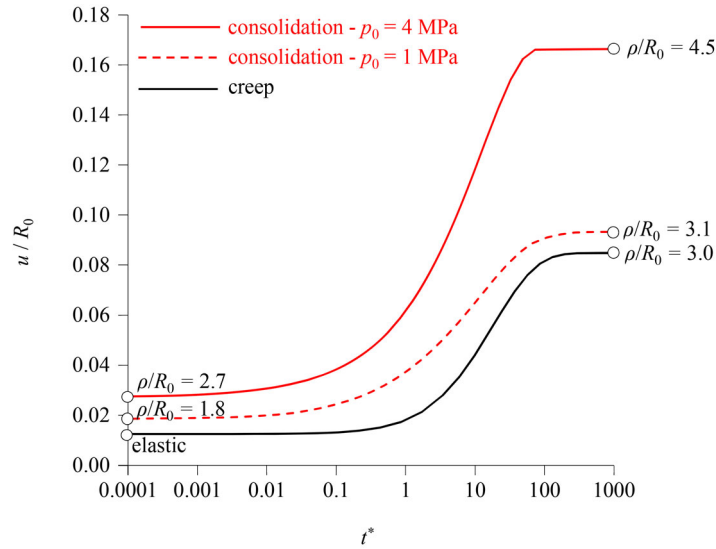
Figure 4.2.   Evolution of radial displacement normalised by the tunnel radius over time in the plane strain
problem (η = 1000 MPa·d, k = 10^{-9} m/s, other parameters: Table 4.1)

One can readily verify that the time-development of displacements is qualitatively similar in both cases: the ground displacement increases at a decreasing rate and ultimately converges asymptotically to a maximum value at steady-state conditions. It can be directly inferred that, with appropriate scaling between the viscosity η and the permeability k and selection of the material parameters, the curves nearly overlap. This demonstrates the difficulty of distinguishing creep from consolidation, as well as of back-analysing ground parameters from – or even simply interpreting – the observed time-dependent deformations.

All strength and stiffness parameters being equal, the instantaneous and steady-state displacements are consistently higher in the case of consolidation, even more so in the case of the higher pore pressure p_0 = 4 MPa, due to the more extensive ground plastification (see values of the normalised plastic radius ρ/R_0 in Fig. 4.2). The latter is observed both in the short term, where the ground response is undrained elastoplastic in the case of consolidation but purely elastic in the case of creep, and at steady state, where the ground response is elastoplastic in both cases, but in the case of consolidation there is the additional, external loading by the seepage forces. Their steady-state magnitude depends solely on the hydraulic boundary conditions and their effect is therefore higher in the case of higher pore pressure p_0 = 4 MPa, causing more extensive plastification and leading to substantially increased displacements of the tunnel boundary.

As the magnitude of the seepage forces does not depend on characteristics of the ground and can be – depending on the *in-situ* pore pressure p_0 – arbitrarily high, it may happen – depending on p_0 and ground strength – that equilibrium in the vicinity of the tunnel boundary is impossible and excessive cavity contraction or even complete cavity closure occurs. In this sense, seepage is a potential destabilising agent for the tunnel cross-section and the tunnel face. This constitutes a distinguishing feature between creep and consolidation, which is examined in more detail in Section 4.5.

4.4 Shield loading during TBM advance and standstills

The average rock pressure acting upon the shield $\bar{\sigma}_R$ depends in general on all independent problem parameters, *i.e.* the *in-situ* stress σ_0, the tunnel radius R_0, the material constants of the ground E, v, f_c, ϕ, ψ, the TBM parameters $K_s, K_l, L, \Delta R$, the advance rate v, and the standstill time t. Analogously to the problem of the tunnel cross-section, in the case of creep it depends additionally on the viscosity η, *i.e.*

$$\bar{\sigma}_R = f\left(\sigma_0, R_0, E, v, f_c, \phi, \psi, \Delta R, L, K_s, K_l, v, t, \eta\right), \tag{4.5}$$

and in the case of consolidation on the permeability k, the *in-situ* pore pressure p_0, the unit weight of the pore water γ_w, and the size of the seepage flow domain R_p:

$$\bar{\sigma}_R = f\left(\sigma_0, R_0, E, v, f_c, \phi, \psi, \Delta R, L, K_s, K_l, v, t, k, p_0, \gamma_w, R_p\right). \tag{4.6}$$

Following dimensional analysis, and considering the inverse proportionality between Young's modulus E and displacements in elastoplastic ground (Anagnostou and Kovári, 1993; Ramoni and Anagnostou, 2010b), the normalised average pressure over the shield $\bar{\sigma}_R/\sigma_0$ can be expressed as

$$\frac{\bar{\sigma}_R}{\sigma_0} = f\left(\frac{E}{\sigma_0}\frac{\Delta R}{R_0}, v, \frac{f_c}{\sigma_0}, \phi, \psi, \frac{L}{R_0}, \frac{K_s R_0}{E}, \frac{K_l R_0}{E}, \frac{v}{R_0}\frac{\eta}{E}, t\frac{E}{\eta}\right), \tag{4.7}$$

in the case of creep, whereas in the case of consolidation the corresponding expression reads as follows:

$$\frac{\bar{\sigma}_R}{\sigma_0} = f\left(\frac{E}{\sigma_0}\frac{\Delta R}{R_0}, v, \frac{f_c}{\sigma_0}, \phi, \psi, \frac{L}{R_0}, \frac{K_s R_0}{E}, \frac{K_l R_0}{E}, \frac{v}{R_0}\frac{\gamma_w R_0^2}{kE}, t\frac{kE}{\gamma_w R_0^2}, \frac{p_0}{\sigma_0}, \frac{R_p}{R_0}\right). \tag{4.8}$$

4.4.1 Shield loading during TBM advance

Figure 4.3 shows the plastic strain contours in the vicinity of the advancing tunnel face (Figs. 4.3a and 4.3b), along with the longitudinal distributions of displacements (Figs. 4.3c and 4.3d), convergences (Figs. 4.3e and 4.3f), and radial stresses (Figs. 4.3g and 4.3h) in the case of creep (black lines) and consolidation (dashed and solid red lines for two values of the *in-situ* pore pressure $p_0 = 1$ and 4 MPa, respectively), for two limit cases of rapid and slow excavation (l.h.s. and r.h.s. diagrams). The latter are considered via the normalised advance rates $v^* = (v/R_0)\eta/E$ and $v^* = (v/R_0)\gamma_w R_0^2/(kE)$ in Eqs. 4.7 and 4.8, which express how fast one tunnel radius is excavated in relation to the rate that the time-dependent deformations develop. The slow and fast excavation cases are directly analogous to those of a very high and a very low normalised time t^*, respectively, in the case of the tunnel cross-section problem examined in Section 4.3: during rapid excavation the ground response is purely elastic in the case of creep and undrained elastoplastic in the case of consolidation; during slow excavation there is sufficient time for steady-state conditions to develop simultaneously with the advance of the face, where all viscoplastic deformations have taken place in the case of creep and drained conditions prevail in the case of consolidation, following the complete dissipation of the excavation-induced excess pore pressures.

Similar to the problem of the tunnel cross-section examined previously, the plastic strains (Figs. 4.3a and 4.3b) and the displacements (Figs. 4.3c and 4.3d) are higher in the case of consolidation than in the case of creep, both during rapid and slow excavation. However, this is not necessarily reflected as a higher rock pressure on the shield (see stress for $x > 0$ in Figs. 4.3g and 4.3h), because the mechanisms underlying the rock-shield interaction are far more complex: The pressure that ultimately develops on the shield is determined by the interplay between two counteracting effects of rock plastification: more plastic yielding on the one hand leads to increased ground convergences around the shield, and thus increased contact area and hence tentatively increased shield loading, but on the other hand it causes more stress relief ahead of the face, which tentatively results in less load transfer to the shield. The differences in the rock pressure between creep and consolidation for the cases of rapid and slow excavation, which are more pronounced in the higher-pore-pressure case (red solid lines in Fig. 4.3), can be interpreted based on this interaction. Both for fast and slow excavation, stress-relief ahead of the face is more pronounced in the consolidation case than in the creep case (compare red and black solid lines for $x < 0$ in Fig. 4.3g and 4.3h), which should tentatively result in a lower shield loading. This is indeed the case for slow excavation (compare red and black solid lines for $x > 0$ in Fig. 4.3h), but for fast excavation it appears that the unfavourable effect of a larger contact area outweighs the favourable effect of more pronounced stress relief and leads to a higher shield loading in the case of consolidation (compare red and black solid lines for $x < 0$ in Fig. 4.3g).
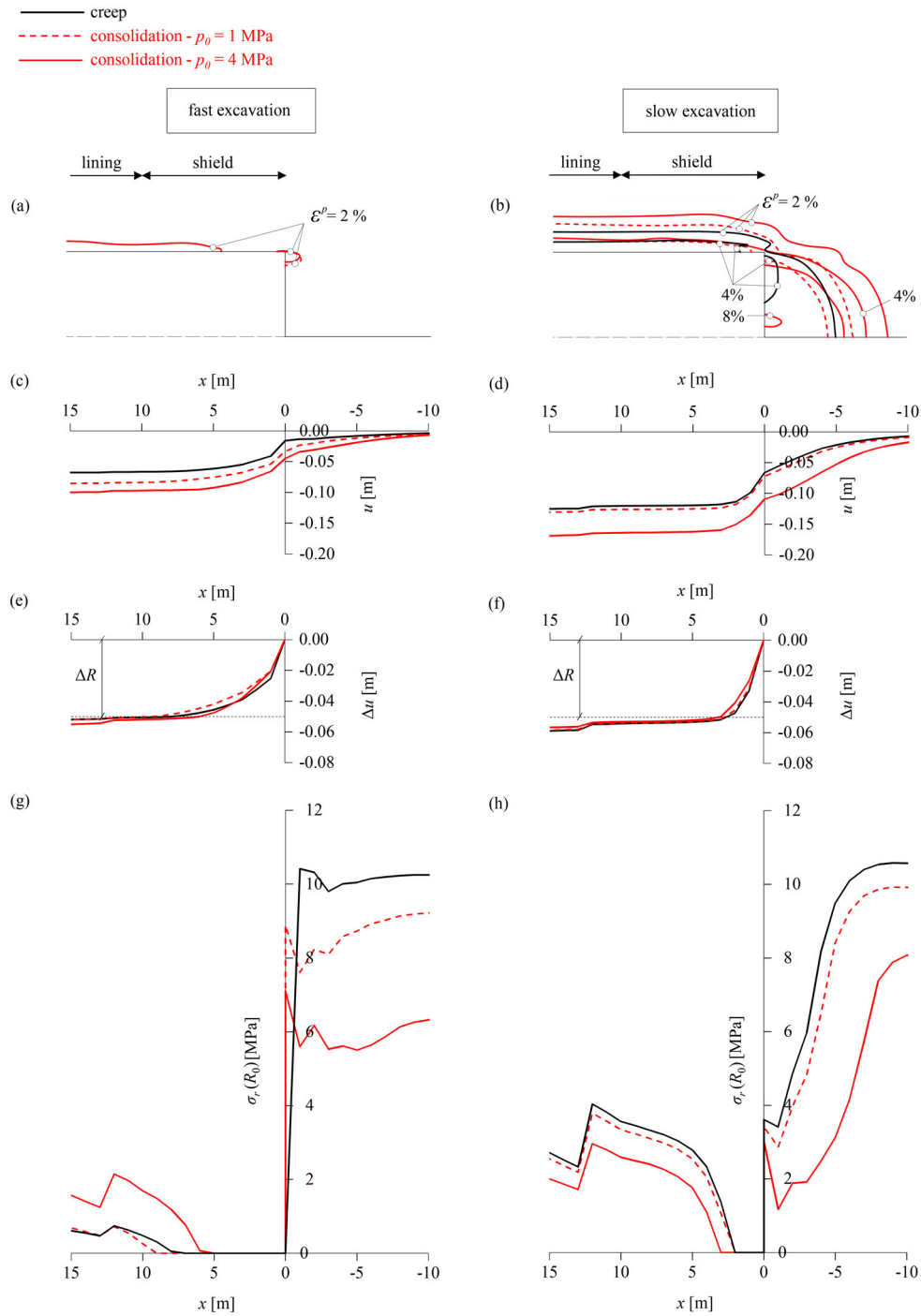
Figure 4.3.   Contour-lines of plastic strain (a,b); longitudinal displacement profiles (c,d); longitudinal convergence profiles (e,f); longitudinal distributions of radial stress at $r = R_0$ over shield and lining as well as ahead of the face (g,h) during fast and slow excavation (slow excavation: $\eta = 2 \ 10^{-3}$ MPa·d, $k = 10^{-4}$ m/s; fast excavation: $\eta = 2 \ 10^{8}$ MPa·d, $k = 10^{-16}$ m/s; other parameters: Table 4.1)

4.4.2   Counter-intuitive effect of advance rate

The interplay of the two competing effects discussed above also produces a counter-intuitive result regarding the effect of advance rate on shield loading. Figure 4.4 shows the average shield pressure $\overline{\sigma}_R$ as a function of the normalised advance rate v^* for creep (black lines) and consolidation (red lines). One would expect the conditions to become increasingly favourable with faster excavation, *i.e.* $\overline{\sigma}_R$ to decrease monotonically with increasing v^*, due to the delay in the development of plastic deformations; however, within a certain range of v^*-values, $\overline{\sigma}_R$ increases with v^* and is higher compared to its value for $v^* \rightarrow 0$, when deformations develop rapidly. This seemingly paradoxical behaviour is observed both in the case of creep and consolidation, with the two distributions being qualitatively identical.

Chapter 2 reported and examined in detail this counter-intuitive behaviour in the case of creep. It showed that it is attributed to the delayed plastic deformation development with increasing viscosity η (or, equivalently, normalised advance rate v^* in this case), which leads to smaller contact area between shield and ground, but also limits the stress relief of the ground ahead of the face, thereby having a stiffening effect. The paradox appears in the range of v^* where the superimposed effect of contact area and ground stiffening is the most unfavourable.

Ramoni and Anagnostou (2011b) originally reported and examined the same paradox for the case of consolidation, explaining it on the basis of the slower development of plastic deformations in the case of lower permeability k, an effect directly analogous to that of a higher viscosity η in the case of creep. In the case of consolidation, however, there exists the additional effect of the negative pore pressures (suction) that may develop upon ground unloading under certain conditions. These have a stabilising effect, as they increase the effective stresses and thus the shearing resistance of the rock, thereby leading to reduced deformations and plastification. The paradox appears in the range of v^* where the most unfavourable situation arises, with pore pressures being negative in the vicinity of the face, thus causing stiffening ahead of it, and simultaneously positive over the shield, thus resulting in larger deformations and contact.
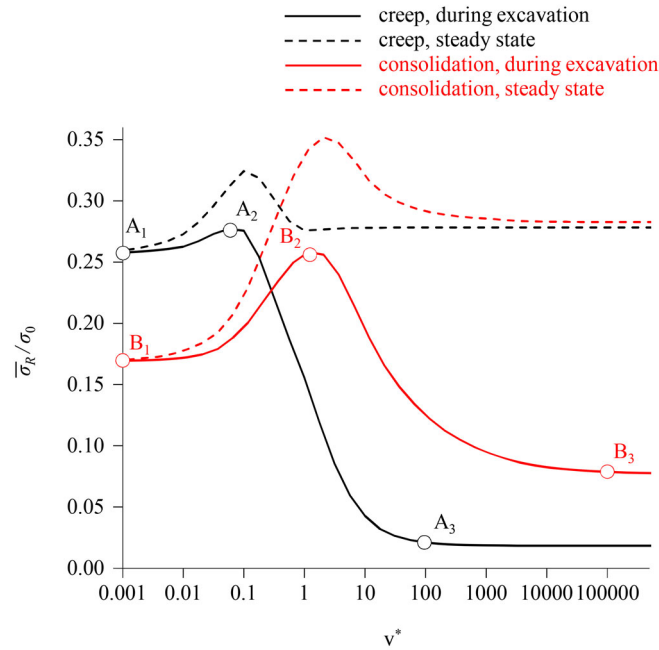
Figure 4.4.   Average rock pressure developing on the shield (normalised by the *in-situ* stress) as a function of the normalised advance rate v^* ($p_0 = 4$ MPa; other parameters: Table 4.1)

4.4.3   Shield loading during a standstill

Within the range of v^* where the paradox discussed previously appears, the conditions are also more unfavourable during a subsequent standstill, where the TBM shield remains static and the ground deforms and exerts additional pressure on it over time. This is evident from the dashed lines in Figure 4.4, which show the shield loading for the limit case of a sufficiently long standstill that allows steady-state conditions to develop. The rock pressure variation is qualitatively similar for both creep and consolidation, but its increase is in general more pronounced in the latter case, since seepage flow progressively starts taking place during the standstill and seepage forces induce more extensive ground plastification. (Expectedly, this increase will be less pronounced in the case of the lower pore pressure $p_0 = 1$ MPa, which is not shown in Figure 4.4).

The above becomes more clearer, when examining the development of the average rock pressure ($\overline{\sigma}_R$) during the standstill, which is shown in Figure 4.5 for the case of creep (black lines) and consolidation (red lines), for the characteristic values of the normalised advance rate v^* corresponding to the 6 points $A_1 - A_3$ and $B_1 - B_3$ annotated on Figure 4.4. The rock pressure development is qualitatively similar for the two mechanisms: for a low v^* (dotted lines; points A_1, B_1 in Fig. 4.4), the behaviour is almost time-independent and steady state is reached practically already during excavation, while for a high v^* (dashed lines; points A_3, B_3 in Fig. 4.4) the behaviour is pronouncedly time-dependent, with the rock pressure progressively increasing and ultimately reaching a maximum value after a very long time. The maximum value is similar to the one in the low v^* case for creep, but higher in the case of consolidation. A qualitatively similar behaviour can be observed for the intermediate v^* corresponding to the range of the paradox (solid lines; points A_2, B_2 in Fig. 4.4), where both the instantaneous and steady-state rock pressure

exceed those of the time-independent model, where deformations develop rapidly, indicating that this case is the most critical from a practical engineering viewpoint.

Conclusively, it is evident that standstills are thoroughly unfavourable in both cases, and ultimately lead to a higher rock pressure for v^* in the range of the paradox, compared to the one that would develop in the case of time-independent ground behaviour ($v^* \rightarrow 0$). Therefore, models that disregard time-dependency of the ground behaviour and assume that plastic deformations develop instantaneously are in no way conservative: they may overestimate the shield loading during excavation, but they considerably underestimate it during standstills – even during short standstills – and this occurs regardless of the mechanism underlying the time-dependency of ground behaviour.
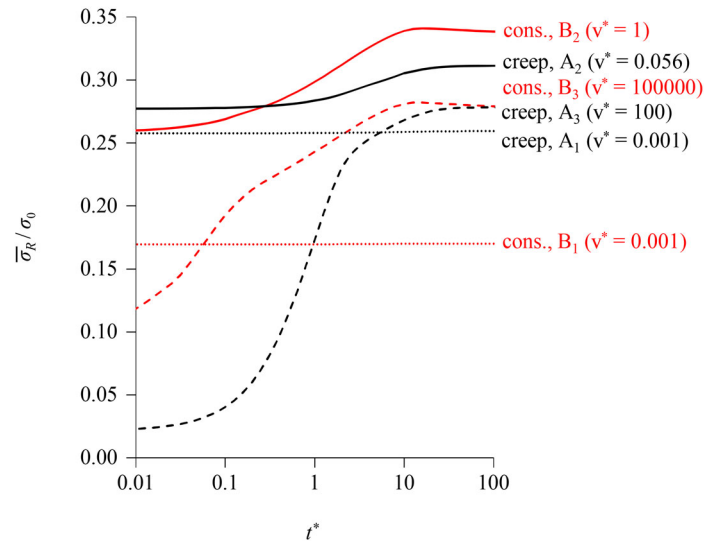

Figure 4.5.   Increase in the normalised average rock pressure developing on the shield during a standstill ($p_0 = 4$ MPa; other parameters: Table 4.1)

4.5   On the destabilising effect of the seepage forces

Permeability governs the rate of squeezing in consolidation, analogously to viscosity, which governs the rate of creep. But in the case of consolidation an additional parameter has to be considered – the *in-situ* pore pressure (or its gradient, the seepage force), which does not exist in the case of creep and – as an external loading – inherently results in fundamental differences in the ground behaviour.

The detrimental effect of seepage flow can best be explained by considering the conditions at the end of the consolidation process. In homogeneous ground the steady-state pore pressure field and thus the magnitude of the seepage forces depend solely on the hydraulic boundary conditions, that is – in the present case – on the *in-situ* pore pressure. To fulfil equilibrium, the seepage forces must be resisted by the stresses in the ground; however, the maximum resistance that the ground can provide depends on its mechanical characteristics and is limited by its strength. So, for example, in the plane of the tunnel cross-section the seepage force f_s acting upon an infinitesimal rock element at an unsupported excavation boundary (Fig. 4.6a) can be kept in equilibrium only by the tangential stresses σ'_t (arching), which however are limited by the uniaxial compressive strength f_c of the ground. At an extruding tunnel face the curvature radius is negative and equilibrium is possible only via catenary action, which presupposes that the ground can sustain tensile stresses f_t (Fig. 4.6b). Considering the above, under certain conditions the magnitude of seepage forces may be sufficiently high to make impossible equilibrium in the vicinity of the tunnel, thereby causing excessive convergences of the tunnel cross-section or extrusion and instability of the tunnel face.

These effects relevant in consolidation must be distinguished from familiar instability phenomena, *e.g.* those that occur in rocks exhibiting strain softening that are relevant both in creep (tertiary creep; Sterpi and Gioda 2009, which has not been implemented in the present creep constitutive model, *cf.* Appendix A) and consolidation, since they are induced by an external agent completely unrelated to the mechanical properties of the ground; therefore, they may also occur in the absence of softening, in perfectly plastic rocks examined in the present chapter.

This role of seepage forces as a potential destabilising agent has been reported by Egger *et al.* (1982) and some basic considerations were also later examined by Anagnostou (2006). The destabilising effect of seepage force on the tunnel boundary and the tunnel face is examined separately in the following subsections, with reference to the problems of the tunnel cross-section under plane strain conditions and the tunnel heading examined in the previous sections of this chapter.
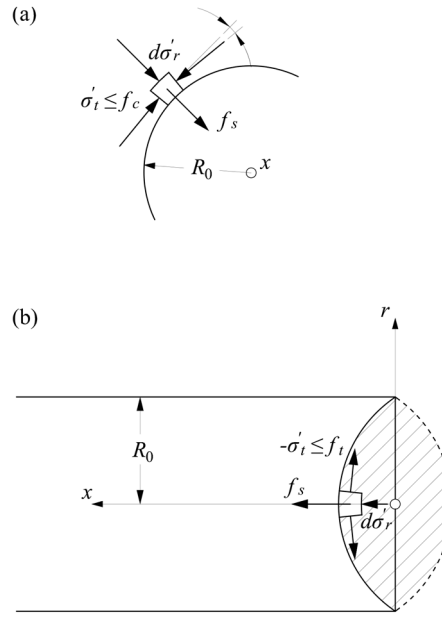
Figure 4.6.   Qualitative interpretation of the destabilizing effect of seepage forces at the unsupported
              tunnel boundary: (a) development of excessive compressive tangential stress in the plane of
              the tunnel cross-section; (b) development of tensile tangential stress at the tunnel face

4.5.1   Tunnel cross-section far behind the face

The rotationally symmetric, plain strain problem of an unsupported tunnel cross-section will be
considered (Fig. 4.6a). Taking account of the steady-state radial pore pressure distribution, the
condition of radial equilibrium at the tunnel boundary reads as follows (Anagnostou and Kovári
2003; Anagnostou 2009b):

$$\left.\frac{d\sigma'_r}{dr}\right|_{r=R} = \frac{1}{R}\left[f_c - \frac{p_0}{\ln\left(R_p/R\right)}\right],$$ (4.9)

where r is the radial coordinate, σ'_r the radial effective stress, R the tunnel radius in the deformed
configuration, f_c the uniaxial compressive strength of the ground, and R_p the far-field radius of the
seepage flow domain.

In Eq. 4.9, the first r.h.s. term denotes the resistance provided by the ground during yielding,
whereas the second term results from the seepage flow. As the pore pressure p_0 can take any value
(depending only on the elevation of the water table, regardless of the strength of the ground), the
r.h.s. term of Eq. 4.9 may become negative if the tunnel is located sufficiently deep under the
water table. In this case, the effective radial stress cannot increase with the radius and therefore
cannot reach a state of equilibrium with the far-field stress σ_0, which according to Egger *et al.*
(1982) means that the opening would be unstable. This points to a qualitative difference to the
ground behaviour in the case of creep, where a stable stress field always exists in the absence of
softening.

This difference is, however, only apparent, because the instability would manifest itself by increasing convergences, which would result in an increasing curvature of the tunnel boundary, and equilibrium can always be reached if the curvature becomes sufficiently big. The maximum radius R' that allows for equilibrium to be achieved can be determined from Eq. 4.9 by equating its r.h.s. term to zero, which leads to the following expression:

$$R' = R_p \, e^{-\frac{p_0}{f_c}}.$$

(4.10)

For the strength and the *in-situ* pore pressures considered in Section 4.3 and 4.4 ($f_c = 2$ MPa, $p_0 = 1 - 4$ MPa), the maximum radius $R' \gg R_0 = 6$ m, which means that equilibrium is possible even when disregarding the favourable effect of the increasing curvature due to cavity contraction. In the sequel, a much lower strength will be considered ($f_c = 0.3$ MPa) in order to illustrate quantitatively the behaviour discussed above. For this strength and the higher *in-situ* pore pressure considered ($p_0 = 4$ MPa), the maximum radius $R' \approx 0$, which means that the equilibrium condition cannot be satisfied, if formulated in the undeformed configuration. This is true even for the lower *in-situ* pore pressure ($p_0 = 1$ MPa), where the maximum radius $R' = 3.56$ m ($< R_0 = 6$ m).

However, considering the deformed configuration, that is performing a geometrically non-linear, large-strain analysis (see, *e.g.*, Vrakas and Anagnostou, 2015), allows finding equilibrium, even if the latter is achieved at elevated convergences or almost complete closure of the opening. This is illustrated by the numerical results of Figure 4.7, which shows the time-development of the tunnel radius R for the two considered values of the *in-situ* pore pressure.

In conclusion, the instability postulated by Egger *et al.* (1982) cannot actually occur and there is no difference between creep and consolidation in respect of equilibrium or lack thereof in the case of a circular opening. The reason is of a geometric nature: at the onset of instability the curvature increases and this stabilises the system, so that an equilibrium can always be found, even if this may happen at big convergences which, in practical terms, may fail to satisfy serviceability criteria.

However, this finding about the effect of the curvature and its change during cavity contraction points to a fundamental difference between the behaviour of the tunnel cross section and the behaviour of the tunnel face: the geometry of the cross-section becomes increasingly more favourable during cavity contraction, whereas the geometry of the face becomes more and more unfavourable during extrusion, as it becomes convex (Fig. 4.6b). The behaviour of the tunnel face during extrusion is examined in the next section.
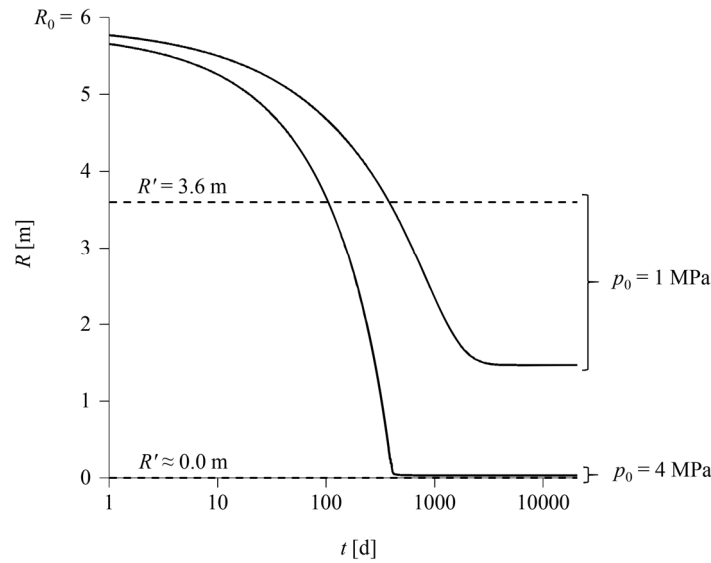
Figure 4.7.   Contraction of a tunnel cross-section far behind the face over time in the case of low strength
                (f_c = 0.3 MPa; other parameters: Table 4.1)

4.5.2   Tunnel face

The seepage forces have an unfavourable effect also on the tunnel face (Egger *et al.* 1982), causing
it to undergo excessive extrusions, as shown in Figure 4.6b. However, the curvature of the
extruded face has an opposite sense to that of the tunnel cross-section, thus necessitating the
ground to develop a catenary action with sufficiently high tensile stresses in order to resist seepage
forces. As the tensile strength f_t of geomaterials is very limited in general, equilibrium can only
be achieved by a reversal of the curvature (see dashed line in Fig. 4.6b), which presupposes the
detachment of the extruded part, as well as of some part of it ahead of the face. In this sense, the
face extrusion due to seepage forces can be classified as an instability, contrary to the contraction
of the cross-section examined previously.

The extrusion of the face is numerically investigated in the sequel over the course of a sufficiently
long TBM standstill to reach steady state conditions, based upon geometrically non-linear, large
strain analyses with the model of the advancing tunnel heading introduced earlier in Section 4.2.3.
The parameters given in Table 4.1 are adopted and two values of *in-situ* pore pressure p_0,
1 and 4 MPa, are considered.

As the model assumes no face support (open shield TBM), it enables examining the system
behaviour during unhindered extrusion of the tunnel face. This case, however, constitutes a purely
theoretical consideration, since in practice the ground establishes contact with the TBM
cutterhead after a certain amount of deformation, upon which further extrusion is constrained, and
thus an axial pressure starts developing over the cutterhead front surface. The face-cutterhead
interaction is considered in the model by introducing nonlinear springs with zero stiffness for

extrusion values that do not exceed the longitudinal gap between face and cutterhead, and a very high stiffness for the portion of extrusion that exceeds this gap (the cutterhead is considered as practically rigid in relation to the ground). The maximum longitudinal gap that is technically feasible in practice by retraction of the cutterhead amounts to nearly 90 cm, as applied, *e.g.,* in a double shield TBM with boring radius of 9.5 m employed in the Guadarrama tunnel (Rostami 2008). However, in most practical situations the retraction is limited to 10-20 cm, to maintain a safety reserve during the TBM operation in the case of unforeseen changes in the ground conditions in later stages of the advance, as well as to avoid the risk of fractured rock inflow behind the rear end of the cutterhead that may cause mechanical damage (Burger, 2023). Taking this into consideration, a longitudinal gap of 20 cm is considered in the model.

From a practical viewpoint, the combined effect of the extrusion and instability of the tunnel face and the contraction of the tunnel cross-section under seepage forces may be particularly critical in respect of the thrust force and the torque of the cutterhead required in order for the TBM to restart advance after a standstill. The model provides the displacement of the tunnel face, the average radial rock pressure $\overline{\sigma}_R$ that develops over the shield length L (*cf.* Section 4.2.3), as well as the axial pressure σ_x that develops on the cutterhead front surface. Considering that the relatively small force required for boring is included in the axial force exerted by the ground upon the cutterhead, the required thrust force can be evaluated in general as

$$F_r = \mu_{st}\, 2\pi R_0\, L\, \overline{\sigma}_R + 2\pi \int\limits_{r=0}^{R_0} \sigma_x(r)\, r\, dr\,, \qquad (4.11)$$

where the first term corresponds to the frictional force exerted over the shield skin, μ_{st} being the static friction coefficient between shield and rock, and the second term corresponds to the axial force exerted on the cutterhead. The friction coefficient μ_{st} is set to a relatively low value of 0.15, considering lubrication of the shield extrados (Ramoni and Anagnostou 2011a). The required torques can be evaluated as:

$$T = \mu_{st,c}\, 2\pi \int\limits_{r=0}^{R_0} \sigma_x(r)\, r^2 dr\,, \qquad (4.12)$$

where $\mu_{st,c}$ is the static friction coefficient between the protruding tools of the cutterhead and the rock. The existing literature concerning this coefficient (for a summary see Bamford and Yaghoubi 2017), indicates values between 0.1 and 0.7, with an average of the maximum values equal to ca. 0.45. The variability is attributed to the rock quality, with softer rocks being associated with higher friction coefficients in general, due to the higher penetration of the cutterhead tools. Considering the above, the simulations are performed for two values of $\mu_{st,c}$: a relatively low value of 0.15 (equal to the shield skin friction coefficient) and the average of the maximum values reported in the literature of 0.45.

The cases of unhindered and hindered extrusion are discussed hereafter with reference to Figures 4.8 and 4.9, considering the two values of the *in-situ* pore pressure p_0, 1 and 4 MPa. Figure 4.8a shows the rock pressure distribution over the shield at the beginning of the standstill (equal to the

pressure acting during excavation) and at steady state. Figure 4.8b shows the radial distribution of the axial displacement of the face at two time-instances before and at the time instance when it establishes first contact with the cutterhead. Figure 4.8c shows radial distributions of the axial pressure acting on the cutterhead shortly upon contact, at an intermediate time instance, and at steady state. Figure 4.9 shows the axial displacement at the centre of the tunnel face, the required thrust force and the required torque (considered only for hindered extrusion) as functions of the standstill duration. Shield jamming and cutterhead blocking are assessed considering relatively high values for the installed torque of 30 MNm (Ramoni and Anagnostou 2010b), and for the installed thrust force of 300 MN. The latter, although higher than values usually reported in the literature, is feasible with the current developments in TBM technology, particularly considering that an installed thrust of 225 MN was materialised 15 years ago in the 10 m-diameter Pajares tunnel in Spain (Ramoni and Anagnostou 2010b).

Examining first the results for $p_0 = 4$ MPa, in the theoretical case of unhindered extrusion the time-development of the face axial displacement (Fig. 4.9a) is qualitatively similar to that of the radial displacement of an unsupported cross-section examined previously (Fig. 4.7); however, as the curvature of the extruding face has a destabilising influence, the extrusion reaches extremely high values that exceed the tunnel diameter of 12 m (even when considering geometric nonlinearity in the stress analysis). This excessive extrusion induces extensive plastification of the ground ahead of the tunnel face and contraction of the tunnel cross-section and, in turn, the pressure that develops on the shield increases due to longitudinal arching of the ground above it. This increase is more pronounced closer to the face, where the extruded ground is less stiff and more plastified (Fig. 4.8a). The skin friction to be overcome at restart thereby increases monotonically with the standstill duration, and the required thrust force exceeds the relatively high installed value of 300 MN after ca. 33 days (Point P_8 in Fig. 4.9b).

In the practically relevant case of hindered extrusion for $p_0 = 4$ MPa, contact between the face and the cutterhead is established after $t_c = ca.$ 3 days and the extrusion subsequently stops (Point P_2 in Fig. 4.9a). In the model, relevant for the assessment of the 20 cm gap closure is the axial displacement of the face that occurs solely during the standstill, that is beyond the instantaneous displacement during advance of 15 cm; this is because in reality the latter would have been previously excavated by the cutterhead, however the model cannot capture this as it does not simulate the cutting process in detail. The axial displacement prior to contact is highest at a point *ca.* 5 m above the centre of the face, and contact is established first at a point *ca.* 1 m below that (Fig. 4.8b). This intuitively appears as implausible, as one would expect first contact to occur at the centre; however, it is attributed to the pore pressure distribution, specifically the development of higher in magnitude negative pore pressures (suction) at the centre of the face than further above, which have a stiffening effect and limit its displacement slightly. This does not occur for $p_0 = 1$ MPa, where the initial distribution of axial displacements is qualitatively similar, but the effect of suction is eliminated prior to contact, and hence this occurs first at the centre (Fig. 4.8b, *cf.* Appendix D). The point of first contact expectedly influences also the respective axial pressure distributions and their development over time (Fig. 4.8c).

The skin friction to be overcome at restart increases monotonically with the standstill duration prior to cutterhead-face contact, following the same line as in the case of unhindered extrusion, due to the continuing contraction of the cross-section and the resulting increased load transfer to the shield. Upon contact, the cutterhead starts preventing further face extrusion and contraction of the core, and thus also further load transfer to the shield, hence the shield load (and consequently the skin friction at restart) remains practically constant and almost all axial loading is resisted by the cutterhead (Point P_6 in Fig. 4.9b); this has also been demonstrated by Ramoni and Anagnostou (2011b). The cutterhead torque also increases monotonically upon contact (Fig. 4.9c). The total required thrust force exceeds the relatively high installed values of 300 MN after ca. 4 days, 8 times faster than in the case of unhindered extrusion (*cf.* Points P_7 an P_8 in Fig. 4.9b). The torque exceeds the installed value of 30 MNm practically simultaneously for the lower cutterhead friction coefficient $\mu_{st,c} = 0.15$ and earlier for the higher $\mu_{st,c} = 0.45$ (Points P_7 in Fig. 4.9b and P_{11}, P_{12} in Fig. 4.9c, respectively).

As seepage forces are higher for $p_0 = 4$ MPa than for $p_0 = 1$ MPa, in the latter case the extrusion is less pronounced and develops slower (Fig. 4.9a), hence its effects in respect of the rock pressure developing on the shield (Fig. 4.8a) and cutterhead (Fig. 4.8c) – and, in turn, the required thrust force (Fig. 4.9b) and torque (Fig. 4.9c) – are less pronounced in comparison. For unhindered extrusion the installed thrust force is exceeded after *ca.* 111 days (*cf.* Point P_5 in Fig. 4.9b). For hindered extrusion it is exceeded after ca. 11 days, 10 times faster (cf. Points P_4 and P_5 in Fig. 4.9b), while the installed torque is exceeded after ca. 20 days for the lower cutterhead friction coefficient $\mu_{st,c} = 0.15$ and much earlier, after about 8 days for the higher $\mu_{st,c} = 0.45$ (Points P_9, P_{10} in Fig. 4.9c).

The results indicate that cutterhead blocking is overall more critical than insufficient thrust. The only exception is the case of the lower cutterhead friction coefficient $\mu_{st,c} = 0.15$ and $p_0 = 1$ MPa, however this is due the very low friction coefficient, which is rather unlikely for weak rocks prone to squeezing.

Conclusively, these results underscore the practical significance of the seepage forces, which may result in significant loading of the cutterhead and have severe implications in respect of the design of the TBM, or even the feasibility assessment of a TBM drive in consolidating ground, an effect which does not exist in the case of creep.
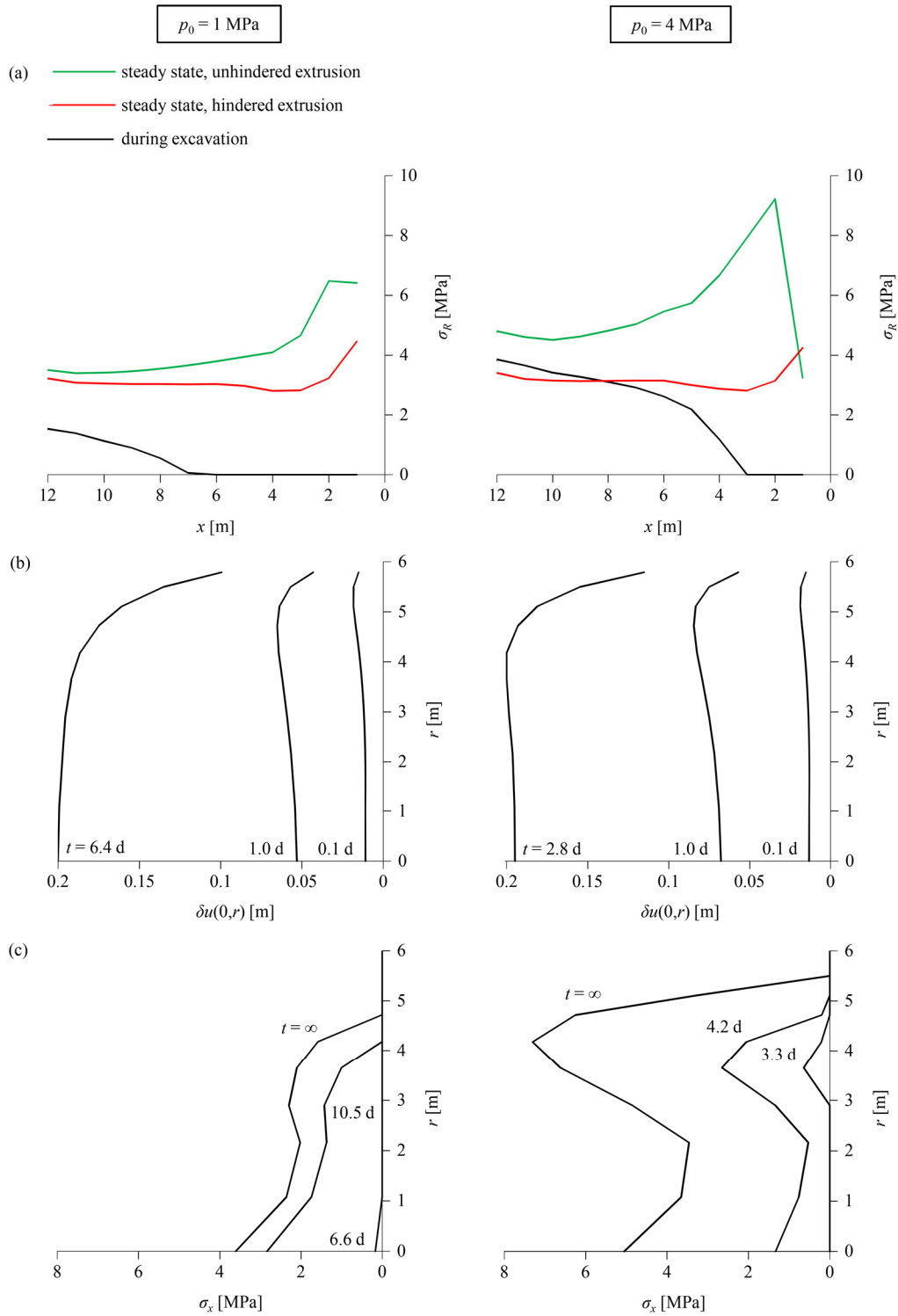
Figure 4.8.   (a) Longitudinal distribution of the radial loading of the shield; (b) radial distribution of the axial displacement of the face; (c) radial distribution of the axial loading of the cutterhead at different time instance after first contact ($f_c = 0.5$ MPa; parameters: Table 4.1)
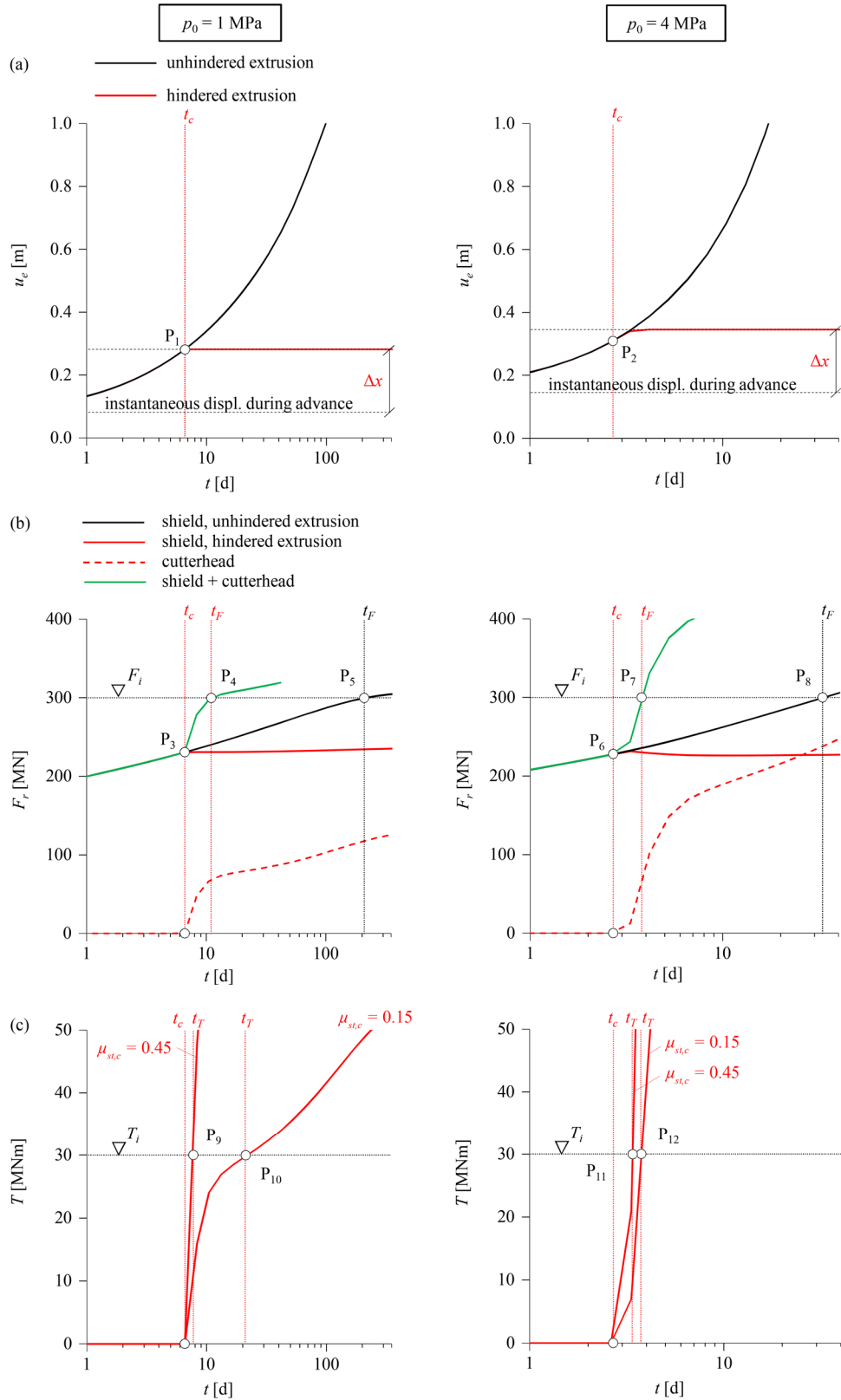
Figure 4.9.   (a) Time-development of face extrusion, (b) frictional force on the shield skin and axial force
on the cutterhead front and (c) torque during standstill (f_c = 0.5 MPa; other parameters: Table
4.1)

4.6   Conclusions

This chapter investigated similarities and differences between the time-dependent effects of creep and consolidation in mechanised shield tunnelling through squeezing ground; however, focusing more on the fundamental aspects, *i.e.* on the mechanisms underlying the evolution of rock deformations and the complex interaction between rock, TBM and tunnel support during excavation and during construction standstills.

The presented investigations highlighted several qualitative similarities between the two mechanisms of time-dependency of the ground behaviour, in respect of: (i), the time-development of the unsupported tunnel boundary displacement between tunnel excavation and steady state conditions; (ii), the dependency of shield loading during excavation on the advance rate of the TBM, which also indicates a similar counter-intuitive behaviour of increasing shield loading with faster advance under certain conditions (Ramoni and Anagnostou 2011b; Chapter 2); and, (iii), the increase in the rock pressure on the static shield during construction standstills, due to the manifestation of additional ground deformations over time.

Despite these qualitative similarities, the present chapter underscored two prominent differences resulting from the fundamentally different nature of the purely mechanical rheological creep processes and the coupled hydromechanical consolidation processes.

The first difference can be attributed to the consistently more pronounced plastification in consolidating compared to creeping ground. In the short term, this is due to the ground partially yielding immediately upon excavation under undrained conditions, but remaining practically elastic in the case of creep, where all plastic deformations are time-dependent and manifest themselves later over time; in the long term, it is due to the additional, external effect of the seepage forces on the solid rock constituents under drained conditions. This chapter demonstrated that, despite the more extensive ground plastification in the case of consolidation leading to higher deformations, this is not necessarily reflected as a higher rock pressure on the shield. Although higher deformations behind the advancing tunnel face are indeed unfavourable and increase the ground-shield contact area and thus the shield loading, the greater plastification ahead of the face induces more ground relaxation and stress relief, and has an opposing, favourable influence on the shield loading. Therefore, depending on the advance rate, the interaction of these effects may lead to a higher or lower shield pressure in consolidating than in creeping ground during TBM advance, as well as to a more or less pronounced increase of this pressure during a subsequent standstill of certain duration.

The second difference can be traced to the seepage forces exerted by the pore water on the solid rock constituents in the case of consolidation. As the magnitude of these forces is completely unrelated to the mechanical ground characteristics and depends only on the hydraulic boundary conditions, while the resistance provided by the ground is limited by its strength, equilibrium may be impossible in the vicinity of the tunnel for a sufficiently high pore pressure. This results in excessive convergences of the tunnel cross-section or extrusion of the tunnel face, which, however, are fundamentally different: in the former case the cavity contraction increases its

curvature and stabilises the system, hence equilibrium is always found, even at very high convergences, whereas in the latter case the convex curvature of the extruded face destabilises the system and equilibrium can never be found. This chapter demonstrated that these phenomena, which are relevant also in the case of perfectly plastic rocks considered, are particularly critical in respect of shield jamming and cutterhead blocking in consolidating ground and must be duly considered in the design of the TBM and the feasibility assessment of the TBM drive.

Returning to the question posed in the introduction, despite the existence of the above fundamental differences, these do not allow for a distinction of creep from consolidation based upon the observed or observable ground behaviour in practice. Even if the more extensive plastification could be observed, it would not enable definitive conclusions to be drawn, as there is no reference value or systematic way of quantifying this, particularly when there is significant uncertainty surrounding the strength and stiffness parameters of the ground. Concerning the instability, there is no way of distinguishing this based on the observed behaviour, whether this is due to seepage forces, other reasons, *e.g.* softening, which is also relevant in creeping ground (tertiary creep; Sterpi and Gioda 2009), or a combination of these aspects. In this sense, the only viable way of distinction is the advance exploration of the hydrogeological conditions of the project site and appropriate laboratory tests to determine the rheological properties as well as the degree of saturation and permeability of the ground.

5 Creep versus consolidation in tunnelling through squeezing ground – Part B: Transferability of Experience [4]

Abstract

This chapter investigates potential differences between creep and consolidation in mechanised tunnelling through squeezing ground, placing focus on the practical question of using experiences gained from existing tunnels about the required thrust force as a reference for tunnels of different diameter or adjacent tunnels. The investigations focus on two aspects. First, the effect of the tunnel diameter on the risk of shield jamming is examined. The chapter demonstrates that larger diameter tunnels are more favourable in poor quality ground, while the opposite holds in better quality ground, as well as in the case of pronouncedly time-dependent ground behaviour due to consolidation or creep. Second, the effect of a tunnel on the required thrust force in a neighbouring tunnel built later is examined. The chapter shows that this interaction effect is particularly important in water-bearing ground of low permeability, where the drainage action of the first tunnel induces pore pressure relief and ground consolidation in an extensive area, leading to a remarkable reduction of the thrust force in the second tunnel. Conversely, in the case of creep the interaction is negligible even under extremely squeezing conditions, due to the fundamentally different nature of the purely mechanical rheological processes from coupled hydromechanical processes. The presented investigations into the transferability of experiences are valuable for tunnelling practice, in cases of twin tunnels as well as in situations where a smaller diameter tunnel is constructed prior to the main tunnel (*e.g.* a pilot tunnel for exploration, advance drainage or ground improvement), or also the opposite (*e.g.*, upgrade of a road tunnel by later construction of a safety tunnel with a smaller diameter).

---

[4]   This chapter has been accepted on 31.01.24 for publication with the following reference: Nordas, A.N., Leone, T., Anagnostou, G. (2024). Creep versus consolidation in tunnelling through squeezing ground – Part B: Transferability of Experience. Rock Mechanics and Rock Engineering (accepted for publication). The contributions of each author are given in Appendix F. The postprint version is considered for the present chapter.

5.1   Introduction

In the previous chapter, fundamental similarities and differences between creep and consolidation in mechanised tunnelling through squeezing ground have been examined, placing focus on the evolution of rock deformations and stresses, as well as – associated with the latter – the required thrust force and the risk of shield jamming. In this chapter, the comparison between creep and consolidation is extended by investigating whether experiences gained from previous tunnels about the required thrust force can be transferred to tunnels of different diameter or to adjacent tunnels of the same diameter built under the same geotechnical conditions (rock properties, pore pressure, overburden, *etc*.). The investigations into experience transferability are valuable in practical situations where a smaller diameter pilot tunnel is constructed prior to the main tunnel for exploration, advance drainage or ground improvement, or also the opposite (*e.g.*, upgrading of a road tunnel by later construction of a safety tunnel with a smaller diameter), as well as in cases of sequentially excavated twin tunnels.

Within this backdrop, this chapter addresses two key aspects: (i), the effect of the tunnel diameter on the risk of shield jamming ("scale effect") and, (ii), the effect of a tunnel on the required thrust force in an adjacent, later excavated tunnel ("interaction"). There is a significant volume of literature on creep and consolidation in tunnelling in general, as well as specifically on the problem of shield jamming in mechanised tunnelling through squeezing ground (see Chapter 4 and Chapter 2 for recent reviews); however, the aforementioned interaction effect has not been studied so far, while the scale effect has only been investigated by Ramoni and Anagnostou (2011b) for the case of consolidation. Therefore, there is sufficient scope for a systematic investigation of both aspects in the present work.

5.1.1   Scale effect

Besides the practical question posed above, the investigation into the scale effect is also motivated by a theoretical consideration – the well-known finding of consolidation theory that consolidation time increases with the 2nd power of the drainage path length, *e.g.*, the thickness of a low permeability layer. Based on this, squeezing would develop slower in a larger diameter tunnel, as the drainage paths around it are longer in relation to a tunnel of smaller diameter, and this should also affect the rock pressure acting on the advancing shield and thus the force required to overcome shield skin friction and the risk of shield jamming. As this scale effect is related to the specific process of transient seepage flow and excess pore pressure dissipation, it is expected that there may be significant differences in scale effects between consolidation and creep – the other principal mechanism of time dependency of squeezing.

Although the aforementioned theoretical considerations are valid concerning the rate of development of squeezing deformations, the effect of the tunnel diameter on the risk of shield jamming is much more complex to assess, due to three reasons. First, depending on the tunnel diameter there are different technical limitations for certain parameters of the tunnel boring machine (TBM), including the overcut, shield length, shield and lining stiffnesses and maximum installable thrust force, which also have mutually competing effects on the rock pressure that

develops on the shield. Second, the tunnel diameter also poses limitations on certain operational parameters, specifically the TBM advance rate and the duration of construction standstills, which must also be considered in cases of time-dependent ground behaviour due to creep or consolidation. Third, a larger cross-section is associated with a higher potential of encountering adverse conditions (*e.g.*, weak zones, water inflows *etc.*; Kovári 1979; Schneider 2002); however, as squeezing ground is often weak even at the small scale of a specimen, the differences in the ground properties between different diameter tunnels is of secondary importance in relation to the above.

Considering all limitations discussed above, Ramoni and Anagnostou's investigations (2011b) showed that a smaller diameter is consistently less prone to shield jamming than a larger one in the case of consolidation, alas the differences between them decrease in weaker ground. Based on these findings, two questions arise: is it possible that a larger diameter is more favourable than a smaller one in weaker ground? is the scale effect the same in the case of creep? These questions are addressed in Section 5.2, which examines the effect of the tunnel diameter both on the rock deformations and on the risk of shield jamming during advance or after a standstill of the TBM, based on exemplary, transient numerical simulations that incorporate the limitations discussed above.

5.1.2 Interaction

Tunnelling through heavily squeezing ground can cause stress-redistribution and deformations in an extended area, in turn affecting other existing or planned underground structures. In the case of a twin tunnel, the excavation of the 1st tube may affect the stress field at the location of the 2nd tube and thus the construction and support of the latter significantly, and *vice versa* – the construction of the 2nd tube may have a relevant effect on the lining of the 1st tube. The interaction effects may be more or less pronounced depending on the construction method. It is expected to be more pronounced in the case of conventional tunnelling with a yielding support, and less pronounced in the case of a construction method that limits ground deformations by foreseeing a stiff support close to the tunnel face (resistance principle). Shield tunnelling is closer to the second case, as the available space is very limited due to the construction equipment, with ground deformations therefore being small in general.

A special situation arises in the case of saturated, water-bearing ground, where the drainage action of a tunnel results in a pore pressure relief over a very extended area (Arn, 1989). In the case of a twin tunnel, pore pressure relief due to the 1st tube has a favourable influence on the subsequently excavated 2nd tube, which is analogous to that of advance drainage (Anagnostou and Zingg, 2013): it results in higher effective stresses, hence in a higher undrained shear strength of the ground and, finally, in lower short-term deformations during excavation. This experience was often made in tunnelling practice. Prominent examples are the Simplon railway tunnel and the Gotthard motorway tunnel in Switzerland (Lombardi 1976, Steiner 1996, Anagnostou 2009a); in the latter case, noteworthy is the influence of consolidation up to *ca.* 10 diameters around the first tunnel, which was also much smaller than the second.

On the one hand, due to the aforementioned large-scale pore pressure relief and consolidation in the case of low-permeability water-bearing ground and, on the other hand, due to the limited excavation-induced stress-redistribution in the case of shield tunnelling through creeping but not water-bearing ground, it is expected that time-dependent interaction effects will be more pronounced in the case of consolidation than in the case of creep. Section 5.3 investigates this hypothesis considering the problem of shield jamming in a twin tunnel, and shows that the required thrust force in the 2nd tube is significantly lower than in the 1st tube in the case of consolidation, even for large spacings of the two tunnels, whereas in the case of creep the 1st tube has a negligible effect on the construction of the 2nd tube.

Other potentially important interactions, such as the effect of the 1st tube on the lining of the 2nd tube and *vice versa*, are beyond the scope of this chapter, which focuses solely on differences/similarities between creep and consolidation with respect to TBM-ground interaction.

5.2   Scale effect

To obtain a basic insight into the effect of the tunnel diameter, our investigations start with a simple plane-strain problem, that of the time development of tunnel convergences in a cross-section far behind the face (Section 5.2.1), and continue with the core subject of this chapter, *i.e.* the scale effect with respect to the risk of shield jamming (Section 5.2.2).

5.2.1   Time-dependent contraction of a deep tunnel

5.2.1.1   *Homogeneous ground*

The problem can be analysed based on the classic, rotationally symmetric, plane-strain model of a deep, cylindrical and uniformly supported tunnel located deep below the ground surface and the water table. The radial displacement of the tunnel boundary u_R can then be expressed as a function of the significant problem parameters as

$$\frac{u_R}{R} = f\left(\frac{E}{\sigma_0}, \nu, \frac{f_c}{\sigma_0}, \ \phi, \ \psi, \ \frac{tE}{\eta}\right) \tag{5.1}$$

in the case of creep, and as

$$\frac{u_R}{R} = f\left(\frac{E}{\sigma_0}, \nu, \frac{f_c}{\sigma_0}, \phi, \psi, \frac{p_0}{\sigma_0}, \frac{R_p}{R}, \frac{tkE}{\gamma_w R^2}\right) \tag{5.2}$$

in the case of consolidation (Chapter 4). In these equations, R is the tunnel radius, R_p is the far-field radius of the seepage flow domain considered in the numerical model – taken to be equal to the depth of the tunnel under the water table (Ramoni and Anagnostou, 2011b) – σ_0 and p_0 are respectively the *in-situ* stress and pore pressure at the depth of the tunnel axis, γ_w is the unit weight of the pore water and t the time that has elapsed upon excavation. The rock is assumed to obey a linear elastic and perfectly plastic constitutive model with a Mohr Coulomb yield condition and

a non-associated plastic flow rule, defined by five parameters: the Young's Modulus, E, the Poisson's ratio, v, the uniaxial compressive strength, f_c, the angle of internal friction, ϕ, and the angle of dilation, ψ. The rheological ground behaviour due to creep is modelled as purely viscoplastic based on Perzyna's overstress theory (Perzyna, 1966), according to which the rate of viscoplastic deformations is governed solely by the ground viscosity η. Seepage flow in water-bearing ground is modelled according to Darcy's law, considering a constant ground permeability k.

The expression of the dimensionless time parameter in Equation (5.2) is identical to that in Terzaghi's 1D consolidation theory (Terzaghi, 1925), the only difference being that the drainage path length is replaced by the tunnel radius R, which is the characteristic length in the present problem. Based on this expression, one can directly infer that the time required to attain a given percentage of the displacement increment during the consolidation process, $e.g.$ 95% (denoted as t_{95} henceforth), is proportional to R^2 for given ground parameters, initial stress and pore pressure. Such a dependency does not exist in the case of creep, as R does not appear in the r.h.s. parameter list of Equation (5.1). In practical terms, this means that, $e.g.$, if the tunnel diameter was four times larger, then the displacements would develop at the same rate in the case of creep, but 16 times slower in the case of consolidation. The same delay in the displacement evolution would be observed in the smaller diameter tunnel if the permeability of the ground was lower by a factor of 16.

The above quadratic dependency holds as long as the tunnel lies deep under the water table ($R_p \gg R$), which fixes the influence of the penultimate term in Equation (5.2) and renders R the only relevant geometric parameter. However, problems also exist that are characterised by more than one significant geometric parameters. This is, for example, the case of tunnelling in a low-permeability layer (aquitard) embedded between two aquifers (Fig. 5.1a). The aquitard thickness induces an additional, non-trivial scale effect, which is examined in the next subsection.

(a)

(b)
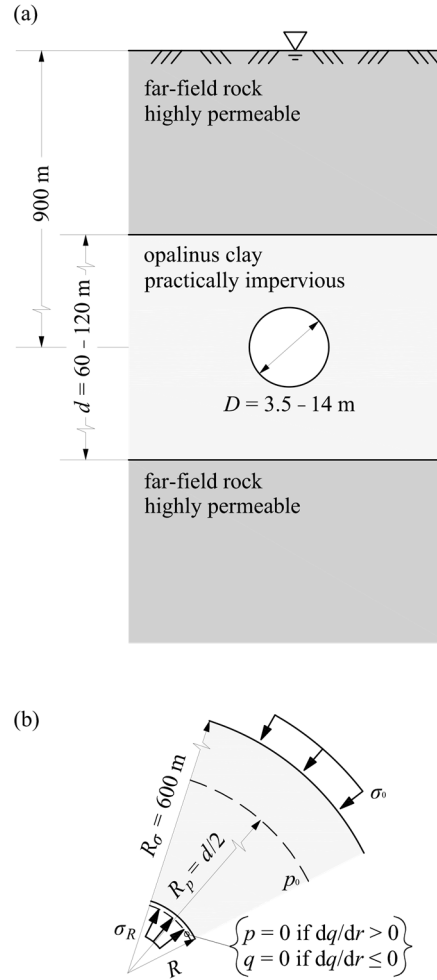
Figure. 5.1   Plane-strain scale problem: (a) geotechnical situation for tunnelling through a horizontal
              aquitard and, (b), simplified rotationally symmetric computational model

5.2.1.2   *Confined aquitard*

In the case of an aquitard confined between permeable layers, the *in-situ* pore pressure p_0 practically acts at the layer interfaces and the hydraulic head difference between aquifer and tunnel is dissipated practically only within the aquitard, along a drainage path whose length corresponds to half the aquitard thickness ($d/2$ in Fig. 5.1a). This constraint may give rise to a secondary, non-trivial scale effect, which becomes relevant when the ratio of the aquitard thickness to the tunnel diameter d/D is small, as this generates two competing effects: on the one hand the drainage path becomes shorter, which accelerates the consolidation process, but on the other hand the hydraulic gradients and thus the seepage forces are higher, which induces more extensive ground plastification and thereby decelerates the consolidation process.

The scale effects related to the tunnel diameter and the size of the seepage flow domain are demonstrated on the example of a deep geological repository for radioactive waste, which is planned to be constructed in Switzerland over the next years. Circular drifts of diameter $D = 3.5$ m will be used for the disposal of high-level waste (Nordas *et al.*, 2023c), while low/intermediate-

level waste will be stored in caverns with four times larger average diameter $D = 14$ m (Morosoli *et al.*, 2023). The repository will be embedded at a maximum depth of 900 m, within a practically horizontal, *ca.* 100 m-thick layer of Opalinus Clay, a claystone with several favourable properties for waste containment, mainly its extremely low permeability. The Opalinus Clay layer is interspersed between substantially more permeable layers of marls, hence the *in-situ* pore pressure $p_0 = 9$ MPa can be considered to act at its boundaries. The problem layout is shown in Figure 5.1a.

For simplicity, variations in the geodetic height are ignored and the low/intermediate-level waste caverns are idealised as circular, which enable analysing the problem under the assumption of rotational symmetry using the plane strain model shown in Figure 5.1b. Apart from the ground heterogeneity, the model specifications are identical to those discussed in the previous chapter, and are given in Table 5.1. Parametric numerical simulations are conducted considering variable distance of the tunnel axis from the drainage boundary (R_p in Eq. 5.2) of 30 – 60 m, which in this case represents the half-thickness $d/2$ of the Opalinus Clay layer wherein seepage flow occurs. The equivalent isotropic material constants for the Opalinus Clay given in Table 5.1 are based on the anisotropic parameters determined from experimental results by Nordas *et al.* (2023b), and consider low, intermediate, and high values of the uniaxial compressive strength $f_c = 7$, 9 and 17 MPa, respectively, to account for the strength anisotropy and brittle softening that the Opalinus clay has been shown to exhibit.

Table 5.1   Parameters adopted in the numerical investigations into the problem of tunnelling through a horizontal aquitard (Section 5.2)

Ground

Young's Modulus, E	[GPa]	8
Poisson's ratio, υ	[-]	0.25
Uniaxial compressive strength, f_c	[MPa]	var.
Angle of internal friction, ϕ	[°]	30
Dilatancy angle, ψ	[°]	3
Depth of cover, H	[m]	900
In-situ stress at tunnel axis, σ_0	[MPa]	22.5
Water table above tunnel axis, H_w	[m]	900
Permeability, k	[m/s]	10^{-13}

Model

Far-field radius of the computational domain, R_σ	[m]	600
Far-field radius of the seepage flow domain, R_p	[m]	var.
Tunnel diameter, D	[m]	3.50 or 14

Figure 5.2 shows the ratio t_{95} (D = 14 m) /t_{95} (D = 3.5 m) between caverns and drifts (Fig. 5.2a), along with the corresponding plastic radii ρ (Fig. 5.2b) and normalised displacements u/R (Fig. 5.2c) at steady-state conditions (*i.e.,* upon completion of the consolidation process), as functions of the distance of the tunnel axis from the drainage boundary $d/2$, for the three values of f_c.

Considering first the lowest f_c (7 MPa), one can observe that in the case of an aquitard thickness d of 120 m, only the basic scale effect is relevant: consolidation in the caverns takes place at a rate that is lower than in the drifts by a factor of 16, according to the ratio of the squares of their diameters, *i.e.* t_{95} (D = 14 m) /t_{95} (D = 3.5 m) = (14 / 3.5)^2 (Fig. 5.2a). The non-trivial scale effect starts to immediately become relevant for smaller d-values, where the ratio of t_{95} can be seen to increase rapidly and monotonically towards very high values (Fig. 5.2a).

The monotonic increase indicates that in the case of the caverns (D = 14 m), where d/D (or, equivalently, R_p/R in Eq. 5.2) is smaller, the acceleration of the consolidation process due to the shorter drainage path is negligible compared to the deceleration imposed by the more extensive ground plastification due to the higher seepage forces. The dominant effect of plastification becomes evident by the increase in the steady-state radius of the plastic zone (Fig. 5.2b) and normalised displacement (Fig. 5.2c) for the caverns; for a lower aquitard thickness d of 60 m, the plastic zone even approaches the boundary of the seepage flow domain, indicating an almost complete plastification of the Opalinus Clay layer. Conversely, for the drifts (D = 3.5 m) where d/D is higher, both the plastic radii and displacement remain constant. The non-trivial scale effect is qualitatively similar but less pronounced for f_c = 9 MPa and can be seen to vanish completely with for f_c = 17 MPa, which indicates that it is only relevant in weaker ground.

For the actual thickness of the Opalinus Clay layer of *ca.* 100 m at the repository sites, consolidation around the caverns is expected to take place 16 – 20 times slower than around the drifts; it can thus be considered to obey the quadratic rule of consolidation theory that holds for deep tunnels in homogeneous ground, with some small deviations. The key take-away from these results, however, is that in confined aquitards the consolidation rate may deviate dramatically from the quadratic rule of consolidation theory – and, this is even more so the case for lower aquitard thickness and weaker ground – indicating that ground deformations may continue to develop for a very long time after excavation. This may prove critical in respect of serviceability requirements or the structural safety of the final lining, as rock pressures will continue developing on it long after its installation.
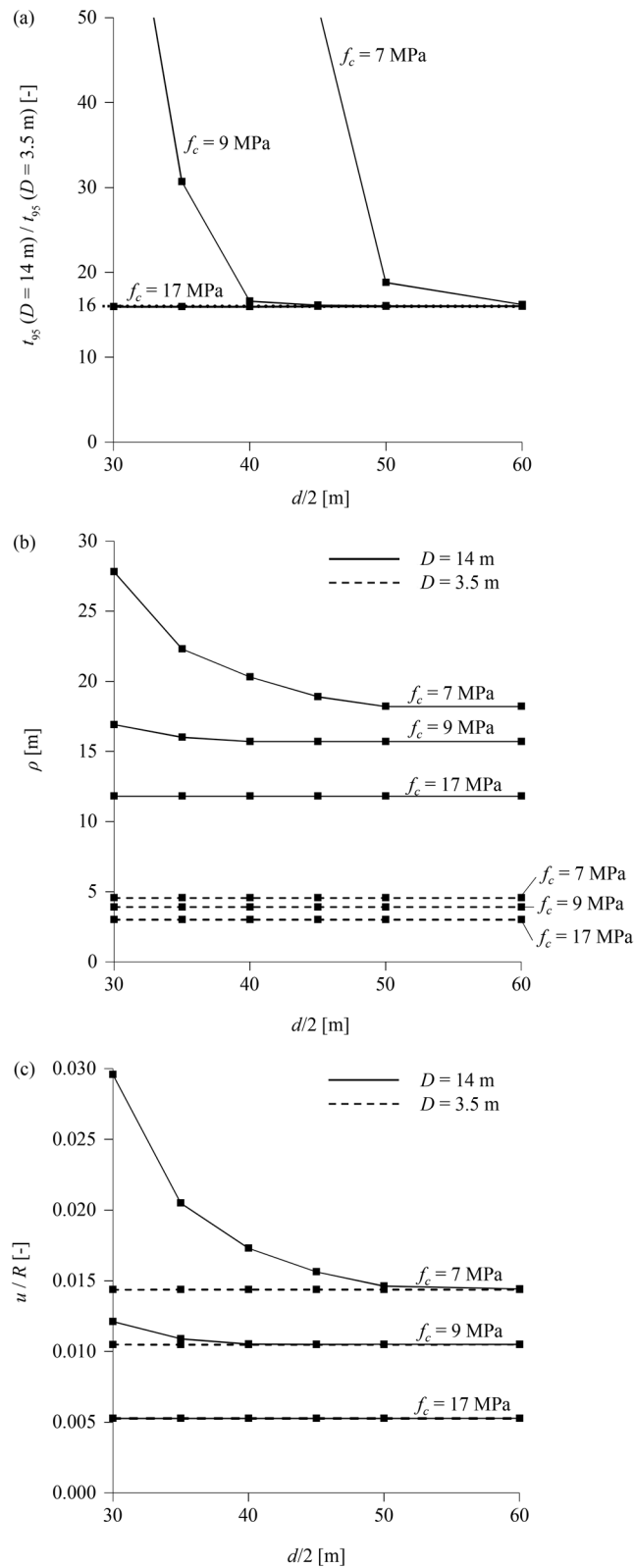
Figure. 5.2   Scale effect in the problem of tunnelling through a horizontal aquitard (Fig. 5.1) associated with the hydromechanical coupling: (a) ratio of the consolidation time t_{95} in a diameter 14 m tunnel to the consolidation time t_{95} in a diameter 3.5 m tunnel, (b), steady-state radius of the plastic zone ρ and, (c), normalised steady-state displacement u/R of the tunnel boundary as functions of the distance of the aquifer from the tunnel axis $d/2$ (parameters: Table 5.1)

5.2.2   Risk of shield jamming

The effect of the tunnel diameter on the risk of shield jamming will be investigated only for homogeneous ground, considering the rotationally symmetric, plane-strain model of a cylindrical and uniformly supported tunnel located deep below the ground surface and the water table. In this case, the average rock pressure that develops on the shield $\overline{\sigma}_R$ can be expressed as a function of the significant problem parameters as

$$\frac{\overline{\sigma}_R}{\sigma_0} = f\left(\frac{E}{\sigma_0}\frac{\Delta R}{R}, \nu, \frac{f_c}{\sigma_0}, \phi, \psi, \frac{L}{R}, \frac{K_s R}{E}, \frac{K_l R}{E}, \frac{\mathrm{v}}{R}\frac{\eta}{E}, t\frac{E}{\eta}\right) \tag{5.3}$$

in the case of creep, and

$$\frac{\overline{\sigma}_R}{\sigma_0} = f\left(\frac{E}{\sigma_0}\frac{\Delta R}{R}, \nu, \frac{f_c}{\sigma_0}, \phi, \psi, \frac{L}{R}, \frac{K_s R}{E}, \frac{K_l R}{E}, \frac{p_0}{\sigma_0}, \frac{R_p}{R}, \frac{\mathrm{v}}{R}\frac{\gamma_w R^2}{kE}, t\frac{kE}{\gamma_w R^2}\right) \tag{5.4}$$

in the case of consolidation, where L is the shield length, ΔR the radial overcut around the shield, K_s and K_l the radial stiffnesses of the shield and lining, respectively, v the average advance rate of the TBM during regular operation, and t the standstill duration (Chapter 4).

Due to technical limitations, the TBM parameters (overcut ΔR, shield length L and shield and lining stiffnesses K_s and K_l) that can be materialised in practice vary within a specific range independently of the tunnel diameter, while the advance rate v decreases with increasing diameter. Consequently, the nondimensional parameters $E\Delta R/(\sigma_0 R)$, L/R, $K_s R/E$, $K_l R/E$, $(\mathrm{v}\eta)/(ER)$ and $(\mathrm{v}\,\gamma_w R^2)/(kE)$ in general cannot take the same values for different diameter tunnels, which gives rise to a scale effect with respect to the risk of shield jamming (Ramoni and Anagnostou, 2011b). The strength and stiffness of the ground may also tentatively decrease with increasing representative volume, and thus tunnel diameter; however, as squeezing ground is often weak even at the small scale of a specimen, the differences with respect to ground parameters in the large scale, between two tunnels of different diameter, are secondary in relation to the above and will be neglected.

Assessing the scale effect qualitatively is cumbersome even in the case of time-independent ground behaviour, since many TBM parameters have mutually competing effects on the rock pressure. Note, for example, that with increasing tunnel diameter both the normalised shield length L/R and the normalised overcut $\Delta R/R$ decrease (Ramoni and Anagnostou, 2010b), however the former is favourable concerning the risk of shield jamming, while the latter is unfavourable (see also Ramoni and Anagnostou, 2011b). The problem becomes even more complex in the case of time-dependent ground behaviour due to creep or consolidation, where the additional influence of the advance rate v and the standstill duration t must be considered. Therefore, resorting to numerical simulations is necessitated.

The section starts with some basic theoretical considerations concerning the influence of the advance rate v and the standstill duration t on the rock pressure in Sections 5.2.2.1 and 5.2.2.2, based upon simplified and realistic assumptions, respectively (the influence of the other TBM

parameters is discussed in Ramoni and Anagnostou, 2010b). Subsequently, it proceeds with investigating numerically the scale effect, based on exemplary computations with realistic specifications for all parameters; first, for the case of time-independent ground behaviour (Section 5.2.2.3), where relevant is only the influence of the TBM parameters, and then for the case of time-dependent behaviour due to creep or consolidation, considering the operational stages during TBM advance (Section 5.2.2.4) and restart after a standstill (Section 5.2.2.5).

5.2.2.1   Simplified theoretical analysis

The influence of the last two parameters in Eqs. (5.3) and (5.4) on the rock pressure is analysed considering an idealised situation where all other ground and TBM parameters are fixed regardless of R.

First, the conditions during restart after a standstill are examined. The rock pressure in this case depends not only on the standstill duration (last term) but also the advance rate (penultimate term), as rock pressure may already develop during the advance phase (Chapter 2). To isolate the influence of the last term, a case where the excavation occurs rapidly (v η or v/$k \rightarrow \infty$) is assumed, where the penultimate term is infinite regardless of R. In this case the last term is identical to the time parameter in the plane strain problem (last term in Eqs. 5.1, 5.2), hence the time development of the rock pressure will be analogous to that of tunnel contraction in Section 5.2.1.1: in the case of creep the pressure develops at a rate that is independent of R, while in the case of consolidation the pressure develops at a rate inversely proportional to R^2, and thus slower in a larger diameter tunnel (effect equivalent to lower permeability).

Next, the conditions during advance are examined. The rock pressure in this case depends only on the penultimate term (last term is irrelevant). In the case of creep R appears in the denominator, which means that for a given v the advance will occur slower in a larger diameter tunnel (equivalent effect to lower viscosity), and hence a higher rock pressure will develop (alternatively, to achieve a given rock pressure the advance rate must be higher in the larger diameter tunnel). In the case of consolidation, R appears in the numerator and the effect is exactly the opposite.

At this point it is important to note that, in order to compare the rock pressure in different diameter tunnels, v alone is not the most suitable measure of the rate of advance. Specifically, when the shield reaches any given tunnel cross-section, it remains exposed to pressure at that section for as long as it is required for its entire length L to pass through it; therefore, the shield pressure ultimately depends on the time required for the TBM to advance by one shield length, that is L/v ($= (L/R) / (v/R))$, which is only a function of v/R since L/R is considered as being fixed. The ratio v/R, which expresses how fast the TBM excavates the length of one radius R, is thus a more suitable measure to compare the rate of advance in different diameter tunnels – a fixed v/R means that the TBM takes the same time to advance by one shield length L regardless of R. For a given v/R, in the case of creep the normalised advance rate (v/R).(η/E) is constant, which means that the pressure develops at the same rate regardless of R; in the case of consolidation the normalised advance rate can be expressed as (v/R) ($\gamma_w R^2$)/(kE) and is proportional to R^2, which means that

the pressure develops at a rate inversely proportional to R^2, and thus slower in a larger diameter tunnel. The effect of the tunnel diameter is thus the same here as in the case of the standstill examined previously.

Conclusively, both during advance and for restart after a standstill of the TBM, in the case of creep there will be no scale effect for tunnels excavated at the same rate v/R, while in the case of consolidation the well-known dependency of consolidation time on the square of the characteristic length – here R – holds.

5.2.2.2   Theoretical analysis under realistic assumptions concerning the advance rate

The assumption adopted in the preceding section that v/R can be the same for the two tunnels (*i.e.* v is proportional to R) is purely theoretical, since in practice it is well-known that the larger the boring diameter the slower the TBM advances, *i.e.* v decreases with increasing R. In fact, v can be assumed inversely proportional to R, as in Ramoni and Anagnostou (2011b), which then makes v/R inversely proportional to R^2. This is explained hereafter.

The operations during mechanised excavation with a TBM can be idealised as a "stop-and-go" process, where intervals of continuous TBM propulsion (ΔT_1) over the length of one prefabricated segmental lining ring (L_T) regularly alternate with intervals where the TBM remains at standstill (ΔT_2) for the installation of the corresponding ring. The net advance rate of the TBM during the continuous propulsion intervals can be expressed as $v_N = L_T /\Delta T_1$, while the average advance rate over the entire "stop-and-go" process adopted in the present chapter (Eqs. 5.3, 5.4) can be expressed as v = $L_T/(\Delta T_1 + \Delta T_2)$ (Chapter 2). The net advance rate is defined as v_N = ROP*RPM, where ROP is the rate of penetration and RPM the number of rotations of the TBM cutterhead per minute (or, more generally, per unit time). It is reasonable to assume that ROP is the same for tunnels under identical ground conditions (strictly speaking, this is valid as long as the installed thrust force is higher in the larger TBM, as is common in practice). It is also reasonable to assume that RPM is inversely proportional to R, considering that an upper limit of 150-200 m/min is imposed on the linear velocity of the gauge cutters to avoid overheating, irrespective of the TBM diameter (Rispoli et al., 2020; Hamburger and Weber, 1992). Under these assumptions, v_N can be considered inversely proportional to R. Assuming that the prefabricated lining rings have the same length L_T irrespective of R, ΔT_1 can be considered proportional to R. Based on this, it is also reasonable to consider ΔT_2 to be proportional to R (*cf.*, among others, Tahernia & Rostami, 2021; Farokh, 2013, 2020), which then makes v inversely proportional to R, as is v_N.

Under the realistic assumption of inverse proportionality between v and R, the situation differs from the simplified one discussed in Section 5.2.2.1: in the case of creep the normalised advance rate (v/R)·(η/E) becomes inversely proportional to R^2, which means that the pressure develops faster in a larger tunnel (effect equivalent to lower viscosity); in the case of consolidation the normalised advance rate (v/R) ($\gamma_w R^2$)/(kE) becomes independent of R, hence the shield pressure develops at the same rate in both tunnels (the favourable effect of a faster advance in the case of a smaller diameter tunnel outweighs the unfavourable effect of faster developing convergences).

The assumption concerning the advance rate does not influence the conditions during a standstill preceded by a rapid advance (v η or v/k → ∞), and the conclusions of Section 5.2.2.1 for this case remain valid. Even so, considering that the tunnel diameter influences each stage differently, the scale effect becomes cumbersome to assess qualitatively for general cases of a standstill preceded by an excavation at a normal advance rate, hence a numerical investigation is necessitated. This is conducted in Sections 5.2.2.4 and 5.2.2.5, based on an example that considers practically relevant parameters; before this, however, the case of time-independent ground behaviour is examined in Section 5.2.2.3, which offers a better understanding of the influence of the TBM parameters isolated from that of the advance rate and standstill time.

5.2.2.3   Time-independent ground behaviour

The theoretical analysis of the previous sections assumed that the first 8 dimensionless parameters on the r.h.s. of Equations (5.3) and (5.4) do not depend on the tunnel radius, when in fact these in general cannot take the same values for a large and a small tunnel, thereby introducing a scale-effect even without time-dependent ground behaviour.

The scale effect related to the TBM parameters is assessed herein by comparing two tunnels with diameters of 12 m and 4 m excavated under identical ground conditions, disregarding creep and consolidation (the scale effect in the case of time-dependent ground behaviour will be analysed in the next two sections). For the numerical simulations, the computational model of the advancing tunnel heading introduced in Section 4.2 of Chapter 4 is employed. The assumed parameter values are given in Table 5.2. The common overcut $\Delta R = 5$ cm and shield length $L = 10$ m adopted for both tunnels are realistic, considering that the corresponding normalised values $(\Delta R/R, L/R)$ (= (2.5%, 5) and (0.8%, 1.7) for $D = 4$ m and 12 m, respectively) are typical (*cf.* Fig. 6 in Ramoni and Anagnostou, 2010b). The thicknesses d_s of the shield and d_l of the lining are assumed proportional to the radius R, which is reasonable and makes the normalised radial stiffnesses $K_s R/E = (E_s/E) d_s/R$ and $K_l R/E = (E_l/E) d_l/R$ identical for the two tunnels, and dependent only on the Young's moduli E_s, E_c and E of steel, concrete and the ground, respectively.

When evaluating potential scale-effects with respect to the risk of shield jamming, it is not sufficient to consider only the shield loading or the required thrust force F_r (which depend on the parameters in Eqs. 5.3 and 5.4), but also the installed or installable thrust force F_i. The latter increases with the tunnel diameter, which also introduces a scale-effect to be considered. The comparison between the two tunnels is thus based on the ratio F_r /F_i, which expresses the percentage of the F_i utilised by F_r and will be hereafter referred to as thrust utilisation factor (TUF). The required thrust force F_r is computed as $\mu\ 2\pi R\ L\ \mu\ \overline{\sigma}R$, where μ denotes the static friction coefficient; this expression holds for the conditions during TBM restart, which is the relevant operational stage in most cases (see Ramoni and Anagnostou, 2010b). The installed TBM thrust force is assumed to increase proportionally to the cross-section area, and thus to R^2, according to the expression $F_i = 5\ R^2$ MN/m^2, which provides values in the high end of the range of technical data collected from various TBMs (cf. Fig. 7 in Ramoni and Anagnostou 2010b; Ates *et al*. 2014).

Table 5.2   Parameters adopted in the numerical investigations into the effect of tunnel diameter on
              thrust force utilisation (Section 5.2)

Ground

Young's Modulus, E	[GPa]	1
Poisson's ratio, v	[-]	0.25
Uniaxial compressive strength, f_c	[MPa]	var.
Angle of internal friction, ϕ	[°]	25
Dilatancy angle, ψ	[°]	5
Depth of cover, H	[m]	400
In-situ stress at tunnel axis, σ_0	[MPa]	10
Water table level above tunnel axis, H_w	[m]	100
Permeability, k	[m/s]	var.
Viscosity, η	[MPa·d]	var.

TBM

Boring Diameter, D	[m]	4 or 12
Radial overcut, ΔR	[cm]	5
Shield length, L	[m]	10
Radial shield stiffness, K_s	[MPa/m]	875 (D = 12m)
		2625 (D = 4m)
Shield thickness, d_s	[m]	0.15 (D = 12m)
		0.05 (D = 4m)
Young's modulus of steel, E_s	[GPa]	210
Average Advance rate, v	[m/d]	30 (D = 12m)
		90 (D = 4m)
Shield skin friction coefficient, μ	[-]	0.15

Lining

Young's modulus of concrete, E_c	[GPa]	30
Lining thickness, d_l	[cm]	0.75 (D = 12m)
		0.25 (D = 4m)
Radial lining stiffness, K_l	[MPa/m]	625 (D = 12m)
		1875 (D = 4m)

Model

Round length, s	[m]	0.5
Far-field radius of the computational domain, R_σ	[m]	400
Far-field radius of the seepage flow domain, R_p	[m]	100

Figure 5.3 shows the thrust utilisation factors of the two tunnels as functions of the rock quality, expressed by its uniaxial compressive strength f_c. The intuitive perception that the smaller diameter tunnel is less vulnerable than the larger diameter tunnel is unconditionally true for other potential hazards (*e.g.*, an instability of the tunnel face) but not for the risk of shield jamming, where it is true only in better quality ground ($f_c > 3.2$ MPa in the example of Fig. 5.3). The opposite holds in weaker ground and, interestingly enough, this has been shown to be generally true for any two tunnels with different radii, by means of a more extensive parametric study considering a wide range of practically relevant *in-situ* stresses, boring radii, ground and TBM parameters (Appendix E). For the parameters adopted herein, the TUF in the larger diameter tunnel is less sensitive to variations of rock quality (expressed by f_c) than in the smaller diameter tunnel, and also consistently lower than unity, indicating that its excavation is feasible irrespective of the ground conditions, whereas the small tunnel excavation is only feasible in better quality ground with $f_c > ca.$ 2.7 MPa.

The TUFs are equal for $f_c = ca.$ 3.2 MPa, which means that the competing effects of the TBM parameters outweigh one other. This situation is thus suitable for investigating the scale effect that results purely from the time-dependency of the ground behaviour due to creep or consolidation in the next sections.
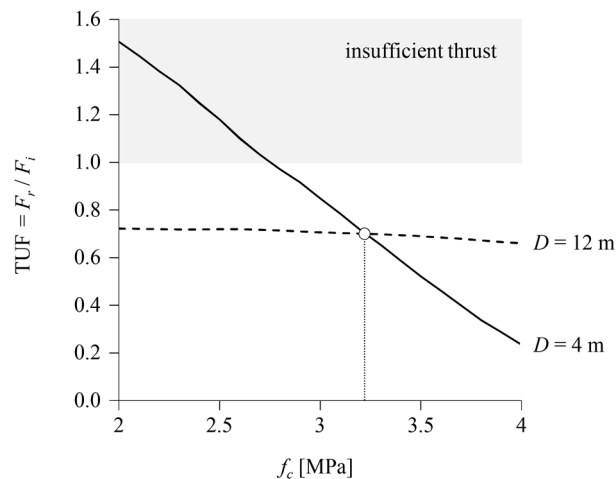

Figure 5.3.   Scale effect in the absence of time-dependency (no creep, no consolidation): Thrust force required to overcome shield skin friction, normalised by the installed thrust force ("thrust utilization factor", TUF), as a function of the uniaxial compressive strength of the ground f_c for a 12 m diameter tunnel and for a 4 m diameter tunnel (parameters: Table 5.2)

5.2.2.4   Time-dependent ground behaviour – TBM advance

The scale effect during TBM advance in the case of creep and consolidation is examined under the same assumptions as in the previous section (Table 5.2), setting f_c = 3.2 MPa to eliminate the influence of the TBM parameters. Based upon Section 5.2.2.2, advance rates of 90 and 30 m/day (average values during the stop-and-go operation) are considered for the 4 m and for the 12 m diameter tunnel, respectively.

Figure 5.4 shows the thrust utilisation factor as a function of the viscosity (creep case, red lines) and of the permeability (consolidation case, blue lines) for the smaller diameter (solid lines) and for the larger diameter (dashed lines). With the exception of high viscosities or low permeabilities, a scale effect clearly exists with respect to the risk of shield jamming (expressed by the TUF) both in creep and consolidation: an increase in diameter results in a higher utilisation of the thrust force (the red dashed line is above the red solid line and the blue dashed line is above the blue solid line), which means that due to the time-dependency, the situation is more favourable for the smaller diameter. This is consistent with the results of the last section shown in Figure 5.4: time-dependency delays squeezing, the rock responds to tunnel excavation as if it were of a higher quality, and the last section showed that an increase in rock quality renders a smaller diameter more favourable.
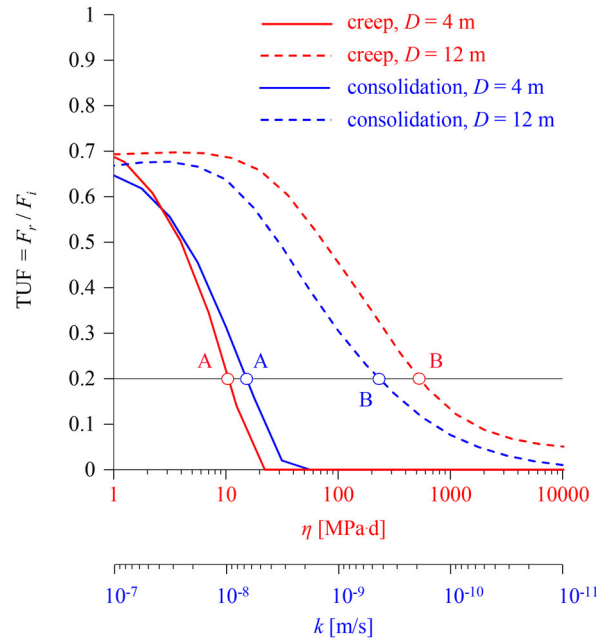

Figure 5.4.   Scale effect in the case of time-dependent ground behaviour: Thrust force required to overcome shield skin friction during TBM advance, normalised by the installed thrust force ("thrust utilisation factor", TUF), as a function of the viscosity η in the case of creep and of the permeability k in the case of consolidation (f_c = 3.2 MPa; other parameters: Table 5.2)

The scale effect is negligible if the viscosity is sufficiently high or the permeability sufficiently low. In this case the convergences around the advancing shield area are nonetheless small regardless of the tunnel diameter, as the rock behaviour is practically elastic (creep case) or undrained (consolidation case).

The vertical distance of the two red lines reflects the scale effect in the case of creep. As it is slightly bigger than the vertical distance of the two blue lines, the scale effect is slightly more pronounced in the case of creep than in the case of consolidation.

In the example of Figure 5.4, TUF < 1 over the entire viscosity and permeability ranges, which means that the thrust force would be sufficient also for the larger diameter tunnel, both in the case of creep and in the case of consolidation. Nevertheless, the assumed values of the installed thrust forces ($F_i = 5\ R^2$ MN/m^2) are very high for rock TBMs (20 MN for a 4 m diameter tunnel and 180 MN for a 12 m diameter tunnel). With a moderate assumption (*e.g.* $F_i = 3\ R^2$ MN/m^2, which gives 12 and 108 MN for the 4 m and 12 m diameter tunnels, respectively), the larger TBM might experience jamming, while the smaller TBM would still be safe; this would happen in the range of $\eta =$ ca. 10–100 MPa·d and $k = 10^{-8} - 10^{-9}$ m/s.

The scale effect can be demonstrated also in another way. Assume that the 4 m diameter tunnel was constructed first (a pilot tunnel) and that the force actually applied was equal to 20% of the installed one (TUF = 0.2). Assuming that the strength and stiffness parameters of the rock are known and correspond to the ones underlying Figure 5.4, the observed (rather low) required thrust force could be explained on the basis of the convergence delay due to creep or to consolidation (points A in Fig. 5.4). What could one expect for the main, larger diameter tunnel? In order for the thrust utilisation factor to remain the same, the viscosity η would have to be higher by a factor of about 50 in the case of creep (red point B vs. red point A), while in the case of consolidation the permeability k would have to be lower by a factor of about 20 (blue point B vs. blue point A). Alternatively, for the given η and k (as in points A), the advance rate in the main tunnel would have to be about 50 (creep) or 20 (consolidation) times higher than assumed (note the dimensionless expressions in Eqs. 5.3 and 5.4), which is of course impossible. These theoretical results provide another view of the scale effect in the case of creep and consolidation.

5.2.2.5   Time-dependent ground behaviour – Standstill

The same conclusions can essentially be drawn for the thrust force needed for restart after a standstill. Figure 5.5 shows the TUF as a function of the standstill duration. The computations have been performed considering the same parameters as before (Table 5.2), as well as a high viscosity (η = 10,000 MPa·d) and low permeability (k = 10^{-10} m/s), which ensure that the behaviour during advance is elastic (in the case of creep) or undrained (in the case of consolidation) and hence relevant shield loading develops only during the standstill (*cf.* TUFs in Fig. 5.4 for η = 10,000 MPa·d and k = 10^{-10} m/s). This enables examining the isolated influence of the standstill duration t.

The distances between the dashed and solid lines in Figure 5.5 clearly indicate the existence of a scale effect with respect to the TUF. The width of the band that is defined by the two red lines reflects the effect of tunnel radius in the case of creep. As this band is wider than the band that is defined by the two blue lines (consolidation), one may say that the scale-effect is more pronounced in the case of creep.
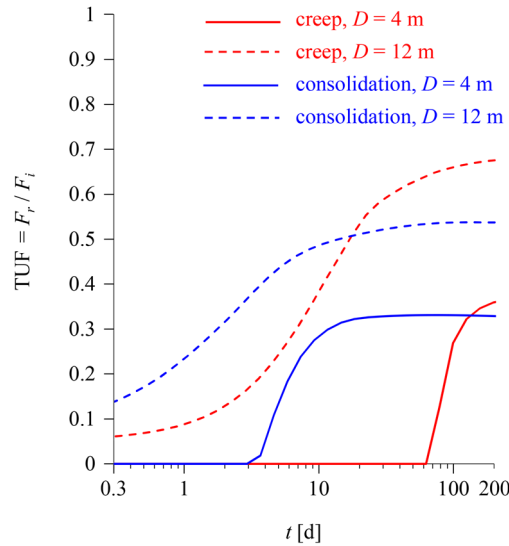

Figure 5.5.   Scale effect in the case of time-dependent ground behaviour: Thrust force required for TBM restart after a standstill, normalised by the installed thrust force ("thrust utilisation factor", TUF), as a function of the standstill duration t (f_c = 3.2 MPa; η = 10^4 MPa·d, k = 10^{-10} m/s; other parameters: Table 5.2)

5.3   Interaction

The hypothesis that interaction is significant in the case of consolidation but negligible in the case of creep (Section 5.1) is tested herein, considering the problem of shield jamming in a twin tunnel (Fig. 5.6) and comparing the thrust forces required to overcome shield skin friction during construction of its two tubes (Tunnels 1, 2). The construction of Tunnel 2 is assumed to take place long after the completion of Tunnel 1, such that steady state conditions have been re-established when it passes through any cross-section A-A (Fig. 5.6). The adopted parameters are given in Table 5.3.

To validate the hypothesis made, it is sufficient to consider and compare only two limit cases: the case of minimum interaction in consolidation *vs.* the case of maximum interaction in creep.

In the case of consolidation, the effect of Tunnel 1 on Tunnel 2 is first due to the stress redistribution associated with the deformations of the ground ahead of the advancing face and around the TBM shield, and, second, the long-term large-scale pore pressure relief and increase in the undrained shear strength (Section 5.1). This effect is minimum when the excavation-induced deformations are as small as possible, which is the case when the ground permeability is very low and its response to excavation is practically undrained.

In the case of creep, the effect of Tunnel 1 on Tunnel 2 is solely due to the aforementioned stress redistribution, as rheological processes are of purely mechanical nature. This effect is maximum if the deformations of the ground ahead of the advancing face and around the shield of Tunnel 1 are as large as possible, which is the case when the advance is very slow and all viscoplastic deformations due to creep occur practically simultaneously with the progress of the excavation (practically time-independent response with instantaneous manifestation of squeezing).
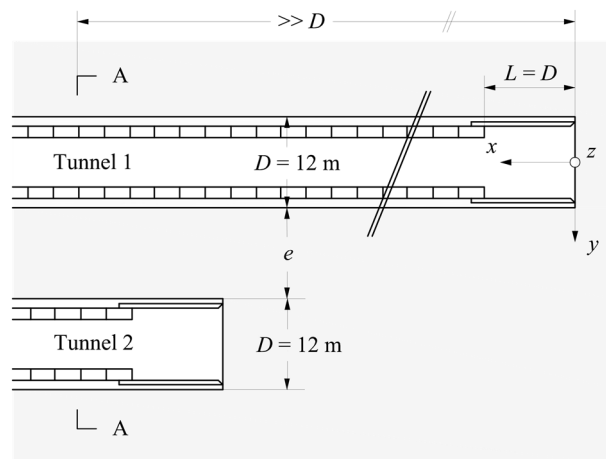

Figure 5.6.   Interaction problem: (geotechnical situation during the advance of the second tunnel, long after construction of the first tunnel (plan view *x-y*)

Table 5.3.   Parameters adopted in the numerical analyses for the interaction problem (Section 5.3)

Ground

Young's Modulus, E	[GPa]	1
Poisson's ratio, v	[-]	0.25
Uniaxial compressive strength, f_c	[MPa]	2
Angle of internal friction, ϕ	[°]	25
Dilatancy angle, ψ	[°]	5
Depth of cover, H	[m]	400[a]
In-situ stress at tunnel axis, σ_0	[MPa]	10[a]
Water table level above tunnel axis, H_w	[m]	400
Viscosity, η	[MPa·d]	10^{-5}
Permeability, k	[m/s]	10^{-11}

TBM

Boring Diameter, D	[m]	12
Radial overcut, ΔR	[cm]	5[a]
Shield length, L	[m]	12
Radial shield stiffness, K_s	[MPa/m]	875
Shield thickness, d_s	[m]	0.15
Young's modulus of steel E_s	[GPa]	210
Average advance rate, v	[m/d]	30
Shield skin friction coefficient, μ	[-]	0.15

Lining

Young's modulus of concrete, E_c	[GPa]	30
Lining thickness d_l	[cm]	0.75
Radial lining stiffness, K_l	[MPa/m]	625

Model

Round length, s	[m]	1.0
Far-field radius of the computational domain, R_σ	[m]	400
Far- field radius of the seepage flow domain, R_p	[m]	400

[a]   For the case of creep, one additional computation was performed assuming $H = 1600$ m, $\sigma_0 = 40$ MPa and $\Delta R = 15$ cm

Based on the above, consideration is given in the sequel to the cases of a water-bearing ground of extremely low permeability that exhibits an undrained response during shield advance ("consolidation case"), and an extremely slow excavation through a non-water-bearing ground ("creep case").

Instead of resorting to more complex, 3D, transient numerical simulations, the problem will be analysed in a simplified manner using sequentially two models: (i) an axisymmetric model of the advancing tunnel heading, which simulates the TBM advance and lining installation step-by-step (Fig. 4.1b of the previous chapter and computational assumptions discussed in Section 4.2.3 of the previous chapter) and, (ii), a plane-strain, twin tunnel model of a cross-section A-A (*cf.* Fig. 5.6) far behind the face of both tubes (Fig. 5.7). To facilitate the connection of the input and output parameters of the models, adequate and well-founded assumptions are adopted. Both models have been developed in Abaqus® (Dassault Systèmes, 2018).

The consolidation case will be examined first. Initially, the short-term shield-lining-ground interaction in Tunnel 1 will be analysed, and the thrust force required to overcome shield skin friction will be determined, using the axisymmetric model (Fig. 4.1b of the previous chapter) This model will be used for the calculation of the required thrust force in Tunnel 2 as well, although it will consider different initial conditions that reflect the stress-redistribution, pore pressure relief and ground consolidation induced by Tunnel 1. The alteration of the initial stress and pore

pressure fields will be quantified using the plane-strain model (Fig. 5.7). The latter will be used also to show that it is adequate to consider uniform and isotropic initial stress and pore pressure fields for simulating the construction of Tunnel 2, thereby verifying also the adequacy of the axisymmetric model (Fig. 4.1b of the previous chapter) for this purpose. Based on these analyses, it will be shown that the required thrust force in Tunnel 2 is significantly lower than in Tunnel 1, even if the tunnel spacing is as large as ten diameters.

The analysis for the creep case essentially follows the same approach and will show that the interaction is negligible for tunnel spacings for which it is substantial in the consolidation case. This is because the construction of Tunnel 1 has a negligible effect on the stresses in the location of Tunnel 2, which will be shown to be true even under extreme squeezing conditions and even considering an unusually large annular gap around the shield.
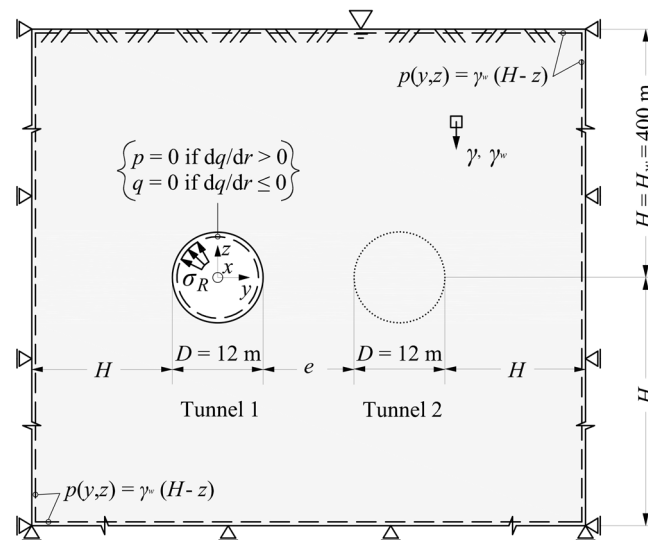

Figure 5.7.   Interaction problem: plane-strain model (cross section A-A of Fig. 5.6) in the computational stage that simulates the excavation of the first tunnel

5.3.1   Results for the consolidation case

Figure 5.8 shows the longitudinal distribution of the rock pressure that develops in the short-term upon the shield and the lining of Tunnel 1, along with the corresponding equilibrium point of the rock (2.3 MPa, 0.10 m), as determined using the axisymmetric model (Fig. 4.1b of the previous chapter).

The excavation of Tunnel 1 is also simulated as an undrained plane-strain problem using the plane strain model (Fig. 5.7), by instantaneously reducing the tractions along the Tunnel 1 boundary from the *in-situ* values. Figure 5.9 shows the numerically computed change in diameter horizontally and vertically ($\Delta D_{h,v}$) as a function of the deconfinement factor λ (Panet, 1995), along with the equilibrium point resulting from the axisymmetric analysis of Figure 5.8 (2.3 MPa, 0.10 m; point A in Fig. 5.9). The small deviation of the actual equilibrium point from the plane strain curve is due to the different stress paths (Cantieni and Anagnostou 2009). As it is impossible to exactly reproduce both the displacement and the rock pressure with the plane strain model, a simplified assumption has to be made to determine the conditions prevailing in the short-term, immediately after excavation of Tunnel 1, considering unloading either down to point B_1 or to point B_2. Here, point B_2 is considered.
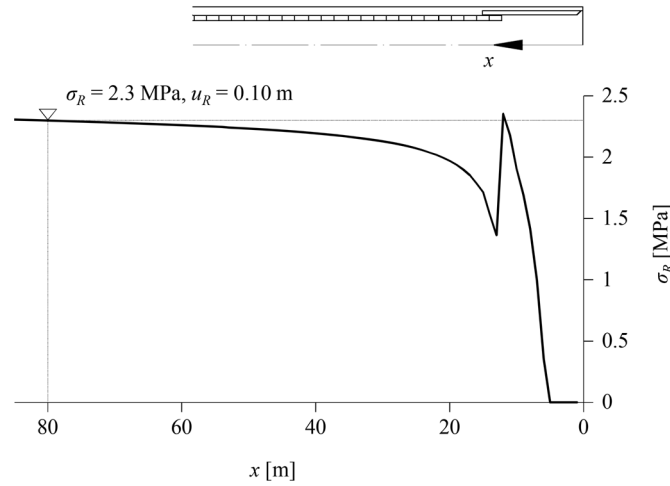

Figure 5.8.   Interaction problem, consolidation case: Radial rock pressure distribution along the shield and lining of Tunnel 1 during rapid excavation ($\sigma_0 = 10$ MPa, $p_0 = 4$ MPa, other parameters: Table 5.3)

Starting from the state at point B_2, beam elements representing the Tunnel 1 lining are activated in the plane-strain model, the boundary is completely unloaded, and a transient consolidation analysis is performed to determine the steady state prevailing long after the construction of Tunnel 1 and before construction of Tunnel 2. Figure 5.10 shows the pore pressure, effective stress, and total stress distributions along the horizontal y-axis, which allow drawing the following conclusions: The drainage action of Tunnel 1 is evident in an extended zone; the pore pressure relief is significant, even at long distances from Tunnel 1 (note the decrease to 50% at a distance of 50 m). The total stresses decrease in general only slightly, except for the immediate vicinity of Tunnel 1 where the ground yields plastically (left of point P in Fig. 5.10). Due to the combination of the above, the effective stresses increase, which – as explained in the Introduction of the present chapter – is expected to have a favourable effect, since it increases the undrained shear strength. The stress-fields are neither uniform nor hydrostatic, which raises the question of whether an axisymmetric model (Fig. 4.1b of the previous chapter) is adequate for simulating the Tunnel 2 excavation.
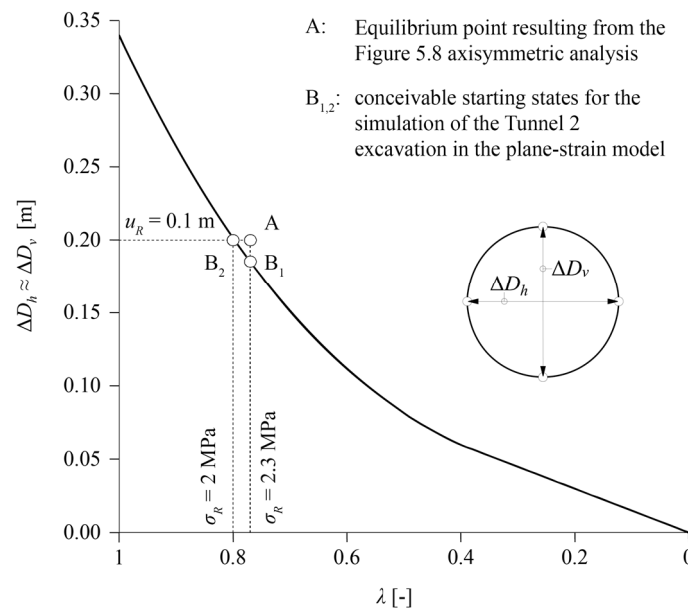

Figure 5.9.   Interaction problem, consolidation case: Relationship between change in diameter $\Delta D_{h,v}$ and deconfinement factor λ, resulting from the simulation of the Tunnel 1 excavation as a plane-strain, undrained cavity unloading problem ($\sigma_0 = 10$ MPa, $p_0 = 4$ MPa, other parameters: Table 5.3)
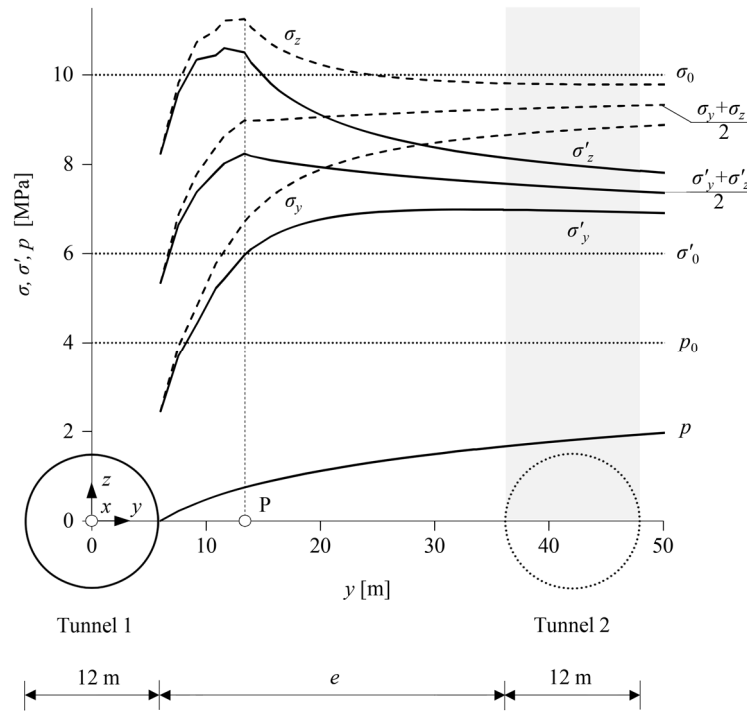
Figure 5.10.   Interaction problem, consolidation case: Stress- and pore pressure distribution along the *y*-axis, long after construction of Tunnel 1 (steady state) but before construction of Tunnel 2, resulting from the Tunnel 1 simulation as a plane-strain problem (σ_0 = 10 MPa, p_0 = 4 MPa, other parameters: Table 5.3)

In order to check the applicability of such a model, an additional computational step with the plane strain model (Fig. 5.7) is performed: starting from the state of Fig. 5.10, the excavation of Tunnel 2 is simulated as an undrained cavity unloading problem. The black lines in Figure 5.11a show the numerically computed change in diameter horizontally and vertically ($\Delta D_{h,v}$) as a function of the deconfinement factor λ for a tunnel spacing of e = 2.5D. The two lines almost coincide, which shows that the response nearly obeys rotational symmetry in spite of the non-uniformity and anisotropy of the stress field prevailing before the Tunnel 2 excavation. The red line is the ground response curve (GRC; computed after Anagnostou and Kovári 1993) in the case of uniform and isotropic initial pore pressure and stress fields with magnitude equal to that prevailing at the centre of Tunnel 2 just before its excavation. The high level of concordance with the numerical response curves justifies the use of the axisymmetric model of Figure 4.1b of the previous chapter (with the same initial values as the red curve) to determine the thrust force for Tunnel 2. (Of course, the adequacy of this simplification would be questionable for smaller spacings between the tunnels, where the differences among the aforementioned curves increase; Fig. 5.11b.)

The use of the axisymmetric model (Fig. 4.1b of the previous chapter), with the initial conditions described above, provides the rock pressure distribution along the shield and finally the thrust force required to overcome shield skin friction. Figure 5.12 shows the rock pressure distribution in Tunnel 1 (according to Fig. 5.8) as well as in Tunnel 2 for various spacings e. The comparison of the rock pressure in the two tunnels reflects the very favourable effect of the drainage-induced consolidation in the vicinity of Tunnel 2. This is also reflected in the pronouncedly reduced thrust force of Tunnel 2 compared to Tunnel 1, as shown in Figure 5.13; it is remarkable that the Tunnel 2 thrust force is about 50% less even if the spacing of the tunnels is as wide as 5 diameters.

Figure 5.11. Interaction problem, consolidation case: Relationship between convergence $\Delta D_{h,v}$ and deconfinement factor λ, resulting from the simulation of the Tunnel 2 excavation as a plane-strain undrained cavity unloading problem for, (a), $e/D = 2.5$ or, (b), $e/D = 1$ ($\sigma_0 = 10$ MPa, $p_0 = 4$ MPa, other parameters: Table 5.3)
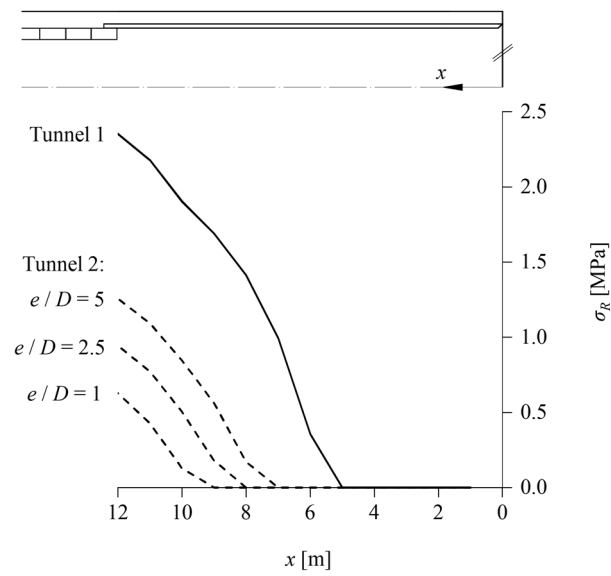
Figure 5.12. Interaction problem, consolidation case: Radial rock pressure distribution along the shield of Tunnel 1 and Tunnel 2 during rapid excavation according to axisymmetric computations with homogeneous and isotropic initial stress and pore pressure fields considering for Tunnel 1 the *in-situ* stress and pore pressure field and for Tunnel 2 the values prevailing at the center of Tunnel 2 according to the results (Fig. 5.10) of the plane-strain analysis of the Tunnel 1 (parameters: Table 5.3)

Figure 5.13. Interaction problem, consolidation case: Required thrust force as a function of the distance between the tunnels (parameters: Table 5.3)

5.3.2   Results for the creep case

Same as in the consolidation case, the computations start with the axisymmetric analysis of Tunnel 1, which provides the longitudinal stress distributions on the shield and lining, as well as and the equilibrium point of the rock. This is shown in Figure 5.14 for the reference case ($\sigma_0 = 10$ MPa and $\Delta R = 0.05$ m; black lines), as well as for an extreme squeezing case with large overcut ($\sigma_0 = 40$ MPa and $\Delta R = 0.15$ m; red lines); the latter is considered to demonstrate later that the effect of Tunnel 1 on Tunnel 2 is negligible even under such extremely unfavourable conditions.

Figure 5.15 shows, analogously to Figure 5.9, the results of the simulation of the Tunnel 1 excavation with the plane-strain model (Fig. 5.7), along with the equilibrium points resulting from the axisymmetric analysis (points A). The deviations of the equilibrium points from the respective plane-strain curves are due to the stress-path dependency of the ground response, as mentioned above, and are expectedly greater in this case than in Figure 5.9, due to the more pronounced ground plastification. The Tunnel 1 excavation is again simulated considering an unloading of its boundary down to point B_2 followed by an installation of the lining.

As the response is effectively time-independent in this case, the stresses at the state corresponding to point B_2 are also those prevailing prior to excavation of Tunnel 2. Figure 5.16 shows the stress distributions along the horizontal y-axis. Again, a significant drop in the stresses can be observed only inside the plastic zone, which is limited – even in the extreme squeezing and large overcut case – to the close vicinity of Tunnel 1 (left of the points P_1 and P_2 in Fig. 5.16). As is well-known (Kirsch 1898), outside the plastic zone the mean stress remains constant and equal to the *in-situ* stress σ_0, while the anisotropy of the stress field decreases with increasing distance from Tunnel 1. This non-uniform, anisotropic stress state is the initial state to be considered in the analysis of the Tunnel 2 excavation.

The adequacy of an axisymmetric model (Fig. 4.1b of the previous chapter) for this purpose is assessed again by simulating the Tunnel 2 cavity unloading using the plane-strain model (Fig. 5.7). Figure 5.17a shows the numerically computed changes in diameter horizontally and vertically ($\Delta D_{h,v}$) as a function of the deconfinement factor λ (black lines), as well as the analytically determined GRC (red lines); the latter assumes rotational symmetry and considers the average stress at the Tunnel 2 centre as initial condition, which is the *in-situ* stress σ_0. The numerically computed curves and the GRC almost coincide, which means that the cavity response is practically rotationally symmetric in spite of the anisotropy and non-uniformity of the stress field. Therefore, the thrust force of Tunnel 2 can be computed with the axisymmetric model (Fig. 4.1b of the previous chapter); as the initial stress to be considered is equal to the *in-situ* stress, the Tunnel 2 thrust force is equal to that of Tunnel 1.

In conclusion, the construction of Tunnel 1 does not have a relevant effect on the Tunnel 2 thrust force for the considered spacing of $e = 2.5\ D$, and this lack of relevant interaction can be observed also in the extreme squeezing and large overcut case (Fig. 5.17b). The difference to the consolidation case is remarkable – at a spacing of $2.5\ D$ or even greater, the interaction in the consolidation case leads to a reduction of the Tunnel 2 thrust force by $40 – 80\%$ (Fig. 5.13).
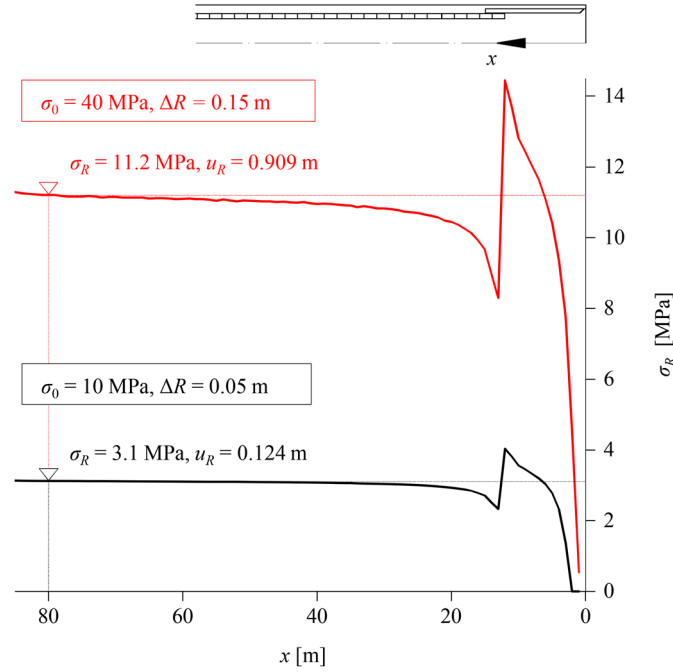
Figure 5.14. Interaction problem, creep case: Radial rock pressure distribution along the shield and lining of Tunnel 1 during extremely slow excavation, allowing steady state to be reached practically simultaneously with the advance of the TBM (parameters: Table 5.3)
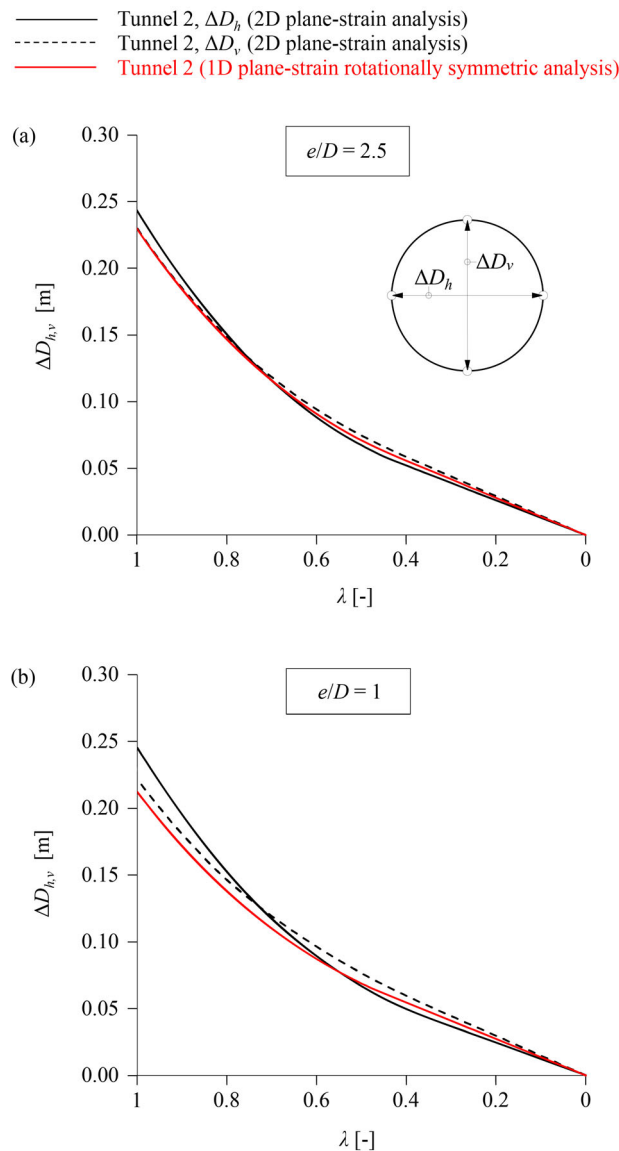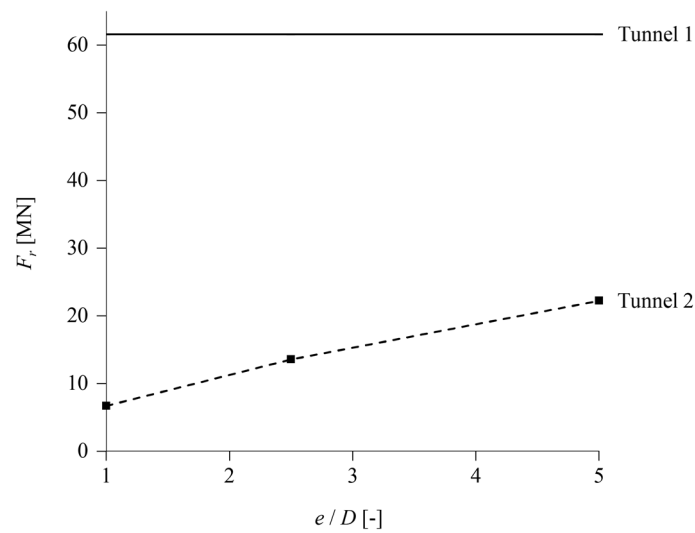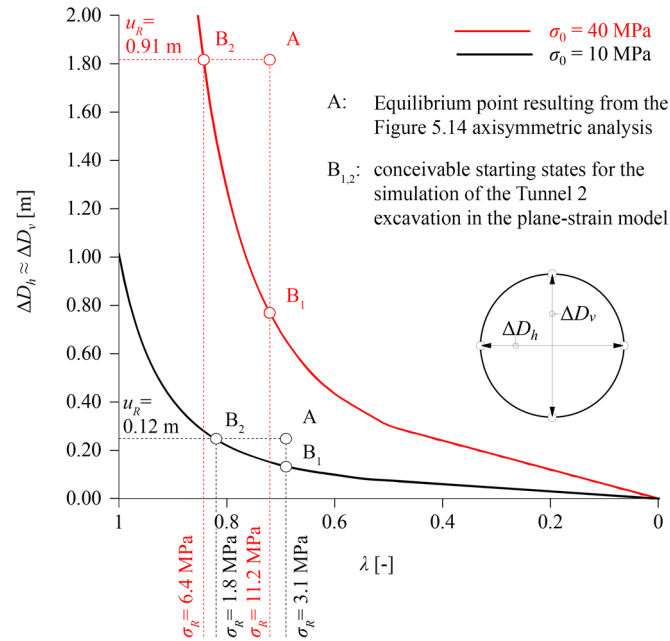

Figure 5.15. Interaction problem, creep case: Relationship between convergence $\Delta D_{h,v}$ and deconfinement factor λ, resulting from the simulation of the Tunnel 1 excavation as a plane-strain, time-independent cavity unloading problem (parameters: Table 5.3)
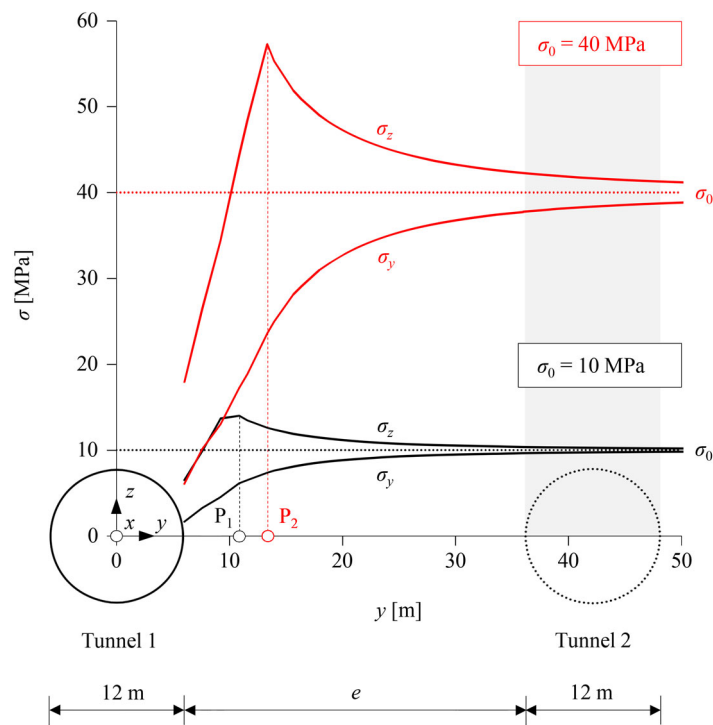
Figure 5.16. Interaction problem, creep case: Stress distribution along the y-axis, after construction of Tunnel 1 but before construction of Tunnel 2, resulting from the Tunnel 1 simulation as a plane-strain problem (parameters: Table 5.3)
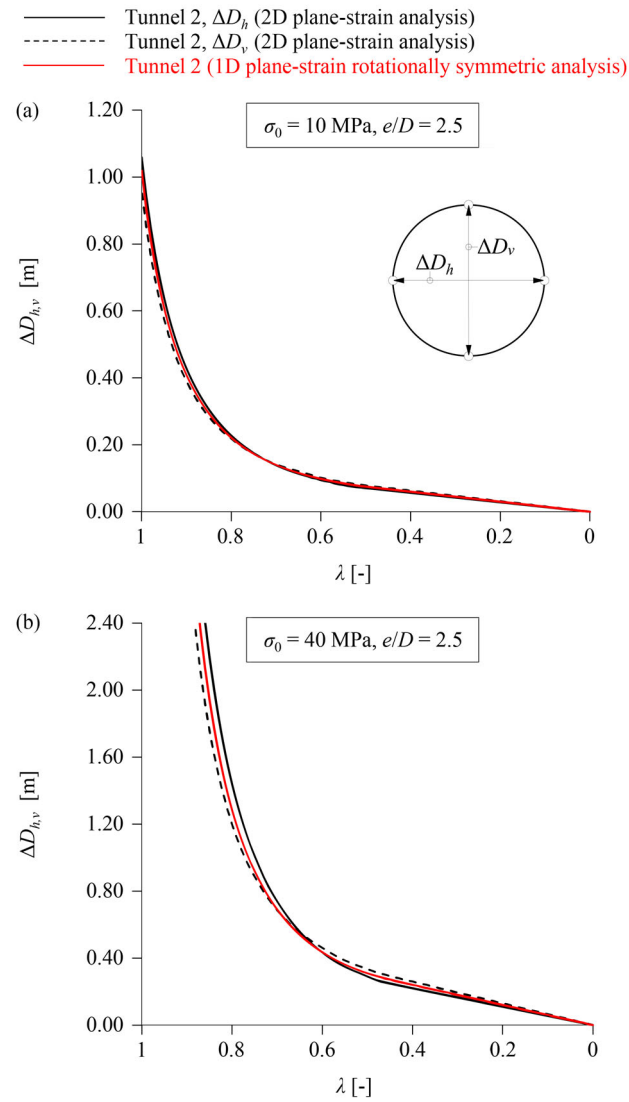
Figure 5.17.   Interaction problem, creep case: Relationship between convergence $\Delta D_{h,v}$ and deconfinement factor λ, resulting from the simulation of the excavation of Tunnel 2 as a plane-strain, 2D or 1D undrained cavity unloading problem (other parameters: Table 5.3)

5.4 Conclusions

This chapter addressed two practical aspects relevant in tunnel construction related to the effect of the tunnel diameter (scale effect) and the interaction between adjacent, sequentially excavated tunnels, placing specific focus on the risk of shield jamming. These investigations are valuable in relation to the applicability of experiences in situations arising in practice.

The investigations into the scale effect examined first the time-development of the convergences of an unsupported opening, demonstrating that this is independent of the tunnel diameter in the case of creep, while in the case of consolidation the convergence rate is inversely proportional to the square of the tunnel diameter, which means that convergences develop slower in larger tunnels. The latter is directly analogous to the well-known quadratic dependency between consolidation time and length of the drainage path in Terzaghi's 1D consolidation theory, but it holds only if there is only one significant geometric parameter, the tunnel diameter. Otherwise, *e.g.* when tunnelling through a confined aquitard, the consolidation rate may be much lower than indicated by consolidation theory.

Subsequently, the more complex problem of rock, TBM and tunnel support interaction was examined, with focus on the risk of shield jamming during advance and during restart after a construction standstill. The mechanisms underlying the scale effect in this case have been shown to be far more complex than indicated by consolidation theory, due to the different influence of and the technical limitations posed on several TBM parameters. The investigations demonstrated that a larger diameter is more favourable than a smaller one in poor quality ground with time-independent behaviour, while the opposite is true in the case of better quality ground, creep or consolidation. This scale effect is slightly more pronounced in the case of creep than in the case of consolidation.

The investigations into the tunnel interaction demonstrated vastly different effects in creep and consolidation, resulting from the fundamentally different nature of the purely mechanical rheological and the coupled hydromechanical consolidation processes.

In the case of creep, the interaction is governed by the stress redistributions and plastic yielding caused by the excavation of the first tunnel. These are limited within a narrow zone, since the construction equipement in mechanised tunnelling does not allow for large ground deformations to occur. The interaction has therefore been shown to be generally minor, even under extreme squeezing conditions and for an unusually large overcut.

In the case of consolidation, the drainage action of the first tunnel causes pore pressures relief and an increase in the effective stresses and undrained shear strength in the surrounding ground; this influence is analogous to that of advanced drainage and generates substantially more favourable conditions for the second tunnel, while it has also been shown to extend over a much larger zone compared to creep. This favourable influence of consolidation results in a dramatically reduced thrust force, a remarkable difference in relation to creep.

6 Conclusions and outlook

6.1 Conclusions of the present thesis

The present thesis aims to bridge the following knowledge gaps concerning the effect of creep on the interaction between TBM, lining and rock:

- The conclusions of existing studies in the literature concerning the effect of creep are mostly limited to specific tunnel projects.
- The assumption of a continuous simulation of the TBM advance may lead to an underestimation of the required thrust force to overcome shield-ground friction, important for assessing the risk of shield jamming.
- Fundamental differences in the phenomenological ground behaviour of a creeping and consolidating ground have not been addressed thus far in literature and could help distinguish creep from consolidation in practical situations.
- The influence of the tunnel size on the risk of shield jamming.
- The influence of an adjacent tunnel on the risk of shield jamming.

Thus, based on the aforementioned knowledge gaps the present thesis shows that:

- The effect of creep is not always favourable for shield jamming during advance, as usually assumed in literature, and is always unfavourable during standstills which is due to a paradox that has to do with the interplay of two counter-acting effects: on the one hand creep limits the ground convergences around the shield during excavation, which reduces the rock pressure acting upon it, but on the other hand it leads to less stress relief of the ground ahead of the tunnel face, which results in increased load transferring to the shield. Moreover, it has shown that creep is always unfavourable for the lining, as viscosity reduces plastic deformations in the vicinity of the tunnel face and hence greater plastic develop over time, which are constrained by the lining, thus increasing the pressure acting upon it.
- Simulations which consider a continuous excavation with the gross advance rate are adequate only where standstills are very short (error smaller than 10% compared to a simulation which simulates them, *e.g.* standstills for lining erection during the stop-and-go shield tunnelling process), but otherwise underestimate the shield loading, even in

cases of regular inspection and maintenance standstills lasting only a few hours. The present thesis presents a novel semi-discrete approach which smears only the standstills due to lining installation and has an error in comparison to the simulation of the actual TBM excavation – consisting of short regular standstills to install the lining and longer maintenance standstills – of maximum 10% if a maintenance standstill is not considered and within 20% otherwise, provided that the normalised net advance rate $\eta\, v_N / E / R$ lie outside the range 1 – 10. Moreover, this thesis provides an equation (metamodel) to quickly assess the risk of shield jamming in creeping ground which bases on existing design nomograms of a time-independent ground and transient numerical simulations considering creep.

- It is not possible to distinguish creep from consolidation in tunnel practice despite of some important differences: (i) consistently more extensive plastic yielding in the case of consolidation because the ground partially plastified immediately upon excavation under undrained conditions, but remaining practically elastic in the case of creep; and (ii) destabilising effect of the seepage forces in the case of consolidation, which does not exist in the case of creep and may be critical for shield and cutterhead jamming and is in addition partially the reason why consistently more plastic yielding occur in the case of consolidation compared to creep. (iii) time-development of the displacements in an unsupported opening are independent of the tunnel size in creeping ground, but proportional to the square of the tunnel radius in consolidating ground; in the latter case, however, the consolidation rate may also be much lower in cases where the geological setting poses limitations on the size of the seepage flow domain, as this may result in increased pore pressure gradients (seepage forces) that induce more extensive plastification. Moreover, numerical simulations indicate several qualitative similarities between the two mechanisms of time-dependency of the ground behaviour, in respect of: (i) the time-development of the unsupported tunnel boundary displacement between tunnel excavation and steady state conditions; (ii) the dependency of shield loading during excavation on the advance rate of the TBM, which also indicates a similar counter-intuitive behaviour of increasing shield loading with faster advance under certain conditions investigated for creep in the present thesis and for consolidation by Ramoni and Anagnostou 2011b; and, (iii) the increase in the rock pressure on the static shield during construction standstills, due to the manifestation of additional ground deformations over time.

- A larger tunnel radius is always unfavourable for the risk of shield jamming both during excavation and standstill in a creeping and consolidating ground and the effect of size being slightly more pronounced in the former case. The present thesis has also shown that in the case of time-independent ground behaviour a larger radius is always more favourable in weak ground, while the opposite holds in better ground.

- The effect of an adjacent tunnel on shield jamming is by far more pronounced and favourable in the case of consolidating ground which can lead to a remarkable reduction in the required thrust force to overcome the risk of shield jamming by 40 – 80% compared to the case without the adjacent tunnel. This because the excavation of the first tunnel relives the pore pressures and increases the effective stresses and the shear strength in the

surrounding ground, and thus being analogous to advance drainage. On the other hand, in the case of creep the interaction is unfavourable for the shield loading, due to the plastified zone that occurs because of the stress redistribution. Although, this effect is usually minor as the tunnel lays outside the plastified zone as it is usually a narrow zone.

6.2   Implications on practice

The present thesis provides implications on tunnel practice, which are discussed hereafter:

- If time-dependent effects can be attributed to the rheology of the material (creep), then the developed design aids can give a first indication of a possible risk of shield jamming thus without the need of performing computational analyses. However, in cases of very low normalised rock pressure the developed design aids are inapplicable and thus numerical TBM simulations must be performed. Moreover, in cases in which no field data is available for determining the viscosity of the ground, results for the whole viscosity range can be considered and used as a basis for the risk assessment of shield jamming. As the thesis has shown these results may be higher than one determined without taking creep into account, due to the counter-intuitive effect seen in Chapter 2.

- The present thesis has shown that it is not possible to distinguish creep from consolidation in tunnel practice. This implies that the influence of time effects (creep and consolidation) on the interaction between TBM, lining and rock cannot be excluded before tunnel construction and if a significant effect of one of the two time-effect can be proven (*e.g.* via laboratory test and numerical simulations), then its effect must be taken into account in the planning phase as well as during construction.

- It has shown that a bigger tunnel size can be favourable in a time-independent ground under weak ground conditions. However the opposite has been shown in the case of a time-dependent ground. Thus, this implies that experience gathered alone from a firstly excavated pilot tunnel are not useful for a secondly excavated bigger diameter tunnel if these experiences are not coupled with laboratory test and numerical simulations that quantify the effect of creep or consolidation and advance explorations of the hydrogeological conditions of the project site.

- It has also shown that the interaction of an adjacent tunnel on the risk of shield jamming is highly influenced by the mechanism of time dependence. If time dependence is given by consolidation, its effect is remarkably favourable for the risk of shield jamming whereas if it is creep it might even be unfavourable if the tunnel is too close to the adjacent tunnel. Thus, this implies, as the previous implication, that laboratory test and numerical simulations are indispensable for determining which of the two time effects mainly govern the ground behaviour coupled with advance exploration of the hydrogeological conditions of the project site. However, this also means that experience gathered from the first tunnel is useful for the construction of the adjacent second tunnel.

6.3   Outlook

The following questions still remain "open" given for each chapter.

Chapter 2 has developed a simple constitutive model, which enables considering the effect of creep with a single additional parameter, the viscosity. Considering this simple constitutive model Chapter 3 provides a simple tool to assess the risk of shield jamming in a creeping ground. This tool however assumes that the additional parameter, the viscosity, is calibrated considering field data (using another tool developed in Chapter 2). If field data is unavailable, one possibility is to consider the full range of viscosities, which has been shown to lead to even higher pressures over the shield than in the case of a time-independent ground, due to the counter-intuitive effect discussed in Chapter 2. Another possibility is calibration via laboratory test. However, this requires that, (i), it is possible to distinguish creep from consolidation, which is difficult in a saturated rock with low permeability and, (ii), the laboratory results are transferable to the scale of the tunnel cross-section (scale effect).

Chapter 4 has shown that it is not possible to distinguish creep from consolidation practically. Thus, in the case both mechanisms are relevant, the influence of their combined effect on the risk of shield jamming is worth investigating, as it has not been studied until now.

Moreover, Chapter 4 has pointed out a major difference between creeping and consolidating ground, the destabilising effect of seepage forces in the latter case, which is particularly relevant for the tunnel face and does not exist in the case of creep. However, in the case of creep softening effects that destabilise the tunnel face may occur, too, related to tertiary creep behaviour, which is characterised by a progressively increasing strain rate. Their influence on the face stability and stand-up time of the face are relevant to investigate only if large deformations at the tunnel face can develop. In the case of mechanised tunnelling, however, tunnel face deformations are limited by the cutterhead. Thus, these softening effects are of secondary importance.

Except the cited differences (see points above) Chapter 4 has also shown fundamental similarities of the two time effects, in particular on the distribution of the shield and lining loads during excavation but also during a standstill, as well as showing similar counter-intuitive behaviour. Thus, the question arises whether it is possible to describe the influence of consolidation on the risk of shield jamming via equivalent creep parameters and thus being able to use the developed tool for assessing the risk of shield jamming in a creeping ground given in Chapter 3 also for the case of a consolidating ground.

Chapter 5 investigated the effect of a firstly built tunnel on a parallel tunnel constructed later under the same ground conditions in the case of creep and consolidation, placing focus on the shield loading and the risk of shield jamming. It remains yet to be assessed how the first tunnel affects the lining of the second one and *vice versa*.

Moreover, Chapter 5 has only considered the case in which the first tunnel has been completed and steady state conditions prevail before excavating the second parallel tunnel. Thus, in more general context, interesting are also intermediate cases, where two tunnel are constructed simultaneously, or one shortly after the other. Therefore, it might be interesting to consider this in the context of further investigations.

Appendix A. Constitutive model formulation and implementation in Abaqus®

This Appendix presents the formulation and implementation of the adopted constitutive model as a user-defined material subroutine (UMAT) in Abaqus® (Dassault Systèmes, 2018). For the general 3D case, the effective stress and strain vectors are denoted as $\widetilde{\boldsymbol{\sigma}} = \{\sigma_{xx}\ \sigma_{yy}\ \sigma_{zz}\ \tau_{xy}\ \sigma_{yz}\ \sigma_{zx}\}$ and $\widetilde{\boldsymbol{\varepsilon}} = \{\varepsilon_{xx}\ \varepsilon_{yy}\ \varepsilon_{zz}\ \gamma_{xy}\ \gamma_{yz}\ \gamma_{zx}\}$, respectively, in the material local coordinate system (x,y,z), and as $\boldsymbol{\sigma} = \{\sigma_1\ \sigma_2\ \sigma_3\ 0\ 0\ 0\}$ and $\boldsymbol{\varepsilon} = \{\varepsilon_1\ \varepsilon_2\ \varepsilon_3\ 0\ 0\ 0\}$ in the principal coordinate system, where the ordering $\sigma_1 \geq \sigma_2 \geq \sigma_3$ is assumed. The geomechanics sign convention is adopted (compressive stresses/strains positive). All quantities are functions of time, and their derivatives with respect to time, henceforth referred to as rates or increments, are denoted with an upper dot symbol " · ".

Elastic constitutive relationship

The linear elastic constitutive relationship is expressed in terms of the stress rate $\dot{\boldsymbol{\sigma}}$ and the elastic strain rate $\dot{\boldsymbol{\varepsilon}}^{el}$ in the principal coordinate system as

$$\dot{\boldsymbol{\sigma}} = \mathbf{D}^{el}\dot{\boldsymbol{\varepsilon}}^{el}, \tag{A.1}$$

where $\mathbf{D}^{el}$ is Hooke's constant elastic stiffness matrix.

Yield condition

The MC yield condition is expressed in the principal stress space as

$$f_1(\boldsymbol{\sigma}) = \sigma_1 - m\sigma_3 - f_c = 0, \tag{A.2}$$

where m is the yield surface slope in the principal stress plane σ_1-σ_3 and f_c the uniaxial compressive strength, which are functions of the friction angle ϕ and the cohesion c:

$$m = \frac{1 + \sin\phi}{1 - \sin\phi}, \tag{A.3}$$

$$f_c = \frac{2c\cos\phi}{1-\sin\phi}\,. \tag{A.4}$$

The yield condition (Eq. A.2) geometrically represents a plane of the pyramidal MC yield surface, where the ordering $\sigma_1 \geq \sigma_2 \geq \sigma_3$ holds. Along its lines of intersection with the adjacent planes, the following yield condition must be considered additionally in the case of triaxial compression $\sigma_1 \geq \sigma_2 = \sigma_3$:

$$f_2(\boldsymbol{\sigma}) = \sigma_1 - m\sigma_2 - f_c = 0\,, \tag{A.5}$$

and the following in the case of triaxial extension $\sigma_1 = \sigma_2 \geq \sigma_3$:

$$f_3(\boldsymbol{\sigma}) = \sigma_2 - m\sigma_3 - f_c = 0\,. \tag{A.6}$$

The point of intersection of all three planes (MC yield surface apex), where the stress state is purely tensile in cohesive geomaterials, is not considered herein, as it is not relevant for the investigated tunnel boundary value problems.

Consistency condition

The rate of change of the yield functions is given by the following expression:

$$\dot{f}_i(\boldsymbol{\sigma}) = \mathbf{n}_i^{\mathrm{T}}\,\dot{\boldsymbol{\sigma}}\,, \tag{A.7}$$

where $\mathbf{n}_i = \mathrm{d}f_i/\mathrm{d}\boldsymbol{\sigma}$ is the normal vector to the yield surface f_i. In classic plasticity theory the stress state upon yielding remains on the yield surface, and hence the rate in Eq. A.7 must be zero to ensure that the stress increments $\dot{\boldsymbol{\sigma}}$ are tangent to the surface boundary. In the framework of overstress theory (Perzyna, 1966), however, viscoplastic deformations occur for stress states lying on or outside the yield surface ($f_i(\boldsymbol{\sigma}) \geq 0$), which means that $\dot{\boldsymbol{\sigma}}$ is not strictly tangent but may also be oriented outwards from the yield surface, and, in turn, $\dot{f}$ in Eq. A.7 is generally non-zero.

Strain decomposition and viscoplastic flow rule

The total strain rate can be decomposed into elastic and viscoplastic counterparts:

$$\dot{\boldsymbol{\varepsilon}} = \dot{\boldsymbol{\varepsilon}}^{el} + \dot{\boldsymbol{\varepsilon}}^{vp}\,, \tag{A.8}$$

where the elastic counterpart $\dot{\boldsymbol{\varepsilon}}^{el}$ obeys Hooke's constitutive relationship in Eq. A.1, and the viscoplastic counterpart $\dot{\boldsymbol{\varepsilon}}^{vp}$ is obtained from the flow rule. A non-associated flow rule is considered, which adopts Koiter's (1953) generalisation for plastic flow along an edge of the yield surface:

$$\dot{\boldsymbol{\varepsilon}}^{vp} = \begin{cases} \dot{\lambda}_1^{vp}\mathbf{r}_1\,, & f_1 \geq 0 \wedge f_2 \leq 0 \wedge f_3 \leq 0, \\ \dot{\lambda}_1^{vp}\mathbf{r}_1 + \dot{\lambda}_2^{vp}\mathbf{r}_2\,, & f_1 \geq 0 \wedge f_2 \geq 0 \wedge f_3 \leq 0, \\ \dot{\lambda}_1^{vp}\mathbf{r}_1 + \dot{\lambda}_3^{vp}\mathbf{r}_3\,, & f_1 \geq 0 \wedge f_2 \leq 0 \wedge f_3 \geq 0. \end{cases} \tag{A.9}$$

In the above expression $\mathbf{r}_i = \mathrm{d}g_i/\mathrm{d}\boldsymbol{\sigma}$ are the normal vectors to the plastic potential surfaces g_i that correspond to the yield surfaces f_i (Eqs. A.2, A.5, A.6):

$$g_1(\boldsymbol{\sigma}) = \sigma_1 - \kappa\sigma_3, \tag{A.10}$$

$$g_2(\boldsymbol{\sigma}) = \sigma_1 - \kappa\sigma_2, \tag{A.11}$$

$$g_3(\boldsymbol{\sigma}) = \sigma_2 - \kappa\sigma_3, \tag{A.12}$$

where κ denotes the dilatancy constant:

$$\kappa = \frac{1 + \sin\psi}{1 - \sin\psi}, \tag{A.13}$$

and $\dot{\lambda}_i^{vp}$ are the viscoplastic multipliers after Perzyna's theory, which are considered analogously to Zienkiewicz *et al.* (1975):

$$\dot{\lambda}_i^{vp} = \frac{f_i(\boldsymbol{\sigma})}{\eta}. \tag{A.14}$$

Using Eq. A.14, Eq. A.7 can be written as follows (Heeres *et al.*, 2002):

$$\mathbf{n}_i^{\mathrm{T}}\dot{\boldsymbol{\sigma}} - \ddot{\lambda}_i^{vp}\eta = 0, \tag{A.15}$$

which evidently reduces to the consistency equation of classic plasticity theory for $\eta = 0$.

Stress integration

The MC-Perzyna model was implemented in Abaqus® (Dassault Systèmes, 2018) as a user-defined material subroutine (UMAT). At a given iteration $j+1$, the UMAT: (i) receives as input the stress state $\widetilde{\boldsymbol{\sigma}}_j$ of the previous iteration and the updated strain increment $\Delta\widetilde{\boldsymbol{\varepsilon}}_{j+1}$ in the local coordinate system; (ii) transforms them into the principal coordinate system as $\boldsymbol{\sigma}_j$ and $\Delta\boldsymbol{\varepsilon}_{j+1}$; (iii) determines the updated stress state $\boldsymbol{\sigma}_{j+1}$ and assembles the viscoplastic tangent stiffness matrix $\mathbf{D}^{vp}$ = $\mathrm{d}\boldsymbol{\sigma}/\mathrm{d}\boldsymbol{\varepsilon}$ in the principal coordinate system, based upon the constitutive equations presented above; and, (iv), returns as output the back-transformed from the principal to the local coordinate system $\widetilde{\boldsymbol{\sigma}}_{j+1}$ and $\tilde{\mathbf{D}}^{vp}$. The assembly and return of $\tilde{\mathbf{D}}^{vp}$ ensures quadratic convergence of the numerical solution algorithm. The algorithmic treatment of the model formulation equations in a discrete form is identical to the one described in Section 4.2 of Heeres *et al.* (2002); the only difference is that the implicit scheme degenerates into an explicit scheme in the present case, due to the planar geometry of the MC yield surface, which enables all quantities to be directly evaluated at the beginning of the iteration.

Appendix B. Constitutive model MC-Perzyna

In this Appendix the code of the constitutive model MC-Perzyna is given. Firstly, an overview of the general processes in the subroutine is given via a flowchart in Figure B.1.
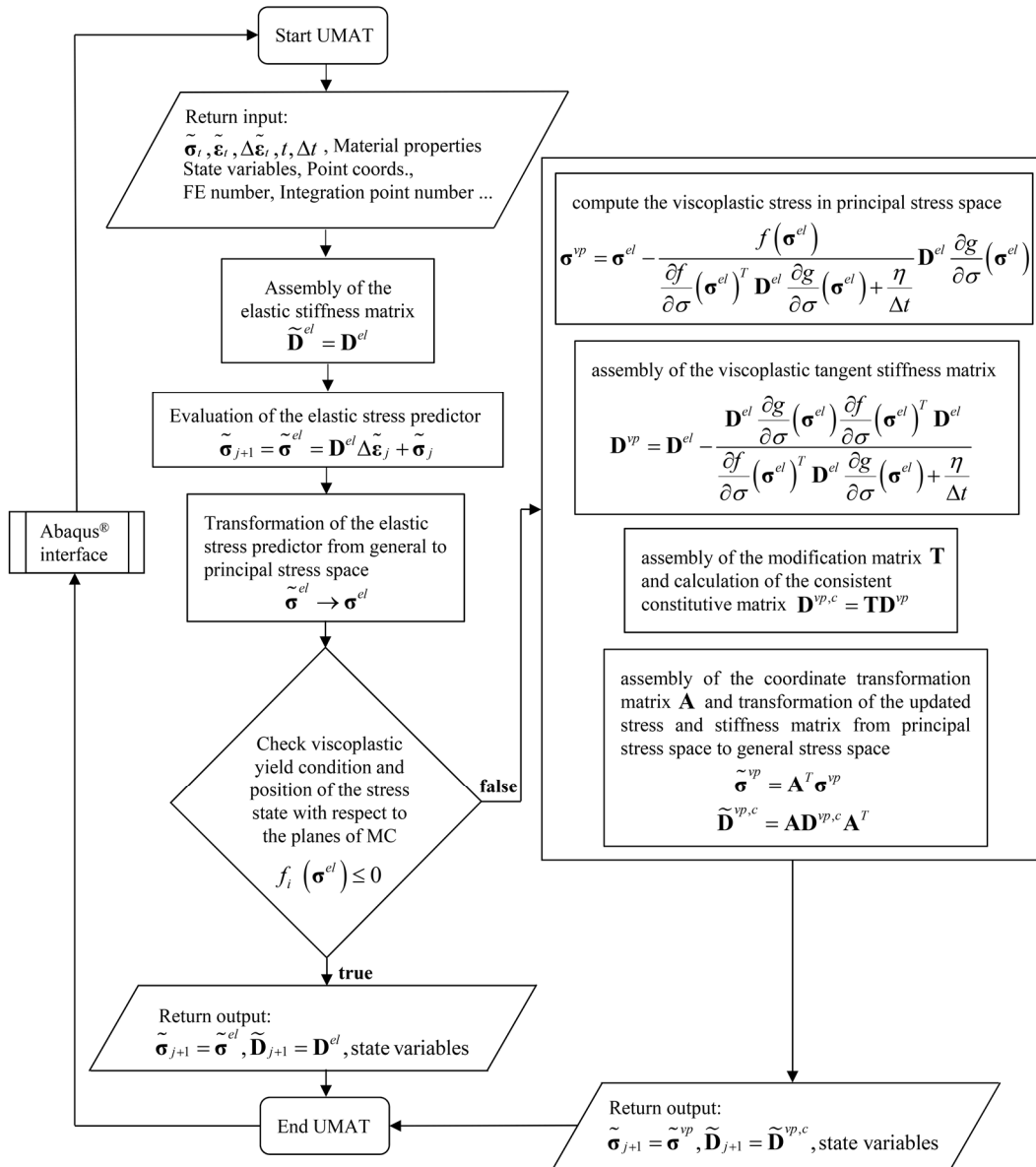
Figure B.1.   Flowchart of the general processes in an Abaqus® subroutine (also called UMAT)

```fortran
!The subroutine UMAT is given herein which gives as input the stress and strain
increment.

      SUBROUTINE UMAT(STRESS,STATEV,DDSDDE,SSE,SPD,SCD,
     1 RPL,DDSDDT,DRPLDE,DRPLDT,
     2 STRAN,DSTRAN,TIME,DTIME,TEMP,DTEMP,PREDEF,DPRED,CMNAME,
     3 NDI,NSHR,NTENS,NSTATV,PROPS,NPROPS,COORDS,DROT,PNEWDT,
     4 CELENT,DFGRD0,DFGRD1,NOEL,NPT,LAYER,KSPT,KSTEP,KINC)

!Declaration of arrays needed for the computation

      INCLUDE 'ABA_PARAM.INC'

      CHARACTER*80 CMNAME
      REAL(8) STRESS(NTENS),STATEV(NSTATV),
     1 DDSDDE(NTENS,NTENS),
     2 DDSDDT(NTENS),DRPLDE(NTENS),
     3 STRAN(NTENS),DSTRAN(NTENS),TIME(2),PREDEF(1),DPRED(1),
     4 PROPS(NPROPS),COORDS(3),DROT(3,3),DFGRD0(3,3),DFGRD1(3,3)

      REAL(8), PARAMETER :: PI = 3.1415926535897932384626433832795_8
      REAL(8) EMOD,NU,LAMBDA,MU,COH,PHI,PSI,K_PHI,M_PSI
      REAL(8) D_STIFF_INV(4,4),D_STIFF(4,4)
      REAL(8) S_SB(4), STRESSN(3,3), SS(3),LAMBDA_IJ(3,3)
      REAL(8) F_YIELD(6),GRAD_F_YIELD(3,6),P_PSI(6),GRAD_P_PSI(3,6)
      REAL(8) S_C(3)
      REAL(8) T1_MOD(6),T2_MOD(6)
      INTEGER(4) region, COUNT,ATTIVA_ADESSO
      INTEGER(4) ATTIVA_ADESSO_PLANE1,ATTIVA_ADESSO_PLANE2,REGG(6)
      INTEGER(4) OK,COUNT_T, SEGNO_APEX
      REAL(8) LAMBDA_IJ_T(3,3)
      REAL(8) STRESSN_PRINC(3,3)
      REAL(8) STRESSN_0(3,3),STRESSN_1(3,3)
      REAL(8) SS_0(3),LAMBDA_IJ_0(3,3)
      REAL(8) DD_EP(4,4),DD_EPC(4,4),T_MAT(4,4),DD_EPC_0(4,4)
      REAL(8) D_EP_LINE1(4,4)
      REAL(8) G_STIFF(4,4),AA_4(4,4),AA_4_T(4,4),BETA
      REAL(8) D_EP_LINE_CORR(4,4)
      REAL(8) ETA_SUB,DTIME_SUB
      REAL(8) VAR_1, DELTA_LAMBDA, ALPHA, DD_EP_APEX(4,4)


!Initial definition of the material constants

       DELTA_LAMBDA = 0.0_8

      DTIME_SUB=DTIME

      region=0
      EMOD=PROPS(1)
      NU=PROPS(2)
      LAMBDA=NU*EMOD/(1.0_8+NU)/(1.0_8-2.0_8*NU)
      MU=EMOD/2.0_8/(1.0_8+NU)
      COH=PROPS(3)
      PHI=PROPS(4)*pi/180.0_8
      PSI=PROPS(5)*pi/180.0_8
      ETA_SUB=PROPS(6)
      K_PHI=(1.0_8+SIN(PHI))/(1.0_8-SIN(PHI))
      M_PSI=(1.0_8+SIN(PSI))/(1.0_8-SIN(PSI))
      BETA=30.0_8
      ALPHA=70.0_8
      SEGNO_APEX=0
```

```fortran
        D_STIFF_INV(1,:)=(/1.0_8/EMOD,-NU/EMOD,-NU/EMOD,0.0_8/)
        D_STIFF_INV(2,:)=(/-NU/EMOD,1.0_8/EMOD,-NU/EMOD,0.0_8/)
        D_STIFF_INV(3,:)=(/-NU/EMOD,-NU/EMOD,1.0_8/EMOD,0.0_8/)
        D_STIFF_INV(4,:)=(/0.0_8,0.0_8,0.0_8,2.0_8*(1.0_8+NU)/EMOD/)

        D_STIFF(1,:)=(/LAMBDA+2.0_8*MU,LAMBDA,LAMBDA,0.0_8 /)
        D_STIFF(2,:)=(/LAMBDA,LAMBDA+2.0_8*MU,LAMBDA,0.0_8 /)
        D_STIFF(3,:)=(/LAMBDA,LAMBDA,LAMBDA+2.0_8*MU,0.0_8 /)
        D_STIFF(4,:)=(/ 0.0_8 , 0.0_8 , 0.0_8 , MU /)

        G_STIFF=0.0_8

        G_STIFF(4,4)=EMOD/2.0_8/(1.d0+NU)

!Elastic stress update
        S_SB=STRESS+MATMUL(D_STIFF,DSTRAN)

!Transform stress from local coordinates to the principal coordinate system
        STRESSN=0.0_8
        STRESSN(1,1)=S_SB(1)
        STRESSN(1,2)=S_SB(4)
        STRESSN(2,1)=S_SB(4)
        STRESSN(2,2)=S_SB(2)
        STRESSN(3,3)=S_SB(3)

         call Jacobi(STRESSN,LAMBDA_IJ_0,1.0e-012_8,3,STRESSN_PRINC)

         SS_0(1)=STRESSN_PRINC(1,1)
         SS_0(2)=STRESSN_PRINC(2,2)
         SS_0(3)=STRESSN_PRINC(3,3)

        CALL PRINT_DIR(SS_0,LAMBDA_IJ_0,SS,LAMBDA_IJ,PROBLEMA)

! Computes the values of the yield condition as well as its derivative and the
! position of the updated elastic stress on the yield surface, i.e. whether the
! stress state lays on the plane, line or apex with the vector REGG

        CALL FAILURE_SURFACE(COH,PHI,K_PHI,SS,F_YIELD,GRAD_F_YIELD)

        CALL FAILURE_SURFACE(0.0_8,PSI,M_PSI,SS,P_PSI,GRAD_P_PSI)

        CALL STRESS_POSITION(K_PHI,M_PSI,COH,F_YIELD,SS,D_STIFF
     1,D_STIFF_INV,REGG,T1_MOD,T2_MOD)

! Checks whether the position of the stress state lays by error outside the
! plane, lines in which the ordering of stresses is Sig1 >= Sig2 >= Sig3
        if (REGG(1)>3) THEN
!        READ(*,*) VAR1
        SEGNO_APEX=1
        END IF

! If the SUM of the variable REGG is 0 then the stress is on the elastic surface.
        IF (SUM(REGG)==0) then
        F_YIELD(1)=-1.0_8
        F_YIELD(2)=-1.0_8
        F_YIELD(3)=-1.0_8
        F_YIELD(4)=-1.0_8
        F_YIELD(5)=-1.0_8
        F_YIELD(6)=-1.0_8
        end if
```

```fortran
! Checks whether the stress state is elastic or viscoplastic, if it is elastic
returns the elastic stress to the UMAT. If it is viscoplastic then computes the
updated viscoplastic stress.

        IF (MAXVAL(F_YIELD)<=0.0_8) THEN
        STRESS=S_SB
        DDSDDE=D_STIFF
        ELSE

        region=1

! Calculates the coordinate transformation matrix in order to transform the
stresses from principal coordinates into local coordinates
        CALL COORD_TRANS_MATRIX(LAMBDA_IJ,SS,S_SB,AA_4)

! Checks the position of the stress with the vector REGG

        ATTIVA_ADESSO=0
        ATTIVA_ADESSO_PLANE1=0
        ATTIVA_ADESSO_PLANE2=0
        COUNT=1
        OK=1

        IF (SEGNO_APEX==0) THEN
        DO WHILE (COUNT<7 .AND. OK==1)

        IF (COUNT<6) THEN

        IF (REGG(COUNT)==1) THEN
        !PLANE
        OK=0
        ATTIVA_ADESSO=COUNT
        COUNT_T=COUNT
        ELSE IF (REGG(COUNT+1)==3 .AND. REGG(COUNT)==2) THEN
        OK=0
        ATTIVA_ADESSO_PLANE1=COUNT
        ATTIVA_ADESSO_PLANE2=COUNT+1
        COUNT_T=COUNT
        END IF

        ELSE

        IF (REGG(6)==1) THEN
        !PLANE
        OK=0
        ATTIVA_ADESSO=COUNT
        ELSE IF (REGG(1)==3 .AND. REGG(6)==2) THEN
        OK=0
        ATTIVA_ADESSO_PLANE1=6
        ATTIVA_ADESSO_PLANE2=1
        END IF

        END IF

        COUNT=COUNT+1
        END DO
        ELSE
        ATTIVA_ADESSO=1
        END IF

! If ATTIVA_ADESSO is equal to zero than the stress state lays on the line, if it
is different then zero then it lays on the plane.
```

```fortran
      IF (ATTIVA_ADESSO==0) THEN !LINE
!     read(*,*) VAR_1
      CALL RETURN_TO_LINE(ETA_SUB,DTIME_SUB,ATTIVA_ADESSO_PLANE1
     1,ATTIVA_ADESSO_PLANE2,F_YIELD,SS,GRAD_F_YIELD,GRAD_P_PSI
     1,D_STIFF,S_C,D_EP_LINE1,DELTA_LAMBDA)

      IF (DOT_PRODUCT(SS-S_C,SS-S_C)
     1>0.0_8)then
       CALL D_EP_ON_LINE_CORRECTION_FACTOR(SS,S_C
     1,K_PHI,M_PSI,ATTIVA_ADESSO_PLANE1,ATTIVA_ADESSO_PLANE2,D_STIFF
     1,D_STIFF_INV,D_EP_LINE_CORR)
      DD_EP=0.0_8
      DD_EP(1:3,1:3)=D_EP_LINE1(1:3,1:3)+D_EP_LINE_CORR(1:3,1:3)/BETA
      DD_EP(4,4)=D_EP_LINE1(4,4)
      ELSE
      DD_EP=D_EP_LINE1
      END IF

      ELSE !PLANE

      CALL RETURN_TO_PLANE(ETA_SUB,DTIME_SUB,ATTIVA_ADESSO,F_YIELD,SS
     1,GRAD_F_YIELD,GRAD_P_PSI,D_STIFF,S_C,DD_EP,DELTA_LAMBDA)

      IF (SEGNO_APEX==1) THEN !APEX
      DD_EP_APEX=0.0_8
      DD_EP_APEX(1:3,1:3)=DD_EP(1:3,1:3)/ALPHA
      DD_EP_APEX(4:4,4:4)=D_STIFF(4:4,4:4)/ALPHA
      DD_EP=DD_EP_APEX
      S_C=2.0_8*COH*SQRT(K_PHI)/(K_PHI-1.0_8)
      END IF

      END IF

! Modification matrix needed for the computation of the consistent constitutive
matrix defined for 2D analysis after Chapter B.2 of Appendix B of Clausen et al.
(2007)

      CALL TRANSFORMATION_MATRIX(S_C,SS,S_SB,T_MAT)

! Calculation of the consistent constitutive matrix consistent with the Newton-
Raphson equilibrium iterations see Chapter 3.2 of Clausen (2007).

      DD_EPC=MATMUL(T_MAT,DD_EP)
      AA_4_T=TRANSPOSE(AA_4)
      DD_EPC_0=MATMUL(AA_4_T,DD_EPC)
      DDSDDE=MATMUL(DD_EPC_0,AA_4)

! Transformation of the stress from principal coordinates to local coordinates

      STRESSN=0.0_8
      STRESSN(1,1)=S_C(1)
      STRESSN(2,2)=S_C(2)
      STRESSN(3,3)=S_C(3)

      LAMBDA_IJ_T=TRANSPOSE(LAMBDA_IJ)
      STRESSN_0=MATMUL(STRESSN,LAMBDA_IJ_T)
      STRESSN_1=MATMUL(LAMBDA_IJ,STRESSN_0)

      STRESS(1)=STRESSN_1(1,1)
      STRESS(2)=STRESSN_1(2,2)
      STRESS(3)=STRESSN_1(3,3)
```

```fortran
        STRESS(4)=STRESSN_1(1,2)

        END IF

! Transform updated stress into principal stress in order to determine the
position of stress with respect to the yield condition.
        STRESSN=0.0_8
        STRESSN(1,1)=STRESS(1)
        STRESSN(1,2)=STRESS(4)
        STRESSN(2,1)=STRESS(4)
        STRESSN(2,2)=STRESS(2)
        STRESSN(3,3)=STRESS(3)

         call Jacobi(STRESSN,LAMBDA_IJ_0,1.0e-012_8,3,STRESSN_PRINC)

         SS_0(1)=STRESSN_PRINC(1,1)
         SS_0(2)=STRESSN_PRINC(2,2)
         SS_0(3)=STRESSN_PRINC(3,3)

        CALL PRINT_DIR(SS_0,LAMBDA_IJ_0,SS,LAMBDA_IJ,PROBLEMA)

        if (isnan(STRESS(1))) stop ! STOP IF NAN

        CALL FAILURE_SURFACE(COH,PHI,K_PHI,SS,F_YIELD,GRAD_F_YIELD,F_TENS)
        STATEV(1) = real(F_YIELD(1),8) !value of the failure surface nr.1

        END SUBROUTINE UMAT

        PURE SUBROUTINE FAILURE_SURFACE(C,PHI,K,S,F,GRAD_F)
! This subroutine calculates the magnitude of the yield function for a given
stress.

        IMPLICIT NONE
        REAL(8), intent(in) :: C,PHI,K
        REAL(8), intent (in) :: S(3)
        REAL(8), intent (out) :: F(6),GRAD_F(3,6)

! Magnitude of the yield function
        F(1)=S(1)*K-S(3)-2.0_8*C*cos(PHI)/(1.0_8-sin(PHI))
        F(2)=S(2)*K-S(3)-2.0_8*C*cos(PHI)/(1.0_8-sin(PHI))
        F(3)=S(2)*K-S(1)-2.0_8*C*cos(PHI)/(1.0_8-sin(PHI))
        F(4)=S(3)*K-S(1)-2.0_8*C*cos(PHI)/(1.0_8-sin(PHI))
        F(5)=S(3)*K-S(2)-2.0_8*C*cos(PHI)/(1.0_8-sin(PHI))
        F(6)=S(1)*K-S(2)-2.0_8*C*cos(PHI)/(1.0_8-sin(PHI))

! Computation of the derivatives of the yield function
        GRAD_F(1,1)=K
        GRAD_F(2,1)=0.0_8
        GRAD_F(3,1)=-1.0_8

        GRAD_F(1,2)=0.0_8
        GRAD_F(2,2)=K
        GRAD_F(3,2)=-1.0_8

        GRAD_F(1,3)=-1.0_8
        GRAD_F(2,3)=K
        GRAD_F(3,3)=0.0_8

        GRAD_F(1,4)=-1.0_8
        GRAD_F(2,4)=0.0_8
        GRAD_F(3,4)=K
```

```fortran
      GRAD_F(1,5)=0.0_8
      GRAD_F(2,5)=-1.0_8
      GRAD_F(3,5)=K

      GRAD_F(1,6)=K
      GRAD_F(2,6)=-1.0_8
      GRAD_F(3,6)=0.0_8

      END SUBROUTINE FAILURE_SURFACE


      PURE SUBROUTINE RETURN_TO_LINE(ETA,DTIME,ATTIVA_ADESSO_PLANE1
     1,ATTIVA_ADESSO_PLANE2,F,S_PRINC,GRAD_F,GRAD_P,D,S_C,D_EP,DELTA_L)
! This subroutine calculates the stress return on the line and the elasto-
viscoplastic constitutive matrix

      IMPLICIT NONE
      INTEGER(4), intent(in) :: ATTIVA_ADESSO_PLANE1
     1,ATTIVA_ADESSO_PLANE2
      REAL(8), intent (in) :: F(6),S_PRINC(3),GRAD_F(3,6),GRAD_P(3,6)
      REAL(8), intent (in) :: D(4,4),ETA,DTIME
      REAL(8), intent (out) :: S_C(3),D_EP(4,4),DELTA_L

      REAL(8) D_GRAD_P1(3),D_GRAD_P2(3),GRAD_P_ACTIVE1(3)
      REAL(8) GRAD_F_ACTIVE1(3),GRAD_P_ACTIVE2(3),GRAD_F_ACTIVE2(3)
      REAL(8) MU1,MU2,MU3,MU4,DELTA_LAMBDA1,DELTA_LAMBDA2
      REAL(8) UU,D_GRAD_F1(3),D_GRAD_F2(3),PARTE1(3),PARTE2(3)
      REAL(8) D_EP0(3,3),D_EP1(3,3)
      INTEGER(4) II,JJ

      GRAD_F_ACTIVE1=GRAD_F(:,ATTIVA_ADESSO_PLANE1)
      GRAD_P_ACTIVE1=GRAD_P(:,ATTIVA_ADESSO_PLANE1)

      GRAD_F_ACTIVE2=GRAD_F(:,ATTIVA_ADESSO_PLANE2)
      GRAD_P_ACTIVE2=GRAD_P(:,ATTIVA_ADESSO_PLANE2)

      D_GRAD_P1=MATMUL(D(1:3,1:3),GRAD_P_ACTIVE1)
      D_GRAD_P2=MATMUL(D(1:3,1:3),GRAD_P_ACTIVE2)

      D_GRAD_F1=MATMUL(D(1:3,1:3),GRAD_F_ACTIVE1)
      D_GRAD_F2=MATMUL(D(1:3,1:3),GRAD_F_ACTIVE2)

      MU1=DOT_PRODUCT(GRAD_F_ACTIVE1,D_GRAD_P1)
      MU2=DOT_PRODUCT(GRAD_F_ACTIVE1,D_GRAD_P2)
      MU3=DOT_PRODUCT(GRAD_F_ACTIVE2,D_GRAD_P1)
      MU4=DOT_PRODUCT(GRAD_F_ACTIVE2,D_GRAD_P2)

      DELTA_LAMBDA1=F(ATTIVA_ADESSO_PLANE1)/MU2*(ETA/DTIME+MU4)
      DELTA_LAMBDA1=DELTA_LAMBDA1-F(ATTIVA_ADESSO_PLANE2)
      DELTA_LAMBDA1=DELTA_LAMBDA1
     1/(-MU3+(ETA/DTIME+MU1)*(ETA/DTIME+MU4)/MU2)

      DELTA_LAMBDA2=F(ATTIVA_ADESSO_PLANE1)
      DELTA_LAMBDA2=DELTA_LAMBDA2-DELTA_LAMBDA1*(ETA/DTIME+MU1)
      DELTA_LAMBDA2=DELTA_LAMBDA2/MU2

      S_C=S_PRINC-DELTA_LAMBDA1*D_GRAD_P1-DELTA_LAMBDA2*D_GRAD_P2

      DELTA_L=DELTA_LAMBDA1+DELTA_LAMBDA2

!!!!!!!!D_EP_LINE
      MU1=MU1+ETA/DTIME
```

```fortran
        MU4=MU4+ETA/DTIME

        UU=-MU3*MU2/MU1+MU4

        PARTE1=(D_GRAD_F1*(UU/MU1+MU3*MU2/MU1/MU1)-D_GRAD_F2*MU2/MU1)/UU

        FORALL(II=1:3,JJ=1:3) D_EP0(II,JJ)=D_GRAD_P1(II)*PARTE1(JJ)

        PARTE2=(D_GRAD_F2-D_GRAD_F1*MU3/MU1)/UU

        FORALL(II=1:3,JJ=1:3) D_EP1(II,JJ)=D_GRAD_P2(II)*PARTE2(JJ)

        D_EP=0.0_8
        D_EP(1:3,1:3)=D(1:3,1:3)-D_EP0-D_EP1
        D_EP(4,4)=D(4,4)
        END SUBROUTINE RETURN_TO_LINE

        PURE SUBROUTINE RETURN_TO_PLANE(ETA,DTIME,ATTIVA_ADESSO,F,S_PRINC
       1,GRAD_F,GRAD_P,D,S_C,D_EP,DELTA_LAMBDA)
! This subroutine calculates the stress return on the plane and the elasto-
viscoplastic stiffness matrix

        IMPLICIT NONE
        INTEGER(4), intent(in) :: ATTIVA_ADESSO
        REAL(8), intent (in) :: F(6),S_PRINC(3),GRAD_F(3,6)
        REAL(8), intent (in) :: GRAD_P(3,6),D(4,4),ETA,DTIME
        REAL(8),  intent (out) :: S_C(3),D_EP(4,4), DELTA_LAMBDA

        REAL(8) D_GRAD_P(3),DENOM,GRAD_P_ACTIVE(3)
        REAL(8) GRAD_F_ACTIVE(3),GRAD_F_D(3),NOM_D(3,3),DENOM_D
        INTEGER(4) II,JJ

        GRAD_F_ACTIVE=GRAD_F(:,ATTIVA_ADESSO)
        GRAD_P_ACTIVE=GRAD_P(:,ATTIVA_ADESSO)

        D_GRAD_P=MATMUL(D(1:3,1:3),GRAD_P_ACTIVE)
        DENOM=DOT_PRODUCT(GRAD_F_ACTIVE,D_GRAD_P)+ETA/DTIME

        S_C=S_PRINC-F(ATTIVA_ADESSO)/DENOM*D_GRAD_P

        DELTA_LAMBDA=F(ATTIVA_ADESSO)/DENOM

        GRAD_F_D=MATMUL(GRAD_F_ACTIVE,D(1:3,1:3))

        FORALL(II=1:3,JJ=1:3) NOM_D(II,JJ)=D_GRAD_P(II)*GRAD_F_D(JJ)

        DENOM_D=DOT_PRODUCT(GRAD_F_D,GRAD_P_ACTIVE)+ETA/DTIME

        D_EP=0.0_8
        D_EP(1:3,1:3)=D(1:3,1:3)-NOM_D/DENOM_D
        D_EP(4,4)=D(4,4)

        END SUBROUTINE RETURN_TO_PLANE


        PURE SUBROUTINE STRESS_POSITION(K,M,C,F,S_B,D,D_INV,REG,T1,T2)
! This subroutine calculates the position of the stress in the principal stress
space with respect to the Mohr Coulomb yield condition after Chapter 3.4.1 of
Clausen et al. 2007

        IMPLICIT NONE
```

```fortran
REAL(8), intent(in) :: K,M,C,S_B(3),D(4,4),F(6),D_INV(4,4)
INTEGER(4), intent(out) :: REG(6)
REAL(8), intent(out) :: T1(6),T2(6)

INTEGER(4) COUNTER
REAL(8) S_APEX(3),A_VEKTOR(3),B_VEKTOR(3),L1(3),L1_G(3),L2(3)
REAL(8) L2_G(3),D_A_VEKTOR(3),DENOM_R_P,R_P(3)
REAL(8) CROSS_PRODUCT_I_III(3),P_I_II,P_I_III,D_INV_S(3)
REAL(8) D_INV_L2(3),TT1,TT2,CROSS_PRODUCT_I_II(3),D_INV_L1(3)

 interface

        pure subroutine CROSS(AAAA,BBBB,CCCC)
IMPLICIT NONE
REAL(8), intent (in) :: AAAA(3),BBBB(3)
REAL(8), intent (out) :: CCCC(3)
        end subroutine CROSS

 end interface

S_APEX(1)=2.0_8*C*sqrt(K)/(K-1.0_8)
S_APEX(2)=2.0_8*C*sqrt(K)/(K-1.0_8)
S_APEX(3)=2.0_8*C*sqrt(K)/(K-1.0_8)

COUNTER=1
REG(1)=0
REG(2)=0
REG(3)=0
REG(4)=0
REG(5)=0
REG(6)=0

DO WHILE (COUNTER<7)

IF (COUNTER .EQ. 1) THEN
A_VEKTOR(1)=K
A_VEKTOR(2)=0._8
A_VEKTOR(3)=-1._8

B_VEKTOR(1)=M
B_VEKTOR(2)=0.0_8
B_VEKTOR(3)=-1.0_8

L1(1)=1.0_8
L1(2)=1.0_8
L1(3)=K

L2(1)=1.0_8
L2(2)=K
L2(3)=K

L1_G(1)=1.0_8
L1_G(2)=1.0_8
L1_G(3)=M

L2_G(1)=1.0_8
L2_G(2)=M
L2_G(3)=M

ELSE IF (COUNTER .EQ. 2) THEN

A_VEKTOR(1)=0.0_8
```

```fortran
A_VEKTOR(2)=K
A_VEKTOR(3)=-1.0_8

B_VEKTOR(1)=0.0_8
B_VEKTOR(2)=M
B_VEKTOR(3)=-1.0_8

L1(1)=K
L1(2)=1.0_8
L1(3)=K

L2(1)=1.0_8
L2(2)=1.0_8
L2(3)=K

L1_G(1)=M
L1_G(2)=1.0_8
L1_G(3)=M

L2_G(1)=1.0_8
L2_G(2)=1.0_8
L2_G(3)=M

ELSE IF (COUNTER .EQ. 3) THEN
A_VEKTOR(1)=-1.0_8
A_VEKTOR(2)=K
A_VEKTOR(3)=0.0_8

B_VEKTOR(1)=-1.0_8
B_VEKTOR(2)=M
B_VEKTOR(3)=0.0_8

L1(1)=K
L1(2)=1.0_8
L1(3)=1.0_8

L2(1)=K
L2(2)=1.0_8
L2(3)=K

L1_G(1)=M
L1_G(2)=1.0_8
L1_G(3)=1.0_8

L2_G(1)=M
L2_G(2)=1.0_8
L2_G(3)=M

ELSE IF (COUNTER .EQ. 4) THEN
A_VEKTOR(1)=-1.0_8
A_VEKTOR(2)=0.0_8
A_VEKTOR(3)=K

B_VEKTOR(1)=-1.0_8
B_VEKTOR(2)=0.0_8
B_VEKTOR(3)=M

L1(1)=K
L1(2)=K
L1(3)=1.0_8

L2(1)=K
```

```fortran
      L2(2)=1.0_8
      L2(3)=1.0_8

      L1_G(1)=M
      L1_G(2)=M
      L1_G(3)=1.0_8

      L2_G(1)=M
      L2_G(2)=1.0_8
      L2_G(3)=1.0_8

      ELSE IF (COUNTER .EQ. 5) THEN
      A_VEKTOR(1)=0.0_8
      A_VEKTOR(2)=-1.0_8
      A_VEKTOR(3)=K

      B_VEKTOR(1)=0.0_8
      B_VEKTOR(2)=-1.0_8
      B_VEKTOR(3)=M

      L1(1)=1.0_8
      L1(2)=K
      L1(3)=1.0_8

      L2(1)=K
      L2(2)=K
      L2(3)=1.0_8

      L1_G(1)=1.0_8
      L1_G(2)=M
      L1_G(3)=1.0_8

      L2_G(1)=M
      L2_G(2)=M
      L2_G(3)=1.0_8

      ELSE IF (COUNTER .EQ. 6) THEN
      A_VEKTOR(1)=K
      A_VEKTOR(2)=-1.0_8
      A_VEKTOR(3)=0.0_8

      B_VEKTOR(1)=M
      B_VEKTOR(2)=-1.0_8
      B_VEKTOR(3)=0.0_8

      L1(1)=1.0_8
      L1(2)=K
      L1(3)=K

      L2(1)=1.0_8
      L2(2)=K
      L2(3)=1.0_8

      L1_G(1)=1.0_8
      L1_G(2)=M
      L1_G(3)=M

      L2_G(1)=1.0_8
      L2_G(2)=M
      L2_G(3)=1.0_8

      END IF
```

```fortran
D_A_VEKTOR=MATMUL(D(1:3,1:3),A_VEKTOR)

DENOM_R_P=DOT_PRODUCT(B_VEKTOR,D_A_VEKTOR)
R_P=MATMUL(D(1:3,1:3),B_VEKTOR)/DENOM_R_P

CALL CROSS(R_P,L1,CROSS_PRODUCT_I_II)

CALL CROSS(R_P,L2,CROSS_PRODUCT_I_III)

P_I_II=DOT_PRODUCT(CROSS_PRODUCT_I_II,(S_B-S_APEX))

P_I_III=DOT_PRODUCT(CROSS_PRODUCT_I_III,(S_B-S_APEX))

D_INV_S=MATMUL(D_INV(1:3,1:3),(S_B-S_APEX))

D_INV_L1=MATMUL(D_INV(1:3,1:3),L1)

D_INV_L2=MATMUL(D_INV(1:3,1:3),L2)

TT1=DOT_PRODUCT(L1_G,D_INV_S)/DOT_PRODUCT(L1_G,D_INV_L1)

TT2=DOT_PRODUCT(L2_G,D_INV_S)/DOT_PRODUCT(L2_G,D_INV_L2)

IF (TT1>0.0_8 .AND. TT2>0.0_8 .AND. F(COUNTER)>0.0_8) THEN
REG(COUNTER)=4
T1(COUNTER)=TT1
T2(COUNTER)=TT2
ELSE

IF (P_I_II>=0.0_8 .AND. P_I_III<=0.0_8 .AND. F(COUNTER)>0.0_8)THEN

!PLANE, REGION 1
REG(COUNTER)=1
ELSE IF(P_I_II<0.0_8.AND.P_I_III<0.0_8.AND. F(COUNTER)>0.0_8)THEN

!LINE1, REGION 2
REG(COUNTER)=2
ELSE IF (P_I_II>0.0_8.AND.P_I_III>0.0_8.AND.F(COUNTER)>0.0_8)THEN

!LINE2, REGION 3
REG(COUNTER)=3
END IF
END IF
COUNTER=COUNTER+1
END DO


IF (MAXVAL(REG,MASK=REG>0)==MINVAL(REG,MASK=REG>0)
1.AND. MAXVAL(REG,MASK=REG>0)==3) then
 REG(1)=0
 REG(2)=0
 REG(3)=0
 REG(4)=0
 REG(5)=0
 REG(6)=0
 END IF

IF (MAXVAL(REG,MASK=REG>0)==MINVAL(REG,MASK=REG>0)
1.AND. MAXVAL(REG,MASK=REG>0)==2) then
 REG(1)=0
 REG(2)=0
```

```fortran
      REG(3)=0
      REG(4)=0
      REG(5)=0
      REG(6)=0
      END IF


      END SUBROUTINE STRESS_POSITION


      PURE SUBROUTINE D_EP_ON_LINE_CORRECTION_FACTOR(S_B,S_C,K,M
     1,ACTIVE_PLANE1,ACTIVE_PLANE2,D,D_INV,D_EP_LINE)
! This subroutine calculates a correction factor for the calculation of the
stiffness matrix, calculated considering the steps in Chapter 8.3 in Clausen
(2007). The correction factor is needed as the matrix is singular in the
directions other than the direction of the plastic strain increment and thus can
lead to numerical instabilities.

      IMPLICIT NONE
      REAL(8), intent(in) :: D(4,4),D_INV(4,4),M,K,S_B(3),S_C(3)
      INTEGER(4), intent(in) :: ACTIVE_PLANE1,ACTIVE_PLANE2
      REAL(8), intent(out) :: D_EP_LINE(4,4)

      INTEGER(4) PLANE_ACT,II,JJ
      REAL(8) L1(3),L1_G(3),COMB_LINE(3,3),D_INV_L1_G(3),DENOM_DEP_LINE
      REAL(8) C_VEK(3),E_PLAST(3)

       interface

            pure subroutine CROSS(AAAA,BBBB,CCCC)
      IMPLICIT NONE
      REAL(8), intent (in) :: AAAA(3),BBBB(3)
      REAL(8), intent (out) :: CCCC(3)
            end subroutine CROSS

       end interface

      E_PLAST=MATMUL(D_INV(1:3,1:3),S_B-S_C)

      IF (ACTIVE_PLANE1==1 .AND. ACTIVE_PLANE2==2) THEN
      PLANE_ACT=1
      END IF

      IF (ACTIVE_PLANE1==2 .AND. ACTIVE_PLANE2==1) THEN
      PLANE_ACT=1
      END IF

      IF (ACTIVE_PLANE1==2 .AND. ACTIVE_PLANE2==3) THEN
      PLANE_ACT=2
      END IF

      IF (ACTIVE_PLANE1==3 .AND. ACTIVE_PLANE2==2) THEN
      PLANE_ACT=2
      END IF

      IF (ACTIVE_PLANE1==3 .AND. ACTIVE_PLANE2==4) THEN
      PLANE_ACT=3
      END IF

      IF (ACTIVE_PLANE1==4 .AND. ACTIVE_PLANE2==3) THEN
      PLANE_ACT=3
      END IF
```

```fortran
IF (ACTIVE_PLANE1==4 .AND. ACTIVE_PLANE2==5) THEN
PLANE_ACT=4
END IF

IF (ACTIVE_PLANE1==5 .AND. ACTIVE_PLANE2==4) THEN
PLANE_ACT=4
END IF

IF (ACTIVE_PLANE1==5 .AND. ACTIVE_PLANE2==6) THEN
PLANE_ACT=5
END IF

IF (ACTIVE_PLANE1==6 .AND. ACTIVE_PLANE2==5) THEN
PLANE_ACT=5
END IF

IF (ACTIVE_PLANE1==6 .AND. ACTIVE_PLANE2==1) THEN
PLANE_ACT=6
END IF

IF (ACTIVE_PLANE1==1 .AND. ACTIVE_PLANE2==6) THEN
PLANE_ACT=6
END IF

IF (PLANE_ACT .EQ. 1) THEN
L1(1)=1.0_8
L1(2)=1.0_8
L1(3)=K

L1_G(1)=1.0_8
L1_G(2)=1.0_8
L1_G(3)=M
ELSE IF (PLANE_ACT .EQ. 2) THEN
L1(1)=K
L1(2)=1.0_8
L1(3)=K

L1_G(1)=M
L1_G(2)=1.0_8
L1_G(3)=M
ELSE IF (PLANE_ACT .EQ. 3) THEN
L1(1)=K
L1(2)=1.0_8
L1(3)=1.0_8

L1_G(1)=M
L1_G(2)=1.0_8
L1_G(3)=1.0_8
ELSE IF (PLANE_ACT .EQ. 4) THEN
L1(1)=K
L1(2)=K
L1(3)=1.0_8

L1_G(1)=M
L1_G(2)=M
L1_G(3)=1.0_8
ELSE IF (PLANE_ACT .EQ. 5) THEN
L1(1)=1.0_8
L1(2)=K
L1(3)=1.0_8

L1_G(1)=1.0_8
```

```fortran
      L1_G(2)=M
      L1_G(3)=1.0_8
      ELSE IF (PLANE_ACT .EQ. 6) THEN
      L1(1)=1.0_8
      L1(2)=K
      L1(3)=K

      L1_G(1)=1.0_8
      L1_G(2)=M
      L1_G(3)=M
      END IF

      CALL CROSS(E_PLAST(1:3),L1_G,C_VEK(1:3))

      FORALL(II=1:3,JJ=1:3) COMB_LINE(II,JJ)=C_VEK(II)*C_VEK(JJ)

      D_INV_L1_G=MATMUL(D_INV(1:3,1:3),C_VEK)

      DENOM_DEP_LINE=DOT_PRODUCT(C_VEK,D_INV_L1_G)

      D_EP_LINE=0.0_8
      D_EP_LINE(1:3,1:3)=COMB_LINE/DENOM_DEP_LINE
      D_EP_LINE(4,4)=D(4,4)

      END SUBROUTINE D_EP_ON_LINE_CORRECTION_FACTOR

       pure subroutine Jacobi(a,x,abserr,n,AA)
        !===========================================================
        ! Evaluate eigenvalues and eigenvectors
        ! of a real symmetric matrix a(n,n): a*x = lambda*x
        ! method: Jacoby method for symmetric matrices
        ! Alex G. (December 2009)
        !from: https://github.com/minar09/parallel-
computing/blob/master/OMP_Fortran.f90
        !-----------------------------------------------------------
        ! input ...
        ! a(n,n) - array of coefficients for matrix A
        ! n      - number of equations
        ! abserr - abs tolerance [sum of (off-diagonal elements)^2]
        ! output ...
        ! a(i,i) - eigenvalues
        ! x(i,j) - eigenvectors
        ! comments ...
        !===========================================================
        implicit none
        INTEGER(4), intent(in) :: n
        REAL(8), intent(in) :: A(n,n),abserr
        REAL(8), intent(out) :: AA(n,n),x(n,n)
        REAL(8)  b2, bar
        REAL(8) beta, coeff, c, s, cs, sc
        INTEGER(4) i, j, k
        ! initialize x(i,j)=0, x(i,i)=1
        ! *** the array operation x=0.0 is specific for Fortran 90/95
      AA=a
        x = 0.0_8
        do i=1,n
              x(i,i) = 1.0_8
        end do

        ! find the sum of all off-diagonal elements (squared)
        b2 = 0.0_8
        do i=1,n
```

```fortran
        do j=1,n
          if (i.ne.j) b2 = b2 + AA(i,j)**2.0_8
        end do
      end do

      if (b2 <= abserr) return

      ! average for off-diagonal elements /2
      bar = 0.5_8*b2/dble(n*n)

      do while (b2.gt.abserr)
        do i=1,n-1
          do j=i+1,n
            if (AA(j,i)**2.0_8 <= bar) cycle  ! do not touch small elements
            b2 = b2 - 2.0_8*AA(j,i)**2.0_8
            bar = 0.5_8*b2/dble(n*n)
      ! calculate coefficient c and s for Givens matrix
            beta = (AA(j,j)-AA(i,i))/(2.0_8*AA(j,i))
            coeff = 0.5_8*beta/sqrt(1.0_8+beta**2.0_8)
            s = sqrt(max(0.5_8+coeff,0.0_8))
            c = sqrt(max(0.5_8-coeff,0.0_8))
      ! recalculate rows i and j
            do k=1,n
              cs =  c*AA(i,k)+s*AA(j,k)
              sc = -s*AA(i,k)+c*AA(j,k)
              AA(i,k) = cs
              AA(j,k) = sc
            end do
      ! new matrix a_{k+1} from a_{k}, and eigenvectors
            do k=1,n
              cs =  c*AA(k,i)+s*AA(k,j)
              sc = -s*AA(k,i)+c*AA(k,j)
              AA(k,i) = cs
              AA(k,j) = sc
              cs =  c*x(k,i)+s*x(k,j)
              sc = -s*x(k,i)+c*x(k,j)
              x(k,i) = cs
              x(k,j) = sc
            end do
          end do
        end do
      end do

      end subroutine



      PURE SUBROUTINE CROSS(AAAA,BBBB,CCCC)
! Calculates the cross product
      REAL(8), intent (in) :: AAAA(3),BBBB(3)
      REAL(8), intent (out) :: CCCC(3)

      CCCC(1)=AAAA(2)*BBBB(3)-AAAA(3)*BBBB(2)
      CCCC(2)=AAAA(3)*BBBB(1)-AAAA(1)*BBBB(3)
      CCCC(3)=AAAA(1)*BBBB(2)-AAAA(2)*BBBB(1)

      end subroutine




      PURE SUBROUTINE COORD_TRANS_MATRIX(LAMBDA_IJ,S,S_B,AA)
```

```
! This subroutine is needed to calculate the coordinate transformation matrix,
needed when transforming the updated stress from principal to local coordinate
system defined for a 2D problem after Appenidx B in Chapter B.1 in Clausen et al.
(2007)
      IMPLICIT NONE
      REAL(8), intent(in) :: LAMBDA_IJ(3,3),S(3),S_B(3)
      REAL(8), intent(out) :: AA(4,4)

      REAL(8) A_5(6,6)


      A_5(1,1)=LAMBDA_IJ(1,1)*LAMBDA_IJ(1,1)
      A_5(1,2)=LAMBDA_IJ(2,1)*LAMBDA_IJ(2,1)
      A_5(1,3)=LAMBDA_IJ(3,1)*LAMBDA_IJ(3,1)
      A_5(1,4)=LAMBDA_IJ(1,1)*LAMBDA_IJ(2,1)
      A_5(1,5)=LAMBDA_IJ(3,1)*LAMBDA_IJ(1,1)
      A_5(1,6)=LAMBDA_IJ(2,1)*LAMBDA_IJ(3,1)

      A_5(2,1)=LAMBDA_IJ(1,2)*LAMBDA_IJ(1,2)
      A_5(2,2)=LAMBDA_IJ(2,2)*LAMBDA_IJ(2,2)
      A_5(2,3)=LAMBDA_IJ(3,2)*LAMBDA_IJ(3,2)
      A_5(2,4)=LAMBDA_IJ(1,2)*LAMBDA_IJ(2,2)
      A_5(2,5)=LAMBDA_IJ(3,2)*LAMBDA_IJ(1,2)
      A_5(2,6)=LAMBDA_IJ(2,2)*LAMBDA_IJ(3,2)

      A_5(3,1)=LAMBDA_IJ(1,3)*LAMBDA_IJ(1,3)
      A_5(3,2)=LAMBDA_IJ(2,3)*LAMBDA_IJ(2,3)
      A_5(3,3)=LAMBDA_IJ(3,3)*LAMBDA_IJ(3,3)
      A_5(3,4)=LAMBDA_IJ(1,3)*LAMBDA_IJ(2,3)
      A_5(3,5)=LAMBDA_IJ(3,3)*LAMBDA_IJ(1,3)
      A_5(3,6)=LAMBDA_IJ(2,3)*LAMBDA_IJ(3,3)

      A_5(4,1)=2*LAMBDA_IJ(1,1)*LAMBDA_IJ(1,2)
      A_5(4,2)=2*LAMBDA_IJ(2,1)*LAMBDA_IJ(2,2)
      A_5(4,3)=2*LAMBDA_IJ(3,1)*LAMBDA_IJ(3,2)
      A_5(4,4)=LAMBDA_IJ(1,1)*LAMBDA_IJ(2,2)+LAMBDA_IJ(1,2)
     1*LAMBDA_IJ(2,1)
      A_5(4,5)=LAMBDA_IJ(3,1)*LAMBDA_IJ(1,2)+LAMBDA_IJ(3,2)
     1*LAMBDA_IJ(1,1)
      A_5(4,6)=LAMBDA_IJ(2,1)*LAMBDA_IJ(3,2)+LAMBDA_IJ(2,2)
     1*LAMBDA_IJ(3,1)

      A_5(5,1)=2*LAMBDA_IJ(1,3)*LAMBDA_IJ(1,1)
      A_5(5,2)=2*LAMBDA_IJ(2,3)*LAMBDA_IJ(2,1)
      A_5(5,3)=2*LAMBDA_IJ(3,3)*LAMBDA_IJ(3,1)
      A_5(5,4)=LAMBDA_IJ(1,3)*LAMBDA_IJ(2,1)+LAMBDA_IJ(1,1)
     1*LAMBDA_IJ(2,3)
      A_5(5,5)=LAMBDA_IJ(3,3)*LAMBDA_IJ(1,1)+LAMBDA_IJ(3,1)
     1*LAMBDA_IJ(1,3)
      A_5(5,6)=LAMBDA_IJ(2,3)*LAMBDA_IJ(3,1)+LAMBDA_IJ(2,1)
     1*LAMBDA_IJ(3,3)

      A_5(6,1)=2*LAMBDA_IJ(1,2)*LAMBDA_IJ(1,3)
      A_5(6,2)=2*LAMBDA_IJ(2,2)*LAMBDA_IJ(2,3)
      A_5(6,3)=2*LAMBDA_IJ(3,2)*LAMBDA_IJ(3,3)
      A_5(6,4)=LAMBDA_IJ(1,2)*LAMBDA_IJ(2,3)+LAMBDA_IJ(1,3)
     1*LAMBDA_IJ(2,2)
      A_5(6,5)=LAMBDA_IJ(3,2)*LAMBDA_IJ(1,3)+LAMBDA_IJ(3,3)
     1*LAMBDA_IJ(1,2)
      A_5(6,6)=LAMBDA_IJ(2,2)*LAMBDA_IJ(3,3)+LAMBDA_IJ(2,3)
     1*LAMBDA_IJ(3,2)
```

```
IF (S(3)==S_B(3)) THEN

AA(1,1)=A_5(1,1)
AA(2,1)=A_5(2,1)
AA(3,1)=A_5(3,1)
AA(4,1)=A_5(4,1)

AA(1,2)=A_5(1,2)
AA(2,2)=A_5(2,2)
AA(3,2)=A_5(3,2)
AA(4,2)=A_5(4,2)

AA(1,3)=A_5(1,3)
AA(2,3)=A_5(2,3)
AA(3,3)=A_5(3,3)
AA(4,3)=A_5(4,3)

AA(1,4)=A_5(1,4)
AA(2,4)=A_5(2,4)
AA(3,4)=A_5(3,4)
AA(4,4)=A_5(4,4)

ELSEIF (S(2)==S_B(3)) THEN

AA(1,1)=A_5(1,1)
AA(2,1)=A_5(2,1)
AA(3,1)=A_5(3,1)
AA(4,1)=A_5(5,1)

AA(1,2)=A_5(1,2)
AA(2,2)=A_5(2,2)
AA(3,2)=A_5(3,2)
AA(4,2)=A_5(5,2)

AA(1,3)=A_5(1,3)
AA(2,3)=A_5(2,3)
AA(3,3)=A_5(3,3)
AA(4,3)=A_5(5,3)

AA(1,4)=A_5(1,4)
AA(2,4)=A_5(2,4)
AA(3,4)=A_5(3,4)
AA(4,4)=A_5(5,4)

ELSEIF (S(1)==S_B(3)) THEN

AA(1,1)=A_5(1,1)
AA(2,1)=A_5(2,1)
AA(3,1)=A_5(3,1)
AA(4,1)=A_5(6,1)

AA(1,2)=A_5(1,2)
AA(2,2)=A_5(2,2)
AA(3,2)=A_5(3,2)
AA(4,2)=A_5(6,2)

AA(1,3)=A_5(1,3)
AA(2,3)=A_5(2,3)
AA(3,3)=A_5(3,3)
AA(4,3)=A_5(6,3)

AA(1,4)=A_5(1,4)
```

```
      AA(2,4)=A_5(2,4)
      AA(3,4)=A_5(3,4)
      AA(4,4)=A_5(6,4)

      END IF

      END SUBROUTINE COORD_TRANS_MATRIX


      PURE SUBROUTINE TRANSFORMATION_MATRIX(S_C_RET,S_PRINC_S
     1,S_B,TRANS_MAT)
! This subroutine calculates the modification matrix needed to calculate the
stiffness matrix of the finite step, calculated after Chapter B.2 of Appendix B
in Clausen et al. 2007.
      IMPLICIT NONE
      REAL(8), intent(in) :: S_C_RET(3),S_PRINC_S(3),S_B(3)
      REAL(8), intent(out) :: TRANS_MAT(4,4)

      INTEGER(4) VALORE_UNO,VALORE_DUE

      TRANS_MAT=0.0_8
      TRANS_MAT(1,1)=1.0_8
      TRANS_MAT(2,2)=1.0_8
      TRANS_MAT(3,3)=1.0_8

      IF (S_PRINC_S(3)==S_B(3)) THEN
      VALORE_UNO=1
      VALORE_DUE=2
      ELSEIF (S_PRINC_S(2)==S_B(3)) THEN
      VALORE_UNO=1
      VALORE_DUE=3
      ELSEIF (S_PRINC_S(1)==S_B(3)) THEN
      VALORE_UNO=2
      VALORE_DUE=3
      END IF

      IF (S_C_RET(VALORE_UNO)-S_C_RET(VALORE_DUE)>0.0_8) THEN
      TRANS_MAT(4,4)=(S_C_RET(VALORE_UNO)-S_C_RET(VALORE_DUE))
     1/(S_PRINC_S(VALORE_UNO)-S_PRINC_S(VALORE_DUE))
      END IF

      END SUBROUTINE TRANSFORMATION_MATRIX


      PURE SUBROUTINE PRINT_DIR(SS_0,LAMBDA_IJ_IN,SS
     1,LAMBDA_IJ,PROBLEMA)
! This subroutine calculates the coordinate transformation matrix needed to
calculate the stresses from principal to local coordinate system.
      IMPLICIT NONE
      REAL(8), intent(in) :: SS_0(3)
     1,LAMBDA_IJ_IN(3,3)
      REAL(8), intent(out) :: LAMBDA_IJ(3,3), SS(3)
      INTEGER(4), intent(out) :: PROBLEMA

      REAL(8) CROSS_PROD(3)
      INTEGER(4) L_MAX(1),L_MIN(1),L_MED(1)


       !---- Explicit interfaces ---------------------
       interface
```

```fortran
         pure subroutine CROSS(AAAA,BBBB,CCCC)
IMPLICIT NONE
REAL(8), intent (in) :: AAAA(3),BBBB(3)
REAL(8), intent (out) :: CCCC(3)
         end subroutine CROSS

 end interface

PROBLEMA=0

IF (SS_0(1)==SS_0(2) .AND. SS_0(1)==SS_0(3)) THEN

SS=SS_0
LAMBDA_IJ=LAMBDA_IJ_IN

ELSE
        L_MAX=MAXLOC(SS_0)
        L_MIN=MINLOC(SS_0)
        L_MED(1)=6-L_MAX(1)-L_MIN(1)

        LAMBDA_IJ(:,1)=LAMBDA_IJ_IN(:,L_MAX(1))
        LAMBDA_IJ(:,2)=LAMBDA_IJ_IN(:,L_MED(1))
        LAMBDA_IJ(:,3)=LAMBDA_IJ_IN(:,L_MIN(1))

        SS(1)=SS_0(L_MAX(1))
        SS(2)=SS_0(L_MED(1))
        SS(3)=SS_0(L_MIN(1))

        IF (SS(1)==SS(2)) then
        CALL CROSS(LAMBDA_IJ(:,1),LAMBDA_IJ(:,2),CROSS_PROD)
            IF (CROSS_PROD(1)==LAMBDA_IJ(1,3) .AND. CROSS_PROD(2)
1==LAMBDA_IJ(2,3).AND. CROSS_PROD(3)==LAMBDA_IJ(3,3)) THEN
            LAMBDA_IJ(:,1)=LAMBDA_IJ_IN(:,L_MED(1))
            LAMBDA_IJ(:,2)=LAMBDA_IJ_IN(:,L_MAX(1))
            end if
        end if

        IF (SS(1)==SS(2)) then
        CALL CROSS(LAMBDA_IJ(:,1),LAMBDA_IJ(:,2),CROSS_PROD)
            IF (CROSS_PROD(1)==LAMBDA_IJ(1,3) .AND. CROSS_PROD(2)
1==LAMBDA_IJ(2,3).AND. CROSS_PROD(3)==LAMBDA_IJ(3,3)) THEN
            PROBLEMA=1
!            stop
            end if
        end if

        IF (SS(2)==SS(3)) then
        CALL CROSS(LAMBDA_IJ(:,1),LAMBDA_IJ(:,2),CROSS_PROD)
            IF (CROSS_PROD(1)==LAMBDA_IJ(1,3) .AND. CROSS_PROD(2)
1==LAMBDA_IJ(2,3).AND. CROSS_PROD(3)==LAMBDA_IJ(3,3)) THEN
            LAMBDA_IJ(:,2)=LAMBDA_IJ_IN(:,L_MIN(1))
            LAMBDA_IJ(:,3)=LAMBDA_IJ_IN(:,L_MED(1))
            end if
        end if

        IF (SS(2)==SS(3)) then
        CALL CROSS(LAMBDA_IJ(:,1),LAMBDA_IJ(:,2),CROSS_PROD)
            IF (CROSS_PROD(1)==LAMBDA_IJ(1,3) .AND. CROSS_PROD(2)
1==LAMBDA_IJ(2,3).AND. CROSS_PROD(3)==LAMBDA_IJ(3,3)) THEN
            PROBLEMA=1
!            stop
            end if
```

```
        end if
END IF


END SUBROUTINE PRINT_DIR
```

Appendix C. Validation of the creep constitutive model MC-Perzyna

This Appendix is structured in three parts and will show the validation of the MC-Perzyna constitutive model implemented in the present thesis. Results of numerical computations considering the MC-Perzyna constitutive model are compared with analytical solutions. In the first section numerical results are compared with results of the analytical solution at laboratory scale derived considering Appendix A. In the second section numerical results of an unsupported tunnel under plane strain conditions are compared with the analytical solutions of an elastic ground after Kirsch (1898) and with the analytical solution of an elastoplastic ground after Anagnostou and Kovári (1993). In the third section numerical results of an axisymmetric TBM step-by-step excavation process are compared with results of Ramoni & Anagnostou (2010b).

C.1. Laboratory scale

One axial symmetric element in the local coordinate system r, y and θ (being radial, axial and out of plane respectively) is subjected to an instantaneous axial compressive stress increment ($\Delta\sigma_y$ at $t = 0^+$) of 10 MPa which then remains constant in time (see the inset in Figure C.1), with parameters given in the same Figure. The ground is modelled considering the MC Perzyna constitutive model discussed in Appendix A, the subroutine of which is given in Appendix B. The initial stress state is $\sigma_r = \sigma_y = \sigma_\theta = 0$. Additional boundary conditions of the problem are $\sigma_r = 0$ and $\varepsilon_\theta = 0$. From the boundary condition results that the principal stresses are $\sigma_y = \sigma_1$, $\sigma_\theta = \sigma_2$, $\sigma_r = \sigma_3$ with $\sigma_1 > \sigma_2 > \sigma_3$ as defined in Appendix A. Due to the boundary conditions of the problem and the material behaving instantaneously only elastically, *i.e.* $\Delta\varepsilon_{vp}$ ($t = 0^+$) = 0, the total strain increment at $t = 0^+$ is equal to the elastic strain increment and can be calculated after Eq. A.1 which is for each component as follows:

$$\begin{cases} \varepsilon_y(t=0^+) = \Delta\varepsilon_1^{el} = \dfrac{\Delta\sigma_1}{E} - \dfrac{\upsilon\Delta\sigma_2}{E} - \dfrac{\upsilon\Delta\sigma_3}{E} = 0.91\% \\[2ex] \varepsilon_\theta(t=0^+) = \Delta\varepsilon_2^{el} = -\dfrac{\upsilon\Delta\sigma_1}{E} + \dfrac{\Delta\sigma_2}{E} - \dfrac{\upsilon\Delta\sigma_3}{E} = 0 \qquad , \rightarrow \Delta\sigma_2 = \Delta\sigma_\theta = 3\text{MPa} \\[2ex] \varepsilon_r(t=0^+) = \Delta\varepsilon_3^{el} = -\dfrac{\upsilon\Delta\sigma_1}{E} - \dfrac{\upsilon\Delta\sigma_2}{E} + \dfrac{\Delta\sigma_3}{E} = -0.39\% \end{cases} , \quad (\text{C.1})$$

For $t > 0^+$ viscous deformations start to develop and the viscoplastic strain must be added to the instantaneous elastic part. The viscoplastic strain is calculated by integrating Eq. A.9 (the first from the three given equations is valid as $\sigma_1 > \sigma_2 > \sigma_3$). Thus, the total strain is equal to

$$\begin{cases} \varepsilon_y(t > 0^+) = \Delta\varepsilon_1^{el} + \Delta\varepsilon_1^{vp} = \dfrac{\Delta\sigma_1}{E} - \dfrac{\upsilon\Delta\sigma_2}{E} - -\dfrac{\upsilon\Delta\sigma_3}{E} + \dfrac{f_1}{\eta} \\[3mm] \varepsilon_\theta(t > 0^+) = \Delta\varepsilon_2^{el} + \Delta\varepsilon_2^{vp} = -\dfrac{\upsilon\Delta\sigma_1}{E} + \dfrac{\Delta\sigma_2}{E} - \dfrac{\upsilon\Delta\sigma_3}{E} \\[3mm] \varepsilon_r(t > 0^+) = \Delta\varepsilon_3^{el} + \Delta\varepsilon_3^{vp} = -\dfrac{\upsilon\Delta\sigma_1}{E} - \dfrac{\upsilon\Delta\sigma_2}{E} + \dfrac{\Delta\sigma_3}{E} - \dfrac{f_1}{\eta}\kappa \end{cases}, \quad (C.2)$$

where f_1 is equal to 9 MPa, after Eq. A.2.

Figure C.1 compares the axial and radial strains as function of time determined from the numerical computation considering the subroutine in Appendix B (black line) and the analytically derived results (red line) considering equations C.1 and C.2. As visible the results coincide.
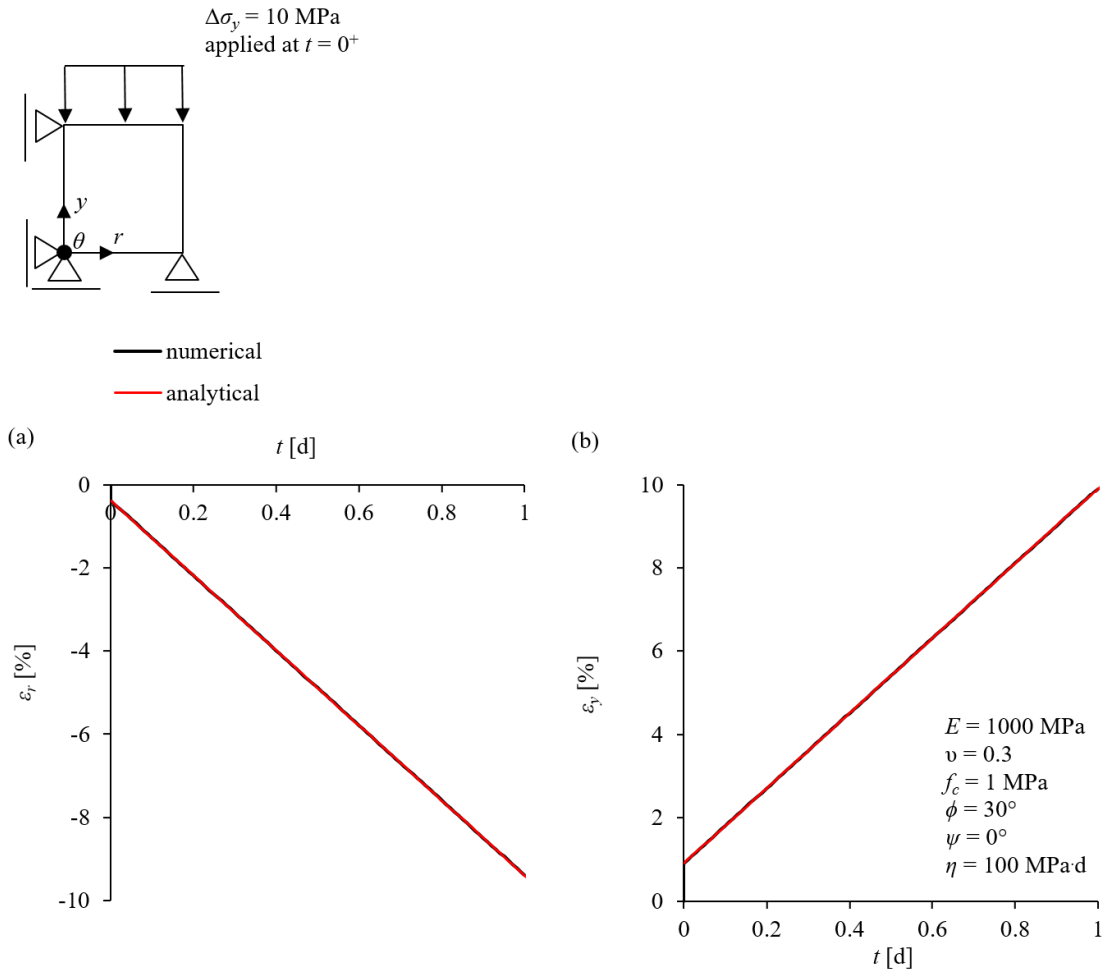

Figure C.1.   (a) Radial and (b) axial strains function of time

C.2. Plane strain unsupported tunnel

The present section shows the validation and plausibility of the constitutive model, MC-Perzyna, for an unsupported tunnel under plane strain conditions. The computational model is the same as presented in Section 4.2.2 and shown in Figure 4.1a.

For the considered constitutive model, the ground will behave instantly as an elastic material, in time viscous deformations will develop until all viscoplastic deformation took place and steady state conditions are achieved (*cf.* Section 2.2). Thus, results for five different viscosities η are presented herein and compared with analytical solutions:

1. $\eta = \infty$, compared with Kirsch's (1898) analytical solution, *cf.* Figure C.2a
2. $\eta = 0$, compared with Anagnostou & Kovári's (1993) analytical solution, *cf.* Figure C.2a
3. Three intermediate viscosities between 0 and ∞, *cf.* Figure C.2b

Both analytical solutions consider the same boundary value problem of an unsupported tunnel under plane strain conditions. On the one hand Kirsch's (1898) solution for an elastic material and on the other hand Anagnostou & Kovári's (1993) solution for an elastic-perfectly plastic material with MC yield condition and non-associated flow rule.

As visible the numerical result for infinite viscosity (practically elastic) coincides with Kirsch's solution, same can be said for zero viscosity (practically elasto-plastic) with Anagnostou & Kovári's (1993) solution. For the three intermediate values it is visible that instantaneous results coincide with Kirsch's solution and steady state results coincide with Anagnostou & Kovari's (1993) solution. The time-development of results for these three viscosities is plausible, as the displacements develop at different rates, more specifically, the time development is inverse proportional to the viscosity as defined in Eq. 2.4 in Section 2.2.
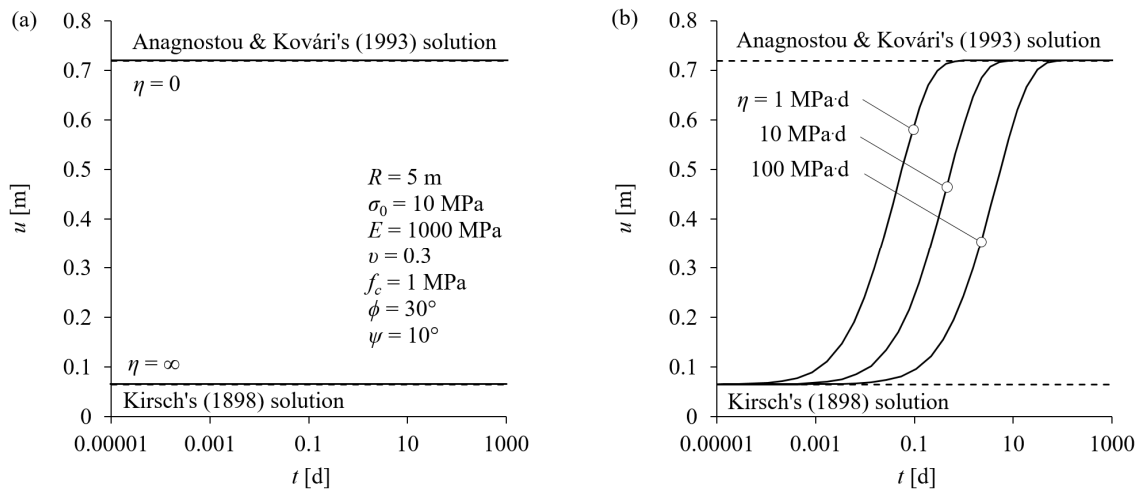

Figure C.2   Evolution of the radial displacements at the tunnel boundary of an unsupported tunnel with parameters given in figure for (a) $\eta = 0$ and ∞, (b) three different viscosities with values given in figure (a).

C.3. TBM step-by-step excavation

The computational model used for validation of the MC-Perzyna constitutive model in the present section is a TBM step-by-step excavation under axisymmetric conditions (presented in Section 2.3). The purpose of the present section is dual: (i) to validate the MC-Perzyna constitutive model for the case of zero viscosity; (ii) to assess the adequacy of the selected round length for the step-by-step simulations considered in Chapter 3 in order to develop the design equation for estimating the required thrust force in creeping rock under squeezing conditions. Results of the considered constitutive model are compared with results of Ramoni & Anagnostou (2010b), which have been performed using the steady state method (Nguyen Minh and Corbetta 1991) and consider a time independent elastic perfectly plastic constitutive model with a MC yield condition and a non-associated flow rule, for further details regarding this computational model the reader is referred to Ramoni & Anagnostou (2010b).

Figure C.3a shows the longitudinal rock pressure distribution after Ramoni & Anagnostou (2010b) and the computational results considering the MC-Perzyna constitutive model for different round length s (ranging from 0.1 m to 1 m). Evidently, the smaller the round length of the step-by-step simulation is, the closer the results to the numerical results of Ramoni & Anagnostou (2010b). Thus, the MC-Perzyna constitutive model is able to map for zero viscosity the same behaviour as a time-independent elastic-perfectly plastic constitutive model with MC yield condition.

Figure C.3b shows the average rock pressure for different round length, for the results shown in Figure C.3a, which is needed in order to determine the thrust force in order to overcome shield jamming. In this figure the results for a round length equal to zero ($s = 0$) are the results of Ramoni & Anagnostou (2010b), black solid line in Figure C.3a. In Figure C.3c the error with respect to the results of Ramoni & Anagnostou (2010b) is shown, for results shown in Figure C.3b. As visible, round lengths between 0.1 and 0.5 m underestimate the numerical solution of Ramoni & Anagnostou (2010b) by 4 – 5 %, in accordance with the results shown in Figure C.3a which clearly underestimate Ramoni & Anagnostou (2010b) results. Although the peak at the shield tail is underestimated by a maximum of 33% for $s = 0.5$ m this leads to only an underestimation of 5% of the average rock pressure. In the case of a a round length of 1 m the results of Ramoni & Anagnostou (2010b) are overestimated by around 3%, this although the peak at the shield tail is underestimated by around 35% (and maximal for the four considered round lengths). The reason is the bigger element discretization and the overestimation next to the tunnel face, at around 2.5 m, *cf.* red dash dotted line compared to solid black line. As the error shown for all round lengths considered ($s = 0.1 - 1$ m) is smaller than ± 5 %, in order to save computational time, a round length of $s = 1$ m is considered for performing the numerical analyses in Chapter 3, as a total of 12,300 computations have been performed.

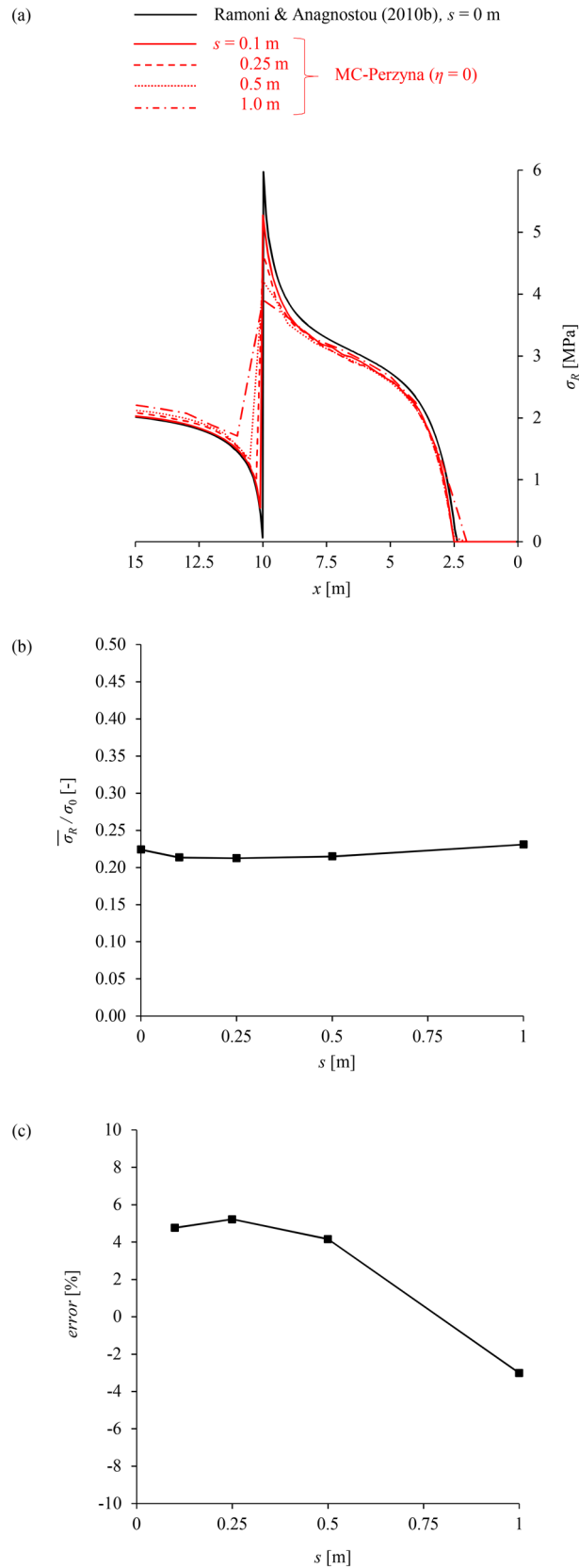Figure C.3   (a) Longitundinal rock pressure distribution, (b) Average rock pressure function of different round length, (b) Error of the step-by-step computation with respect to results of Ramoni & Anagnostou (2010b) ($s = 0$) (parameters: $R = 5$ m, $\Delta R = 0.05$ m, $L = 10$ m, $\sigma_0 = 10$ MPa, $E = 1$ GPa, $v = 0.25$, $f_c = 3$ MPa, $\phi = 25°$, $\psi = 5°$, $K_s = 1008$ MPa/m, $K_l = 360$ MPa/m).

Appendix D. Influence of pore pressures on the cutterhead pressure

D.1   Introduction

Section 4.5.2 discusses the unfavourable effect of seepage forces on the tunnel face, causing excessive extrusions, which can lead to cutterhead jamming. More specifically, Figure D.1 shows that for an *in-situ* pore pressure, p_0 of 1 and 4 MPa, the axial displacement prior contact is maximum at *ca*. 5 m above the centre of the face. For $p_0 = 1$ MPa, this effect vanishes (Fig. D.1; $t > 2.6$ d); however, for p_0 of 4 MPa, this effect remains and leads to a maximum pressure at the cutterhead closer to the tunnel boundary than to the centre of the tunnel (Fig. D.2). This pressure development is counter-intuitive, as one would expect the highest pressure to develop at the centre of the face, as seen for $p_0 = 1$ MPa (Fig. D.2).

The counter-intuitive behaviour is explained in Section D.2, and thus the behaviour prior contact with the cutterhead, whereas Section D.3 shows the behaviour after contact with the cutterhead.
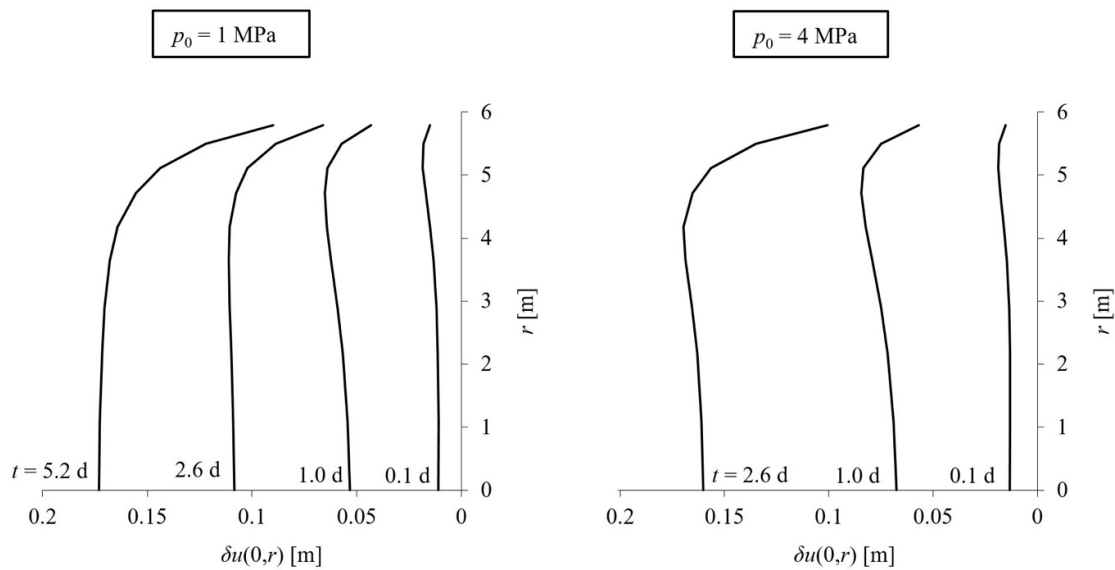

Figure D.1.   Radial distribution of the axial displacement of the face during standstill considering different time instances before contact with the cutterhead.
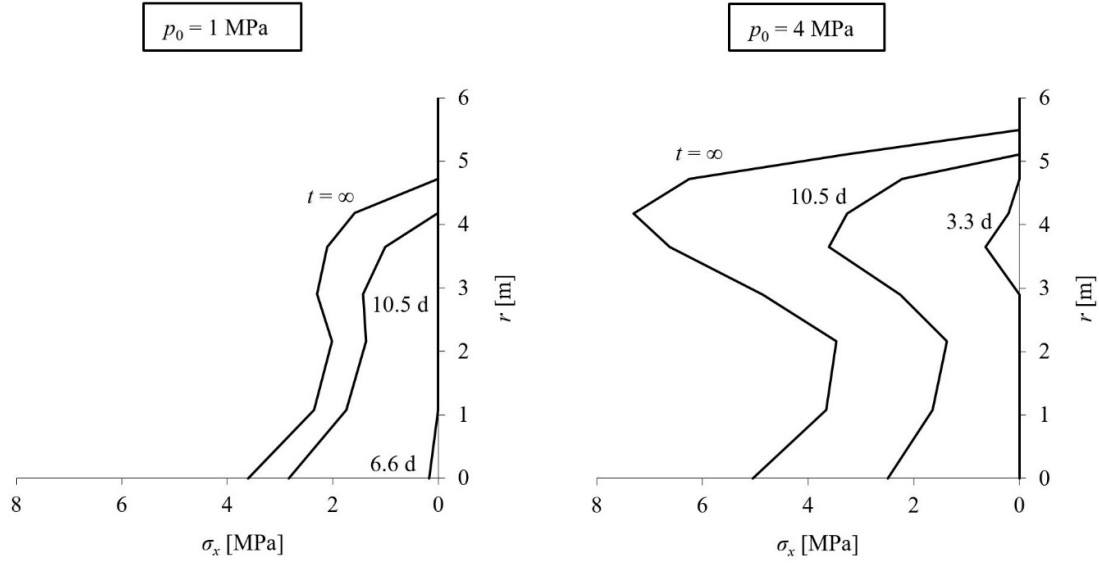
Figure D.2.   Radial distribution of the axial loading of the cutterhead during standstill at different time instances

D.2   Before contact with the cutterhead

This counter-intuitive behaviour is explained based on the following Figures D.3, D.4 and D.5. Figure D.3 shows the extrusion vs. time, Figure D.4 shows the plastic zone around the tunnel for different time instances prior contact with the cutterhead, and Figure D.5 shows the pore pressure contours for the same time instances as Figure D.4.

Both for $p_0 = 1$ MPa and 4 MPa, the plastic zones ahead of the face embed a core of elastic material in the initial state (Fig. D.4; $t = 0.1$d). This is due to the stabilisation offered by the negative pore pressures (Fig. D.5; $t = 0.1$d). This is wider at the centre of the face than further above, hence it stabilises the ground more at the centre, and this explains the smaller extrusion there than above.

As the plasticity is higher for $p_0 = 4$ MPa (*cf.* plastic zones in Fig. D.4), the ground undergoes larger extrusion, hence contact with the cutterhead is established first at around 3 days, half of the required *ca.* 6 days in the case $p_0 = 1$ MPa (Fig. D.3).

Over time, as the excess pore pressures start dissipating, the elastic core vanishes for both $p_0 = 1$ MPa and 4 MPa (Fig. D.4; $t > 0.1$d), hence the stiffening effect progressively vanishes, too.

At 2.6 days, shortly before contact is established in the case $p_0 = 4$ MPa, the stiffening effect has not yet vanished; this is also true for the lower $p_0 = 1$ MPa (Fig. D.1). Therefore, contact is established first at $r = ca.$ 5 m for $p_0 = 4$ MPa.

At around 6 days, however, when contact is established in the case $p_0 = 1$ MPa, sufficient time has elapsed for the stiffening effect to vanish, hence the largest extrusion is at the centre (Fig. D.1, $t = 5.2$ d) and thus contact is established first there (Fig. D.2; $t = 6.6$ d).

The point where contact occurs for the first time affects also the radial distribution of the axial pressure on the cutterhead, which is thus maximum at $r = 4$ - 5 m for $p_0 = 4$ MPa, and at the centre for $p_0 = 1$ MPa (Fig. D.2).
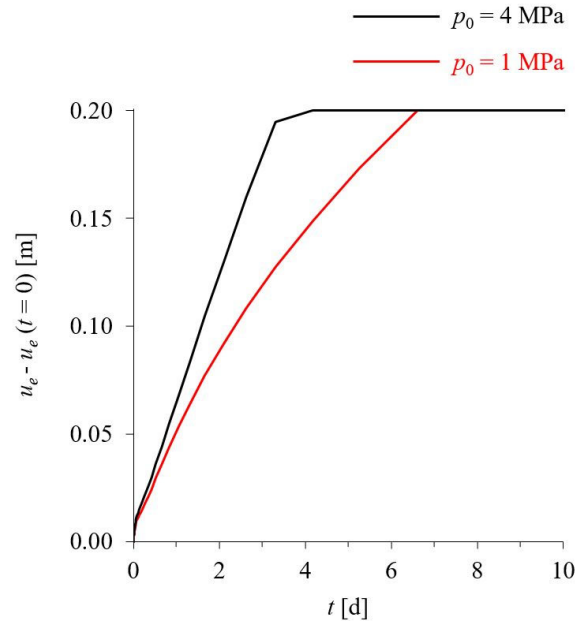
Figure D.3.   Time development of the face extrusion during standstill, at 0.2 m contact with the cutterhead is established.

$p_0 = 1$ MPa

$p_0 = 4$ MPa

lining   shield

lining   shield

$t = 0.1$ d

$t = 0.1$ d

$t = 1.0$ d

$t = 1.0$ d

$t = 2.6$ d

$t = 2.6$ d

$t = 5.2$ d
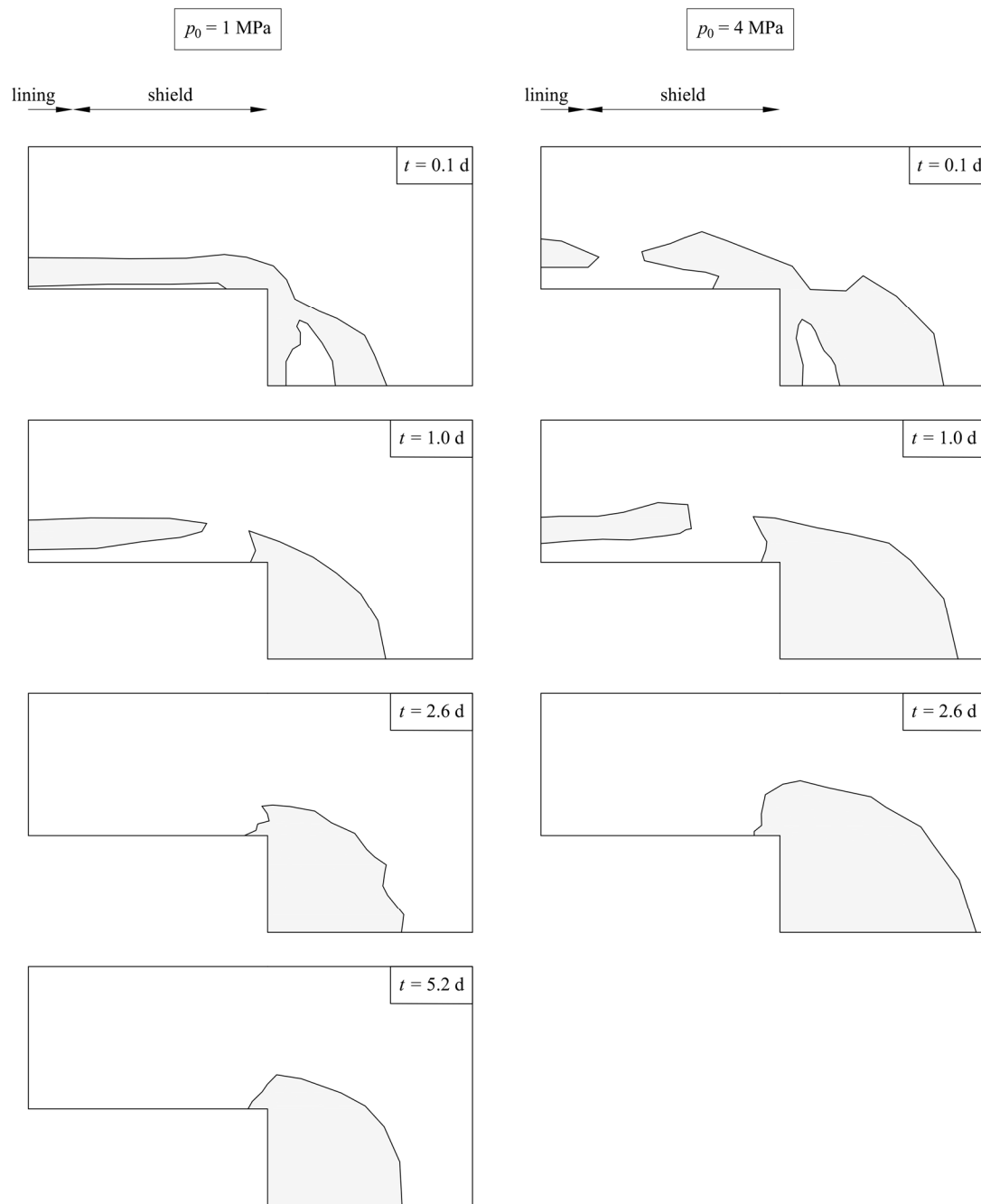
Figure D.4.   Plastic zone for different time instances before contact with the cutterhead.

$p_0 = 1$ MPa

$p_0 = 4$ MPa

lining   shield

lining   shield
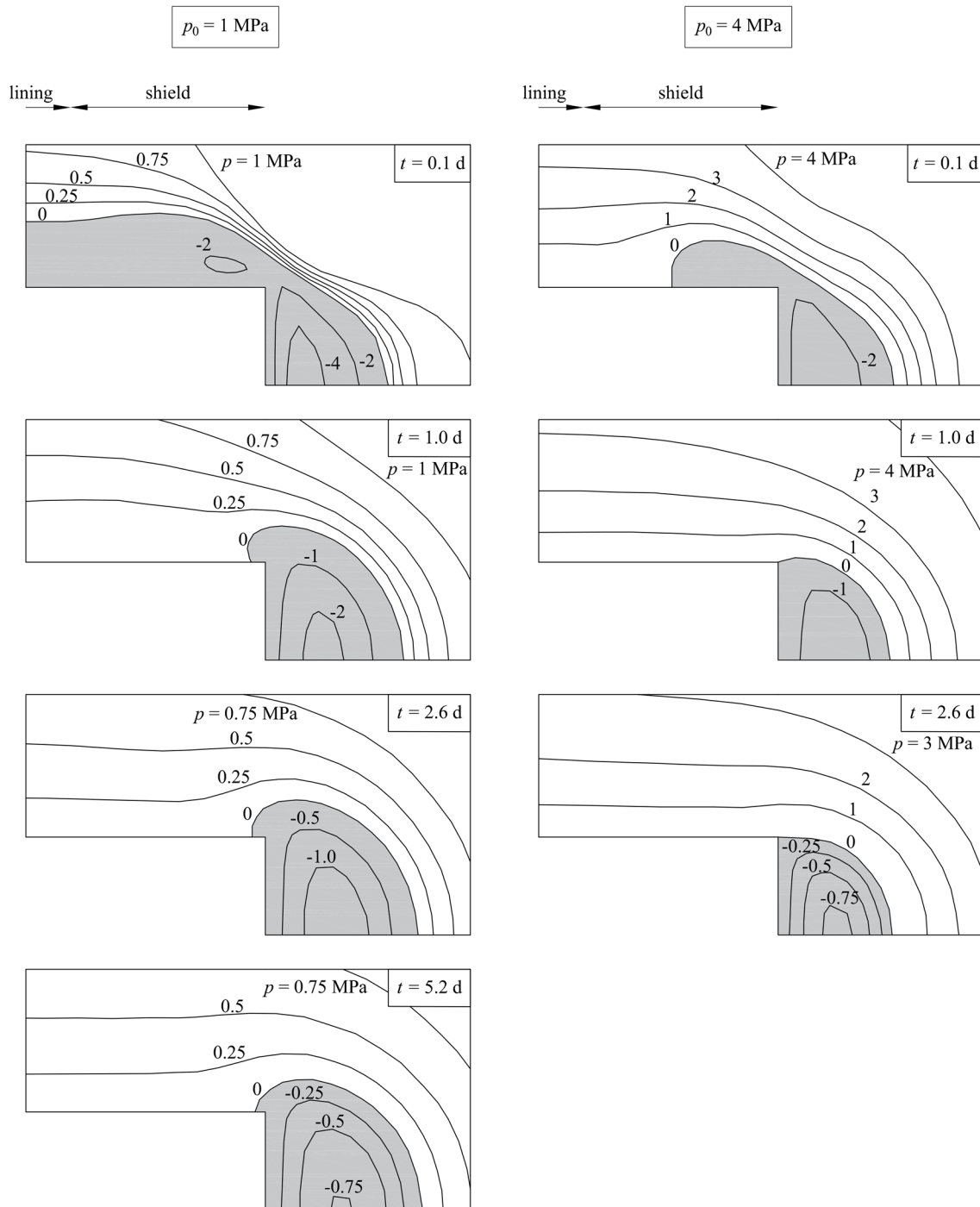
Figure D.5.   Contour-lines of pore pressure at different time instance before contact with the cutterhead.

D.3   After contact with the cutterhead

After contact, the plastic zones indicate that the ground returns to an elastic state, *cf.* Figure D.6, showing the plastic zone after contact with the cutterhead. This is attributed to the so called "elastic re-compression" (see Gärber 2003) and occurs also behind the shield, as shown by Ramoni and Anagnostou (2011c). The ground has experienced partially irreversible deformations; however, its stress state is located within the elastic domain, also called "past-yield zone" (Ramoni and Anagnostou 2011c).

$p_0 = 1$ MPa $p_0 = 4$ MPa

lining   shield   lining   shield

$t = 6.6$ d $t = 3.3$ d

$t = 10.5$ d $t = 10.5$ d

$t = \infty$ $t = \infty$

Figure D.6.   Plastic zone for different time instances after contact with the cutterhead.

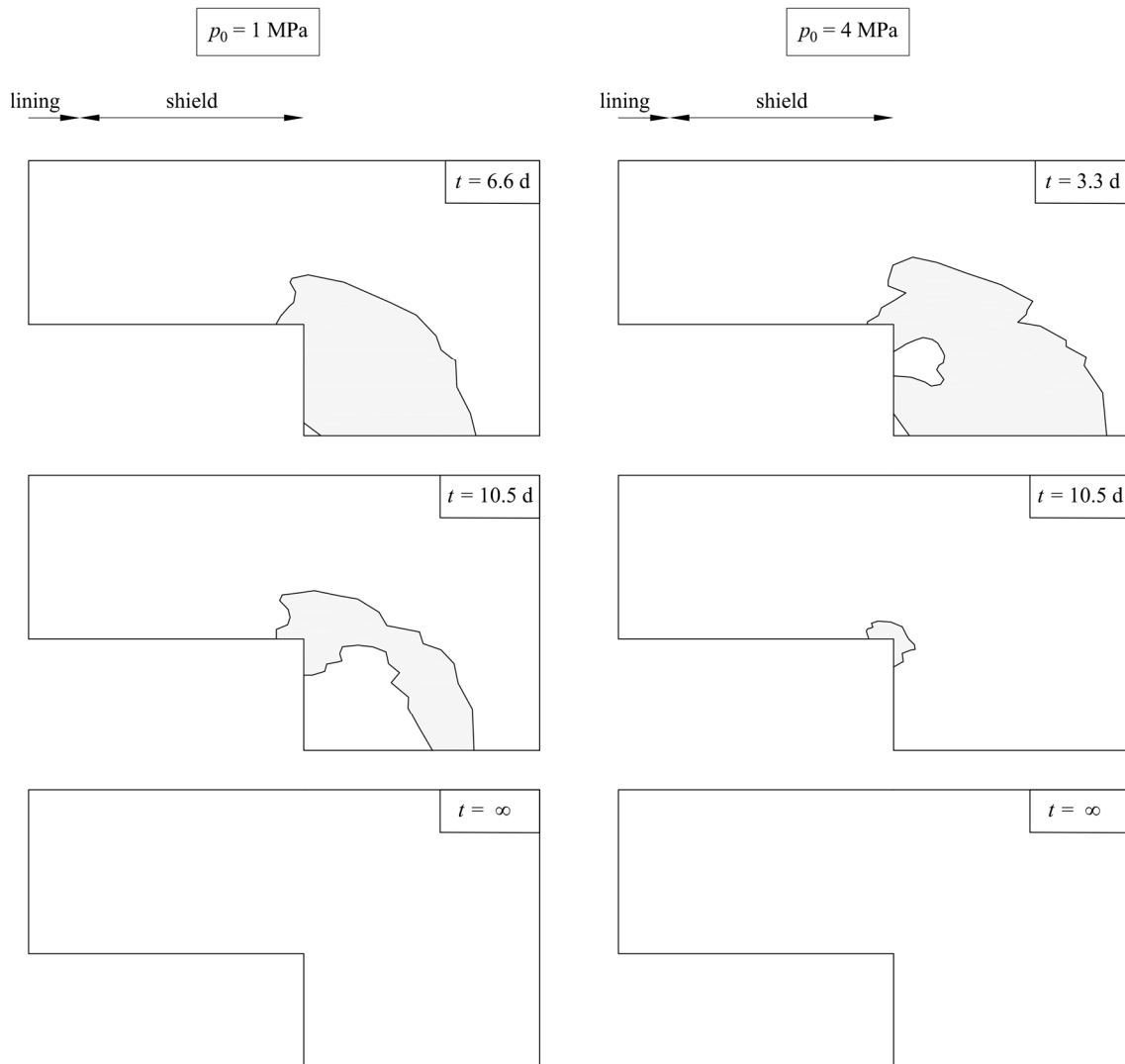# Appendix E. Systematic investigation on the effect of the tunnel diameter on the risk of TBM entrapment[5]

Abstract

A notable hazard in shield tunnelling through squeezing ground is the entrapment of the tunnel boring machine (TBM) due to insufficient thrust force. One often associates larger tunnel diameters with higher risks compared to smaller ones, mainly due to the higher propensity for problems related to an increased tunnel face size. However, depending on the tunnel diameter, different technical limitations exist that are associated with particular TBM parameters and the construction process, the effects of which are complex to assess and often mutually competing with respect to the TBM entrapment risk; all such limitations considered, the question arises: is a larger tunnel diameter always more critical? The present appendix addresses this question by numerically investigating the effect of the tunnel diameter on the risk of TBM entrapment during mechanised excavation and after construction standstills, considering relevant technical limitations, a broad range of geotechnical conditions, as well as the effect of time-dependency of squeezing. The investigations yield an interesting finding – larger diameter tunnels are more favourable in poor quality ground, while the opposite holds in higher quality ground, as well as in the case of pronouncedly time-dependent ground behaviour. Besides their theoretical value, the results of the presented investigations also provide practice guidance concerning the use of experiences acquired from existing tunnels about the required thrust force as a reference for different diameter tunnels constructed under the same geotechnical conditions.

E.1   Introduction

A situation sometimes encountered in tunnelling practice is that of different diameter tunnels constructed under practically the same geotechnical conditions, *e.g.* a smaller diameter pilot tunnel constructed prior to the main tunnel for exploration, advance drainage or ground improvement; or a road tunnel upgraded by later construction of a safety tunnel of smaller diameter. In such cases, the larger diameter tunnel usually poses a higher risk during construction, as a large cross-section is unconditionally less favourable for certain hazards (*e.g.*, collapse of the tunnel face), and more likely to encounter adverse conditions (*e.g.*, weak zones, water inflow etc.; Kovári 1979; Schneider 2002). In the cases of mechanised construction with a shielded tunnel boring machine (TBM), one of the most critical hazards is TBM entrapment due to insufficient thrust force ("shield jamming"; Ramoni and Anagnostou 2010). Although one may tend to think that a larger diameter tunnel is also more critical in relation to this hazard, this is not always straightforward when it comes to assessment for two reasons.

First, depending on the tunnel diameter, there are different technical limitations for certain TBM parameters, including the annular overcut around the shield, shield length, shield and lining stiffnesses and installable thrust force (Ramoni and Anagnostou 2010b). These limitations often have mutually competing influences on the risk of shield jamming, which render their combined effect complex to assess.

Second, the tunnel diameter also poses limitations on certain parameters of the construction process, including the TBM advance rate during excavation and the duration of construction standstills. These are only relevant in the cases of time-dependent ground behaviour, and thus in squeezing ground. The latter may undergo rapid convergences following excavation, but its behaviour is often characterised by continuous deformations over a period of days, weeks, or even months due to creep or consolidation (Kovári and Staus 1996; Barla 2001; Anagnostou and Kovári 2005; Anagnostou 2007).

Considering all aforementioned factors, the question of whether a larger diameter tunnel is more critical than a smaller one in relation to the risk of shield jamming becomes complex and far from straightforward to answer qualitatively. Although the problem of shield jamming in mechanised tunnelling through squeezing ground – additionally considering creep and consolidation effects – has overall attracted significant attention in the literature (for a recent review see Chapter 2), the effect of the tunnel diameter on the risk of shield jamming (henceforth referred to as "scale effect") has not been addressed thus far in the literature.

This question will be numerically investigated here, considering all factors mentioned above, a broad range of geotechnical conditions including pronounced creep of the ground, and the main two operational conditions – ongoing excavation and restart after a construction standstill. For details concerning the case of consolidation, the reader is referred to Chapter 5, which focuses principally on time-dependent ground behaviour and examines the differences between creep and consolidation.

This appendix starts with the problem definition and the computational assumptions adopted in the numerical investigations (Section E.2). Subsequently, it presents some theoretical considerations that improve the understanding of the problem (Section E.3), as well as the practical considerations and limitations concerning the TBM and construction process parameters which must be considered in the simulations (Sections E.4 and E.5). Finally, it presents the results of the numerical investigations into the scale effect; first, for the case of time-independent ground behaviour, where the scale effect is associated solely with the TBM parameters (Section E.6), and then for the case of time-dependent behaviour, where the construction process parameters are also relevant and a distinction must be made between the conditions prevailing during excavation (Section E.7) and those during restart after a longer standstill (Section E.8).

E.2 Computational assumptions

Consideration is given to the rotationally symmetric problem of a deep, cylindrical tunnel of radius R, crossing homogeneous and isotropic rock subjected to a hydrostatic *in-situ* stress field (σ_0). A numerical model of the advancing tunnel heading has been developed in Abaqus® (Dassault Systèmes, 2018) to simulate the mechanised excavation and lining installation, as well as the conditions during a sub-sequent TBM standstill of arbitrary duration (Fig. E.1). A detailed description of the computational assumptions can be found in Chapter 5, while some key aspects of the model are discussed hereafter.

On account of rotational symmetry, the model assumes uniform overcut ΔR and backfilling around the segmental lining. The excavation process, which in reality consists of intervals of continuous TBM propulsion (with the net advance rate v_N) regularly alternating with standstills for lining erection (zero advance rate), is simulated as continuous with an average advance rate v; this simplification has been shown to be sufficiently accurate in most cases (Chapter 2). At each numerical excavation step, part of the ground equal to the 0.5 m round length (Fig. E.1) is removed ahead of the face and an equal part of lining is installed immediately behind the shield tail (step-by-step simulation method; see, *e.g.*, Franzius and Potts, 2005). The tunnel face is considered unsupported, taking into account the fact that open shield TBMs are employed in most practical cases of mechanised tunnelling through squeezing rocks. The tunnel support is modelled by radial springs that account for the shield and lining stiffnesses (K_s and K_l) as well as for the radial overcut ΔR (for details see Ramoni and Anagnostou, 2010b).

In transient analyses considering creep, a linear elastic-viscous perfectly plastic constitutive model is adopted for the rock, with a Mohr-Coulomb yield condition and a non-associated viscoplastic flow rule based on Perzyna's theory (Perzyna, 1966); this is suitable for modelling rheological processes in squeezing ground, where the dominant portion of time-dependent deformations is plastic. The model has six parameters – Young's Modulus E, Poisson's ratio v, uniaxial compressive strength f_c, angle of internal friction ϕ, angle of dilation ψ, and the viscosity η, which determines the rate of viscoplastic deformations. Details on its formulation and numerical implementation in Abaqus® can be found in Chapter 2. In the absence of creep ($\eta = 0$), the constitutive model degenerates into the classic elastoplastic model.

The model provides the longitudinal distribution of the rock pressure $\sigma_R(x)$ on the shield at any time instance. The simulated excavation length is set equal to 60 excavation steps which is sufficiently long for achieving steady state with respect to the advancing heading; the standstill phase of duration t is initiated thereafter.
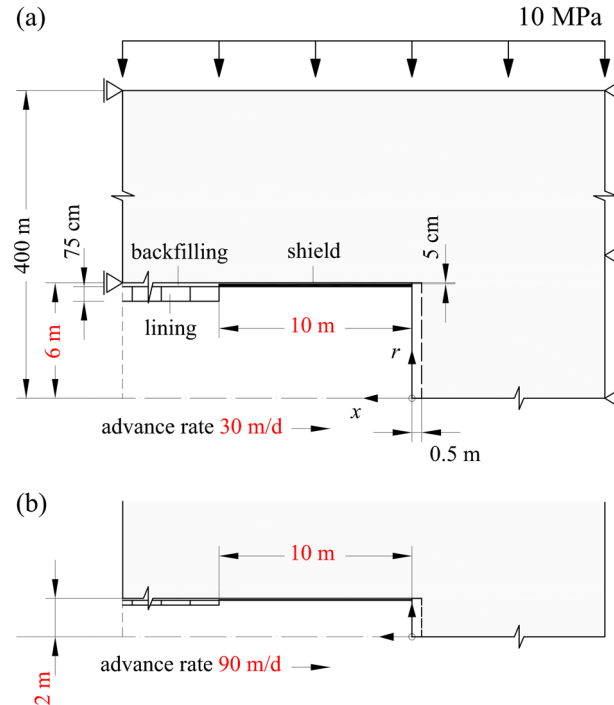

Figure E.1   Axisymmetric computational model of the advancing tunnel heading for tunnels with diameter of 12 m (a) and 4 m (b) (Parameters: Table E.1)

E.3. Theoretical considerations

The risk of shield jamming is assessed based on the required thrust force to overcome shield skin friction, which depends on the rock pressure exerted on the shield (Ramoni and Anagnostou, 2010b). In the following, the average pressure $\overline{\sigma}_R$ will be considered. It is obtained via integration over the shield length L and depends in general on all problem parameters, including the *in-situ* stress σ_0, tunnel radius R, ground parameters E, v, f_c, ϕ, ψ, η, TBM parameters K_s, K_l, L, ΔR, and process parameters, i.e. advance rate v, and standstill duration t (Chapter 5):

$$\frac{\overline{\sigma}_R}{\sigma_0} = f\left(\frac{E}{\sigma_0}, \frac{\Delta R}{R}, v, \frac{f_c}{\sigma_0}, \phi, \psi, \frac{L}{R}, \frac{K_s R}{E}, \frac{K_l R}{E}, \frac{v}{R}\frac{\eta}{E}, t\frac{E}{\eta} \right)$$

(E.1)

In practice, different technical constraints exist for the TBM parameters and the advance rate depending on the size of the tunnel cross-section (here the tunnel radius R), while the rock parameters may also differ at the representative material volume which, however, is not as relevant in weak, squeezing ground (Section E.4). Therefore, the dimensionless parameters in Eq. (E.1) cannot in general take the same values for tunnels of different size, which gives rise to the scale effect.

Evidently, there is not much use in trying to quantify the combined influence of all parameters qualitatively; even by neglecting time-dependency to simplify matters (the last two terms in Eq. E.1 become irrelevant), the combined influence of the TBM parameters is cumbersome to assess, due to their mutually competing effects (*e.g.*, L/R and $\Delta R/R$ both decrease with increasing R, but the former is favourable for the rock pressure, while the latter is unfavourable). Therefore, one must resort to numerical simulations. However, before undertaking this it is useful to understand the influence of each parameter, as it offers a better comprehension of the problem. The influence of the TBM parameters is generally known (Ramoni and Anagnostou, 2010b), and so in this instance we focus on the last two parameters related to the advance rate v and the standstill duration t, which are only relevant in the cases of time-dependent ground behaviour due to creep. To examine their influence, we consider an idealised situation where all other dimensionless parameters in Eq. (E.1) related to the ground and TBM are fixed regardless of R.

First, let us examine the isolated influence of the last term related to the standstill duration t. We can do this by considering a case where the excavation occurs rapidly in relation to the rate at which the ground to responds to it (v $\eta \rightarrow \infty$), which renders the penultimate parameter infinite regardless of R and the rock pressure only dependent on the last parameter. Since R does not appear in the last parameter of Eq. (E.1), one can conclude that the rock pressure develops at the same rate regardless of the cross-section size.

Next, let us examine the influence of the penultimate term related to the advance rate v, by considering a case where the excavation is not followed by a standstill and the last term becomes irrelevant. First of all, in order to compare the rock pressure in tunnels with different R, v alone is not the most suitable measure of the rate of advance. When the shield reaches any given tunnel cross-section, it remains exposed to pressure at that section for as long as it is required for its entire length L to pass through it; therefore, the shield pressure that ultimately develops depends

on the time required for the TBM to advance by one shield length, i.e. L/v ($= (L/R) / (v/R)$), which is only a function of v/R since L/R is considered fixed here regardless of R. A more suitable measure of the rate of advance would thus be v/R – considering the same v/R means that the TBM takes the same time to advance by one shield length irrespective of R. For a given v/R, the normalised advance rate $(v/R)\cdot(\eta/E)$ is constant, which means that the pressure develops at the same rate irrespective of R – exactly as in the case of the standstill examined previously.

Combining the above, for both conditions – during advance and for restart after a standstill of the TBM – there would be no scale effect in the case of time-independent ground behaviour, but also in the case of creep, if the same dimensionless parameters related to the ground and the TBM could be specified for different diameter tunnels and these could be excavated with the same rate v/R. In all other cases, there will be a scale effect, which can only be quantified numerically.

E.4. Practical considerations

Notwithstanding the value of the theoretical considerations discussed in Section 3, the scale effect resulting from the combined influence of all parameters is far more complex due to the aforementioned constraints and limitations concerning the advance rate, the TBM parameters and, possibly, also the ground parameters. These are discussed in the following subsections.

E.4.1 Advance rate

The assumption adopted in Section 3 – that v/R can be the same for the two tunnels, i.e. v is proportional to R – is particularly erroneous, as it means that a larger diameter tunnel could be excavated at a higher rate. In practice, it is well-known that the larger the boring diameter, the slower the TBM advances, i.e. v decreases with increasing R. In fact, v can be assumed inversely proportional to R, which then makes v/R inversely proportional to R^2, as discussed hereafter.

Mechanised excavation can be idealised as a "stop-and-go" process, where intervals ΔT_1 of continuous TBM propulsion over the length of one prefabricated segmental lining ring L_T regularly alternate with standstill intervals ΔT_2 for the corresponding ring installation. The net advance rate of the TBM during continuous excavation can thus be expressed as $v_N = L_T/\Delta T_1$, while the average advance rate during the "stop-and-go" process considered in this work (Section E.2) can be expressed as $v = L_T/(\Delta T_1 + \Delta T_2)$ (Chapter 2).

The net advance rate is defined as $v_N = $ ROP*RPM, where ROP is the rate of penetration and RPM the number of rotations of the TBM cutterhead per minute. For tunnels under identical ground conditions ROP can be assumed to be the same, provided that the installed thrust force is higher in the larger TBM, as is common in practice. RPM can be assumed inversely proportional to R, considering that the linear velocity of the gauge cutters is limited to 150-200 m/min to avoid overheating, irrespective of the TBM diameter (Rispoli et al., 2020; Hamburger and Weber, 1992). Under these assumptions, v_N becomes inversely proportional to R. Assuming that the lining ring length L_T is the same regardless of R, ΔT_1 becomes proportional to R. It is reasonable to assume that ΔT_2 is also proportional to R (see, e.g., Tahernia and Rostami, 2021; Farokh, 2013, 2020), which then makes v inversely proportional to R.

It is indicatively noted here that, by incorporating the above realistic assumption in the theoretical analysis of Section E.3, the conclusions concerning the scale effect during advance already change completely – the normalised advance rate $(v/R)(\eta/E)$ becomes inversely proportional to R^2, which means that the pressure develops faster in a larger tunnel. In practice, this means that if the tunnel diameter was, e.g., four times larger, the pressure would develop 16 times faster (as if the ground viscosity η was lower by a factor of 16). On the other hand, the scale effect during a standstill preceded by a rapid advance (v $\eta \to \infty$) is not influenced; however, as the tunnel size influences the advance and standstill phases differently, the overall scale effect already becomes very complex to assess – this is even more so the case when the technical constraints for the TBM parameters are additionally considered, as discussed next. This underscores the importance of incorporating these limitations in our numerical investigations.

E.4.2   TBM parameters

The TBM parameters (overcut ΔR, shield length L and shield and lining stiffnesses K_s and K_l) that can be materialised in practice are limited to a specific range, regardless of the tunnel diameter. Therefore, the nondimensional parameters $E\Delta R/(\sigma_0 R)$, L/R, $K_s R/E$ and $K_l R/E$ cannot in general take the same values for a large and small tunnel. Furthermore, when evaluating potential scale-effects with respect to the risk of shield jamming, it is not sufficient to only consider the shield loading or the required thrust force (which depend on the parameters in Eq. E.1), but also the installed or installable thrust force. The latter increases with the tunnel diameter, which introduces an additional scale effect to be considered. Typical values for these parameters based on technical data gathered from various TBMs can be found in Ramoni and Anagnostou (2010b).

E.4.3   Ground parameters

The strength and stiffness of the ground tentatively decrease with increasing representative volume and, in turn, tunnel diameter, hence scale-effects may exist also in relation to the ground parameters. However, as squeezing ground is often weak at the scale of specimen, the differences between a small and a large diameter tunnel with respect to the ground parameters are not significant and can be neglected.

E.5.   Assumptions of quantitative analysis

Two tunnels with diameters $D = 4$ m and 12 m excavated under identical ground conditions will be analysed numerically using the computational model introduced in Section E.2 (Fig. E.1) and considering practically relevant TBM and process parameters based on the limitations discussed in Section E.4, as given in Table E.1.

The average advance rates during the stop-and-go operation are selected to be inversely proportional to the diameter (Section E.4.1). The common overcut $\Delta R = 50$ mm and shield length $L = 10$ m adopted for both tunnels are realistic, considering that the corresponding normalised values $\Delta R/R = 2.5\%$ and 0.8%, and $L/R = 5$ and 1.7, are typical for $D = 4$ m and 12 m, respectively (*cf.* Fig. E.6 in Ramoni and Anagnostou, 2010b). The thicknesses ds of the shield and dl of the lining are assumed proportional to the radius R; this assumption is reasonable and makes the

normalised radial stiffnesses $K_s R/E = (E_s/E)\, d_s/R$ and $K_l R/E = (E_l/E)\, d_l/R$ identical for the two tunnels, and dependent only on the Young's moduli E_s, E_c and E of steel, concrete and the ground, respectively.

To assess the risk of shield jamming, the required thrust force F_r must be considered in combination with the installed thrust force F_i. Therefore, the comparison between the two tunnels is based on the ratio F_r/F_i, which expresses the percentage of F_i utilised by F_r and will be hereafter referred to as "thrust utilisation factor" (TUF). The required thrust force F_r is computed as $\mu\, 2\pi R\, L\, \mu\, \overline{\sigma}_R$, where μ denotes the static friction coefficient. Strictly speaking, this expression holds for the conditions during TBM restart after a standstill and not during advance; however, the former is the most critical operational stage in most cases (see Ramoni and Anagnostou, 2010b), hence the expression in general provides a conservative estimate. The installed TBM thrust force is assumed to increase proportionally with the cross-section area, and thus with R^2, according to the expression $F_i = 5\, R^2$ MN/m^2 which provides values in the high end of the range of technical data collected from various TBMs (*cf*. Fig. 7 in Ramoni and Anagnostou 2010b).

The scale effect is first analysed by disregarding creep (rapid squeezing development), where it is solely influenced by the TBM parameters (Section E.6). Subsequently, the case of time-dependent ground behaviour due to creep is examined, considering the conditions during TBM advance (Section E.7) and at restart after a 200-day long TBM standstill (Section E.8).

Table E.1.   Parameters considered in the numerical simulations

Ground

Young's Modulus, E	[GPa]	1
Poisson's ratio, v	[-]	0.25
Uniaxial compressive strength, f_c	[MPa]	var.
Angle of internal friction, ϕ	[°]	25
Dilatancy angle, ψ	[°]	5
Depth of cover, H	[m]	400
In-situ stress at tunnel axis, σ_0	[MPa]	10
Viscosity, η	[MPa·d]	var.

TBM

Boring Diameter, D	[m]	4 or 12
Radial overcut, ΔR	[cm]	5
Shield length, L	[m]	10
Radial shield stiffness, K_s	[MPa/m]	875 ($D = 12$m)
		2625 ($D = 4$m)
Shield thickness, d_s	[m]	0.15 ($D = 12$m)
		0.05 ($D = 4$m)
Young's modulus of steel, E_s	[GPa]	210
Average Advance rate, v	[m/d]	30 ($D = 12$m)
		90 ($D = 4$m)
Shield skin friction coefficient, μ	[-]	0.15
Installed thrust force, F_i	[MN]	180 ($D = 12$ m)
		20 ($D = 4$ m)

Lining

Young's modulus of concrete, E_c	[GPa]	30
Lining thickness, d_l	[cm]	0.75 ($D = 12$m)
		0.25 ($D = 4$m)
Radial lining stiffness, K_l	[MPa/m]	625 ($D = 12$m)
		1875 ($D = 4$m)

E.6. Results disregarding creep

Figure E.2 shows the thrust utilisation factors of the two tunnels with $D = 4$ m (solid lines) and $D = 12$ m (dashed lines) as functions of the rock quality, expressed by its uniaxial compressive strength f_c.
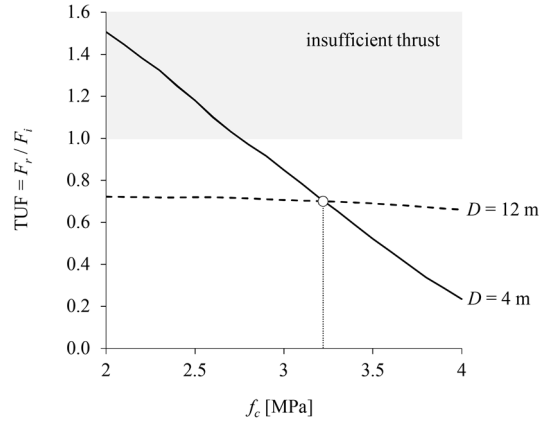
Figure E.2   Thrust force required to overcome shield skin friction normalised by the installed thrust force ("thrust utilisation factor", TUF), as a function of the uniaxial compressive strength of the ground f_c (no creep; parameters: Table E.1)
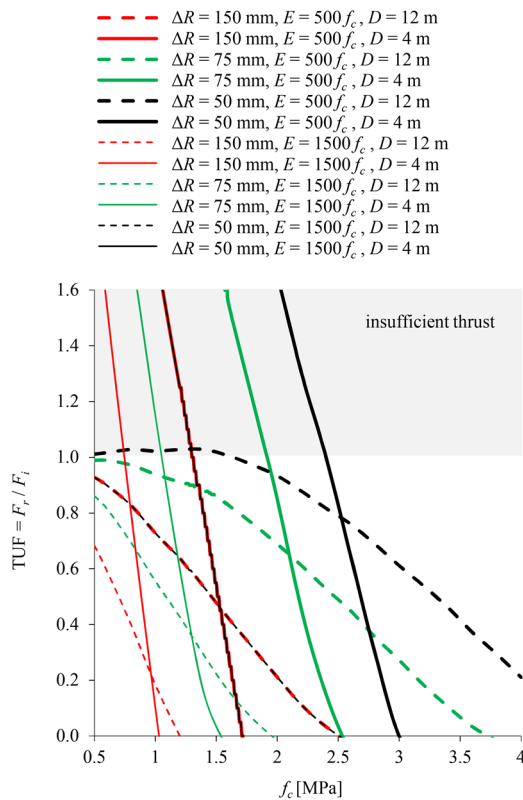
Figure E.3   Results of a parametric study about the effects of rock strength f_c, rock stiffness E and overcut ΔR on the thrust utilisation factor (TUF) (F_r after the design nomograms of Ramoni and Anagnostou, 2010b, for a 400 m deep tunnel with $\sigma_0 = 10$ MPa, $v = 0.25$, $f_c = 0.5 – 4$ MPa, $\phi = 25°$, $\psi = 5°$, $L = 10$ m, $K_sR/E = 10$, $K_lR/E = 0.5$, $\mu = 0.15$, $F_i = 20$ and 180 MN for $D = 4$ and 12 m, respectively)

The results of Figure E.2 contradict the common perception that a smaller diameter tunnel is less vulnerable than a larger one. This may be unconditionally true for other potential hazards (*e.g.*, instability of the tunnel face), but not for shield jamming, where it is only true in higher quality ground ($f_c > 3.2$ MPa), while the opposite holds in weaker ground. The TUF of the TBM in the larger diameter tunnel is generally less sensitive to variations of rock quality than in the smaller diameter tunnel and is consistently lower than 1, which means that the tunnel excavation is feasible for the considered strength range, whereas the small tunnel excavation is only feasible in higher quality ground ($f_c > ca.$ 2.7 MPa).

Considering this interesting finding, a more extensive parametric study was conducted to assess its general validity. The computations concern a 400 m deep tunnel ($\sigma_0 = 10$ MPa) and have been performed using the design nomograms of Ramoni and Anagnostou (2010b). Concerning ground parameters, consideration is given to variable uniaxial compressive strength $f_c = 0.5 – 4$ MPa, Young's moduli $E = 500\,f_c$ and $1500\,f_c$, which respectively correspond to the lower and upper limits of possible stiffnesses for a geomaterial with given f_c, and otherwise identical parameters to those given in Table E.1, which were also considered by Ramoni and Anagnostou (2010b).

Concerning TBM parameters, consideration is given to overcuts $\Delta R = 50$, 75 and 150 mm, which respectively correspond to the relatively small value adopted in the computational example (Table E.1), an intermediate value and an unusually large value. The shield length and installed thrust force are as given in Table E.1, but different normalised radial stiffnesses of the shield $K_sR/E = 10$ and the lining $K_lR/E = 0.5$ are considered, which correspond to those assumed by Ramoni and Anagnostou (2010b) for producing the design nomograms; although the latter assumption leads to more conservative predictions for the required thrust force, it does not affect the conclusions of the study otherwise.

The results of the parametric study (Fig. E.3) confirm that a larger diameter tunnel is always less vulnerable than a smaller one in weak ground (dashed lines for $D = 12$ m consistently below solid lines for $D = 4$ m in the range of low f_c). Moreover, it is less sensitive to variations of the ground quality and its excavation is practically feasible in all cases considered, in contrast to the smaller diameter tunnel, which exhibits a much higher sensitivity to the ground quality and its excavation is only feasible in higher quality ground.

E.7.   Results for creep and TBM advance

In the example of Figure E.2, the TUFs of the two TBMs are equal for $f_c = ca.$ 3.2 MPa, which means that the competing effects of the TBM parameters (Section E.3) outweigh one another and the scale effect associated with these is eliminated. Therefore, the transient computations have been performed for this strength (and the parameters of Table E.1). This enables examining the isolated influence of the advance rate v or, equivalently, the viscosity η in the case of creep (note the dimensionless expressions in Eq. E.1).

Figure E.4 shows the thrust utilisation factor as a function of η for the two tunnels with $D = 4$ m (solid lines) and $D = 12$ m (dashed lines).
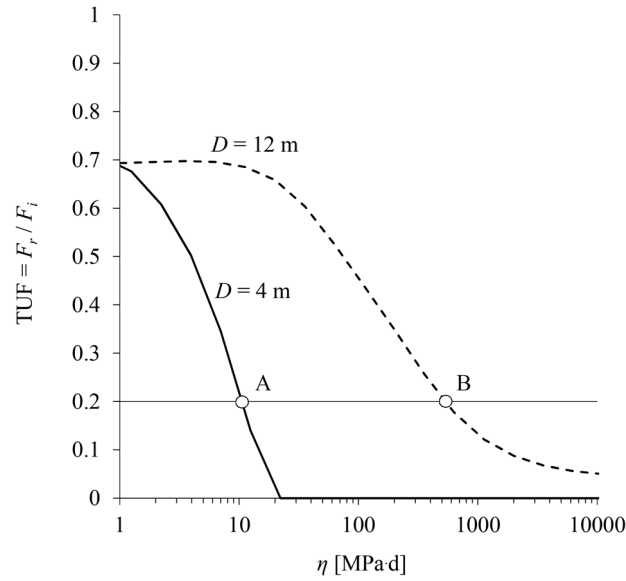
Figure E.4   Thrust utilisation factor (TUF) as a function of the viscosity η ($f_c = 3.2$ MPa; other parameters: Table E.1)

With the exception of the range of high viscosities, a scale effect clearly exists with respect to the risk of shield jamming: an increase in diameter results in a higher utilisation of the thrust force, as reflected by the vertical distance between the dashed line and the solid line that is consistently below it. This means that in the case of time-dependent ground behaviour, the situation is more favourable for the smaller diameter, which is also consistent with the results discussed in Section E.6 and shown in Figure E.2: time-dependency delays squeezing, hence the rock responds to tunnel excavation as if it were of a higher quality, and an increase in rock quality renders a smaller diameter more favourable. It is noted here that this result is qualitatively consistent with the theoretical considerations discussed in Section E.4.1, according to which the rock pressure on the shield develops faster on the larger TBM for a given advance rate (or, equivalently, viscosity η herein).

The scale effect is negligible in the range of high viscosities because the rock behaviour is practically elastic, hence the convergences around the advancing shield area are small anyway, regardless of the tunnel diameter.

The scale effect can also be demonstrated in an alternative way. Let us consider a case where the 4 m diameter tunnel was constructed first, and the actual applied force was equal to 20% of the installed one (TUF = 0.2). Assuming that the strength and stiffness parameters of the rock are known and correspond to the ones in Figure E.4, the rather low required thrust force could be explained on the basis of the convergence delay due to time-dependency (point A in Fig. E.4). What could one expect for the main, larger diameter tunnel? In order to limit the effect of squeezing and maintain the same, low TUF = 0.2, the viscosity η would have to be higher by a factor of about 50 (point B vs. A); equivalently, for the same η (as in point A), the advance rate v in the main tunnel would have to be about 50 times higher (note dimensionless expressions in Eq. E.1). This is, of course, impossible, but provides another interpretation of the scale effect.

For the parameters adopted in this example, the TUFs of both TBMs are consistently lower than the value of ca. 0.7 which corresponds to time-independent behaviour (very low viscosity; *cf*. Fig. E.2), indicating that the excavation of both tunnels is thoroughly feasible. However, the assumed values for the installed thrust force $F_i = 5$ R^2 MN/m^2 (20 MN for $D = 4$ m, 180 MN for $D = 12$ m; Table E.1) are very high for rock TBMs; with a moderate assumption, *e.g.* $F_i = 3$ R^2 MN/m^2 (12 MN for $D = 4$ m, 108 MN for $D = 12$ m), jamming of the larger TBM might occur in the range of $\eta = ca.$ 10–100 MPa·d, while the smaller TBM would remain entirely in the safe region.

E.8. Results for creep and restart after standstill

Transient computations have been performed considering the same parameters as before (Table E.1 and $f_c = 3.2$ MPa), as well as a high viscosity $\eta = 10,000$ MPa·d to ensure that the behaviour during advance is elastic and, therefore, relevant shield loading develops only during the standstill (see TUF < 0.1 for $\eta = 10,000$ MPa·d in Fig. E.4). This enables an examination of the isolated influence of the standstill duration t.

Figure E.5 shows the thrust utilisation factor as a function of t for the two tunnels with $D = 4$ m (solid lines) and $D = 12$ m (dashed lines).

The same conclusions as for the advance stage examined in Section E.7 can basically be drawn also here. There is a clear effect of the tunnel diameter on the thrust force required for restart after a standstill and the associated shield jamming risk, as expressed by TUF. This scale effect is reflected by the width of the band defined by the dashed and solid lines.
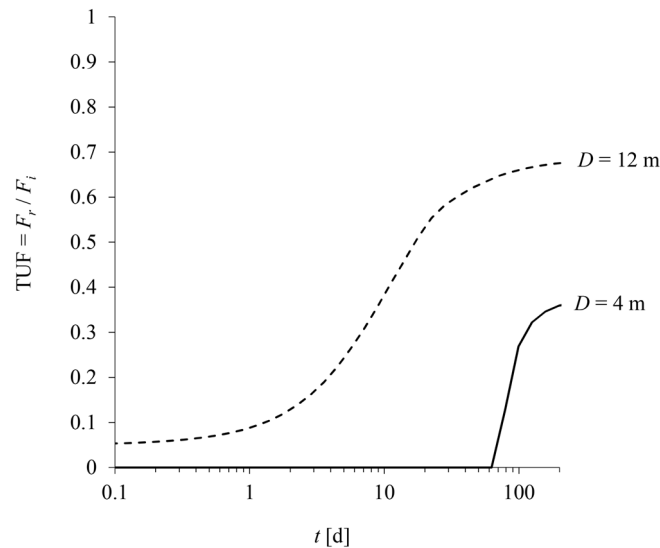

Figure E.5   Thrust utilisation factor (TUF) as a function of the standstill duration t ($f_c = 3.2$ MPa; $\eta = 10^4$ MPa·d, other parameters: Table E.1)

E.9. Conclusions

The present appendix numerically investigated the effect of the tunnel diameter on the risk of shield jamming during mechanised tunnel construction in squeezing ground, considering the various technical limitations concerning the TBM and construction process parameters depending on the tunnel diameter and the markedly time-dependent response that squeezing ground often exhibits. Exemplary numerical simulations with practically relevant parameters demonstrated that a larger diameter is always more favourable than a smaller one in poor quality ground, while the opposite is true in the case of higher quality ground or ground exhibiting time-dependent behaviour, where the delay in ground deformations is equivalent to an improvement of the ground quality.

The appendix only considered time-dependency due to creep, but the conclusions drawn hold also for the case of consolidation – the other common mechanism of time-dependency in squeezing ground. Scale effect in this case is slightly less pronounced. For more details, the reader is referred to Chapter 5.

Provided that data are available concerning the required thrust force in an existing tunnel, the findings of the present appendix provide useful indications and guidance concerning the risk of shield jamming during the later construction of an adjacent, different diameter tunnel.

Appendix F. Publications from the present thesis and contributions

Chapter 2 is a paper which has been published with the following reference: Leone, T., Nordas, A.N. & Anagnostou, G. (2023). Effects of creep on shield tunnelling through squeezing ground. Rock Mechanics and Rock Engineering, doi: 10.1007/s00603-023-03505-x.

Chapter 3 is a paper which has been published with the following reference: Leone, T., Nordas, A.N. & Anagnostou, G. (2024). An estimation equation for the TBM thrust force in creeping rock. Computers and Geotechnics, 165, 105802, doi: 10.1016/j.compgeo.2023.105802

Chapter 4 is a paper which has been published with the following reference: Leone, T., Nordas, A.N. & Anagnostou, G. (2024). Creep versus consolidation in tunnelling through squeezing ground—Part A: Basic Time Effects. Rock Mechanics and Rock Engineering. doi: 10.1007/s00603-023-03720-6.

Chapter 5 is a paper which has been accepted on the 31.01.2024 for publication with the following reference: Nordas, A. N., Leone, T. & Anagnostou, G. (2024). Creep versus consolidation in tunnelling through squeezing ground – Part B: Applicability of Experience. Rock Mechanics and Rock Engineering (accepted for publication).

Appendix E is a conference paper which has been accepted for publication on 02.01.2024 in the World Tunnel Congress 2024 with the following reference:

Nordas, A. N., Leone, T., & Anagnostou, G. (2024). Is a large TBM diameter unfavourable under squeezing conditions? ITA-AITES World Tunnel Congress 2024, Shenzhen, China, 19-25 April 2024 (accepted for publication)

The present thesis considers the postprint version of the papers for Chapters 2, 3, 4 and 5, and Appendix E.

Following are the contributions of each author for the papers in Chapters 2 and 4: Thomas Leone: Numerical analyses, Formal analysis, Writing – original draft. Dr. Alexandros N. Nordas: Conceptualization, Formal analysis, Writing – review & editing. Prof. Dr. Georgios Anagnostou: Supervision, Conceptualization, Review.

Following are the contributions of each author for the paper in Chapters 3: Thomas Leone: Numerical analyses, Formal analysis, Writing – original draft. Dr. Alexandros N. Nordas: Formal analysis, Writing – review & editing. Prof. Dr. Georgios Anagnostou: Supervision, Conceptualization, Review.

Following are the contributions of each author for the paper in Chapter 5 and Appendix E: Thomas Leone: Numerical analyses, Formal analysis. Dr. Alexandros N. Nordas: Conceptualization, Formal analysis, Writing – original draft, review & editing. Prof. Dr. Georgios Anagnostou: Supervision, Conceptualization, Review.

Notation

A	coefficient used in the time function g
$\mathbf{A}$	coordinate transformation matrix
B	coefficient used in the approximation of $\sigma^*_{t=0}$
c	cohesion of the ground
C_1	coefficient used in the approximation of $\Delta\sigma^*_{t=\infty}$
C_2	coefficient used in the approximation of $\Delta\sigma^*_{t=\infty}$
D	tunnel diameter
D_1	coefficient used in the time function g
D_2	coefficient used in the time function g
D_3	coefficient used in the time function g
D_4	coefficient used in the approximation of t^*_c
$\mathbf{D}^{el}$	constant elastic stiffness matrix according to Hooke's law
$\mathbf{D}^{vp}$	viscoplastic tangent stiffness matrix in the principal coordinate system
$\mathbf{D}^{vp,c}$	consistent viscoplastic tangent stiffness matrix in the principal coordinate system
$\tilde{\mathbf{D}}^{vp}$	viscoplastic tangent stiffness matrix in the local coordinate system
d_l	thickness of the lining
d_s	thickness of the shield
E	Young's modulus of the ground
E_c	Young's modulus of the lining
E_s	Young's modulus of the shield
e	internal distance between the tunnel boundaries
F_b	thrust force required for boring
F_i	installed thrust force
F_r	thrust force required to overcome shield skin friction
f_c	uniaxial compressive strength of the ground
f_c^*	normalised f_c

182

f_i	yield function
f_s	seepage force
f_t	tensile strength of the ground
g	time function describing rock pressure development during standstills
g_i	plastic potential function
H	depth of cover
H_w	Water table level above tunnel axis
K_l	stiffness of the lining
K_s	stiffness of the shield
k	permeability of the ground
L	length of the shield
L_T	length of one lining segment
m	yield surface slope in the principal stress planes
$\mathbf{n}$	normal vector to the tunnel boundary
$\mathbf{n}_i$	normal vector to the yield surface f_i
N	number of TBM stroke-lining ring erection ("stop-and-go") cycles
p	pore pressure
p_0	*in-situ* pore pressure
q	flux
$\mathbf{r_i}$	normal vector to the plastic potential surface g_i
R	tunnel radius; in Chapter 4: tunnel radius in the deformed configuration
R'	maximum tunnel radius for achieving equilibrium
R_p	size of the seepage flow domain
R_σ	size of the computational domain
R_0	tunnel radius in the undeformed configuration
R^2	coefficient of determination
ROP	rate of penetration
RPM	number of rotations of the TBM cutterhead per minute
r	radial coordinate (distance from the tunnel axis)
s	round length
T	torque required to restart cutterhead rotation
$\mathbf{T}$	modification matrix
T_i	installed torque
TBM	tunnel boring machine
TUF	thrust utilisation factor
t	time
t_c	time at which contact between ground and shield occurs in Chapter 3, and at which contact between ground and cutterhead occurs in Chapter 4

t_F	time at which the frictional force to overcome shield jamming is equal to the installed thrust force of the machine
t_T	time at which the torque needed to overcome cutterhead jamming is equal to the installed torque of the machine
t^*	normalised t
t_{95}	time to achieve 95% of the time-dependent displacement or lining load increment
u	radial displacement of the ground at the tunnel boundary
u_R	radial displacement of the ground at the tunnel boundary in Chapter 5
u_e	axial displacement at the centre of the face
v	advance rate
v^*	normalised advance rate
v_N	net advance rate over the TBM strokes
v_N^*	normalised v_N
v_G	gross advance rate over one full excavation cycle
v_S	smeared advance rate over the "stop-and-go" phase
v_S^*	normalised v_S
x	axial coordinate (distance behind the tunnel face)
x_f	distance of the tunnel face from the left model boundary
y	horizontal coordinate
z	vertical coordinate
γ	unit weight of the ground
γ_{ij}	shear strain component over the plane ij of the local coordinate system
γ_w	unit weight of the pore water
$\Delta\boldsymbol{\varepsilon}_j$	strain increment in the principal coordinate system at iteration j
$\Delta\widetilde{\boldsymbol{\varepsilon}}_j$	strain increment in the local coordinate system at iteration j
$\Delta\sigma$	increase in rock pressure during a standstill
$\Delta\sigma^*$	normalised $\Delta\sigma$
$\Delta\sigma_{t=\infty}$	increase in rock pressure during a standstill that reaches steady state
$\Delta\sigma^*_{t=\infty}$	normalised $\Delta\sigma_{t=\infty}$
$\Delta\sigma_{t=\infty,vs=\infty}$	$\Delta\sigma_{t=\infty}$ for infinite advance rate
$\Delta\sigma^*_{t=\infty,vs=\infty}$	normalised $\Delta\sigma_{t=\infty,vs=\infty}$
ΔD_h	convergence in y-coordinate
ΔD_v	convergence in z-coordinate
ΔT_1	duration of one TBM stroke
ΔT_2	duration of one lining ring erection
ΔT_3	duration of TBM standstill following the "stop-and-go" phase
ΔT	duration of one full excavation cycle
ΔR	annular gap (overcut)

ΔR^*	normalised ΔR
Δx	longitudinal gap between cutterhead and tunnel face
δu	additional displacement occurring during standstill
$\boldsymbol{\varepsilon}$	strain vector in the principal coordinate system
$\widetilde{\boldsymbol{\varepsilon}}$	strain vector in the local coordinate system
$\dot{\boldsymbol{\varepsilon}}$	total strain rate vector in the principal coordinate system
$\dot{\boldsymbol{\varepsilon}}^{el}$	elastic strain rate vector in the principal coordinate system
$\dot{\boldsymbol{\varepsilon}}^{vp}$	viscoplastic strain rate vector in the principal coordinate system
ε_i	normal strain component along the principal coordinate axis i
ε_{ii}	normal strain component along the local coordinate axis i
ε^p	equivalent plastic strain
η	viscosity of the ground
κ	dilatancy constant
λ	deconfinement factor
$\dot{\lambda}_i^{vp}$	viscoplastic multiplier of plastic potential surface g_i
μ	sliding shield skin friction coefficient
μ_{st}	static shield skin friction coefficient
$\mu_{st,c}$	static friction coefficient between cutterhead and ground
v	Poisson's ratio of the ground
ρ	radius of the plastic zone
$\boldsymbol{\sigma}$	stress vector in the principal coordinate system
$\widetilde{\boldsymbol{\sigma}}$	stress vector in the local coordinate system
$\dot{\boldsymbol{\sigma}}$	stress rate vector in the principal coordinate system
$\boldsymbol{\sigma}^{el}$	elastic stress predictor
$\boldsymbol{\sigma}_j$	stress vector in the principal coordinate system at iteration j
$\widetilde{\boldsymbol{\sigma}}_j$	stress vector in the local coordinate system at iteration j
σ	rock pressure average over the shield
σ^*	normalised σ
σ_0	*in-situ* vertical stress
σ_i	normal stress component along the principal coordinate axis i
σ_{ii}	normal stress component along the local coordinate axis i
σ_R	radial ground pressure at the tunnel boundary
$\overline{\sigma}_R$	average radial ground pressure over the shield
σ_r	radial stress
σ'_t	effective tangential stress
$\sigma_{t=0}$	rock pressure average over the shield during advance
$\sigma^*_{t=0}$	normalised $\sigma_{t=0}$

$\sigma_{t=\infty}$	rock pressure average over the shield during a standstill that reaches steady state
$\sigma_{t=0,\,\eta=0}$	rock pressure average over the shield during advance for zero viscosity
$\sigma^{*}_{t=0,\,\eta=0}$	normalised $\sigma_{t=0,\,\eta=0}$
σ_x	longitudinal ground pressure on the cutterhead
σ_y	total stress in y-coordinate
σ'_y	effective stress in y-coordinate
σ_z	total stress in z-coordinate
σ'_z	effective stress in z-coordinate
τ_{ij}	shear stress component over the plane ij of the local coordinate system
ϕ	angle of internal friction of the ground
ψ	dilatancy angle of the ground

References

Anagnostou, G. (2006). Tunnel stability and deformations in water-bearing ground. Paper presented at the Eurock 2006: ISRM Symposium of Multiphysics coupling and long term behaviour in rock mechanics, Liège, Belgium, May 9-12, 2006. doi: 10.3929/ethz-a-010819313

Anagnostou, G. (2007). Practical consequences of the time-dependency of ground behavior for tunneling. Proceedings - Rapid Excavation and Tunneling Conference, 255-265

Anagnostou, G. (2009a). The effect of advance-drainage on the short-term behaviour of squeezing rocks in tunneling. In Proceedings of the 1st International Symposium on Computational Geomechanics (pp. 668-679). International Center of Computational Engineering.

Anagnostou, G. (2009b). Pore pressure effects in tunneling through squeezing ground. In Proceedings of the Second International Conference on Computational Methods in Tunnelling: Ruhr University Bochum, September 9-11, 2009 (pp. 361-368). Aedificatio Publ.

Anagnostou, G. (2014). Some critical aspects of subaqueous tunnelling. Muir Wood Lecture WTC 2014, Iguassu.

Anagnostou, G. (2016). Role played by ETH chair of underground construction in the Gotthard base tunnel. In: "Tunnelling the Gotthard", Ehrbar et al. (Eds.), 684-689.

Anagnostou, G., Kovári, K. (1993): Significant parameters in elasto-plastic analysis of underground openings. ASCE, Journal of Geotechnical Engineering, 119 (3), 401-419. Switzerland. doi: 10.1061/(ASCE)0733-9410(1993)119:3(401)

Anagnostou, G., Kovári, K. 2003. The stability of tunnels in grouted fault zones. ETH, IGT, Vol. 220.

Anagnostou, G., Kovári, K. (2005) Tunnelling through geological fault zones. In: International symposium on design, construction and operation of long tunnels, Taipei, vol 1. Chinese Taipei Tunnelling Association, Taipei, pp 509–520

Anagnostou, G., Zingg, S. (2013). On the stabilizing effect of advance drainage in tunnelling. Geomechanics and Tunnelling, 6(4), 338-354.

Anagnostou, G., Schuerch, R., Perazzelli, P., (2018). Lake Mead Intake No 3 tunnel – Design considerations and construction experiences. Geomech. Tunnelling 11, 15–23. doi: 10.1002/geot.201700067.

Anagnostou, G., Pimentel, E., Cantieni, L. (2008). AlpTransit Gotthard Basistunnel, Teilabschnitt Sedrun, Felsmechanische Laborversuche Los 378, Schlussbericht, Bericht Nr. 080109. Zurich, Switzerland: IGT, ETH Zurich (in German)

Anagnostou G, Cantieni L, Nicola A, Ramoni M (2010) Lake Mead No 3 Intake Tunnel— geotechnical aspects of TBM operation. In: Tunnelling: sustainable infrastructure, North American Tunnelling Conference, Portland. SME Inc., Littleton, pp 125–135

Arn, T. (1989). Numerische Erfassung der Strömungsvorgänge im geklüfteten Fels. Ph.D. Thesis. ETH Zurich. (In German) doi: 10.3929/ethz-a-000507798

Arora, K., Gutierrez, M., Hedayat, A. (2021a). New Physical Model to Study Tunnels in Squeezing Clay-Rich Rocks. Geotechnical Testing Journal, 44(4), 1055-1078. doi: 10.1520/GTJ20200081

Arora, K., Gutierrez, M., Hedayat, A. (2022). Physical model simulation of rock-support interaction for the tunnel in squeezing ground. Journal of Rock Mechanics and Geotechnical Engineering, 14(1), 82-92. doi: 10.1016/j.jrmge.2021.08.016

Arora, K., Gutierrez, M., Hedayat, A., Cruz, E. C. V. (2021b). Time-Dependent Behavior of the Tunnels in Squeezing Ground: An Experimental Study. Rock Mechanics and Rock Engineering, 54(4), 1755-1777. doi: 10.1007/s00603-021-02370-w

Ates, U., Bilgin, N., Copur, H. (2014). Estimating torque, thrust and other design parameters of different type TBMs with some criticism to TBMs used in Turkish Tunnelling projects. Tunnelling and Underground Space Technology, 40, 46-63. doi: 10.1016/j.tust.2013.09.004

Bamford, W., Yaghoubi, E. (2017). Cutter/rock interface friction: Worth measuring accurately? In Barton, ACT (eds.): 16th Australasian Tunnelling Conference 2017 - Challenging Underground Space: Bigger, Better, More. Engineers Australia. doi: 10.3316/informit.380552563012939

Barla G (2001) Tunnelling under squeezing rock conditions. In: Eurosummer-school in tunnel mechanics, Innsbruck. Logos Verlag, Berlin, pp 169–268

Barla, G. (2018). Challenges in the Understanding of TBM Excavation in Squeezing Conditions. Gallerie e grandi opere sotteranee, 125 - marzo 2018, 67-82

Barla, G., Bonini, M., Debernardi, D. (2008). Time Dependent Deformations in Squeezing Tunnels. In: The 12th international conference of International Association of Computer Methods and Advances in Geomechanics (IACMAG), Goa, India

Barla, G., Barla, M., Bonini, M., Debernardi, D. (2014). Guidelines for TBM tunnelling in squeezing conditions – a case study. Géotechnique Letters, 4, 83–87. doi: 10.1680/geolett.13.00065

Barla, G., Debernardi, D., Sterpi, D. (2012). Time-Dependent Modeling of Tunnels in Squeezing Conditions. International Journal of Geomechanics, 12(6), 697-710. doi: 10.1061/(ASCE)GM.1943-5622.0000163

Bernaud, D. (1991) Tunnels profonds dans les milieux viscoplastiques : approches expérimentale et numérique. Modeling and Simulation. École Nationale des Ponts et Chaussées, France, French. Available at: https://tel.archives-ouvertes.fr/tel-00529719

Boidy, E., Bouvard, A., Pellet, F. (2002). Back analysis of time-dependent behaviour of a test gallery in claystone. Tunnelling and Underground Space Technology, 17(4), 415-424. doi: 10.1016/S0886-7798(02)00066-4

Bonini, M., Debernardi, D., Barla, M., Barla, G. (2007). The Mechanical Behaviour of Clay Shales and Implications on the Design of Tunnels. Rock Mechanics and Rock Engineering, 42(2), 361. doi:10.1007/s00603-007-0147-6

Bufalini, M., Dati, G., Rocca, M. and Scevaroli, R. (2017). The Mont Cenis Base Tunnel. Geomechanics and Tunnelling, 10: 246-255. doi:10.1002/geot.201700009

Burger, W. (2023). Personal communication.

Burgers, J. M. (1935). Mechanical considerations - model systems - phenomenological theories of relaxation and of viscosity. J.M. Burgers (Ed.), First Report on Viscosity and Plasticity, Nordemann Publishing Company, New York

Cantieni, L., Anagnostou, G. (2009). The Effect of the Stress Path on Squeezing Behaviour in Tunnelling. Rock Mechanics and Rock Engineering 42, 289–318. doi: 10.1007/s00603-008-0018-9

Cantieni, L., Anagnostou, G., Hug, R. (2011). Interpretation of Core Extrusion Measurements When Tunnelling Through Squeezing Ground. Rock Mechanics and Rock Engineering, 44. doi: 10.1007/s00603-011-0170-5

Clausen, J. (2007). Efficient Non-Linear Finite Element Implementation of Elasto-Plasticity for Geotechnical Problems. Esbjerg Institute of Technology, Aalborg University.

190

Clausen, J., Damkilde, L., & Andersen, L. (2007). An efficient return algorithm for non-associated plasticity with linear yield criteria in principal stress space. Computers & Structures, 85(23–24), 1795–1807. doi :10.1016/J.COMPSTRUC.2007.04.002

Corbetta, F. (1990). Nouvelles méthodes d'étude des tunnels profonds : calculs analytiques et numériques. Thèse. École Nationale Supérieure des Mines de Paris, France, French. Available at: http://www.theses.fr/1990ENMP0227

Dassault Systèmes (2018). ABAQUS 2018 Theory manual. Dassault Systèmes Simulia Corp., Providence, Rhode Island

Debernardi, D. (2008). Viscoplastic behaviour and design of tunnels. Ph.D. Thesis, Politecnico di Torino, Department of Structural and Geotechnical Engineering, Italy.

De la Fuente, M., Sulem, J., Taherzadeh, R., Subrin, D. (2020). Tunneling in Squeezing Ground: Effect of the Excavation Method. Rock Mechanics and Rock Engineering, 53(2), 601-623. doi: 10.1007/s00603-019-01931-4

Debernardi, D. (2008). Viscoplastic behaviour and design of tunnels. Ph.D. Thesis, Politecnico di Torino, Italy

Egger, P., Ohnuki, T., & Kanoh, Y. (1982). Bau des Nakayama-Tunnels Kampf gegen Bergwasser und vulkanisches Lockergestein. In Engineering Geology and Geomechanics as Fundamentals of Rock Engineering: Contributions to the 30th Geomechanical Colloquium of the Austrian Society for Geomechanics, Salzburg 7.–9. Oktober 1981. pp. 275-293. Springer Vienna.

Ehrbar, H., Gruber, Luzi. R., Sala, A., Zbinden, P. (2016). Tunnelling the Gotthard - the success story of the Gotthard Base Tunnel Published by the STS Swiss Tunnelling Society

Farrokh, E. (2013). Study of utilization factor and advance rate of hard rock TBMs. Ph.D. thesis, Pennsylvania State University, USA.

Farrokh, E. (2020). A study of various models used in the estimation of advance rates for hard rock TBMs. Tunnelling and Underground Space Technology, 97, 103219. doi: 10.1016/j.tust.2019.103219

Franzius, J. N., Potts, D. M. (2005). Influence of mesh geometry on three-dimensional finite-element analysis of tunnel excavation. International Journal of Geomechanics, 5(3), 256-266. doi: 10.1061/(ASCE)1532-3641(2005)5:3(256)

Fritz, P. (1981). Numerische Erfassung rheologischer Probleme in der Felsmechanik. ETH Zürich, Switzerland. Available at: http://hdl.handle.net/20.500.11850/137161

Gärber, R. (2003). Design of deep galleries in low permeable saturated porous media. Thèse No 2721, EPFL Lausanne

Ghaboussi, J., Gioda, G. (1977). On the time-dependent effects in advancing tunnels. International Journal for Numerical and Analytical Methods in Geomechanics, 1(3), 249-269. doi: 10.1002/nag.1610010303

Graziani A, Ribacchi R (2001) Short- and long-term load conditions for tunnels in low permeability ground in the framework of the convergence–confinement method. Adachi et al. (eds), Modern Tunneling Science and Technology, Swets and Zeitlinger1, 83–88

Hamburger, H., Weber, W., 1992. Tunnelbau im Untertagebau – Tunnelvortrieb mit Vollschnitt- und Erweiterungsmaschinen für grosse Durchmesser im Festgestein. Taschenbuch für den Tunnelbau 1993, 139–197, Verlag Glückauf GmbH Essen.

Hasanpour, R., Rostami, J., Barla, G. (2015). Impact of Advance Rate on Entrapment Risk of a Double-Shielded TBM in Squeezing Ground. Rock Mechanics and Rock Engineering, 48(3), 1115-1130. doi: 10.1007/s00603-014-0645-2

Heeres, O. M., Suiker, A. S. J., de Borst, R. (2002). A comparison between the Perzyna viscoplastic model and the Consistency viscoplastic model. European Journal of Mechanics - A/Solids, 21(1), 1-12. doi: 10.1016/S0997-7538(01)01188-3

Hou, S., Liu, Y., Zhuang, W., Zhang, K., Zhang, R., Yang, Q. (2022). Prediction of shield jamming risk for double-shield TBM tunnels based on numerical samples and random forest classifier. Acta Geotechnica. doi: 10.1007/s11440-022-01567-9

Itasca Consulting Group, Inc. (2019) FLAC — Fast Lagrangian Analysis of Continua, Ver. 8.1. Minneapolis: Itasca

Kirsch, E. G. (1898). Die Theorie der Elastizität und die Bedürfnisse der Festigkeitslehre. Zeitschrift des Vereines deutscher Ingenieure, 42, 797–807

Koiter, W. T. (1953). Stress-strain relations, uniqueness and variational theorems for elastic-plastic materials with a singular yield surface. Quarterly of Applied Mathematics, 11(3), 350-354. Available at: http://www.jstor.org/stable/43634060

Kovári, K. (1979). Basic considerations on the design of underground openings. IABSE Surveys = Revues AIPC = IVBH Berichte, 3, 23. doi: 10.5169/seals-44930

Kovári, K., Ehrbar, H. (2008): The tunnel stretches with squeezing rock in the TZM-Nord of the Gotthard Base Tunnel - Design and Execution. Swiss Tunnel Congress, Lucerne. Band 7; SIA Dokumentation, 39-47 (in German)

Kovári K, Staus J (1996) Basic considerations on tunnelling in squeezing ground. Rock Mech Rock Eng 29(4):203–210

Liu, Y., Hou, S., Yang, Q., Jin, F., Chaoyi, L., Qin, P., Zhou, H. (2019). Excavation simulation and support time study of deep buried double-shield TBM tunnel. Fontoura, Rocca & Pavón

Mendoza (Eds). Rock Mechanics for Natural Resources and Infrastructure Development, 2950-2957

Lombardi, G. (1976). Gotthardtunnel: Gebirgsdruckprobleme beim Bau des Strassentunnels.

Lombardi, G., Neuenschwander, M., Panciera, A., 2009. Gibraltar tunnel project update–the geomechanical challenges. Geomech. Tunnelling 2 (5), 578–590.

Lussu, A., Grüllich, S., Kaiser, C. and Fontana, A. (2019). 15 km TBM exploratory tunnel excavation in the construction Lot H33 of the Brenner Base Tunnel. Geomechanics and Tunnelling, 12: 595-603. doi: 10.1002/geot.201900039

Mezger, F., Anagnostou, G., Ziegler, H. J. (2013). The excavation-induced convergences in the Sedrun section of the Gotthard Base Tunnel. Tunnelling and Underground Space Technology, 38, 447-463. doi: 10.1016/j.tust.2013.07.016

Mezger, F. Anagnostou, G. (2019). On the variability of squeezing behaviour in tunnelling. Bundesamt für Strassen, FB 1664 AGT. doi: 10.3929/ethz-b-000424080. Available at: https://www.mobilityplatform.ch/fileadmin/mobilityplatform/normenpool/21754_1644_Inhalt.pdf. Access date: 10.08.2022

Mezger, F. (2019). On the variability of squeezing behaviour in tunnelling. Doctoral dissertation 25638, ETH Zurich. doi: 10.3929/ethz-b-000359768

Mohammadzamani, D., Mahdevari, S., Bagherpour, R. (2019). Evaluation of required thrust force based on advance rates in shielded TBMs under squeezing conditions. Journal of Geophysics and Engineering, 16(5), 842-861. doi: 10.1093/jge/gxz050

Morosoli, D., Cantieni, L., Anagnostou, G. (2023). Design considerations for deep caverns in Opalinus Clay. In Anagnostou, G., Benardos, A., & Marinos, V. P. (Eds.) Expanding Underground-Knowledge and Passion to Make a Positive Impact on the World: Proceedings of the ITA-AITES World Tunnel Congress 2023 (WTC 2023), 12-18 May 2023, Athens, Greece. CRC Press.. pp. 2114-2121. doi: 10.3929/ethz-b-000614352

Nguyen Minh, D., Corbetta, F. (1991). Nouvelle méthodes de calcul des tunnels revêtus incluant l'effet du front de taille. In: 7th congress of the International Society for Rock Mechanics (ISRM), Aachen. A.A. Balkema, Rotterdam, vol 2, pp 1335–1338.

Nordas, A., Natale, M., Leone, Th., Anagnostou, G. (2023a): Thrust force requirements in fault zones with squeezing ground. Computers and Geotechnics, Volume 160, doi: 10.1016/j.compgeo.2023.105479

Nordas, A.N., Brauchart, A, Anthi, M., Anagnostou, G. (2023b). Calibration method and material constants of an anisotropic, linearly elastic and perfectly plastic Mohr-Coulomb constitutive model for Opalinus Clay. Rock Mechanics and Rock Engineering (accepted for publication).

Nordas, A. N., Natale, M., Anagnostou, G., & Cantieni, L. (2023c). Study into the TBM jamming hazard in Opalinus clay. In Anagnostou, G., Benardos, A., & Marinos, V. P. (Eds.) Expanding Underground-Knowledge and Passion to Make a Positive Impact on the World: Proceedings of the ITA-AITES World Tunnel Congress 2023 (WTC 2023), 12-18 May 2023, Athens, Greece. CRC Press. pp. 2146-2153. doi: 10.3929/ethz-b-000614351

Pellet, F. (2004). Viscoplasticity and Rock Damage Applied to Modelling of the Long Term Behaviour of Underground Structures. G. Barla (Ed.). X Ciclo di Conferenze di Meccanica e Ingegneria delle Rocce, Patron Editore, Chapter 14, 423-448

Pellet, F. (2009). Contact between a Tunnel Lining and a Damage-Susceptible Viscoplastic Medium. Computer Modeling in Engineering and Sciences, 52, 279-296. doi: 10.3970/cmes.2009.052.279

Perzyna, P. (1966). Fundamental Problems in Viscoplasticity. In G. G. Chernyi, H. L. Dryden, P. Germain, L. Howarth, W. Olszak, W. Prager, R. F. Probstein, H. Ziegler (Eds.), Advances in Applied Mechanics, Elsevier, Vol. 9, 243-377

Pliego JM (2005) Open session—the Gibraltar Strait Tunnel. An overview of the study process. Tunnelling and underground space technology 20(6):558–569

Ramond, P., Schivre, M. (2019). État de l'art concernantles évolutions des tunnelierset de leurs capacités de 2000 à 2019. AFTES (Recommandation de l'AFTES n°GT4R6F2 du 23 mai 2019) (In French)

Ramoni, M. (2010). On the feasibility of TBM drives in squeezing ground and the risk of shield jamming. (236). Ph.D. Thesis. ETH Zurich. doi: 10.3929/ethz-a-006080779. Available at : http://hdl.handle.net/20.500.11850/30138

Ramoni, M., Anagnostou, G. (2010a). Tunnel boring machines under squeezing conditions. Tunnelling and Underground Space Technology 25(2), 139-157. doi: 10.1016/j.tust.2009.10.003

Ramoni, M., Anagnostou, G. (2010b). Thrust force requirements for TBMs in squeezing ground. Tunnelling and Underground Space Technology, 25(4), 433-455. doi: 10.1016/j.tust.2010.02.008

Ramoni, M., Anagnostou, G. (2011a). Design aids for the planning of TBM drives in squeezing ground. Research project FGU 2007/005 of the Swiss Federal Roads Office (FEDRO), Report 1341. Zürich

Ramoni, M., Anagnostou, G. (2011b). The Effect of Consolidation on TBM Shield Loading in Water-Bearing Squeezing Ground. Rock Mechanics and Rock Engineering, 44(1), 63-83. doi: 10.1007/s00603-010-0107-4

Ramoni, M., Anagnostou, G. (2011c). The Interaction Between Shield, Ground and Tunnel Support in TBM Tunnelling Through Squeezing Ground. Rock Mechanics and Rock Engineering, 44(1), 37-61. doi: 10.1007/s00603-010-0103-8

194

Rispoli, A., Ferrero, A. M., Cardu, M. (2020). From Exploratory Tunnel to Base Tunnel: Hard Rock TBM Performance Prediction by Means of a Stochastic Approach. Rock Mechanics and Rock Engineering, 53(12), 5473-5487. doi: 10.1007/s00603-020-02226-9

Rostami, J. (2008). Hard Rock TBM Cutterhead Modeling for Design and Performance Prediction. Geomechanics and Tunnelling, 1(1), 18-28. doi: 10.1002/geot.200800002

Sänger, B., 2006. Disc cutters for hardrock TBM 1986–2006 – History and tendencies of development. Felsbau 24 (6), 46–51

Schivre, M., Bochon, A., Vinnac, A., Ramond, P., Bianchi, G. W., Fuoco, S. (2014). TBM excavation of the Frejus safety tunnel through highly deformable schistous rock mass under high rock cover. Proceedings of the World Tunnel Congress 2014, Foz do Iguaçu, Brazil

Schneider, A. (2002). Sicherheit gegen Niederbruch im Untertagbau. Ph.D. Thesis. ETH Zurich. (in German) doi: 10.3929/ethz-a-004466621

Skuk, S., Wegscheider, D. (2015). Brenner Base Tunnel – a 10.5 km double shield TBM drive in granite / Brenner Basistunnel – 10,5 km Doppelschild-TBM im Granit. Geomechanik Tunnelbau, 8: 221-238. doi: 10.1002/geot.201500006

Steiner, W. (1996). Tunnelling in squeezing rocks: case histories. *Rock Mechanics and Rock Engineering*, *29*(4), 211-246.

Sterpi, D., Gioda, G. (2009). Visco-Plastic Behaviour around Advancing Tunnels in Squeezing Rock. Rock Mechanics and Rock Engineering, 42(2), 319-339. doi: 10.1007/s00603-007-0137-8

Swannell, N., Palmer, M., Barla, G., Barla, M. (2016). Geotechnical risk management approach for TBM tunnelling in squeezing ground conditions. Tunnelling and Underground Space Technology, 57, 201-210. doi: 10.1016/j.tust.2016.01.013

Tahernia, T., Rostami, J. (2021). The effect of TBM Diameter on Ring installation time, Rapid Excavation and Tunneling Conference 2021. Proceedings Jarrett E. Carlson, Gregg W. Davidson Society for Mining, Metallurgy & Exploration, 6 juin 2021 - 1248 pages.

Terzaghi, K. (1925). Erdbaumechanik auf bodenphysikalischer Grundlage. Deuticke. Wien

Vinnac, A., Marcucci, E., Schivre, M., Semeraro, M., Chiriotti, E. (2014). Performance monitoring for back-analysis of hard rock TBM tunnelling: the case of the Frejus safety tunnel. Proceedings of the World Tunnel Congress 2014, Foz do Iguaçu, Brazil

Vlachopoulos, N., Diederichs, M.S., 2009. Improved longitudinal displacements profiles for convergence confinement analysis of deep tunnel. Rock Mech. Rock Eng. 42, 131–146. doi: 10.1007/s00603-009-0176-4

Vogelhuber, M. (2007). Der Einfluss des Porenwasserdrucks auf das mechanische Verhalten kakiritisierter Gesteine. Doctorate thesis dissertation No. 17079, Institut für Geotechnik, ETH Zürich, Zurich, Switzerland (in German).. doi: 10.3929/ethz-a-005399238

Vogelhuber, M., Pimentel, E., Anagnostou, G. (2023). Strength, deformability and permeability of kakiritic rocks from the Gotthard base tunnel. Journal of Rock Mechanics and Geotechnical Engineering. doi: 10.1016/j.jrmge.2023.03.009

Vrakas, A., Anagnostou, G. (2015). A simple equation for obtaining finite strain solutions from small strain analyses of tunnels with very large convergences. Géotechnique, 65(11), 936-944. doi:10.1680/jgeot.15.P.036

Vrakas, A., Dong, W., Anagnostou, G. (2018). Elastic deformation modulus for estimating convergence when tunnelling through squeezing ground. Géotechnique, 68(8), 713-728. doi:10.1680/jgeot.17.P.008

Zhang, J.-Z., Zhou, X.-P. (2017). Time-dependent jamming mechanism for Single-Shield TBM tunneling in squeezing rock. Tunnelling and Underground Space Technology, 69, 209-222. doi: 10.1016/j.tust.2017.06.020

Zhang, Y., Xu, W.-y., Shao, J.-f., Zhao, H.-b., Wang, W. (2015). Experimental investigation of creep behavior of clastic rock in Xiangjiaba Hydropower Project. Water Science and Engineering, 8(1), 55-62. doi: 10.1016/j.wse.2015.01.005

Zienkiewicz, O. C., Cormeau, I. C. (1974). Visco-plasticity—plasticity and creep in elastic solids—a unified numerical solution approach. International Journal for Numerical Methods in Engineering, 8(4), 821-845. doi: 10.1002/nme.1620080411

Zienkiewicz, O. C., Humpheson, C., Lewis, R. W. (1975). Associated and non-associated visco-plasticity and plasticity in soil mechanics. Géotechnique, 25(4), 671-689. doi: 10.1680/geot.1975.25.4.671